To the Graduate Council:

I am submitting herewith a thesis written by M. Vasudevan entitled "Characterization and Control of Slugging Behavior of Geldart's Group D Particles in a Laboratory Scale Fluidized Bed." I have examined the final copy of this thesis for form and content, and recommend that it be accepted in partial fulfillment of the requirements for the degree of Master of Science, with a major in Mechanical Engineering.

Ke Nguyen, Major Professor

We have read this thesis and
recommend its acceptance:

Accepted for the council:

Associate Vice Chancellor and
the Dean of the Graduate School

STATEMENT OF PERMISSION TO USE

In presenting this thesis in partial fulfillment of the requirements for a master's degree at The University of Tennessee, Knoxville, I agree that the library shall make it available to borrowers under rules of the library. Brief quotations from this thesis are allowable without special permission, provided that accurate acknowledgement of the source is made.

Requests for permission for extensive quotation from or reproduction of this thesis in whole or parts may be granted by the copyright holder.

Signature M. Vasudevan

Date 07/28/95

CHARACTERIZATION AND CONTROL OF SLUGGING BEHAVIOR OF GELDART'S GROUP-D PARTICLES IN A LABORATORY SCALE FLUIDIZED BED

A thesis presented for the Master of Science degree

The University of Tennessee, Knoxville

M. Vasudevan

August 1995

Copyright © M. Vasudevan, 1995

All rights reserved

ACKNOWLEDGEMENTS

I would like to express my sincere gratitude to my advisor Dr. Ke Nguyen and to Dr. C.S. Daw for their invaluable guidance, support and patience throughout the course of this research. I would like to thank Dr.JR. Parsons, Dr. J.W. Hodgson and Dr. D.D. Bruns for sparing their valuable time to serve on my graduate committee. I would like to thank Charles E.A. Finney for sparing a considerable amount of his time during the experiments and for his numerous computer programs and Nick van Goor for his critical control routine. I would like to thank my friends K.D. Edwards, C.E.A. Finney and C. Pitchaiah for making this phase of my life a pleasure.

Finally, I would like to thank the three persons who made my dream of higher studies come true. Dr. R.P. Krishnan for getting me this opportunity to study at the University of Tennessee, my wife Gomathi for patiently putting up with my crazy work habits and my mother for allowing me to leave my country and come here for higher education.

I gratefully acknowledge the Morgantown Energy Technology Center and Oak Ridge National Laboratory for financial support of this research.

ABSTRACT

Fluidization behavior of Geldart's group D particles was investigated for characterization of slugging and for developing control strategies using the recent developments in the field of nonlinear dynamics and chaos.

Results demonstrate that chaotic time series analysis of pressure drop measurements can be used for characterization of slugging behavior. Dynamic features associated with different regimes have been identified. The transition from regular slugging to chaotic behavior at increased gas flow rates was identified as intermittency route to chaos.

A feedback control method based on nonlinear sensitivity of chaotic systems to small perturbations was developed and implemented. Control perturbations are made by injecting small pulses of fluidization gas through a nozzle located on the bed wall just above the distributor. A control routine determines the dynamical state of the bed from the pressure signal and introduces the pressure pulse based on an empirically learned rule base. The pressure drop is measured much faster than the slugging frequency, while control perturbations are made at time scales on the order of the bed frequency. The time-averaged gas flow through the injector is typically less than four percent of the total gas flow through the bed.

Results demonstrate that selective application of small perturbations to a slugging bed of Geldart's group D particles can greatly change the overall dynamics, permitting stabilization or destabilization of the slugging. Based on the experimental results we conclude that it may be possible to employ similar feedback control strategies in commercial fluidized beds of Group D particles to enhance or reduce slugging.

TABLE OF CONTENTS

1. INTRODUCTION 1

2. LITERATURE REVIEW 7

2.1 MODIFICATION OF FLUIDIZATION BEHAVIOR 7

2.1.1 SONIC ENERGY PULSING 10

2.1.2 INTERMITTENT GAS FLOW PULSING 11

2.2 INTERMITTENCY ROUTE TO CHAOS 13

2.3 CONTROLLING CHAOS 16

3. EXPERIMENTAL APPARATUS AND PROCEDURE 21

3.1 DESCRIPTION OF THE EXPERIMENTAL APPARATUS 21

3.1.1 LABORATORY SCALE FLUIDIZED BED 21

3.1.2 AIR DISTRIBUTOR PLATE 23

3.1.3 BED PARTICLES 25

3.1.4 DIFFERENTIAL PRESSURE TRANSDUCERS 26

3.1.5 DUAL HI / LO FILTERS 27

3.1.6 DIGITAL OSCILLOSCOPE 27

3.1.7 CONTROL SYSTEM 28

3.2 OVERVIEW OF EXPERIMENTAL PROCEDURE 28

4. DATA ANALYSIS TECHNIQUES 30

4.1 MUTUAL INFORMATION 30

4.2 PHASE SPACE TRAJECTORY RECONSTRUCTION FOR VISUALIZATION 31

4.3 CORRELATION DIMENSION 33

4.4 KOLMOGOROV ENTROPY 35

4.5 CYCLE PERIOD AND MAGNITUDE 36

4.6 TIME RETURN MAPS 37

5. EXPERIMENTAL RESULTS AND DISCUSSIONS 38

5.1 CHARACTERIZATION OF SLUGGING BEHAVIOR 38

5.1.1 GENERAL OBSERVATIONS 39

5.1.2 CYCLE MAGNITUDE AND PERIOD 44

5.1.3 POWER SPECTRA 49

5.1.4 CORRELATION DIMENSION AND ENTROPY 50

5.1.5 PHASE SPACE TRAJECTORIES FOR VISUALIZATION 56

5.1.6 TIME RETURN MAPS 59

5.1.7 TRANSITION TO CHAOS 63

5.2 CONTROL STRATEGY 66

5.2.1 EMPIRICAL DETERMINATION OF CONTROL PARAMETERS 68

5.2.2 DIFFERENCES BETWEEN PLENUM AND LOCAL SIGNAL . 74

5.3 EVALUATION OF CONTROL SCHEME 79

5.3.1 PHYSICAL EXPLANATION OF CONTROL PERTURBATION 79

5.3.2 COMPARISON BETWEEN CONTROL BASED ON LOCAL SIGNAL AND PLENUM SIGNAL 79

5.3.3 EVALUATION OF CONTROL AT DIFFERENT FLUIDIZATION CONDITIONS WITH STEEL 88

5.3.4 EVALUATION OF CONTROL AT DIFFERENT FLUIDIZATION CONDITIONS WITH GLASS 106

5.3.5 SUMMARY OF CONTROL EVALUATION EXPERIMENT RESULTS 117

6.0 CONCLUSIONS AND RECOMMENDATIONS 119

REFERENCES 121

APPENDICES 124

APPENDIX A 125

APPENDIX B 129

APPENDIX C 157

VITA 177

LIST OF TABLES

TABLE		PAGE
1.	Physical properties of particles and fluidization velocities	26
2.	Control parameters for determining the optimum pulse timing for steel at U_{MSS}	69
3.	Control parameters for determining the optimum pulse width for steel at U_{MSS}	72
4.	Operating conditions for the set of experiments for comparing plenum and local control effectiveness	80
5.	Operating conditions for control evaluation experiments for steel	92
6.	Operating conditions for control evaluation experiments for glass	109
B1.	Dimension results based on the local signal for slugging characterization experiments using steel over a velocity range of U/U_{MF} = 1.07 To 2.07	153
B2.	Dimension results based on the local signal for slugging characterization experiments using glass over a velocity range of U/U_{MF} = 1.04 To 1.99	154
B3.	Entropy results based on the local signal for slugging characterization experiments using steel over a velocity range of U/U_{MF} = 1.07 To 2.07	155
B4.	Entropy results based on the local signal for slugging characterization experiments using glass over a velocity range of U/U_{MF} = 1.04 To 1.99	156
C1.	Dimension results for evaluation of control experiments at different control modes for steel	174
C2.	Entropy results for evaluation of control experiments at different control modes for steel	175

C3. Dimension results for evaluation of control experiment for glass at the breaking slug regime (U/U_{MF} = 1.59) 176

C4. Entropy results for evaluation of control experiment for glass at the breaking slug regime (U/U_{MF} = 1.59) 176

LIST OF FIGURES

Figure Page

1. Classification of fluidization based on gas-solid contacting 2

2. Classification of particles based on their fluidization behavior in air at ambient conditions 4

3. Sonic energy pulsing scheme : Sonic energy imposed at the plenum (A) or at the bed boundary (B) 8

4. Intermittent gas flow pulsing scheme 9

5. Illustration for transition behavior of the Lorenz model using Z variable for increasing r values 14

6. Intermittency behavior of the iterates near the formerly stable fixed point 14

7. Illustrations for the OGY method of controlling chaos 17

8. Schematic of the laboratory scale fluidized bed apparatus 22

9. Cross sectional view of the lower portion of the bed showing pressure tap arrangement 24

10. Side view of the lower portion of the bed showing pressure tap locations, pulse nozzle and distributor 24

11. Illustration for cycle period and magnitude 36

12. Typical time series segments of local pressure signal for steel at four different fluidization conditions 40

13. Typical time series segments of local pressure signal for glass at four different fluidization conditions 41

14. Composite plot illustrating the variation in cycle magnitude for steel over a velocity range of U/U_{MF} = 1.07 to 2.07 45

15. Composite plot illustrating the variation in cycle magnitude for glass over a velocity range of U/U_{MF} = 1.04 to 1.99 46

16. Composite plot illustrating the variation in cycle period for steel over a velocity range of U/U_{MF} = 1.07 to 2.07 47

17. Composite plot illustrating the variation in cycle period for glass over a velocity range of U/U_{MF} = 1.04 to 1.99 48

18. Fourier power spectra of local pressure signal for steel at four different fluidization regimes 51

19. Fourier power spectra of local pressure signal for glass at four different fluidization regimes 52

20. Variation of dimension and entropy based on local signal for steel over a velocity range of U/U_{MF} = 1.07 to 2.07 54

21. Variation of dimension and entropy based on local signal for glass over a velocity range of U/U_{MF} = 1.04 to 1.99 55

22. Two dimensional projection of reconstructed trajectories from local pressure signal for steel at four different fluidization regimes [Time span = 50 s] 57

23. Two dimensional projection of reconstructed trajectories from local pressure signal for glass at four different fluidization regimes [Time span = 50 s] 58

24. Time return maps using local pressure signal for steel at four different fluidization regimes 60

25. Time return maps using local pressure signal for glass at four different fluidization regimes 61

26. Intermittency route to chaos power law fit curves for steel using U_{MSS} = 4.61 m/s as R_C; for glass using U_{MSS} = 1.73 m/s as R_C and for Lorenz system (b = 8/3 and σ = 10) using r = 166.07 as R_C 65

27. Illustration for the control scheme 67

28. Effect of pulse timing on dimension and entropy estimations for steel at a constant pulse width of 50 ms and a velocity of U/U_{MF} = 1.28 71

29. Effect of pulse width on dimension and entropy estimations for steel at optimum pulse timing 0.93 kPa & up and stabilization control at a velocity of U/U_{MF} = 1.28 73

30. Effect of pulse width on dimension and entropy estimations for steel at optimum pulse timing -0.48 kPa & down and destabilization control at a velocity of U/U_{MF} = 1.28 75

31. Complexity differences in plenum and local signals, illustrated using typical time series segments for steel in the maximum stable slugging state (U/U_{MF} = 1.28) 77

32. Typical time series segments illustrating the effect of transient disturbances introduced by pulsing 78

33. Typical segments of time series for steel with no control and stabilization control modes using plenum or local signal as the control signal [U/U_{MF} = 1.28] 81

34. Typical segments of time series for steel with destabilization control using plenum or local signal as the control signal [U/U_{MF} = 1.28] 82

35. Fourier power spectra for steel illustrating the effect of using different signals for stabilization control compared with the no control case at the maximum stable slugging state [U/U_{MF} = 1.28] 84

36. Fourier power spectra for steel illustrating the effect of using different signals for destabilization control compared with no control case at the maximum stable slugging state [U/U_{MF} = 1.28] 85

37. Variation in cycle magnitudes for steel with different control signals compared with no control case at the maximum stable slugging state [U/U_{MF} = 1.28] 86

38. Variation of dimension and entropy for steel with different control signals for various control modes at the maximum stable slugging state [U/U_{MF} = 1.28] 87

39. Typical time series segments for steel with different control modes at the developing slug regime (Run C1; U/U_{MF} = 1.16) 89

40. Typical time series segments for steel with different control modes at the maximum stable slugging state (Run C2; U/U_{MF} = 1.28) 90

41. Typical time series segments for steel with different control modes at the breaking slug regime (Run C3; U/U_{MF} = 1.55) 91

42. Fourier power spectra for steel with different control modes at the developing slug regime (Run C1; U/U_{MF} = 1.16) 93

43. Fourier power spectra for steel with different control modes at the maximum stable slugging state (Run C2; U/U_{MF} = 1.28) 94

44. Fourier power spectra for steel with different control modes at the breaking slug regime (Run C3; U/U_{MF} = 1.55) 95

45. Three dimensional projection of the reconstructed trajectories for steel with different control modes at the developing slug regime (Run C1; U/U_{MF} = 1.16; Time span = 25 s) 97

46. Three dimensional projection of the reconstructed trajectories for steel with different control modes at the maximum stable slugging state (Run C2; U/U_{MF} = 1.28; Time span = 25 s) 98

47. Three dimensional projection of the reconstructed trajectories for steel with different control modes at the breaking slug regime (Run C3; U/U_{MF} = 1.55; Time span = 25 s) 99

48. Variation in cycle magnitudes for steel with different control modes at the developing slug regime (Run C1; U/U_{MF} = 1.16) 100

49. Variation in cycle magnitudes for steel with different control modes at the maximum stable slugging state (Run C2; U/U_{MF} = 1.28) 101

50. Variation in cycle magnitudes for steel with different control modes at the breaking slug regime (Run C3; U/U_{MF} = 1.55) 102

51. Time return maps for steel with different control modes at the developing slug regime (Run C1; U/U_{MF} = 1.16) 103

52. Time return maps for steel with different control modes at the maximum stable slugging state (Run C2; U/U_{MF} = 1.28) 104

53. Time return maps for steel with different control modes at the breaking slug regime (Run C3; U/U_{MF} = 1.55) 105

54. Variation in dimension with control mode for steel at three different fluidization regimes 107

55. Variation in entropy with control mode for steel at three different fluidization regimes 108

56. Typical time series segments for glass with different control modes at the breaking slug regime (U/U_{MF} = 1.59) 110

57. Fourier power spectra for glass with different control modes at the breaking slug regime (U/U_{MF} = 1.59) 111

58. Three dimensional projection of the reconstructed trajectories for glass with different control modes at the breaking slug regime (U/U_{MF} = 1.59; Time span = 20 s) 113

59. Variation in cycle magnitudes for glass with different control modes at the breaking slug regime (U/U_{MF} = 1.59) 114

60. Time return maps for glass with different control modes at the breaking slug regime (U/U_{MF} = 1.59) 115

61. Variation in dimension and entropy with different control modes for glass at the breaking slug regime (U/U_{MF} = 1.59) 116

APPENDIX A

A1. Pressure drop characteristics of the tuyere-nozzle distributor used in the experiments 126

A2. Minimum fluidization velocity for steel BB 127

A3. Minimum fluidization velocity for glass 128

APPENDIX B

B1. Typical time series segments of local pressure signal for steel over a velocity range of U/U_{MF} = 1.07 to 1.20 130

B2. Typical time series segments of local pressure signal for steel over a velocity range of U/U_{MF} = 1.28 to 1.68 131

B3. Typical time series segments of local pressure signal for steel over a velocity range of U/U_{MF} = 1.80 to 2.07 132

B4. Fourier power spectra of local pressure signal for steel over a velocity range of U/U_{MF} = 1.07 to 1.40 133

B5. Fourier power spectra of local pressure signal for steel over a velocity range of U/U_{MF} = 1.55 to 2.07 134

B6. Two dimensional projection of reconstructed trajectories from local pressure signal for steel over a velocity range of U/U_{MF} = 1.07 to 1.40 [Time span = 50 s] 135

B7. Two dimensional projection of reconstructed trajectories from local pressure signal for steel over a velocity range of U/U_{MF} = 1.55 to 2.07 [Time span = 50 s] 136

B8. Time return maps using local pressure signal for steel over a velocity range of U/U_{MF} = 1.07 to 1.40 137

B9. Time return maps using local pressure signal for steel over a velocity range of U/U_{MF} = 1.55 to 2.07 138

B10. Typical time series segments of local pressure signal for glass over a velocity range of U/U_{MF} = 1.04 to 1.19 139

B11. Typical time series segments of local pressure signal for glass over a velocity range of U/U_{MF} = 1.24 to 1.39 140

B12. Typical time series segments of local pressure signal for glass over a velocity range of U/U_{MF} = 1.44 to 1.69 141

B13. Typical time series segments of local pressure signal for glass over a velocity range of U/U_{MF} = 1.79 to 2.24 142

B14. Typical time series segments of local pressure signal for glass over a velocity range of U/U_{MF} = 2.49 to 2.99 143

B15. Fourier power spectra of local pressure signal for glass over a velocity range of U/U_{MF} = 1.04 to 1.29 144

B16. Fourier power spectra of local pressure signal for glass over a velocity range of U/U_{MF} = 1.34 to 1.69 145

B17. Fourier power spectra of local pressure signal for glass over a velocity range of U/U_{MF} = 1.79 to 2.74 146

B18. Two dimensional projection of reconstructed trajectories from local pressure signal for glass over a velocity range of U/U_{MF} = 1.04 to 1.29 [Time span = 50 s] 147

B19. Two dimensional projection of reconstructed trajectories from local pressure signal for glass over a velocity range of U/U_{MF} = 1.34 to 1.69 [Time span = 50 s] 148

B20. Two dimensional projection of reconstructed trajectories from local pressure signal for glass over a velocity range of U/U_{MF} = 1.79 to 2.74 [Time span = 50 s] 149

B21. Time return maps using local pressure signal for glass over a velocity range of U/U_{MF} = 1.04 to 1.29 150

B22. Time return maps using local pressure signal for glass over a velocity range of U/U_{MF} = 1.34 to 1.69 151

B23. Time return maps using local pressure signal for glass over a velocity range of U/U_{MF} = 1.79 to 2.74 152

APPENDIX C

C1. Typical time series segments for steel illustrating the effect of pulse timing at a velocity of U/U_{MF} = 1.28, a fixed pulse width of 50 ms and over a range of pulse timing (No control to -0.47 kPa & up) 158

C2. Typical time series segments for steel illustrating the effect of pulse timing at a velocity of U/U_{MF} = 1.28, a fixed pulse width of 50 ms and over a range of pulse timing (0.0 Kpa & up to +0.93 kPa & up) . . 159

C3. Typical time series segments for steel illustrating the effect of pulse timing at a velocity of U/U_{MF} = 1.28, a fixed pulse width of 50 ms and over a range of pulse timing (+0.93 kPa & down to 0.0 kPa & down) . 160

C4. Typical time series segments for steel illustrating the effect of pulse timing at a velocity of U/U_{MF} = 1.28, a fixed pulse width of 50 ms and over a range of pulse timing (-0.47 kPa & down to -0.93 kPa & down) . 161

C5. Three dimensional projection of the reconstructed trajectory for steel illustrating the effect of pulse timing at a velocity of U/U_{MF} = 1.28, a fixed pulse width of 50 ms and over a range of pulse timing (No control to -0.47 kPa & up) [Time span = 25 s] 162

C6. Three dimensional projection of the reconstructed trajectory for steel illustrating the effect of pulse timing at a velocity of U/U_{MF} = 1.28, a fixed pulse width of 50 ms and over a range of pulse timing (0.0 kPa & up to +0.93 kPa & up) [Time span = 25 s] 163

C7. Three dimensional projection of the reconstructed trajectory for steel illustrating the effect of pulse timing at a velocity of U/U_{MF} = 1.28, a fixed pulse width of 50 ms and over a range of pulse timing (+0.93 kPa & down to 0.0 kPa & down) [Time span = 25 s] 164

C8. Three dimensional projection of the reconstructed trajectory for steel illustrating the effect of pulse timing at a velocity of U/U_{MF} = 1.28, a fixed pulse width of 50 ms and over a range of pulse timing (-0.47 kPa & down to -0.93 kPa & down) [Time span = 25 s] 165

C9. Typical time series segments for steel illustrating the effect of pulse width at a velocity of U/U_{MF} = 1.28, a fixed pulse timing of +0.93 kPa & up and over a range of pulse width (No control to 50 ms) 166

C10. Typical time series segments for steel illustrating the effect of pulse width at a velocity of U/U_{MF} = 1.28, a fixed pulse timing of +0.93 kPa & up and over a range of pulse width (75 ms to 150 ms) . . 167

C11. Typical time series segments for steel illustrating the effect of pulse width at a velocity of U/U_{MF} = 1.28, a fixed pulse timing of -0.47 kPa & down over a range of pulse width (25 ms to 75 ms) 168

C12. Typical time series segments for steel illustrating the effect of pulse width at a velocity of U/U_{MF} = 1.28, a fixed pulse timing of -0.47 kPa & down and over a range of pulse width (100 ms to 150 ms) 169

C13. Three dimensional projection of the reconstructed trajectories for steel illustrating the effect of pulse width at a velocity of U/U_{MF} = 1.28, a fixed pulse timing of +0.93 kPa & up and over a range of pulse width (No control to 50 ms) [Time span = 25 s] 170

C14. Three dimensional projection of the reconstructed trajectories for steel illustrating the effect of pulse width at a velocity of U/U_{MF} = 1.28, a fixed pulse timing of +0.93 kPa & up and over a range of pulse width (75 ms to 150 ms) [Time span = 25 s] 171

C15. Three dimensional projection of the reconstructed trajectories for steel illustrating the effect of pulse width at a velocity of U/U_{MF} = 1.28, a fixed pulse timing of -0.47 kPa & down and over a range of pulse width (25 ms to 75 ms) [Time span = 25 s] 172

C16. Three dimensional projection of the reconstructed trajectories for steel illustrating the effect of pulse width at a velocity of U/U_{MF} = 1.28, a fixed pulse timing of -0.47 kPa & down and over a range of pulse width (100 ms to 150 ms) [Time span = 25 s] 173

LIST OF SYMBOLS

ρ_P	density of solid particles
ρ_G	density of the fluidizing medium
d_P	mean diameter of the solid particles
r	parameter in the Lorenz system of equations
r_C	critical parameter of r beyond which the regular behavior of the Lorenz system is interrupted by irregular bursts.
U	superficial gas velocity of the fluidizing gas
U_{MF}, Umf	minimum fluidization velocity
U_{MSS}, Umss	superficial gas velocity at the maximum stable slugging state

CHAPTER 1

INTRODUCTION

Fluidization is a process in which a mass of particulate solids are suspended in a fluid-like state by the upward flow of a gas or liquid. When the velocity of the fluid flow exceeds a minimum value at which the frictional force (drag) between the fluid and particles counter-balances the gravitational force of the particles, the solid particles become suspended and behave like a fluid. In this state, there is a high degree of turbulent mixing and gas-solid contacting in the bed resulting in increased mass and heat transfer coefficients. In addition to good mixing, fluidized beds have other advantages such as ease of large-scale operation and continuous processing. On the negative side, fluidized beds have numerous design and operation problems such as erosion/corrosion of in bed surfaces, elutrition of particles, and agglomeration of particles at certain operating conditions. However, because of the overwhelming advantage of efficient mixing and gas-solid contacting, fluidized beds are widely used in industrial applications such as chemical reactors, dryers and combustors.

Mixing and gas solid contacting in a fluidized bed are significantly influenced by solid particle properties such as density, size, and size range and operating conditions such as fluid velocity, pressure and temperature. Based on gas-solid contacting, fluidization can be classified in to different regimes as shown in Figure 1 (Kunii and Levenspiel [1]). At gas flow rates below minimum fluidization, the bed will act like a fixed bed. At gas flow rate sufficient enough to overcome the gravitational forces, the particles will be lifted up and will be simmering with little bed expansion. This state is

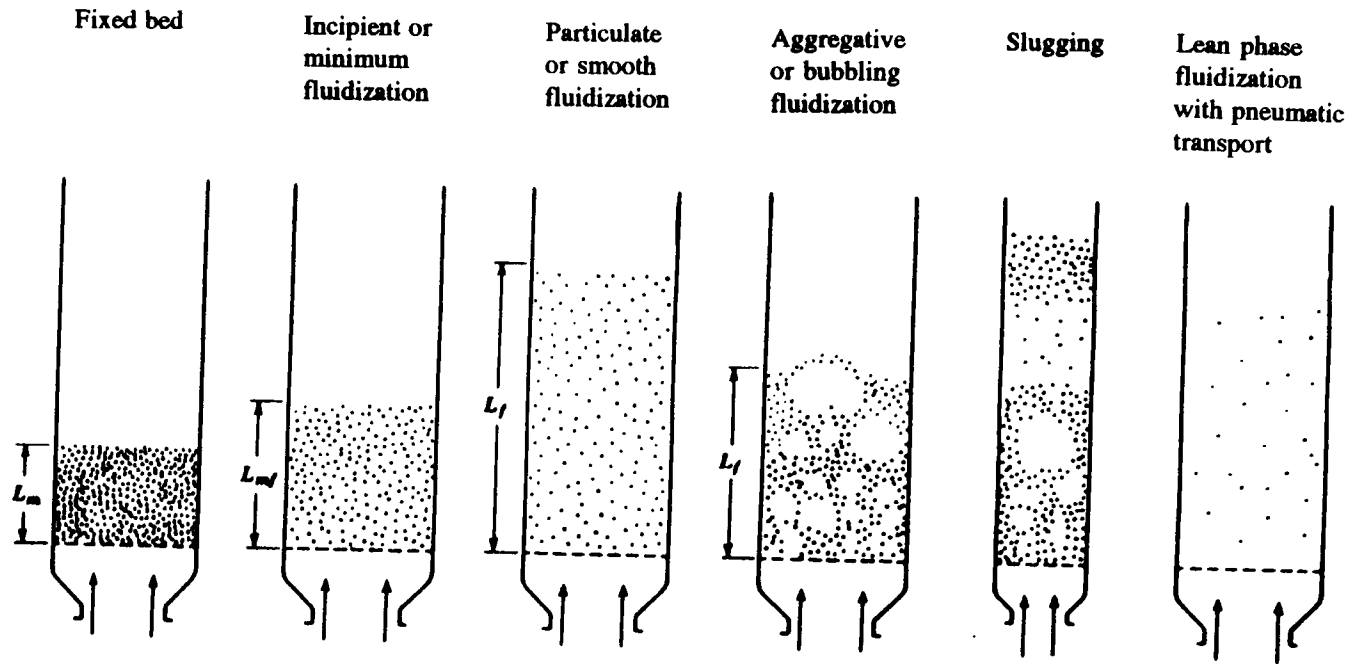


Figure 1. Classification of fluidization based on gas-solid contacting.

Source : Kunni, D., and Levenspiel, D., 1969, "Fluidization engineering", *Robert E. Krieger publishing company, Inc.*

classified as incipient or minimum fluidization. Beyond this flow rate, some beds will expand considerably without bubbling and this condition is known as particulate fluidization. With further increase in flow rate bubbles or voidages will appear in the bed and complex coalescence patterns can be observed. This behavior is known as aggregative or bubbling fluidization. Further increase in flow rate results in larger bubbles. At certain flow rates depending on parameters such as particle size, density and bed dimension, large bubbles/voidages spanning the entire cross section of the bed can be seen. This type of behavior is classified as slugging. With further increase in velocity, particles are entrained in the gas stream and pneumatic transport occurs.

For a wide range of velocities, the fluidization regimes exhibited by a bed is strongly influenced by the physical properties of the solid particles. Geldart [2] classified a wide range of particles in to different groups based on their fluidization behavior using particle and gas densities and size range. Geldart's classification scheme is illustrated in Figure 2. Very fine particles have considerable cohesive forces, which inhibit free flowing particulate behavior. These solids are poorly fluidized at any gas flow rate and are prone to channeling. Particles exhibiting such behavior are classified as group C. Some fine and low density particles exhibit considerable bed expansion without bubbling at gas velocities above minimum fluidization velocity. A distinct minimum bubbling velocity and very fast bubbles are seen in these beds. Such particles are classified as group A. Medium size and density particles like common sand do not expand considerably before bubbling. These particles start bubbling immediately beyond minimum fluidization and are classified as group B. Large, coarse particles of high

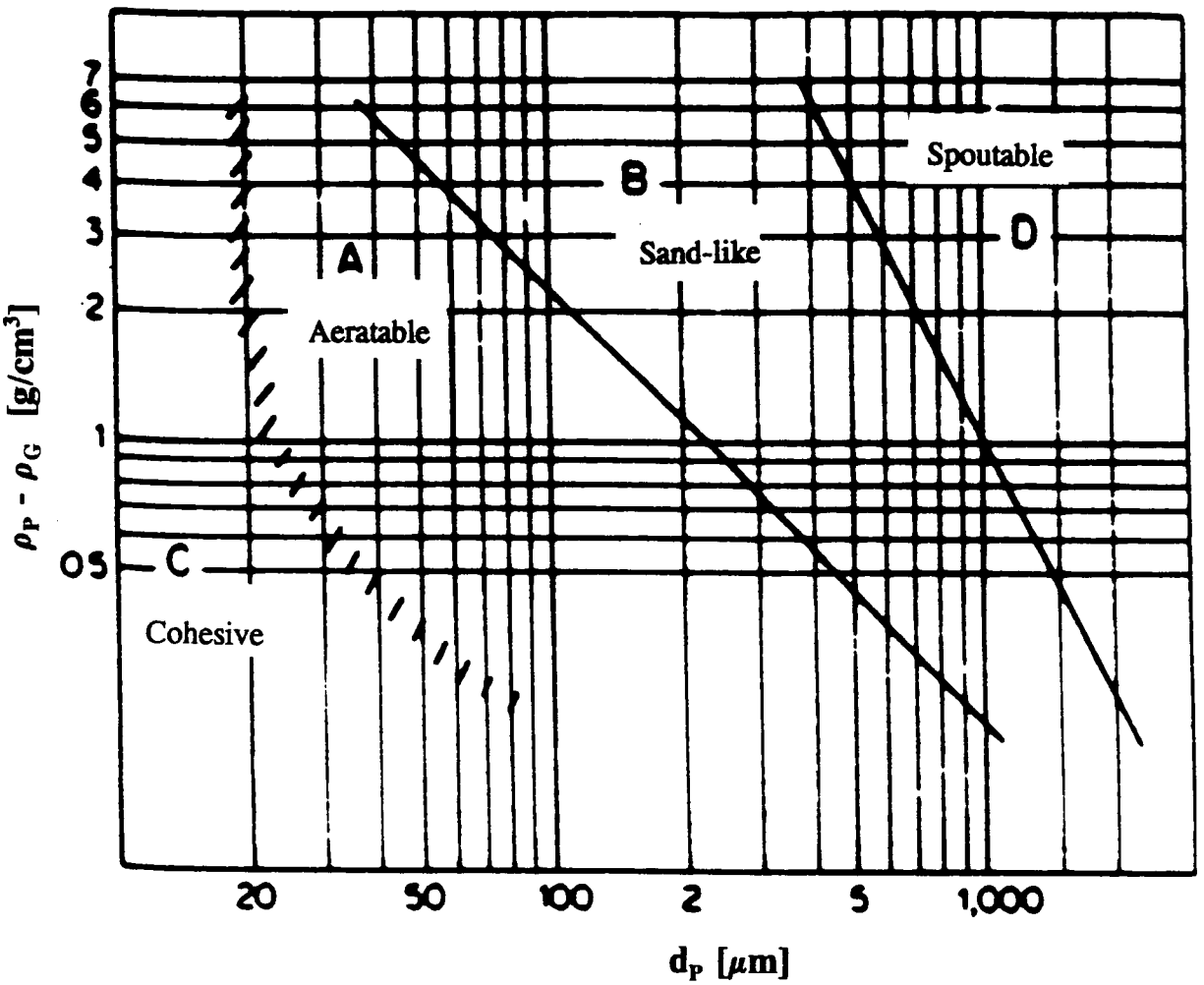


Figure 2. Classification of particles based on their fluidization behavior in air at ambient conditions, where $(\rho_P-\rho_G)$ is the density difference between the particle and fluidizing air, and d_P is the mean diameter of the solid particles.

Source : "Gas fluidization technology", 1986, edited by Geldart, D., *A Wiley-Interscience publication.*

density classified as group D , tend to produce bubbles that are flattened in the vertical direction and move sluggishly in the bed. Although slow moving bubbles or voidages are seen for gas flows just above minimum fluidization velocity, further increase in velocity results in large bubbles or gas pockets of the order of bed diameter. Mixing and gas-solid contacting are typically poor in this regime.

Many industrial fluidized beds use group B or D particles and operate in the bubbling or slugging regime. Bubbles promote solid circulation and bed-mass homogeneity, but when they are excessively large, they serve as conduits for gas by-pass, reducing gas-solid contacting.

Different distributor designs, introducing baffles or packing in the bed etc., have been tried to improve gas-solid contacting by reducing the size or inducing break up of bubbles in the bed. Concepts like pulsing the fluidized bed with sonic energy or intermittent gas flows to increase gas-solid contacting have also been investigated. The results were mixed and are not always practical for a wide variety of applications.

Recent studies by Skrzycke, Nguyen and Daw [3], Daw et al. [4], Daw and Hallow [5,6] and Schouten and Van den Bleek [7] have shown that fluidized beds exhibit many features associated with deterministic chaos. The concept of using the well-known sensitivity of chaotic systems to small perturbations for control, originally proposed by Ott, Gregobi and Yorke [8] and implemented experimentally by Ditto et al. [9] has stimulated much interest in the area of control of chaotic systems. These developments have motivated the present study.

The objectives of this study are to characterize group D slugging behavior using chaotic time series analysis techniques and to develop and implement a control strategy utilizing the sensitivity of chaotic systems to small perturbation to control the slugging. A laboratory scale fluidized bed, operated intentionally in the slugging regime with Geldart's group D particles is used in this study. Differential pressure signals, known to correlate well with the fluidization dynamics are used for assessing system behavior and for taking control actions.

This thesis presents the results of the work done towards achieving the objectives and is organized as follows. A brief review of literature relevant to the present study is presented in chapter 2. Experimental apparatus and procedures used in the study are described in chapter 3. Chapter 4 gives a brief review of the theoretical background of the data analysis techniques and the calculation procedures used. Results from this study are discussed in chapter 5, and chapter 6 presents the conclusions drawn from this study and recommendations for future work.

CHAPTER 2

LITERATURE REVIEW

In this chapter, the focus will be on the most relevant past work in the area of fluidization and control of chaotic systems. A brief review of earlier work done on modification of fluidization behavior is presented in section 2.1. Literature on intermittency route to chaos is reviewed in section 2.2. Section 2.3 reviews the recent developments in the control of chaotic systems.

2.1 MODIFICATION OF FLUIDIZATION BEHAVIOR

Various researchers have investigated pulsing fluidized beds with sonic energy or intermittent gas flows to improve gas solid contacting. With sonic pulsing, sound energy is imposed on the bed from the plenum or at the bed exit boundary to introduce pressure fluctuations in the fluidizing medium. Schematically the two different methods are shown in Figure 3.

The intermittent gas flow pulsing scheme relies on modulating the entire fluidizing gas flow as shown in Figure 4. The fluidizing gas is admitted in the bed allowing bubbles to form and the bed to expand. Then the gas flow is cut off, inducing the bubbles to collapse and the bed to shrink. By repeating this in a cyclic manner at an optimum frequency, the bed behavior is modified.

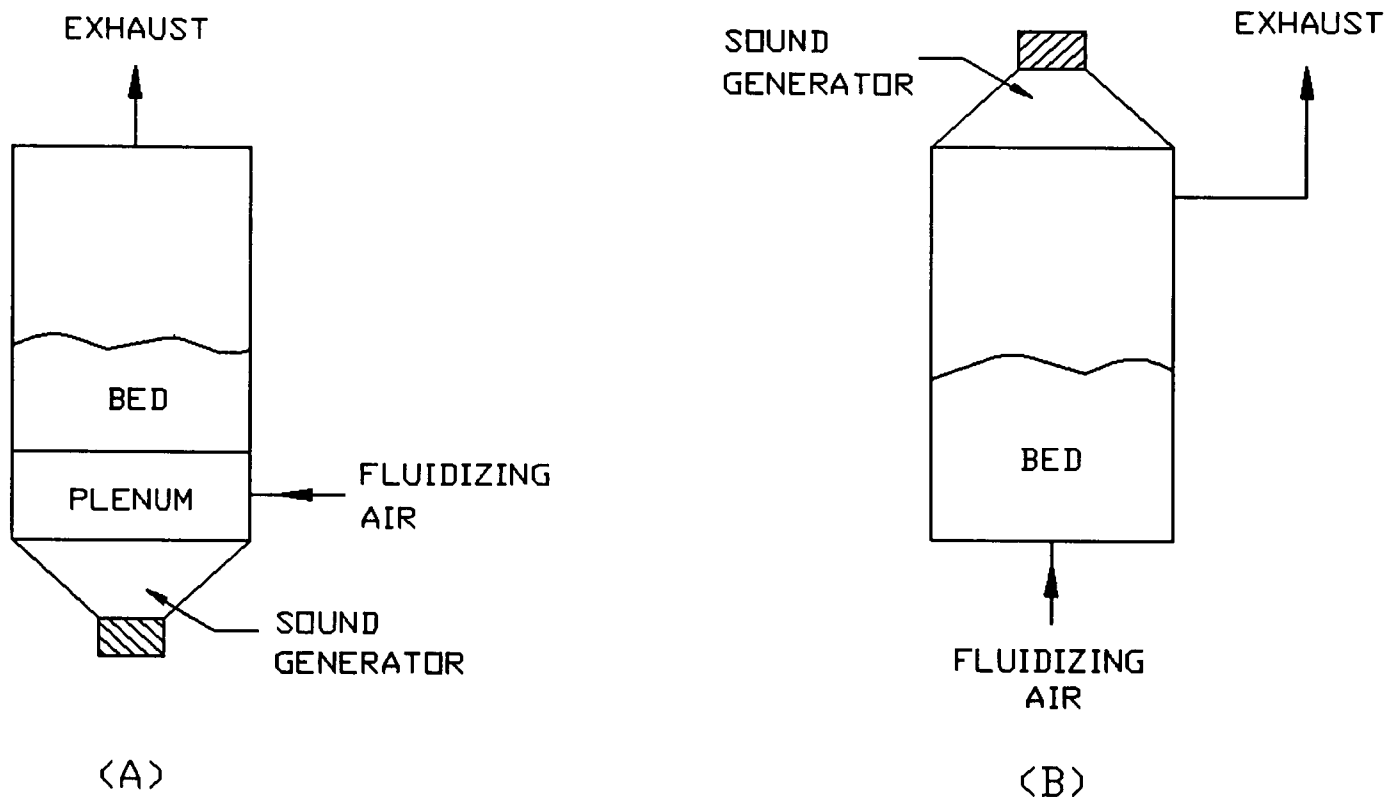


Figure 3. Sonic energy pulsing scheme : Sonic energy imposed at the Plenum (A) or at the bed boundary (B)

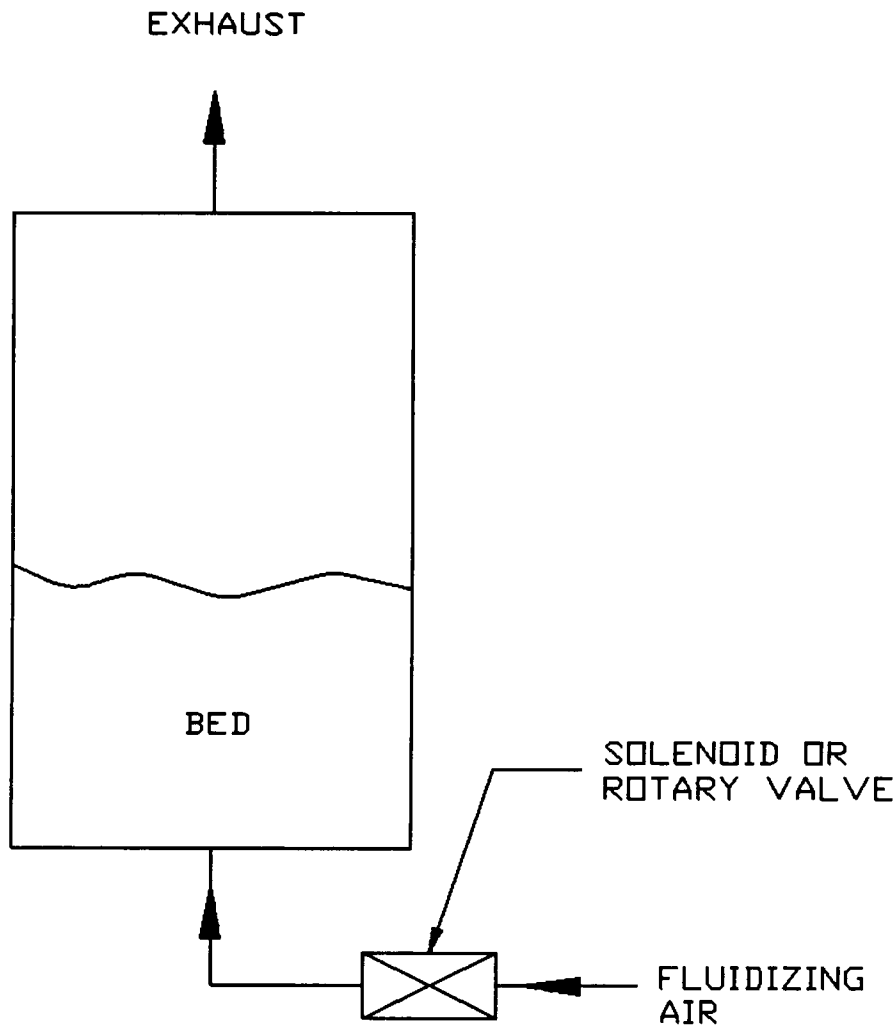


Figure 4. Intermittent gas flow pulsing scheme

2.1.1. SONIC ENERGY PULSING

R.D.Morse [10] investigated the effect of imposing sonic energy in the plenum on fluidization quality with different materials. The fluidization column used in the study was a glass column 3.75 inches inside diameter and 5 feet long. Thin, finely woven cloth screen was used as the distributor. A 25 watts speaker was used to impose sonic energy on the bed. The results of this investigation showed that low frequency (50 to 500 Hz) high intensity (above 110 decibels) sonic energy improves the fluidization of fine grained group C powders such as plaster of paris and pigments. However, for experiments with group B coarse spherical beads of polyvinyl acetate, the fluidization quality was not improved.

Moussa et al [11] have done a modelling study to investigate the potential effects of imposing sonic energy from the free board on the bed boundary. In an atmospheric fluidized bed combustor for sonic energy at a high frequency range of 1 to 2 k.Hz, they predict a significant increase in the burning rate of coal particles due to the unsteady developing boundary layers. They conclude based on their model, that the sound wave penetration is limited to around 10 to 20 cm and noise attenuation may be a problem.

Various other researchers have also observed improved fluidization of group C particles with sonic pulsing. However, for group B and D particles widely used in the commercial fluid bed devices, experimental results and theoretical predictions for sonic pulsing method are not encouraging.

2.1.2. INTERMITTENT GAS FLOW PULSING

In the past many researchers including Zabroski and Bokun [12,13], Massimilla et al [14], Kobayashi et al [15] and Moussa et al [16] have worked with the concept of intermittent gas flow pulsing and observed improved gas-solid contacting.

The effect of intermittent gas flow pulsing with 50% on-period and pulsing frequencies varying from 0.5 Hz to 2.0 Hz on heat transfer between an immersed heater and a bed of sand particles (180 to 815 μm) was investigated by Zabrodski and Bokun [13]. A 5.7 cm diameter bed with cloth distributor was used in the study. A higher heat transfer coefficient was observed for the pulsed bed compared to the regular fluidized bed for the same integral gas flow. The maximum heat transfer coefficient was observed at relatively lower (30 to 40%) integral gas flow in the pulsed bed. They have also used the same bed for drying of moist tetracycline, which is difficult to dry in a normal fluidized bed [12]. Channeling observed with steady flow is disrupted by pulsing the air flow and this resulted in improved mixing and better utilization of the drying gas. The pulsing frequency varied from 0.5 to 2 Hz and 1.5 Hz was suggested as the optimum. For a drying time of one hour, 30% reduction in relative moisture was observed with pulsing compared to 7% with a regular fluidized bed.

Massimilla et al [14] have done a detailed investigation of pulsed beds using a rectangular bed of dimensions 20 x 15 x 64 cm and a cylindrical bed of dimension 20 x 120 cm, and with various particles such as sand, glass, ceramic chips and limestone. Still photography and trace particles were used to study the effect of pulsing on mixing and bed expansion characteristics. Pulsing frequency was varied between 0 to 6 Hz with

50% on-period. Increased pressure drop was observed with pulsed beds for comparable integral air flow rates. With pulsing, channeling and bubbling were attenuated and solids mixing was improved. They infer improved gas-solid contacting from the increased pressure drop.

Kobayashi et al [15] have investigated the behavior of pulsed beds using a cylindrical bed (4 inch dia and 48 inch high) and varying the pulsing frequency and on/off ratios. Bulk particle motion, mixing of solids, bed expansion and pressure drop patterns were investigated. Bed expansion was consistently higher with pulsing for the same integral air flow rate and the entire bed was observed to expand during pulsing, whereas only top layers expanded with steady flow. Bed mixing was studied with segregated particles in different layers. With pulsing the particles mixed thoroughly in a few minutes and remained well mixed during a 6 hr operation, while in regular operation even at the end of the run, no appreciable mixing was observed.

Moussa et al [16] have worked with a 4 inch bed using sand (500 μm). Overall pressure drop and movie pictures were used to study the effect of pulsing. Pulsing frequency up to 8 Hz and various ratios of on/off periods were used. Increased interstitial gas velocity and resultant improved heat and mass transfer were inferred from the observed increase in the peak pressure drop with pulsing.

In the intermittent gas flow pulsing approach, the pulsing frequency and duration are fixed for a particular fluidized bed and operating condition, with no provision for feedback from the bed. The various difficulties associated with this scheme such as modulating the entire fluidizing flow and in applying to continuous operations have

limited its application. The approach adopted in this investigation is based on small time-dependant air pulses less than four percent of the fluidization gas flow and has a dynamical feedback component.

2.2 INTERMITTENCY ROUTE TO CHAOS

In many physical systems, as some system parameter is varied the system dynamical behavior changes from periodic or regular motion to apparently erratic or chaotic motion. In literature, this transition is referred to as route to chaos. In some systems, the periodic motion is interrupted by irregular bursts when a system parameter deviates from a critical value. As the deviation increases, the irregular bursts become progressively more frequent until the system becomes fully chaotic. This progression is referred to as intermittency route to chaos.

Manneville and Pomeau [17] studied the transition of Lorenz model from a stable limit cycle behavior to a strange attractor or chaos at a critical value of 166.07 for the parameter "r" in the Lorenz system of equations.

Lorenz system of equations : $dX/dt = \sigma (Y - X)$

$$dY/dt = rX - Y - XZ$$

$$dZ/dt = XY - bZ$$

They observed characteristic behavior associated with the intermittency route to chaos. The transition behavior is illustrated using the Z-variable in Figure 5. The transition behavior is explained using a simple mapping of $Y_{N+1} = F(Y_N)$, derived from taking a Poincaré section of the Lorenz attractor at $X = 0$ and considering the fact that

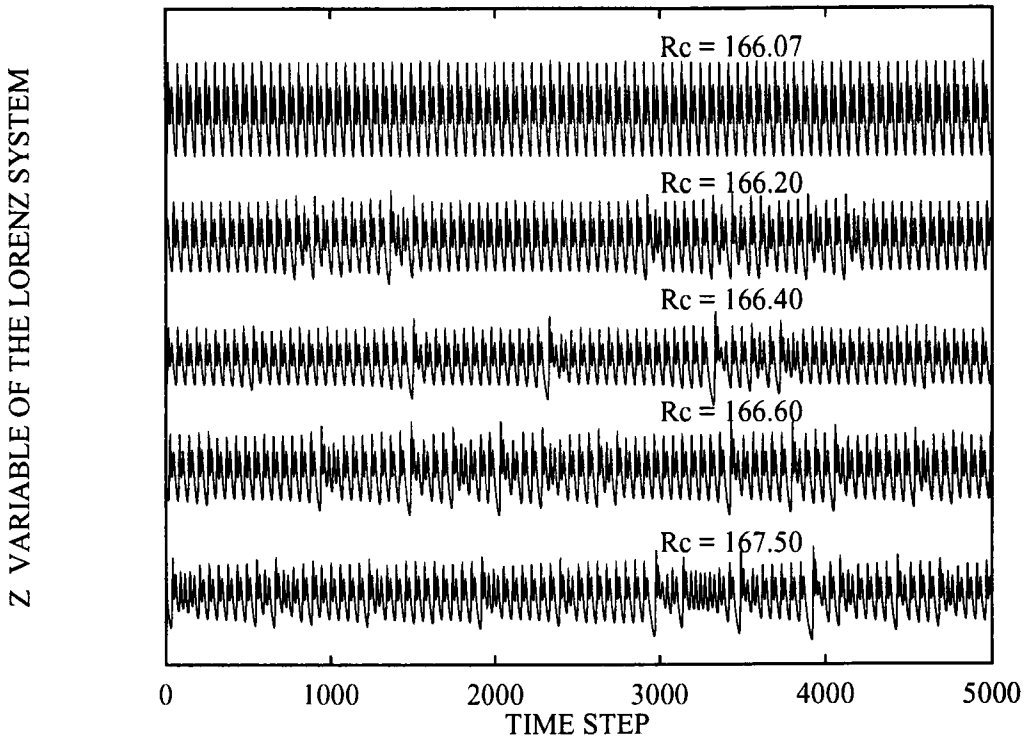


Figure 5. Illustration for transition behavior of the Lorenz model using Z variable for increasing r values.

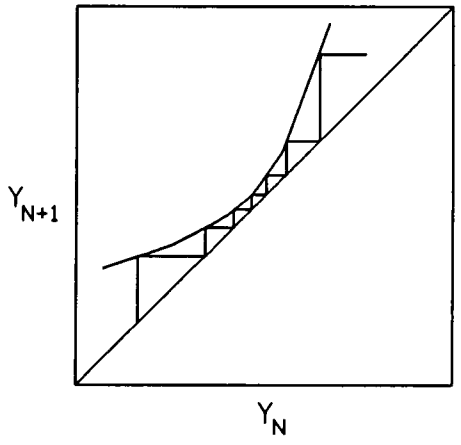


Figure 6. Intermittency behavior of iterates near the formerly stable fixed point.

Z_N is roughly a smooth valued function of Y_N. Typical map of $F(Y_N)$ vs Y_N for r value greater than r_C is shown in Figure 6, the curve traced by the successive iterates no longer touches the bisectrix. As the iteration proceeds, the point converges towards the formerly stable fixed point and stays in the neighborhood for some time (regular or periodic behavior) and then departs (irregular burst). Once in the irregular regime, the system can revisit the regular region and the process repeats itself. The transition to stochasticity is then continuous in the sense that close to the critical value, the average duration of the regular phase diverges as $1/(r-r_C)^{1/2}$, where r_C is the critical value.

Carson Jeffries and Jose Perez [18] observed Pomeau-Manneville intermittency route to chaos in a non-linear oscillator. The system consists of an inductor L, resistance R and a nonlinear diode driven by an oscillator Vo $\sin(2\pi t/T)$, connected in series. Voltage across the diode is measured and used to identify regular behavior. Voltages within 1% of the regular mode voltage is considered regular. They have conducted two sets of experiments: in the first set, the driving voltage is varied and the average duration of the regular phase and ϵ proportional to the deviation of the voltage from the critical value were fit to a curve of the form $<1> \propto 1/\epsilon^{\beta}$. Average value of β for a series of experiments was reported as 0.45 ± 0.05.

In the second set of experiments, the driving voltage is set at the critical value ($\epsilon = 0.0$), and noise of voltage V_N was added to the driving voltage. The average duration of the regular phase and g proportional to the noise voltage V_N were fit to a curve of the form $<1> \propto 1/g^{\gamma}$. Average value of γ for a series of experiments was reported as 0.65 ± 0.05.

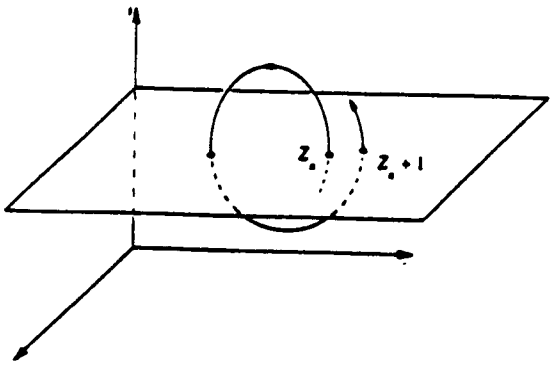
Fluidized beds also exhibit certain features associated with intermittency in some operating regimes. The approach used in the literature discussed above is modified to suit the inherently noisy nature of fluidization and the results seem to be in reasonable agreement. The methodology adopted and the results will be discussed in section 5.1.7.

2.3 CONTROLLING CHAOS

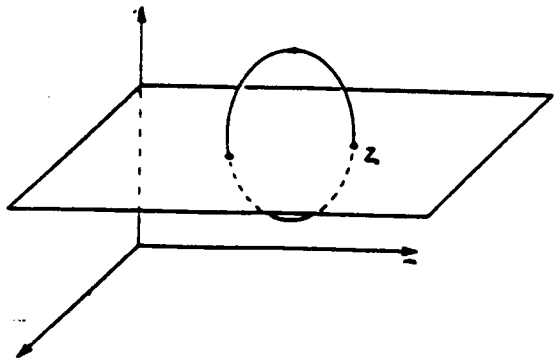
Chaotic systems are characterized by extreme sensitivity to small perturbations. In the past, this sensitivity is considered highly undesirable in physical systems. Recently Edward Ott, Celso Gregobi and James A. Yorke [7] suggested a method to use this sensitivity for controlling chaos. Their method (commonly referred to as OGY method) is based on the observation that a chaotic attractor has embedded in it an infinite number of periodic orbits.

Their approach is based on the following three assumptions: First, the dynamics of the system can be represented as an N-dimensional non-linear map such as Poincaré section (shown in Figure 7a) or time return map, and whose iterates are given by $Z_{N+1} = F(Z_N,p)$ where Z is an N-dimensional vector and p is a system parameter. Two, the system parameter p is accessible for making small time-dependant perturbations. Three, an orbit which gives the desired system behavior can be identified (e.g. a period-1 orbit as shown in Figure 7b). Then small time-dependant perturbations are applied to the system parameter p to stabilize the selected orbit.

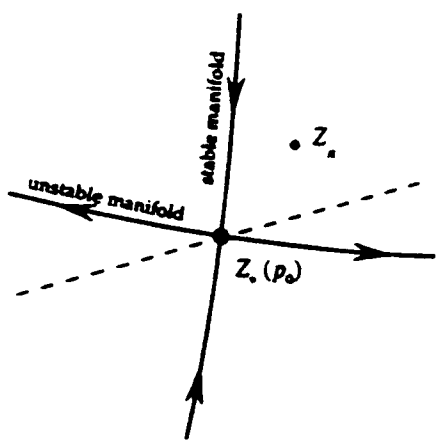
The local dynamics around the selected orbit indicated by Z_* at a parameter value of p_0 in the map is observed using nearby iterates and is approximated by a linear map,



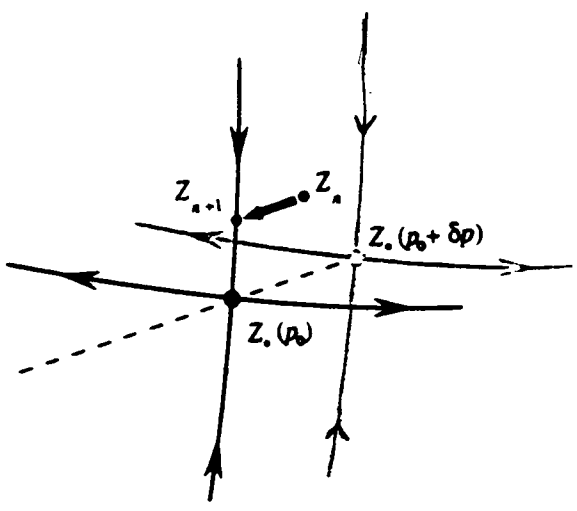
(a) Illustration for a typical Poincaré section (using X3 = constant)



(b) Poincaré section of a period-1 orbit



(c) Dynamics of the period-1 orbit in the local region.



(d) Illustration for control methodology.

Figure 7. Illustrations for the OGY method of controlling chaos.

Source : Shinbrot et al. [28], 1993, "Using Small Perturbations to Control Chaos", *Nature*.

$(Z_{N+1} - Z_*) = A\,(Z_N - Z_*) + B\,(p - p_o)$, where A is an N x N dimensional Jacobian matrix and B is an N-dimensional column vector.

$A = \partial F/\partial z$; $B = \partial F/\partial p$ evaluated at $Z = Z_*$ and $p = p_o$.

The local stable and unstable manifolds associated with the selected orbit are indicated by the eigen vectors of the Jacobian. Iterates starting in the stable manifold or region will remain in it and move exponentially towards Z_* and iterates starting in the unstable manifold move exponentially away from Z_*.

The parameter p is then varied within a small amount of p_o, say δPmax, such that the local linearization holds and the shift in Z_* is observed. Taking the effect of this parameter on Z for the small variation to be linear, the relationship is reduced to $(p_N - p_o) = -K^T (Z_N - Z_*)$, where K is a constant N-dimensional column vector and K^T is its transpose. Combining with the previous equation,

$$\delta Z_{N+1} = (A - BK^T)\,\delta Z_N$$

The selected orbit will be stable, if the column vector K is chosen such that the matrix $(A - BK^T)$ has all its eigen values with modulus less than unity. This condition will force $\delta Z_N \to 0$ as $N \to \infty$.

The approach is easily understood by considering a two dimensional map where the desired period-1 orbit has one stable and unstable manifold. The dynamics of the system in the local region around the period-1 orbit is illustrated in Figure 7c. Z_* is the period-1 orbit at a parameter value $p = p_o$ and the path of Z_* as the parameter p_o is changed is shown by the dashed line. Consider an iterate Z_N which falls near Z_* but away from the manifolds as shown in Figure 7c. If the parameter is perturbed to $(p + \delta p_o)$, such

that Z_* is shifted to a new location shown in Figure 7d, then during the next iteration the orbit will be simultaneously attracted and repelled parallel to the new stable and unstable manifolds. If, the perturbation δp is properly chosen, the next iterate Z_{N+1} can be made to fall on the original stable manifold associated with $Z_*(p_o)$. Then the parameter is restored to its original value p_o from $(p_o + \delta p)$ and the orbit is attracted exponentially towards Z_*. The choice of δp and the rate of convergence are determined by the column matrix K.

W.L. Ditto, S.N. Rauseo and M.L. Spano [8] were the first researchers to implement the OGY chaos control method in an experimental system. A gravitationally buckled, amorphous magneto elastic ribbon, which exhibits reversible changes of Young's modulus with the application of small magnetic fields is used in the experiment. The ribbon is clamped at the base and is placed in the magnetic field. The Young's modulus of the ribbon was varied by applying a vertical magnetic field having the form $H = H_{DC} + H_{AC} \cos(2\pi ft)$. An optical sensor measures the displacement of the beam near the base and output voltages are collected at the drive period of the magnetic field. Return maps of the form X(n) vs X(n+1) were constructed using the sensor output voltage sampled at the drive period of the ac field. By applying the OGY method, the authors were able to stabilize different periodic orbits in the system. For a detailed and cogent review of chaos control theory and applications, refer to the review article by Shinbrot et al [19].

Garfinkel et al [20] employed a modified version of OGY method for stabilizing cardiac arrhythmias (apparent random heart beats) induced by the drug ouabain in rabbit

ventricle. By administering time-dependant external perturbations in the form of electrical stimuli to the heart muscles, control was achieved.

The basic differences between their approach and the OGY method are as follows: In the OGY method, a system parameter is varied to move the stable manifold to the current iterate whereas in the latter scheme, a system variable is perturbed such that the next iterate is moved towards the stable manifold of the desired fixed point. Then the iterate naturally flows in to the fixed point in the subsequent iterations. Perturbations are decided based on the local dynamics of the fixed point similar to the OGY method. Authors refer to this control approach as the proportional perturbation feedback (PPF) method. Results of the experiments showed that with this method it was possible to stabilize arrhythmias into a period-3 orbit. Also, very short interval beats are eliminated resulting in increased average interval between beats.

Both the OGY and the PPF control methods are not model based and computations required at each iterate are minimal, and different periodic orbits embedded in the attractor can be stabilized. The control approach adopted in this study has a lot of similarities to the proportional perturbation feedback method. Instead of using parameter perturbations, small time-dependant external perturbations in the form of high pressure pulses admitted at one point in the fluidized bed, are used for control. The methodology adopted and results will be discussed in detail in chapter 5.

CHAPTER 3

EXPERIMENTAL APPARATUS AND PROCEDURE

The experimental apparatus and procedure used in this study are discussed in this chapter. The experimental apparatus is described in section 3.1. An overview of experimental procedure and the test conditions are given in section 3.2

3.1 DESCRIPTION OF THE EXPERIMENTAL APPARATUS

3.1.1 LABORATORY SCALE FLUIDIZED BED

The fluidized bed is contained in a 10.2 cm diameter and 140 cm high cylindrical tube. A schematic of the experimental apparatus is shown in Figure 8. The cylindrical tube is made up of two sections of plexiglass pipe with flanges. A tuyere-nozzle type distributor is mounted at the bottom for distributing the fluidizing gas uniformly across the bed cross section. A 90° elbow (10.2 cm inside dia) serves as the plenum chamber and is connected to the building air supply via a cut off valve, pressure regulator, flow meter and a throttle valve. The tube exit is connected to a cyclone dust collector through a reducer and flexible hose. All the sections are assembled to form the bed containment, and rubber gaskets are used to seal the flanges. The whole assembly is supported on a stand and is attached to the wall at the middle flange. Two equally spaced copper strips (1 cm wide) are glued along the walls of the lower plexiglass section. These strips and the distributor are grounded to prevent static charge build-up.

In control experiments, a pressure pulse is used as the external perturbation for controlling the bed behavior. The pressure pulse is introduced in the bed using a pulse

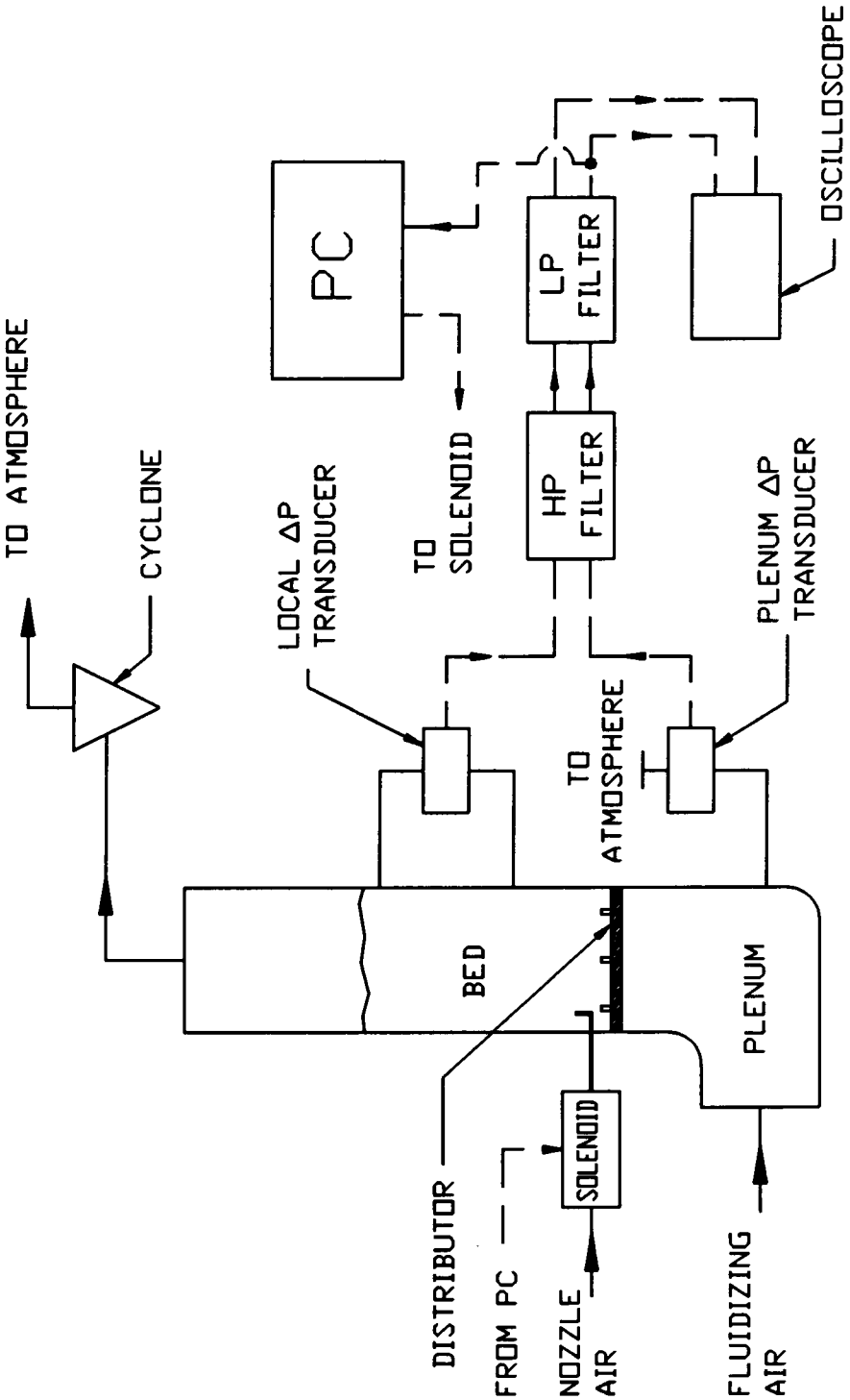


Figure 8. Schematic of the laboratory scale fluidized bed apparatus.

nozzle 0.605 cm inside diameter stainless steel bent tube pointing upwards. The nozzle is located at 4.8 cm above the distributor and projects 1 cm in to the bed. The pulse air supply can be either tapped from upstream of the regulating valve in the fluidizing air line or supplied through an independent air supply line.

There are four equally-spaced pressure taps on the bed circumference at three different elevations. These taps are interconnected at each elevation and a horizontally averaged pressure can be measured from that elevation. In addition to these taps, there is a tap at the plenum to measure plenum pressure fluctuations. Standard 1/8" pipe fittings are used for pressure taps and wire mesh is glued across the cross section of tap openings to prevent plugging by solids. The pressure taps are connected using 1/8" outside diameter vinyl tubing. Figures 9 and 10 illustrate the pressure tap configuration. In this study, differential pressure measurements are done at two locations in the bed; one measurement between the plenum below the distributor and atmosphere designated as "plenum signal" and another between two elevations in the bed designated as "local signal".

3.1.2 AIR DISTRIBUTOR PLATE

A tuyere-nozzle type distributor was used to enhance uniform fluidization air distribution in the bed. A schematic of the air distributor is also shown in Figures 9 and 10. The distributor plate was fabricated from an aluminum disk 15.9 cm in diameter and 12.7 cm in thickness and has seven threaded holes to accommodate the tuyeres. The tuyeres were made using 3.81 cm long, 12.7 cm diameter brass tubes with threaded ends.

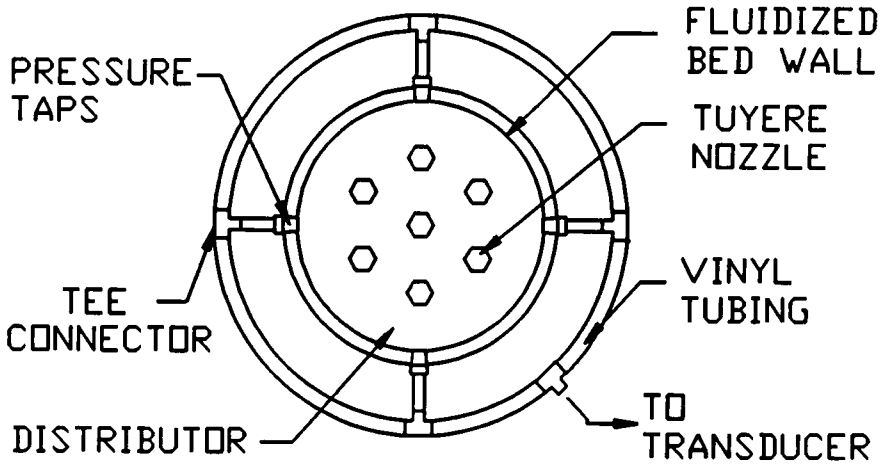


Figure 9. Cross sectional view of the lower portion of the bed showing pressure tap arrangement.

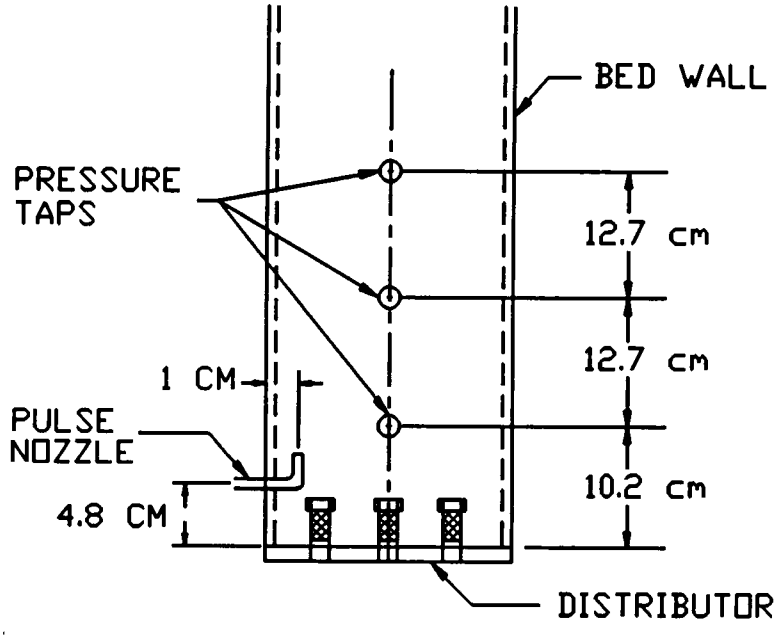


Figure 10. Side view of the lower portion of the bed showing pressure tap locations, pulse nozzle and distributor.

The center nozzle has eight 0.63 cm diameter holes, drilled 90 degrees apart and all the other nozzles have six holes of 0.63 cm holes, drilled 90 degrees apart. To prevent erosion at the fluidized bed wall, the outer nozzles are turned in such a way that no holes are facing the wall. An end cap was placed on one end of the tuyeres and the other end is threaded in to the distributor plate. Fine mesh screen was wrapped around the tuyeres and wired in place to prevent bed material seepage into the plenum. Distributor pressure drop is a function of the fluidization gas flow and the pressure drop characteristics of the tuyere-nozzle distributor is furnished in Appendix A. In this study, over the velocity range investigated distributor pressure drop varied between 52 and 185 percent of the bed pressure drop for steel and between 22 and 217 percent of the bed pressure drop for glass beads. Other equipment used in this study will be described in detail in the later sections.

3.1.3 BED PARTICLES

Slugging behavior of two Geldart's group D particles, spherical steel ball bearings (Steel) and glass beads (Glass) was investigated over a wide range of fluidization velocity from minimum fluidization velocity up to transition to turbulence. Steel BB's were uniform in size and shape whereas, glass beads had some size distribution. Both particles exhibited slugging behavior expected of group D particles. A static bed height of 23.5 cm was used. The physical properties and operating velocities are listed in Table 1.

Table 1. Physical properties of particles and fluidization velocities.

Description	Steel BB	Glass
Particle Density [gm/cc]	7.5	2.6
Mean Diameter [mm]	4.5	2.9
Minimum Fluidization Velocity [m/s]	3.60	1.47
Velocity Range Investigated [U/U_{MF}]	1.07 - 2.07	1.04 - 2.99

3.1.4 DIFFERENTIAL PRESSURE TRANSDUCERS

In slugging and bubbling, the important physical phenomena occur over time scales as small as 40 ms. Hence, transducers with response times shorter than this are needed to make dynamic observations. Baratron Model 223-BD rapid response differential pressure transducers with a time response of less than 16 ms were used to measure the plenum and local pressure drops in this study. Transducers rated for differential pressures of 50 inches or 500 inches of water column were used depending on the magnitude of the pressure drop.

The major components of the Baratron transducer are the sensor and the signal conditioner. The sensor contains a stretched metal diaphragm, one side of which is exposed to gas whose pressure is to be measured. The other (reference) side is adjacent to an electrode assembly which is terminated in another like port. The diaphragm deflects with changing differential pressure, causing a capacitance change between the diaphragm and the adjacent electrode assembly. The signal conditioner contains a fixed frequency oscillator, amplifier, demodulator, and calibration circuitry. The capacitance change with

pressure generates an AC voltage which is amplified, demodulated, and converted into a DC voltage output linear with pressure.

3.1.5 DUAL HI/LO FILTERS

Two Wavetek Model 452 Dual Hi/Lo filters were used to remove the D.C. bias and electrical noise from the signal generated by the rapid response differential pressure transducers. The band-pass filters were set to attenuate signals with frequencies less than 0.1 Hz to remove the D.C. bias and greater than 40 Hz to remove the power line noise. D.C. bias is removed to maximize the resolution of the analog to digital conversion. Each Wavetek Model 452 Dual Hi/Lo filter consists of two identical channels in a common cabinet. Each filter channel has separate input/output terminals, offers high and low pass functions, and has 1-digit resolution for cutoff frequency selection.

3.1.6 DIGITAL OSCILLOSCOPE

A four channel, 12 bit resolution, Model 440 Nicolet digital oscilloscope was used to acquire signals from the rapid response differential pressure transducers. The oscilloscope can record a maximum of 63342 data points from four channels and the sampling rate can be varied between 0.1 to 20,000 Hz. In this study, data sets of 60,000 points each were recorded at a sampling rate of 200 Hz for data analysis. Two channels were used to simultaneously store the plenum and local pressure-drop measurements.

3.1.7 CONTROL SYSTEM

Bed behavior is monitored by a 80486 PC based control routine using a control signal (either plenum or local) and depending on the rule base appropriate control actions are taken. The control action introduces a high pressure pulse in the bed through the pulse nozzle. The data acquisition board used, is a DT-2821 series high speed analog and digital I/O board and can handle Analog/Digital conversion with 12 bit resolution and 50 kHz throughput. The control routine was developed in C^{++} to read in the data and to generate a control pulse based on the rule base [20]. The routine samples the data at around 2 kHz and depending on the rule base generates a 10 mA pulse for a set pulse duration. This control signal is converted to a 115 V signal by a solid state relay to trigger the solenoid valve. The three-way fast acting solenoid valve (Alkon model P-140-SS-115/60) is rated for 1500 cycles/min duty.

3.2 OVERVIEW OF EXPERIMENTAL PROCEDURE

In this study, the laboratory-scale fluidized bed described in the previous sections is used to investigate the slugging behavior of Geldart's group D particles. Differential pressure measurements, known to correlate well with the bed dynamics, were used to characterize and monitor the bed behavior, and to take appropriate control actions. Conventional and chaotic time series analysis techniques were used in the analysis. For slugging characterization study and control experiments, a static bed height of 23.5 cm was used. Pulse air was tapped from the fluidizing air line upstream of the regulating valve for all the control experiments.

Plenum and/or local signals are measured using rapid-response differential pressure transducers. The transducer signals are then band-pass filtered using analog filters between 0.1 and 40 Hertz. For data analysis, these band-pass filtered signals are sampled at 200 Hertz and stored with 12 bit precision by a digital oscilloscope. For control, a 80486 PC based data acquisition board reads in the bandpass filtered control signal (either plenum or local signal). The control routine samples the control signal at a very high rate (around 2000 Hz), monitors the bed dynamical state and takes control action based on its rule base. The control action is of the form of triggering a solenoid valve and introducing a gas pulse in the bed.

In the present study, all experiments were performed at room temperature in an atmospheric fluidized bed. Compressed dry-air from the building air compressor system at a pressure of 6.9 bar is throttled to 2.1 bar and used as the fluidizing gas and pulse gas. Temperature, pressure and the volumetric flow rate of the fluidizing air were recorded for all the runs.

The effect of bed height on slugging behavior was also investigated as a part of this study. In this study, perforated plate and tuyere nozzle type distributors were used and steel BB was used as the bed material. Pressure measurements were taken at various locations in the bed.

CHAPTER 4

DATA ANALYSIS TECHNIQUES

Conventional Fourier analysis and chaotic time series analyses including phase space trajectory reconstruction, mutual information and time return maps are used to describe and quantify changes in fluidization. This chapter introduces the theoretical background for the time series analysis techniques and describes briefly our adaptation of the computational procedures used in this study.

4.1 MUTUAL INFORMATION

The mutual information function is a measure of the general dependance between successive time series measurements and indicates how far into future one can predict based on the present measurement. This can be considered as a nonlinear analog of the auto correlation function, and is directly determined from the measured time series.

The basis for the mutual information function is the uncertainty concept as discussed by Shannon and Weaver [22], which states that the uncertainty of any measurement depends on the probabilities for the various possible outcomes. Mutual information is determined by evaluating the difference between the average unconditional uncertainties of making two successive measurements and the average conditional or joint uncertainties. For a time series, the range of the measurement value is divided into N bins and the unconditional p(i) and conditional probability, p(i,j) for a measurement to fall in a bin are determined. The uncertainties and the mutual information function are then determined as follows

$$H(s) = -\sum_i p(i)\ \log_2 p(i)$$

$$H(s+k) = -\sum_j p(j)\ \log_2 p(j)$$

$$H(s, s+k) = -\sum_i p(i,j)\ \log_2 p(i,j)$$

$$I(k) = H(s) + H(s+k) - H(s, s+k)$$

where, I(k) represents the average number of bits that can be predicted correctly for a measurement **k** time steps in the future based on the present measurement at s.

4.2 PHASE SPACE TRAJECTORY RECONSTRUCTION FOR VISUALIZATION

The phase space of a dynamical system depending on N parameters is a space of N dimension with orthogonal coordinate directions representing each dynamical variable and the trajectory traced by the system in this space is known as phase space trajectory. But to construct this phase space, we need to know all the dynamical variables, which is impractical in the case of many experimental systems. This problem can be side-stepped by using the phase space reconstruction method based on "Takens' embedding theorem" [23]. According to Takens' theorem, it is possible to extract a mathematically equivalent facsimile of the original attractor from any single time series measurement of a dynamical variable which correlates with the system dynamics by proper embedding. In the embedding procedure, a m-dimensional vector with time series measurements with a time lag k as its components is constructed from the scalar time series. Where m is embedding dimension and k is the time delay or time lag.

A simple embedding in 5 dimensions and using a time lag of 3 is as follows:

Time series : {x(1),x(2),x(3),x(4),x(5),x(6),x(7),x(8)...,x(N-1),x(N)}

Vector p(t) : {x(1),x(4),x(7),x(10),x(13)}
{x(2),x(5),x(8),x(11),x(14)}
{x(3),x(6),x(9),x(12),x(15)}
.
.
{x(N-13),x(N-10),x(N-7),x(N-4),x(N-1)}
{x(N-12),x(N-9),x(N-6),x(N-3),x(N)}

The trajectory traced by the vectors p(t) over time represents the reconstructed trajectory. However, for proper reconstruction of the trajectories, embedding dimension and lag are crucial. According to Takens, an embedding dimension of m is sufficient if it satisfies the criteria $m \geq 2d + 1$; where "d" is the actual dimension of the attractor. The time delay or lag should be selected such that the consecutive points are not overly correlated or totally uncorrelated. The optimal choice of lag is somewhat ambiguous, with varied recommendations from literature. In the present study, the lag is taken as the number of time steps for the mutual information function to decay to fifty percent of its initial value. It was found by experience that the latter choice is quite suitable for observing fluidized bed dynamics.

It is also convenient to map the embedded trajectories on to a new set of orthogonal axes called principal axes using "principal component analysis" or "singular value decomposition" method of Broomhead and King [24]. With this method, the trajectories can be visualized as projections on a standard set of coordinate axes.

4.3 CORRELATION DIMENSION

Correlation dimension is an estimation of the minimum dynamical degrees of freedom of the attractor in phase space. Chaotic attractors (either constructed directly from the dynamical variables or by using time series embedding of a single variable) are characterized by a correlation exponent D that is defined on the basis of a long time series $\{X_i\}$ of N points on the attractor by considering the correlation integral,

$$C(l) = \frac{1}{N(N-1)} \sum_{i \neq j} \mathrm{H}\,(l - \|X_i - X_j\|)$$

where H *is the Heaviside function and* $\|X_i - X_j\|$ *is the Euclidean norm*

The correlation integral C(l) scales according to a power law $C(l) = l^D$ for small distances "l" and correlation dimension is given by

$$D = \lim_{l \to 0} \frac{\ln[C(l)]}{\ln(l)}$$

This classical procedure has some limitations, the correlation integral values tend to be inaccurate at very small values of "l", because of very few qualifying pairs and noise from experimental systems.

Schouten, J.C., Takens F. and Van den Bleek, C.M. [25] have proposed an estimation procedure based on the maximum likelihood method for time series experimental data. In this method, a set of inter-point distances between M randomly chosen pairs of embedded points(X_i, X_j) are generated. Instead of the euclidian norm, maximum norm is used for calculating distances. Then, all the distances exceeding a

cutoff distance are thrown out and the qualifying distances are normalized with a cutoff distance l_o. This procedure results in a new set of distances r_i, where $0 \leq r_i \leq 1$ and the correlation integral C(r) represents a normalized cumulative probability distribution $C(r) = r^{\alpha}$.

Using Fisher's maximum likelihood rule, for the sample $(r_1,r_2,\ldots r_M)$, the probability p_M of finding a sample in $\{(r_1,r_1+dr_1),(r_2,r_2+dr_2),\ldots,(r_M,r_M+dr_M)\}$ dependant on D is given by

$$p_M = \prod_{i=1}^{M} D\, r_i^{D-1}\, dr_i$$

and the value of D, for which p_M is maximum is given by

$$D_{ML} = -\,[\ln(r_i)]^{-1}$$

i.e., the most likely value D_{ML} of the correlation dimension, given at the sample $(r_1,r_2,\ldots r_M)$, is equal to the inverse of the average value of $-\ln(r_i)$, with i = 1,2,..,M, where M is the number of sampled pairs.

A unique aspect of the Schouten et al procedure is that they recommend using an embedding lag of one sample time step and an embedding time window (time equal to embedding dimension minus one times the sample time) of the average cycle time about the mean. This approach was adopted for this study and the average absolute deviation about the mean was used as the cut-off distance. For each data set, 30 replicate random sampling (each typically involving several thousand pairs) was done and 30 estimates of D_{ML} were produced. The final D_{ML} estimate is the average of the 30 independent estimates and the uncertainty is estimated as two times the standard deviation of the D_{ML} replicate estimates.

4.4 KOLMOGOROV ENTROPY

Kolmogorov entropy can be considered as an invariant measure for the rate of information loss along an attractor or a measure for the degree of predictability of points along an attractor given an initial point. Periodic or cyclic phenomenon are characterized by zero entropy and random or stochastic phenomenon by infinite entropy. Chaotic systems are characterized by finite positive entropy values.

Entropy estimations are done using a modified version of the maximum likelihood procedure outlined by Schouten, J.C., Takens F. and Van den Bleek, C.M. [26]. Entropy values are estimated by tracking the divergence of initially near-by orbits of an attractor over time. The rate of divergence of these orbits are expected to be exponential for chaotic systems. Two orbits are considered close, when two points on the orbits represented by the state vectors within a set length of time (normally equal to the average cycle time) are within a maximum cut-off distance (normally the average absolute deviation). For M randomly selected orbit pairs, the qualifying near-by pair of orbits are identified. Then the identified nearby orbits are tracked over time to generate a function F(t) equal to the fraction of the originally identified near-by pairs not yet diverged beyond the cut-off value. Based on the expected exponential divergence of the trajectories in a chaotic system, the function F(t) can be expressed as

$$F(t) = e^{-kt} \quad \textit{where } k \textit{ is Kolmogorov entropy}$$

The function F(t) for the qualifying pairs is generated for the sample and the Kolmogorov entropy is estimated by a least square regression fit. Generally the estimation is done for 30 random sample replicates and an average entropy value and uncertainty are reported.

As with D_{ML}, the entropy uncertainty is estimated as twice the standard deviation of the replicate estimates.

4.5 CYCLE PERIOD AND MAGNITUDE

Cycle period and magnitude comparisons are also used in this analysis to give an over all picture of the trends in system behavior. Figure 11 illustrates the determination of cycle period and magnitude from the differential pressure signal. A cycle is defined as trough to trough oscillation of the differential pressure signal, physically it corresponds to the passage of a bubble or slug in the observation window.

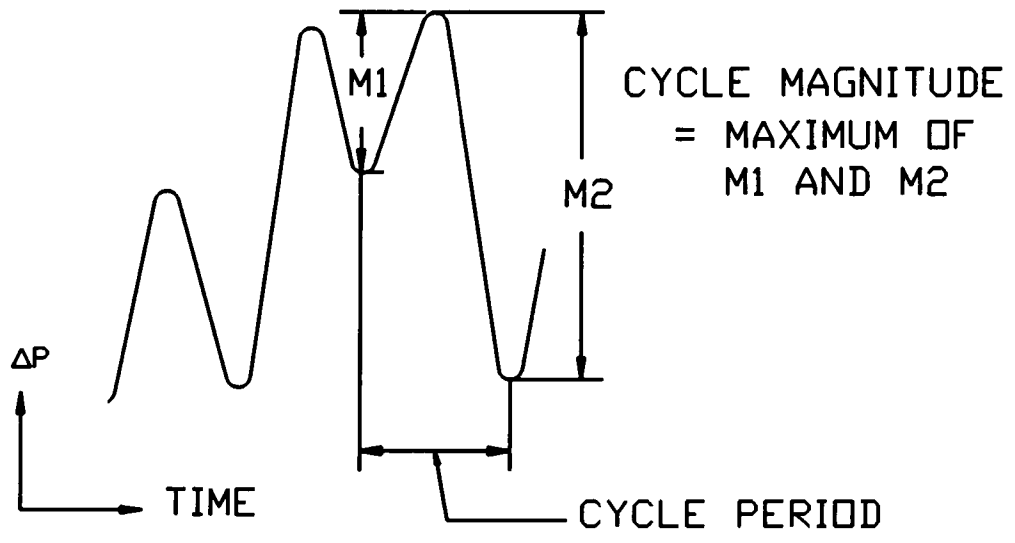


Figure 11. Illustration for cycle period and magnitude

4.6 TIME RETURN MAPS

Time return maps are actually snap-shots of the system behavior. The time interval between a characteristic event in the system behavior can be plotted as a two or three-dimensional map to give an understanding of the system dynamics [27]. Time return maps for this study are constructed with time taken for the phase space trajectories to complete one orbit about the plane defined by principal component 2 = 0. The orbital times are generated as a sequence $\{T_1, T_2, T_3, T_4, T_5, T_6, \ldots\ldots, T_{N-1}, T_N)$. Then a three-dimensional map $T_N = f(T_{N-1}, T_{N-2})$ is constructed with the orthogonal axes representing T_I, T_{I+1} and T_{I+2}. Each iterate in the map is defined as follows:

Iterate 1 : (T_1, T_2, T_3)
(T_2, T_3, T_4)
(T_3, T_4, T_5)
..
..
$(T_{N-3}, T_{N-2}, T_{N-1})$
(T_{N-2}, T_{N-1}, T_N)

CHAPTER 5

EXPERIMENTAL RESULTS AND DISCUSSIONS

This study was organized into three phases, characterization of slugging behavior of Geldart's group-D particles, development and implementation of a control strategy and evaluation of control. Results from the experimental work done for each phase are presented in this chapter. Section 5.1 presents the results from the characterization study. Development of control strategy and empirical determination of control parameters are discussed in section 5.2. Results from the control evaluation experiments are presented in section 5.3.

In this chapter, only typical data sets and figures essential for a clear and concise presentation of results are used. Complete data analysis results for all the conditions investigated are presented in the Appendices. The operating conditions are identified by either the fluidization velocity U defined as the superficial gas velocity in the bed cross section or by the ratio of fluidization velocity to the minimum fluidization velocity (U/U_{MF}).

5.1 CHARACTERIZATION OF SLUGGING BEHAVIOR.

Results of a detailed investigation to understand the dynamical behavior of slugging fluidized beds are presented in this section. Slugging behavior of two Geldart's group D particles, spherical steel ball bearings (Steel) and glass beads (Glass) was investigated over a wide range of fluidization velocities. A static bed height of 23.5 cm was used and the physical properties of bed materials and operating velocities are listed

in Table 1. Bed behavior was analyzed using the local differential pressure signal and experimental apparatus and procedures are as described in chapter 3.

5.1.1 GENERAL OBSERVATIONS

Visual observations during the experiments and general trends observed in the pressure-drop time series form the basis for this discussion. Both solids exhibit similar behavior over the velocity range investigated. Typical time series segments corresponding to different fluidization conditions for steel and glass are shown in Figures 12 and 13, respectively. The time series are plotted with adjusted scale ranges to clearly illustrate the detailed signal structure for each condition. When the fluidization velocity is well below the minimum fluidization velocity (U_{MF}), the bed behaves like a static bed and there is no particle motion at all. As the fluidization velocity approaches U_{MF}, some activity can be seen in the top layer of the bed. Some particles bounce or flutter at the top surface, but there is no convective mixing. With further increase in velocity, the active layer grows and at U_{MF} the bed is fluidized with very little bed expansion and mixing in bed. Small scale particle vibration or bouncing dominates the system behavior. Just above minimum fluidization velocity, bubbles or voids begin to form in the bed. These voids tend to promote an organized or collective motion of particles. The system behavior is a mixture of the small scale particle vibration and the large scale collective or organized convective motion of particles in groups. Pressure signals corresponding to this regime are shown in Figures 12a and 13a. A characteristic sequential building up of bubble size is seen in this flow condition for both the solids. Successive bubbles grow

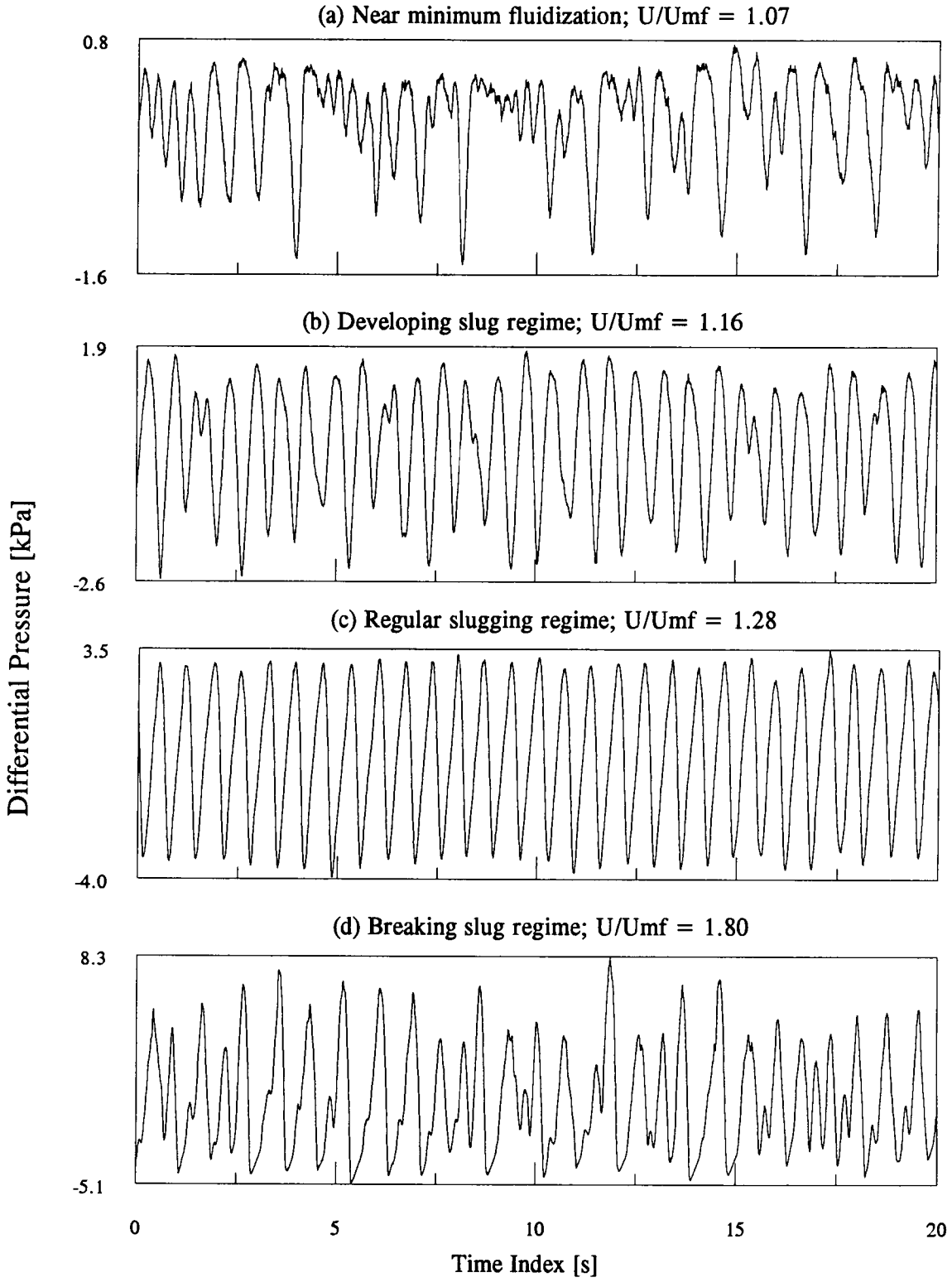


Figure 12. Typical time series segments of local pressure signal for steel at four different fluidization conditions.

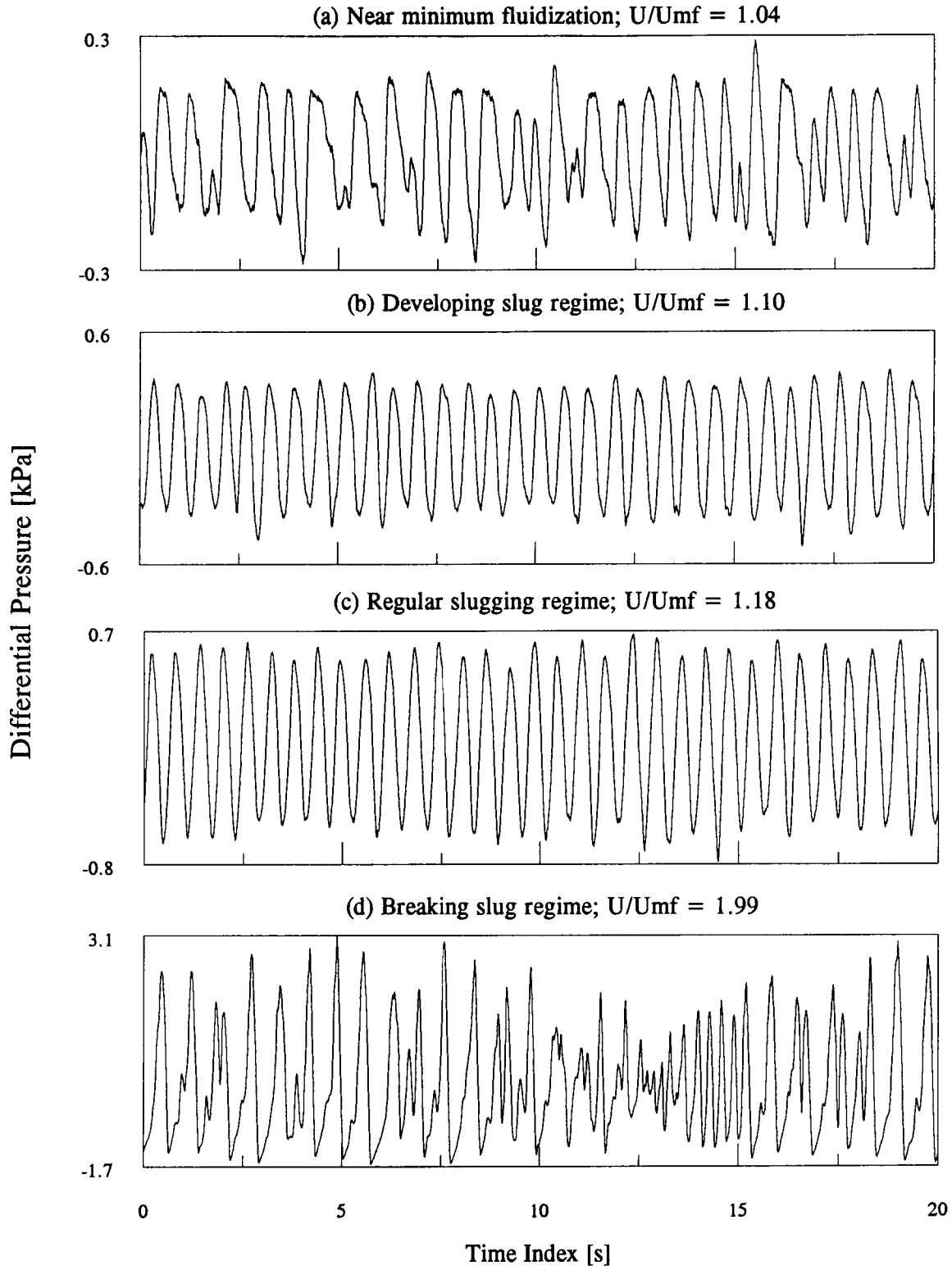


Figure 13. Typical time series segments of local pressure signal for glass at four different fluidization conditions.

larger resulting in increasingly large bed level fluctuations up to a maximum point and then the next bubble is suddenly very small, beginning the process all over. This build up and decay process continues to repeat as shown in Figure 12a.

With further increase in velocity, the bubbles grow larger and occupy a considerable portion of the bed volume. These large bubbles or voids are referred to as slugs in this discussion. Slugs rising in the bed tend to lift the mass of particles above like a piston. Bed behavior is dominated by the organized or collective motion of large groups of particles. For a gas velocity range above U_{MF} (up to approximately 112% of U_{MF} velocity), the slugs are still smaller than the full cross-section of the bed. Successive slugs display considerable variation from one another and the bed level fluctuation is not uniform over time. This regime is classified as developing slug regime to note that full size slugs have not yet developed. Pressure signals corresponding to this regime are shown in Figures 12b and 13b. The signals are less complex compared to the near minimum fluidization condition, but they are more complex than those from the regular slugging condition described next.

With further increase in fluidization velocity, the slugs grow larger and start to fill up the cross section of the bed. Individual slugs moving up slowly and scraping the side walls were seen in the bed. Pistoning of solid particles above a rising slug occurs. A small portion of the material trapped in the pistoning mass is returned to the lower portion along the wall, but the bulk of the material rains down on the lower portion of the bed as the slug escapes the bed surface. At some fluidization condition in this range, the individual slugs in the slug train are similar to each other and the bed level

fluctuation is nearly periodic. This condition is classified as the regular slugging regime and the corresponding pressure signals are shown in Figures 12c and 13c.

Bed level fluctuations and slugs become increasingly irregular with further increases in fluidization velocity. Large fluctuations in bed level and unstable slugs are more frequently observed. The mass of particles lifted up by a slug rains down on the next slug tending to break the latter apart. This regime is classified as the breaking slug regime and typical pressure signals for this regime are shown in Figures 12d and 13d. Beyond this regime, bed behavior enters the turbulence transition regime characterized by swirling motion of the particles interspersed with violent pistoning of particle to considerable heights. Pressure signals in this regime are very complex. This transition occurs at fluidization velocities of U/U_{MF} around 2 for both the materials. Fluidized beds are normally operated well below this transition regime and hence our study is also restricted to operating conditions below this regime.

As has been described, with increase in fluidization velocity above U_{MF}, the bed behavior changes from a complex or irregular state dominated by the small-scale particulate motion to an almost regular state dominated by the large scale slug motion at regular slugging regime. Beyond regular slugging, the bed behavior becomes progressively irregular or disordered with increasing gas velocity. This transition of bed behavior between disordered and ordered states is discussed in terms of quantitative measures of the pressure drop signals in the following sub-sections.

5.1.2 CYCLE MAGNITUDE AND PERIOD

As a way to study the time variation in bubble size and frequency, a cycle is defined as a trough to peak to trough oscillation of the pressure signal. This definition corresponds to the passage of a bubble or slug in the observation window. This definition is further used to compute cycle magnitudes and periods as discussed in chapter 4.

Composite plots generated by combining the results from selected time series to illustrate the overall picture of bed behavior transitions are presented in this section. The composite magnitude plots for steel and glass are shown in Figures 14 and 15 respectively. Near minimum fluidization, the cycle magnitudes are lower and widely distributed. With increase in fluidization velocity, the distribution becomes more narrow (i.e., the bed oscillations are more regular) and clustering around a dominant magnitude emerges. The size of this cluster is progressively narrowed with increasing fluidization velocity and is smallest at a velocity of $U/U_{MF} \approx 1.28$ for the steel BB's and at a velocity of $U/U_{MF} \approx 1.19$ for the glass. These latter flows correspond to the most regular slugging conditions. For flows beyond the regular slugging regime, cycle magnitude become more variable. One of the more notable features of this transition is the occurrence of small or incomplete cycles, which is referred to as "stutters" in this discussion. The frequency of stutters increases as gas flow is increased beyond the regular slugging regime. In the breaking slug regime cycle magnitudes are very widely distributed and stutters occur very frequently.

Composite cycle period plots for steel and glass are shown in Figures 16 and 17. At fluidization velocities close to minimum fluidization, the cycle periods are widely

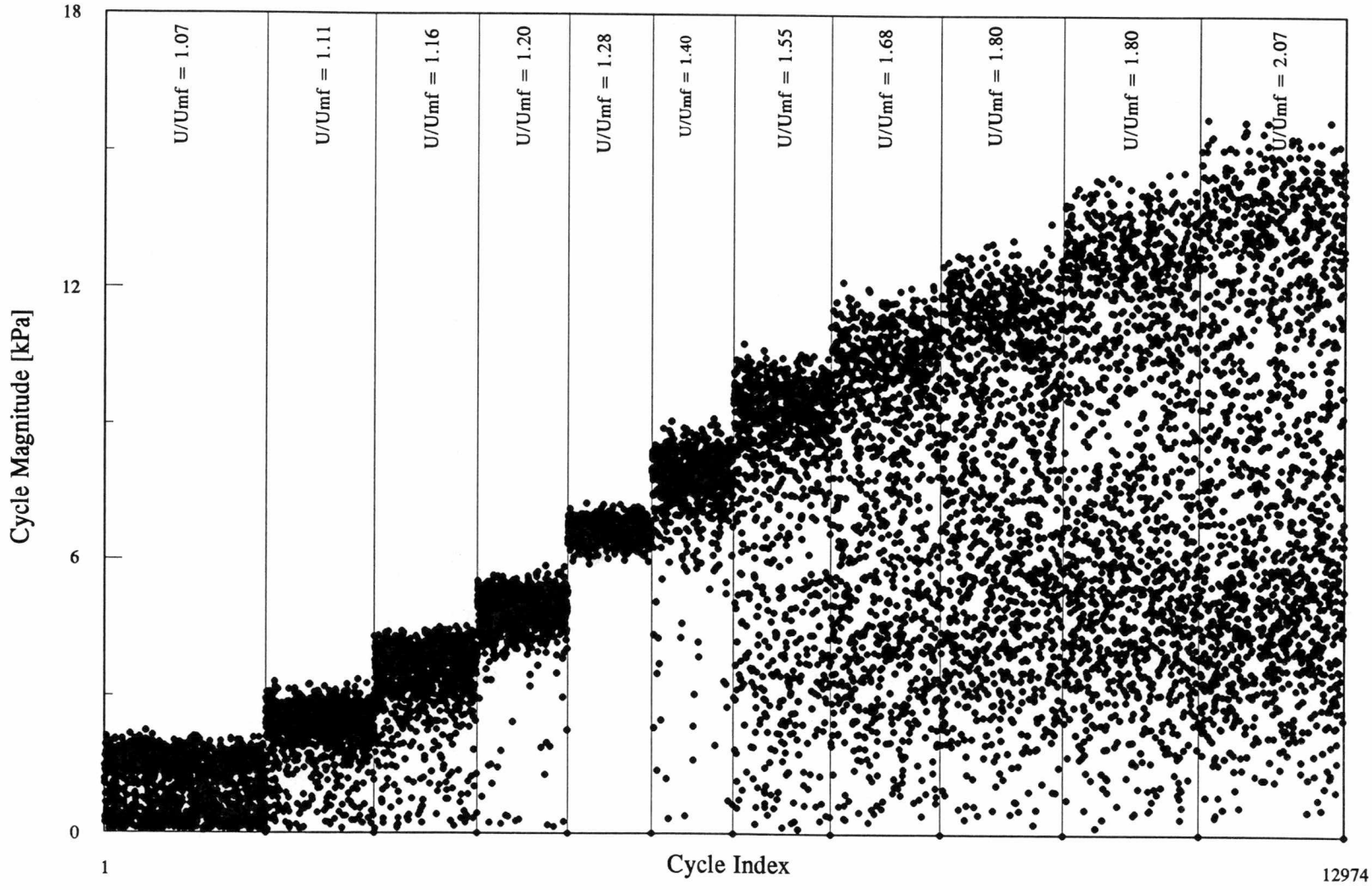


Figure 14. Composite plot illustrating the variation in cycle magnitude for steel over a velocity range of U/Umf = 1.07 to 2.07.

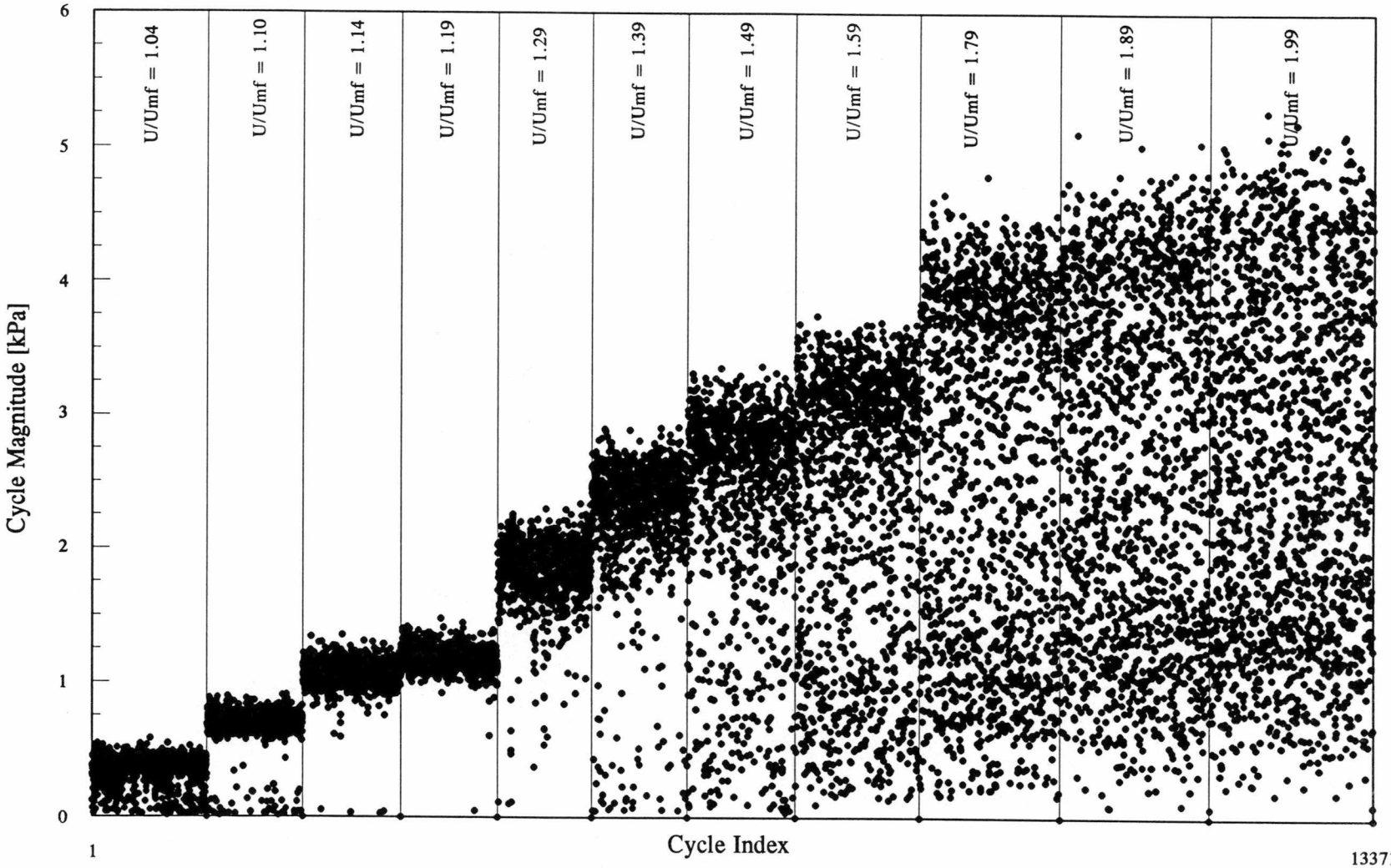


Figure 15. Composite plot illustrating the variation in cycle magnitude for glass over a velocity range of U/Umf = 1.04 to 1.99.

Figure 16. Composite plot illustrating the variation in cycle period for steel over a velocity range of U/Umf = 1.07 to 2.07.

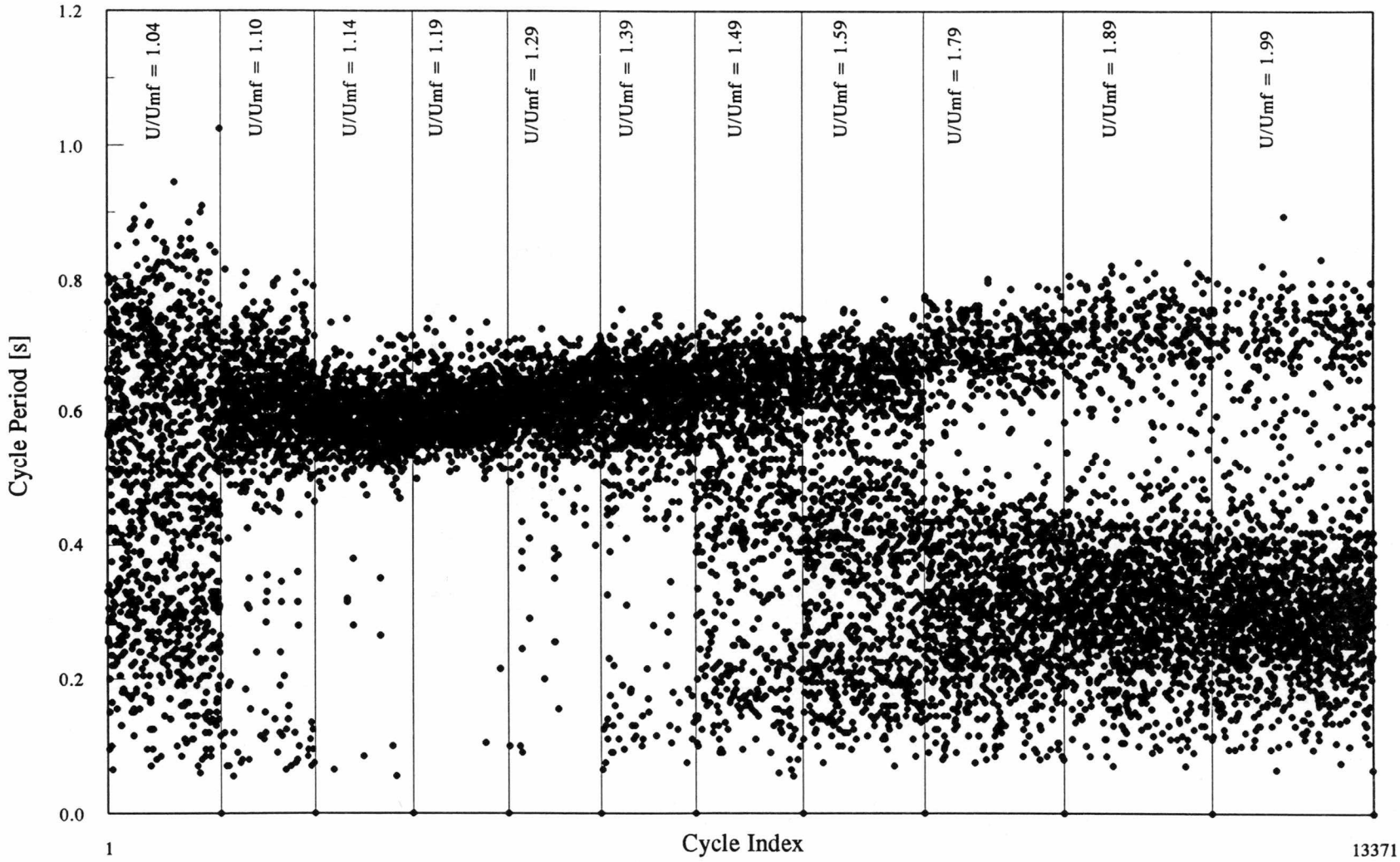


Figure 17. Composite plot illustrating the variation in cycle period for glass over a velocity range of U/Umf = 1.04 to 1.99.

distributed and small time scale oscillations associated with boiling or fluttering and irregular small bubbles dominate the system behavior. For steel, a weak cluster can be seen around 0.3 s. With increase in gas velocities, the system behavior moves towards longer time scale oscillations with a dominant period around 0.65 s for steel and 0.6 s for glass. This dominant period is stabilized with further increase in gas velocity. At regular slugging, the cluster is at its narrowest indicating the system behavior is nearly periodic (i.e., a noisy limit cycle). As flow is increased to the breaking slug regime, the small time scale oscillations associated with the stutters tend to become more dominant. These small scale oscillations also are clustered around a value of 0.3 to 0.4 s similar to that observed in the close to minimum fluidization condition for steel.

5.1.3 POWER SPECTRA

Power spectra were generated by making Fast Fourier Transforms of Hanning-windowed, 1024 point data blocks. Twenty data blocks were transformed for each condition and the results averaged to produce composite spectra. Complete results are given in Appendix B. Selected power spectra of local pressure signal corresponding to the fluidization conditions, near minimum fluidization, developing slug regime, regular slugging regime and breaking slug regime are used in this section to discuss the overall trends.

For both steel and glass, the dominant features and power are in the 0 to 10 Hz region. Above 10 Hz the power drops by five decades and these frequencies are not considered further here. The dominant peak in the 0 to 2 Hz region observed in most

cases is due to the global or large time scale oscillations associated with slugging or large bubbles. The small time-scale and low amplitude oscillations associated with collective particle bouncing or fluttering and small bubbles are manifested in the 2 - 10 Hz region.

Near minimum fluidization, the power spectra are broad banded for both materials as seen in Figures 18a and 19a. The broad band structure reflects the complex particle fluttering or bouncing, irregular bubbling and occasional slugging observed in this regime. As the fluidization velocity increases the slugging becomes dominant in the bed and correspondingly the 0-2 Hz peak is more dominant (Figures 18b and 19b). At regular slugging regime, the power spectra illustrated in Figures 18c and 19c are characterized by a sharp peak in the 0 to 2 Hz region and the least power in 2 - 10 Hz region indicating that the bed behavior is almost regular. In the case of steel, harmonics of the dominant peak are observed in the 2 to 10 Hz region. With further increase in velocity, the power spectra again become more broad banded with more significant power in the 2 to 10 Hz region.

The observed changes in the power spectra such as transition from a broad band to a sharp peak and then back to broad banding reflect transitions from complex to nearly periodic to more complex oscillations.

5.1.4 CORRELATION DIMENSION AND ENTROPY

Correlation dimension and entropy are used for estimating the complexity of the system behavior, and for observing trends over the velocity range. Dimension and entropy values were calculated using the maximum-likelihood approach outlined in

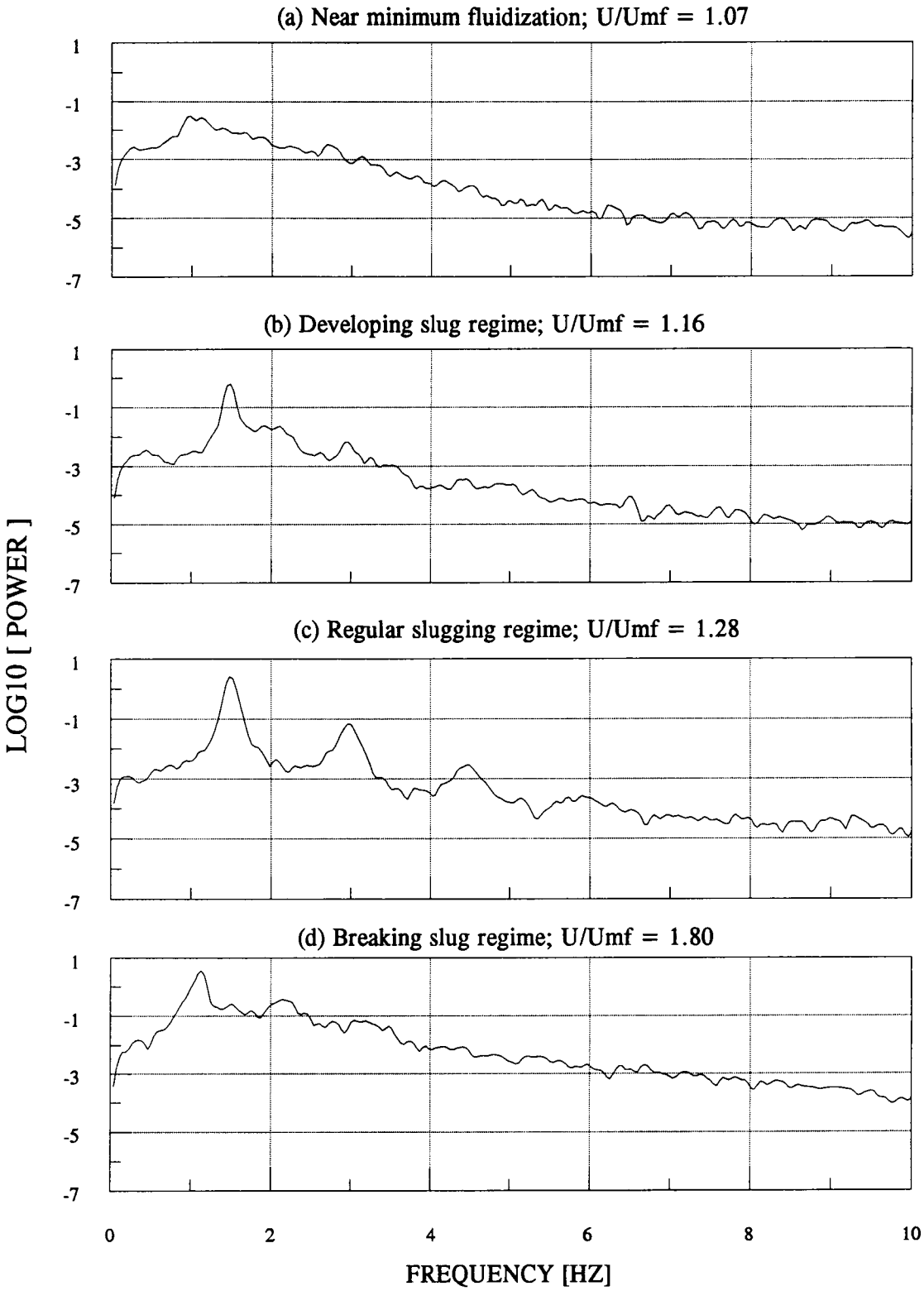


Figure 18. Fourier power spectra of local pressure signal for steel at four different fluidization regimes.

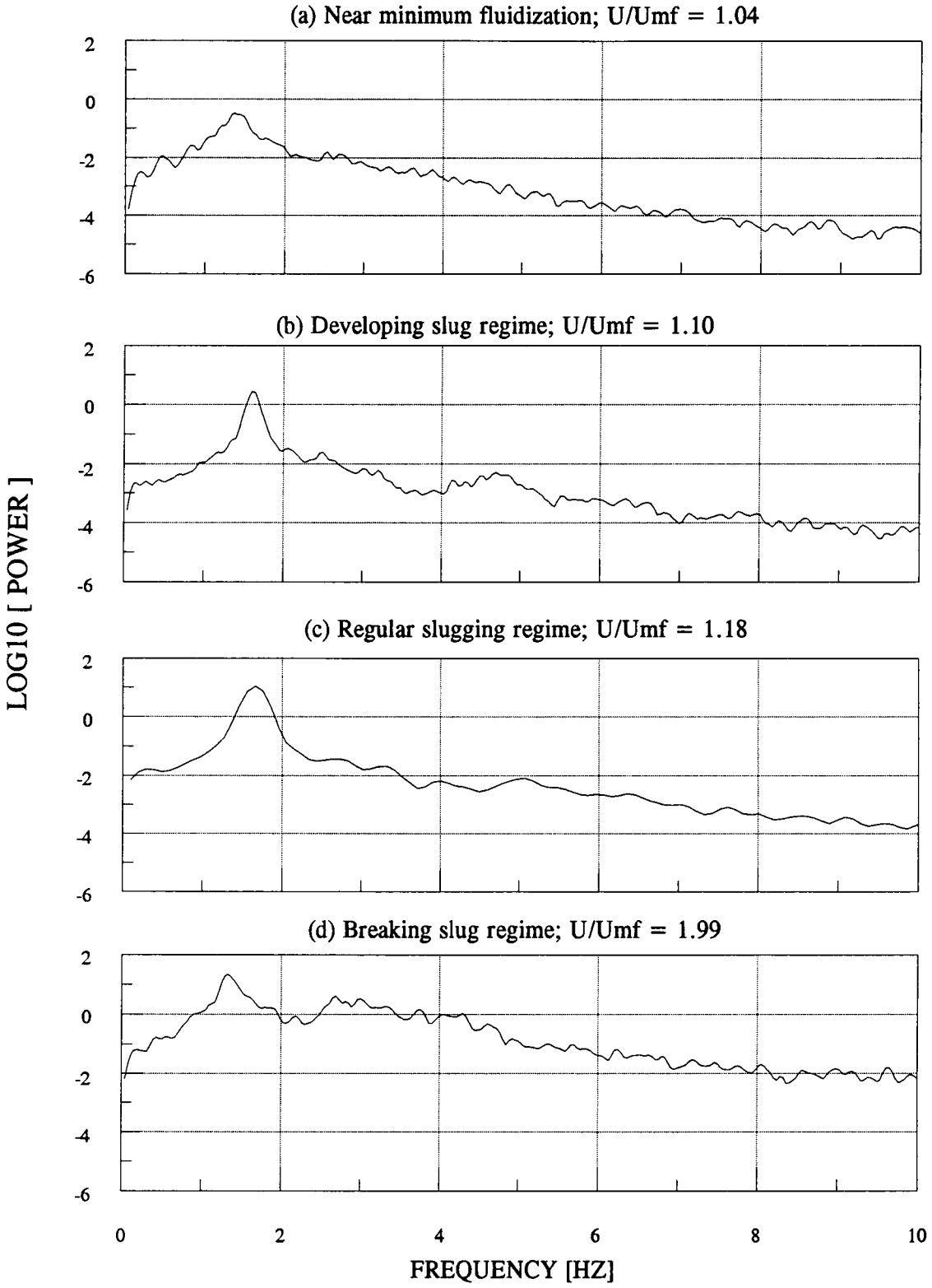


Figure 19. Fourier power spectra of local pressure signal for glass at four different fluidization regimes.

chapter 4. As described, a cut-off length of one average absolute deviation about the mean and embedding segment lengths of one average cycle time for each data set was used. It should be noted here that these conventions for applying the dimension and entropy algorithms result in different cut-off scales and different embedding segment lengths for each signal. In particular the complex behavior of the small scale oscillations at low gas flows is more apparent because the cut-off length used is adjusted to be smaller as well. An alternative approach is to use one cut-off length and one embedding segment length for all the data sets (e.g., the largest values observed over the range), so that the scales of observation are maintained constant. this latter approach is not discussed here, but is the subject of ongoing research.

Using the adjustable cut-off length procedure, near minimum fluidization velocity the bed behavior is characterized by high dimension and entropy as shown in Figures 20 and 21. With increasing gas flow, the bed becomes increasingly ordered resulting in reduced dimension and entropy values. This trend continues up to the velocities corresponding to the regular slugging regime. With still further increases in velocity, the system becomes disordered and dimension and entropy values increase.

The state at which the system has the minimum values of dimension and entropy was labeled as the maximum stable slugging state and the corresponding fluidization velocity was termed as the maximum stable slugging velocity (U_{MSS}). This maximum stabilization of slugging (U_{MSS}) occurs for steel at $U/U_{MF} = 1.28$ and for glass at $U/U_{MF} = 1.18$. Beyond U_{MSS}, the system becomes progressively more disordered, characterized by higher dimension and entropy values. The observed transitions of the bed from a

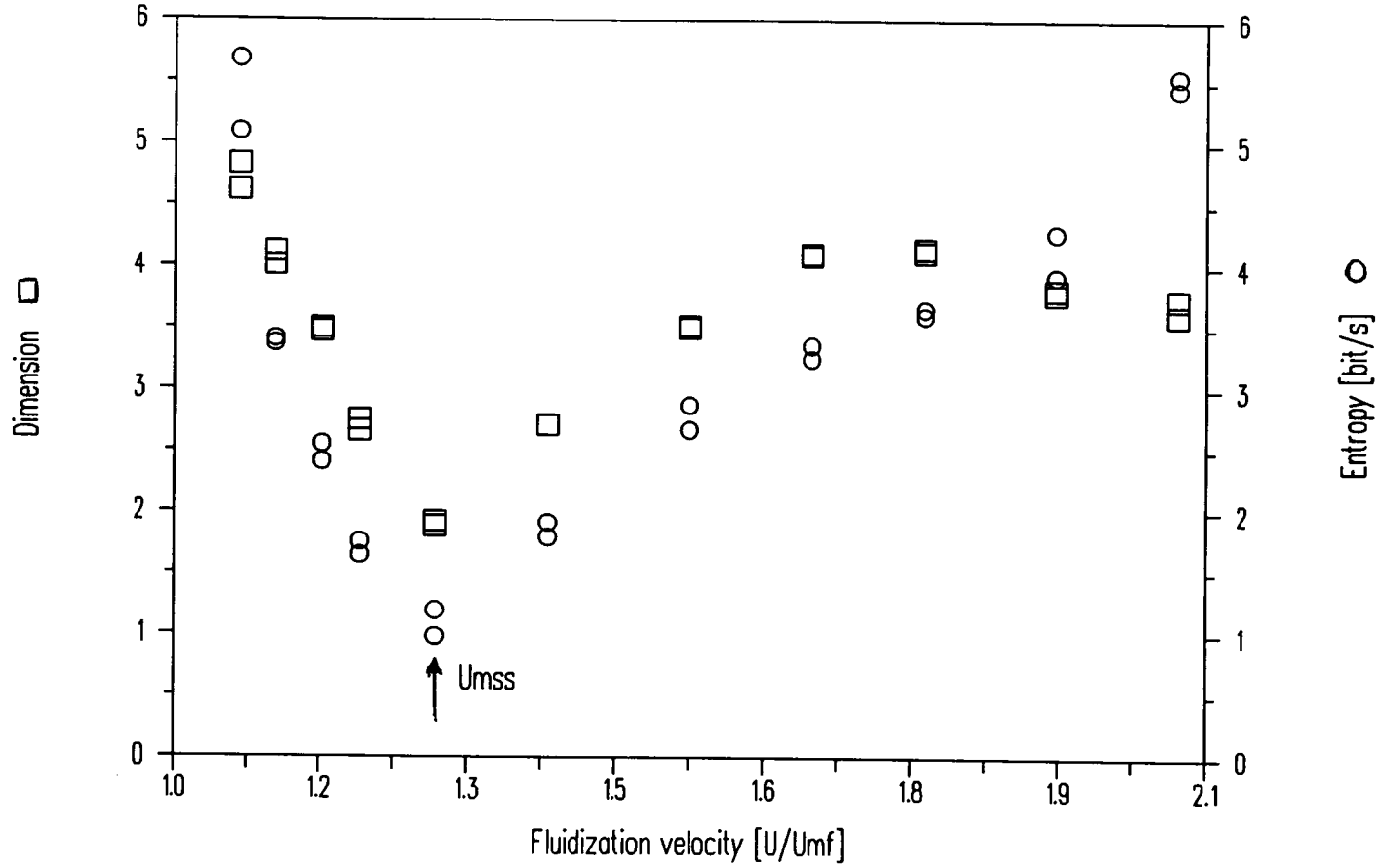


Figure 20. Variation of dimension and entropy based on local signal for steel over a velocity range of U/U_{MF} = 1.07 to 2.07.

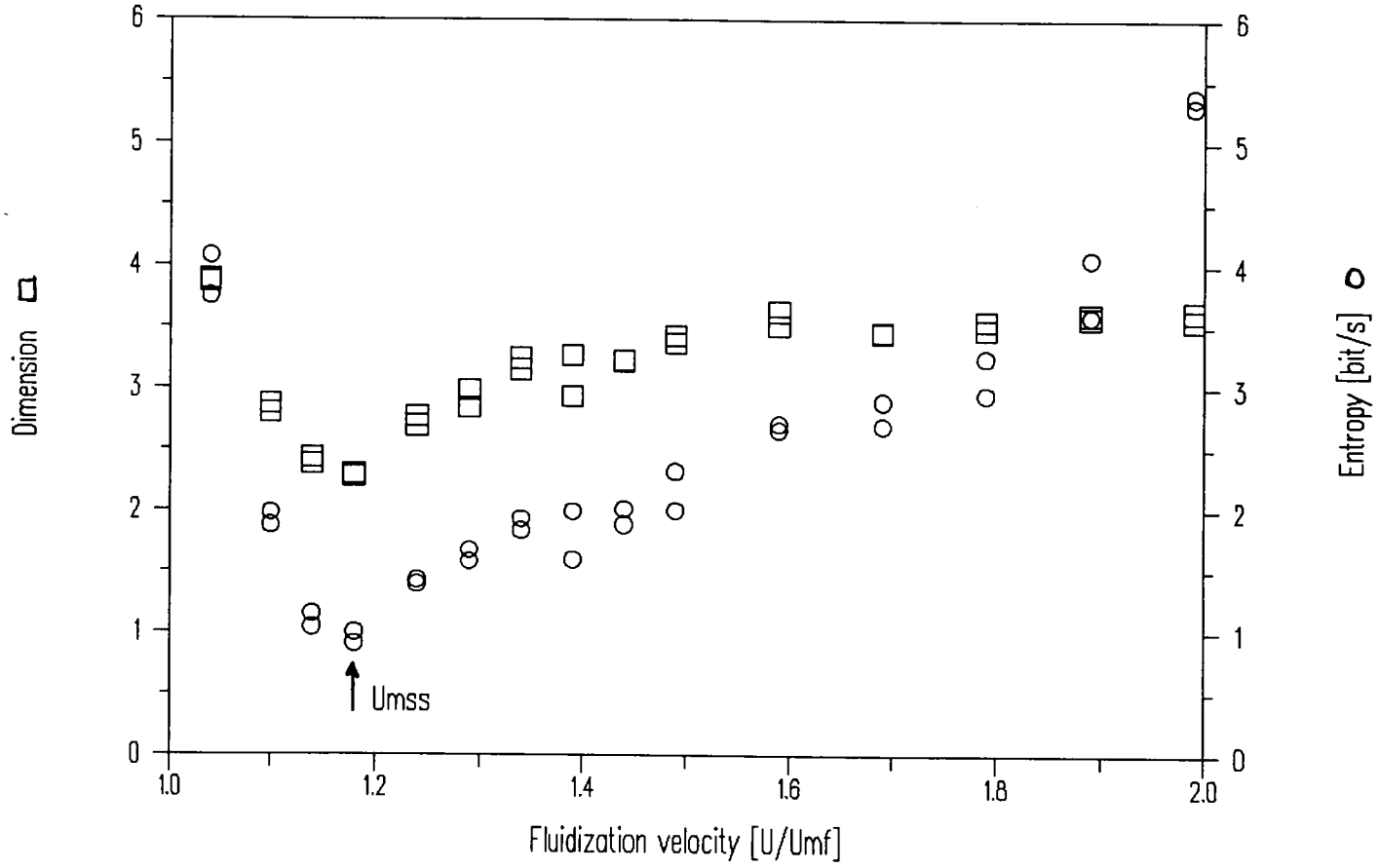


Figure 21. Variation of dimension and entropy based on local signal for glass over a velocity range of U/U_{MF} = 1.04 to 1.99.

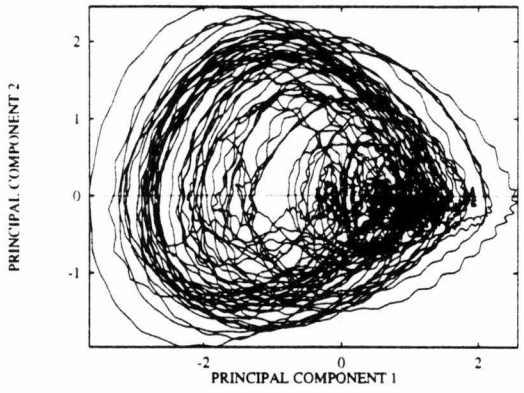
complex to regular and then from regular to complex behaviors over the velocity range are thus reflected in the dimension and entropy results.

5.1.5 PHASE SPACE TRAJECTORIES FOR VISUALIZATION

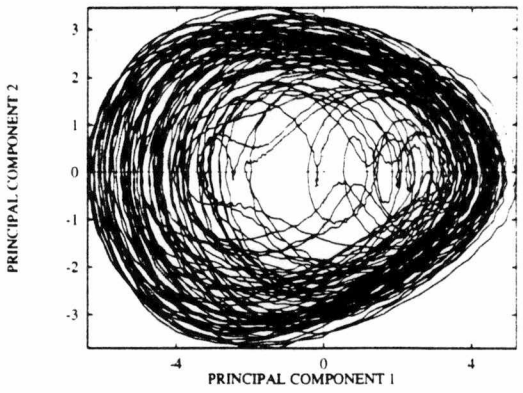
For visualization purposes, phase space trajectories are reconstructed from the time series using time lag embedding and principal component analysis as discussed in chapter 4. Two dimensional projections of typical segments of the reconstructed trajectories for all the conditions investigated are in Appendix B. Typical phase plots for fluidization conditions corresponding to near minimum fluidization, developing slug regime, maximum stable slugging state and breaking slug regime are described in this section and illustrated for steel and glass in Figures 22 and 23, respectively.

Phase plots for the near minimum fluidization condition illustrated in Figures 22a and 23a are complex and dominated by smaller orbits associated with collective motion of particles and small bubbles/voidages. With increase in velocity, the system enters the developing slug regime dominated by slugging. The phase plots become less complex and opens up in the middle as seen in Figures 22b and 23b, indicating the system is becoming more ordered.

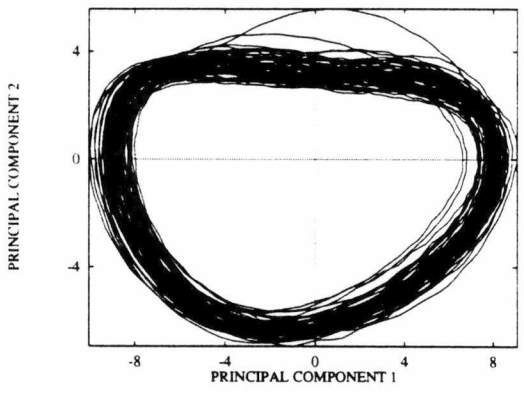
In the maximum stable slugging state, the system is at its most ordered or regular behavior. The phase plots for steel and glass open up into ring shaped patterns. It appears that at this condition, the system behavior can be considered as a noisy limit cycle, and slight variability from cycle to cycle (causing the ring to have its thickness) can be attributed to the small-scale particle to particle interactions. In a fluidized bed the small-



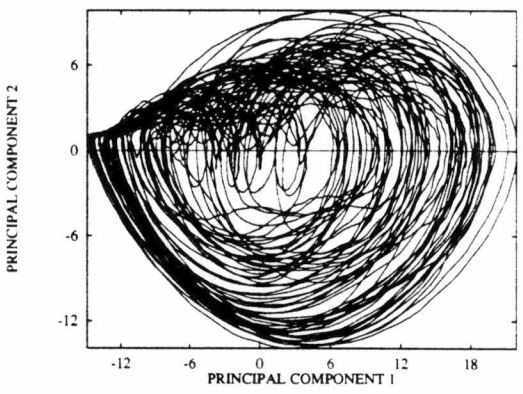
(a) Near minimum fluidization;
U/U_{MF} = 1.07



(b) Developing slug regime;
U/U_{MF} = 1.16

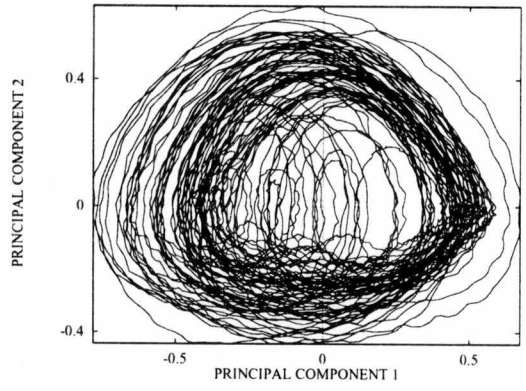


(c) Maximum stable slugging state;
U/U_{MF} = 1.28

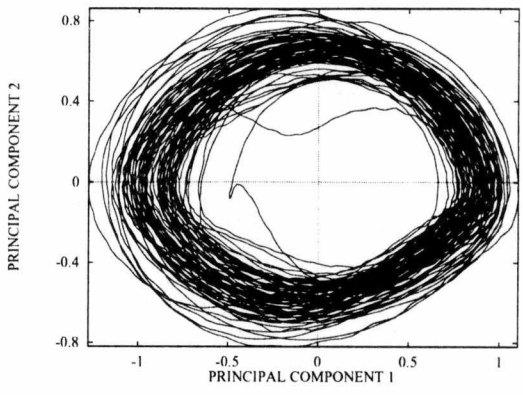


(d) Breaking slug regime;
U/U_{MF} = 1.80

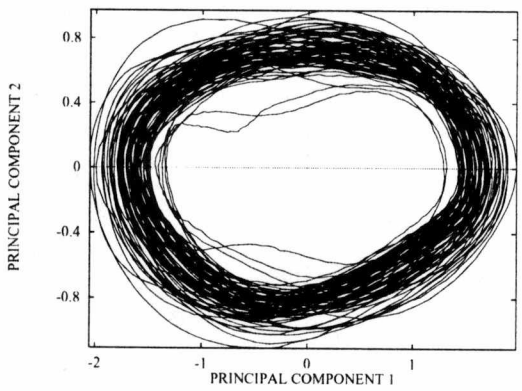
Figure 22. Two dimensional projection of reconstructed trajectories from local pressure signal for steel at four different fluidization regimes [Time span = 50 s].



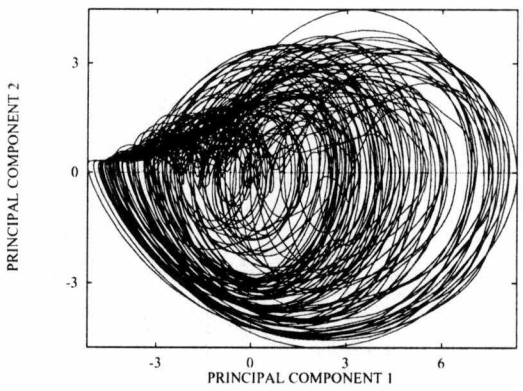
(a) Near minimum fluidization;
U/U_{MF} = 1.04



(b) Developing slug regime;
U/U_{MF} = 1.10



(c) Maximum stable slugging state;
U/U_{MF} = 1.18



(d) Breaking slug regime;
U/U_{MF} = 1.99

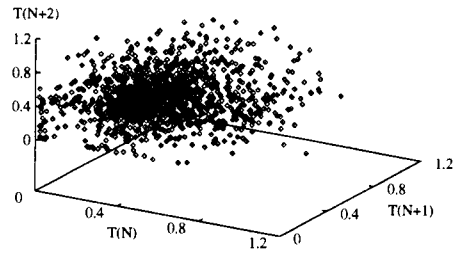
Figure 23. Two dimensional projection of reconstructed trajectories from local pressure signal for glass at four fluidization conditions [Time span = 50 s].

scale dynamics associated with single particles or small number of particle are always present in addition to bubbling or slugging. It is believed that this small scale dynamics is effectively stochastic in nature and is superimposed on the large scale bulk dynamics of interest here. Beyond U_{MSS}, the phase plots become more complex and smaller orbits associated with the break up of slugs appear in the plots (Figures 22d and 23d).

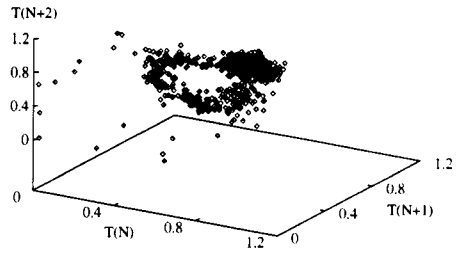
5.1.6 TIME RETURN MAPS

As described in chapter 4, the orbital period used to construct time return maps is defined as the time taken for the trajectory to complete one orbit about the principal component 2 plane (PC2 = 0.0). These maps provide another perspective on the dynamic transition. Time return maps for all the conditions investigated are in Appendix B. Selected maps for both material at fluidization flows corresponding to near minimum fluidization, developing slug regime, maximum stable slugging state and breaking slug regime are illustrated in Figures 24 and 25.

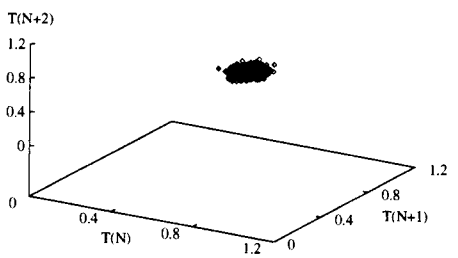
Near minimum fluidization velocity (Figure 24a and 25a), the small time-scale fluctuations are aperiodic except for a weak clustering around 0.35 s for steel. This results in a time return map with a broad dispersion of points. As the fluidization flow is increased, the system is progressively dominated by the larger time-scale fluctuations associated with slugging. A new dense cluster of points around 0.7 s for steel and around 0.6 s for glass emerges. These periods correspond to the dominant peaks seen at 1.4 Hz and 1.7 Hz for steel and glass, respectively in the power spectra. This trend is seen clearly in Figures 24b and 25b, which corresponds to the developing slug regime. The



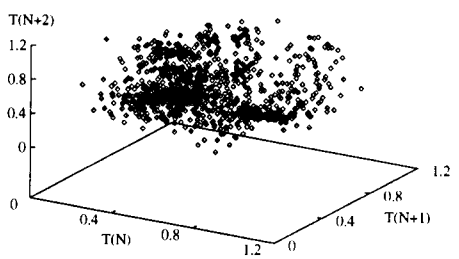
(a) Near minimum fluidization;
U/U_{MF} = 1.07



(b) Developing slug regime;
U/U_{MF} = 1.16

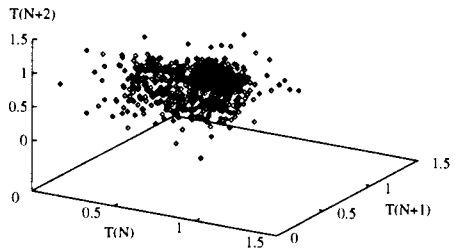


(c) Maximum stable slugging state;
U/U_{MF} = 1.28

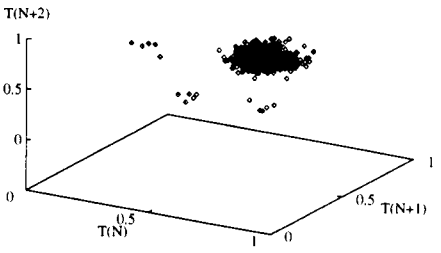


(d) Breaking slug regime;
U/U_{MF} = 1.80

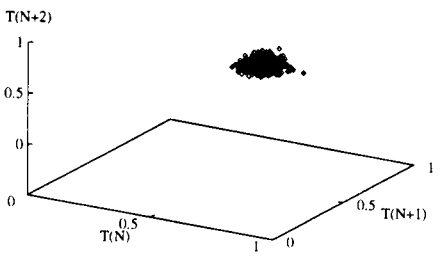
Figure 24. Time return maps using local pressure signal for steel at four different fluidization regimes.



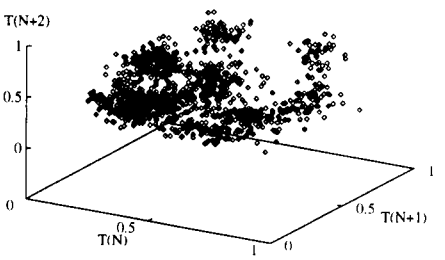
(a) Near minimum fluidization;
U/U_{MF} = 1.04



(b) Developing slug regime;
U/U_{MF} = 1.10



(c) Maximum stable slugging state;
U/U_{MF} = 1.18



(d) Breaking slug regime;
U/U_{MF} = 1.99

Figure 25. Time return maps using local pressure signal for glass at four fluidization conditions.

system wanders in and out of this cluster forming some clearly non-random patterns on the time return maps. As the gas velocity approaches the regular slugging regime, the return points collapse together in to a much tighter cluster. At maximum stable slugging, a single dense cluster of points is seen in the time return maps (Figures 24c and 25c).

Beyond U_{MSS} for a small range of gas velocities, the dense cluster shifts to slightly higher periods and become diffuse with more points outside the cluster. With further increase in velocity, the return maps become more diffuse and the cluster also becomes more diffuse (see appendix B). A new cluster of points begins to emerge at lower periods. This cluster is associated with the smaller time-scale oscillations caused by the break-up of slugs and is clustered around a period of 0.4 s for steel and around 0.3 s for glass. With further increase in gas velocity, this lower period cluster is stabilized and the upper cluster is no longer distinct as seen in the breaking slug regime time return maps (Figures 24d and 25d). In this regime also, the points outside the cluster form a non-random distribution.

In the terminology of nonlinear dynamics, the dense clusters seen in the maps are manifestations of a large number of similar orbits and appear to reflect fixed points associated with unstable limit cycles. Slugging beds seem to have two unstable fixed points, except within a small range of flows in the vicinity of U_{MSS}. Depending on the gas flow, one point is relatively more stable than the other. Away from the maximum stable state, the patterns in the organization of the points outside the cluster are important in understanding the system dynamics. In these cases, the map is characterized by a dense cluster and two "arms" delineated by the points outside the cluster.

The time sequence of points followed on these maps shows important non-random patterns. The system frequently moves into the cluster using one arm and exits the cluster using the other arm. It is believed that the arms reflect the stable and unstable manifolds associated with the unstable fixed points. In the developing slug regime the upper arm is used for flow in to the cluster and the lower arm for exiting the cluster. In the breaking slug regime, however the lower arm is used for flow in and the upper arm for flow out of the cluster.

5.1.7 TRANSITION TO CHAOS

To better understand the nature of the transition from periodic to aperiodic oscillations as gas flow is increased beyond U_{MSS}, the possibility that this transition reflects an intermittency route to chaos was evaluated. In nonlinear dynamics literature, intermittency is described as nearly periodic motion interrupted by irregular bursts when a system parameter (r) deviates from a critical value (r_C). As the deviation from critical value increases, the irregular bursts become progressively frequent until the system becomes chaotic. As discussed in the Manneville and Pomeau [17], the average time between bursts is expected to follow a power law $t \propto (r-r_C)^{-0.5}$, where t is the average time between irregular bursts.

It is conjectured that the stuttering phenomenon described earlier might be a manifestation of intermittent bursts of chaotic behavior. For fluidized beds, even though the system parameter fluidization velocity and the critical value U_{MSS} are apparent, the inherent noisy nature of the process (i.e., the small-scale dynamics) presents some

additional problems. Even at U_{MSS}, the limit cycle is not sharply defined as in the case of numerical models or clean experimental systems. Also, it is problematic to quantitatively distinguish stutters from noisy oscillations. To circumvent these limitations an approach that uses variation in cycle magnitude to distinguish between regular and irregular behavior was adopted.

The inherent noisy nature of system was quantified as the distribution band of cycle magnitudes at U_{MSS}. At any operating condition, the average cycle magnitude corresponding to the regular behavior is identified using histograms and the tolerance for system noise (equal to the distribution width at U_{MSS}) is applied to this value to identify regular behavior. Using this method, the average time interval between bursts was calculated.

As suspected, the average time interval between bursts declines with increasing deviation from the critical value and follows a power law. This methodology was applied to the Lorenz model as well as to the fluidized bed data for steel and glass and the results are illustrated in Figure 26. The resulting power law fit for fluidized bed data with exponents ranging from 0.49 to 0.73 appears to be reasonable. The confirmation of an intermittency pattern in the slugging bed also suggests that the control approach described later may have wider applicability to other systems exhibiting intermittent chaos.

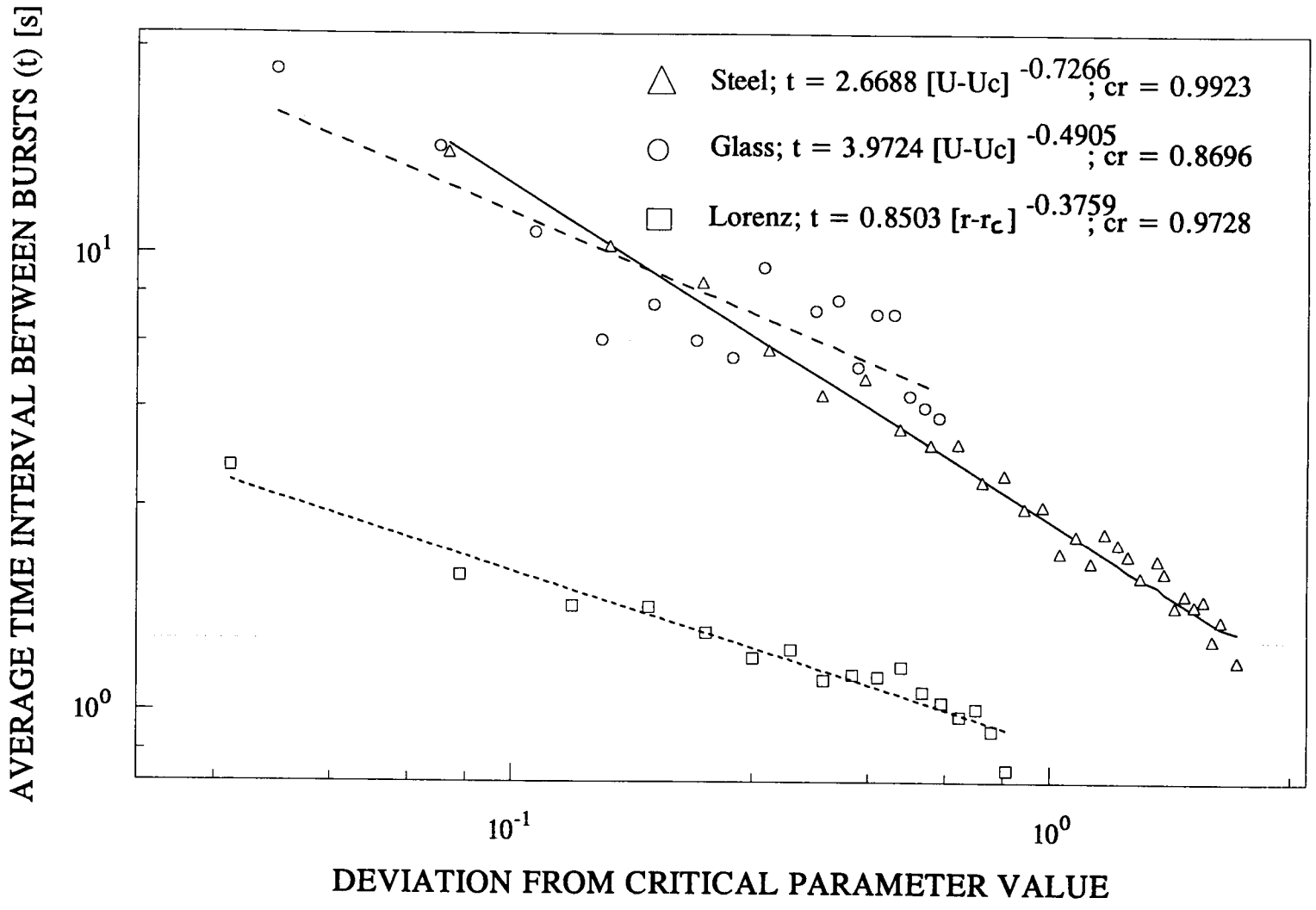


Figure 26. Intermittency route to chaos power law fit curves for steel using Umss = 4.61 m/s as Rc; for glass using Umss = 1.73 m/s as Rc and for Lorenz system (b = 8/3 and sigma = 10) using r= 166.07 as Rc; where Rc is the critical parameter value and cr is the correlation coefficient for the curve fit.

5.2 CONTROL STRATEGY

Apparent low dimensionality of slugging behavior of group D particles (at least for the bulk scale behavior) and the presence of unstable fixed points over a wide range of fluidization velocities gave hope that control of system behavior could be achieved. In the so called OGY method discussed in chapter 2, an accessible system parameter on which the location of fixed points are dependant is identified and by manipulating the selected parameter, stabilization and destabilization of system behavior are achieved. In the case of fluidized beds, a modification of OGY approach which has similarities to Garfinkel's approach for controlling cardiac chaos [20] was used. As described below, this modified control method employs short time-scale perturbations at one point in the bed, based on a measured observable (pressure). Using this method, both stabilization and destabilization system behavior were achieved.

The external perturbation used was a small high pressure gas pulse admitted in the bed through the side wall. Initially a manually-triggered solenoid valve was used to introduce the pulses and it was found to have considerable effect on the system dynamics. Various nozzle diameters, location and orientation of nozzle were tried to arrive at the optimum configuration described in the experimental apparatus chapter. Depending on when the pulse is introduced relative to the natural slugging cycle in the bed and the duration of the pulse, it was possible to enhance or disrupt the slugs. As both the plenum and local pressure signals correlate well with the slugging dynamics, a PC-based control scheme using one of these signals was devised. Two parameters of critical importance in this method are pulse timing and pulse duration.

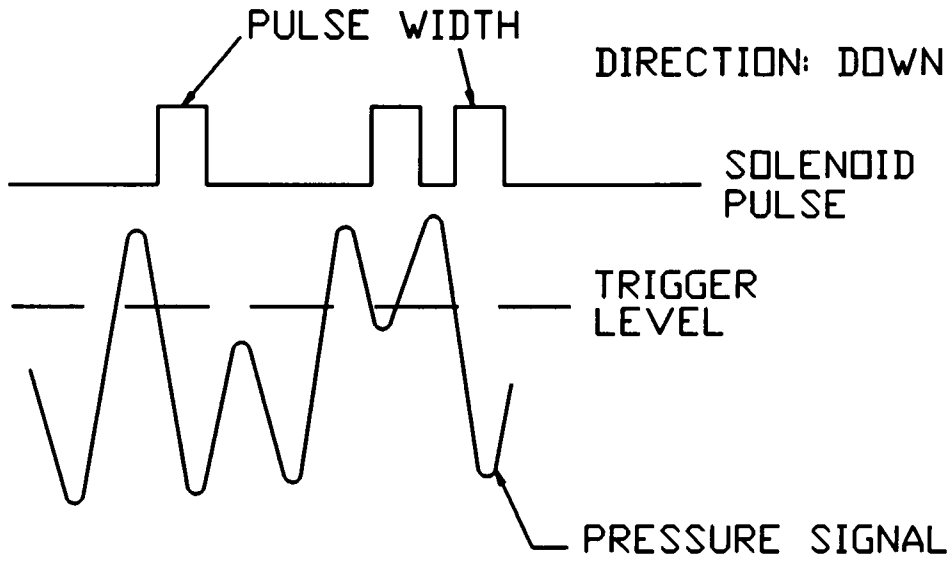


Figure 27. Illustration for the control scheme

The control signal either (local or plenum) signal, after being bandpass filtered is input to the data acquisition board mounted on a PC. A control routine samples the data at a rate of approximately 2 kHz, determines the dynamical state of the bed and takes appropriate control action. The control action is to generate a 10 mA pulse for the set pulse duration which is converted to 115 V signal by a solid state relay to open the solenoid valve.

In the present version of the control scheme (Figure 27), the pulse timing is determined based on the occurrence of a specific dynamic event; i.e., when the signal crosses a specified threshold known as the "trigger level" in the specified direction "up or down" and the solenoid valve is opened for the duration of a specified pulse width. This control strategy produces dynamical feedback, since each control action reflects the

dynamical response of the system to the previous control action and allows the system to lock on to a particular mode of behavior. For each operating condition, the trigger timing and pulse width have to be empirically learned based on a set of control experiments which are explained in the next section.

5.2.1 EMPIRICAL DETERMINATION OF CONTROL PARAMETERS

In order to implement the present control scheme, it is necessary to determine the optimum control parameters at each operating condition. The optimum parameters are determined based on two sets of control experiments. The basic procedure is summarized in this section using the maximum stable state for steel (with plenum signal as the control signal) as an example.

Optimum pulse timing

Pulse timing, fixed by trigger level and direction, is the most critical parameter in this control scheme, and by varying the pulse timing a wide variety of bed behavior from slug stabilization to destabilization can be achieved. A set of experiments (details listed in Table 2) varying the pulse timing and with a constant pulse width of 50 ms was performed for a systematic evaluation of effect of pulse timing. Qualitative information about the effect of pulse timing can be inferred from visual observation of time series, Fourier analysis, cycle magnitude distribution, and phase plots. Results from some of these qualitative analysis tools for all runs are in Appendix C.

Pulsing during control experiments introduces a direct disturbance in the "local" pressure signals in this condition, and the results must be carefully interpreted. For

Table 2. Control parameters for determination of optimum pulse timing for steel at U_{MSS}

Run No	Pulse Timing		Pulse Width [ms]
	Trigger Level [kPa]	Direction	
A1	-0.93	up	50
A2	-0.48	up	50
A3	0.0	up	50
A4	+0.47	up	50
A5	+0.93	up	50
A6	+0.93	down	50
A7	+0.48	down	50
A8	0.0	down	50
A9	-0.47	down	50
A10	-0.93	down	50

determination of optimum pulse timing for the desired control objective, dimension and entropy, which are measures of the complexity of system behavior were used. Results for the pulse timing set of experiments are shown in Figure 28.

The highest or lowest dimension and entropy values indicate that slugging is at its most irregular or regular behavior, respectively. For runs 1-5, as the trigger level increases with the upward direction, the dimension and entropy values steadily decrease for both plenum and local signal. However, at Run 6, when the crossing direction is changed to down, the dimension values increase, but entropy values remain nearly the same and increase in the subsequent runs. When the trigger level is decreased further with direction being down (Run 6 to 10), the dimension and entropy values increase steadily up to Run 9. After that, except the plenum signal dimension, the dimension and entropy estimates for both local and plenum signal decrease. From the observed trend, it can be inferred that the system is most ordered at Run 5 and most disordered at Run 9. Hence, the optimum pulse timing for stabilization of slugging behavior are trigger level of +0.93 kPa and direction up. For destabilization, a trigger level of -0.48 kPa and direction down are optimum.

Optimum pulse width

For optimum pulse width determination, the pulse timing was set at the optimum stabilizing and destabilizing conditions determined from the preceding experiments, and the pulse width was varied between 25 and 150 ms to study the effect of pulse width. Table 3 lists the operating conditions for these experiments. Pulse width as a control parameter does not affect the system behavior in a drastic way as the trigger level does.

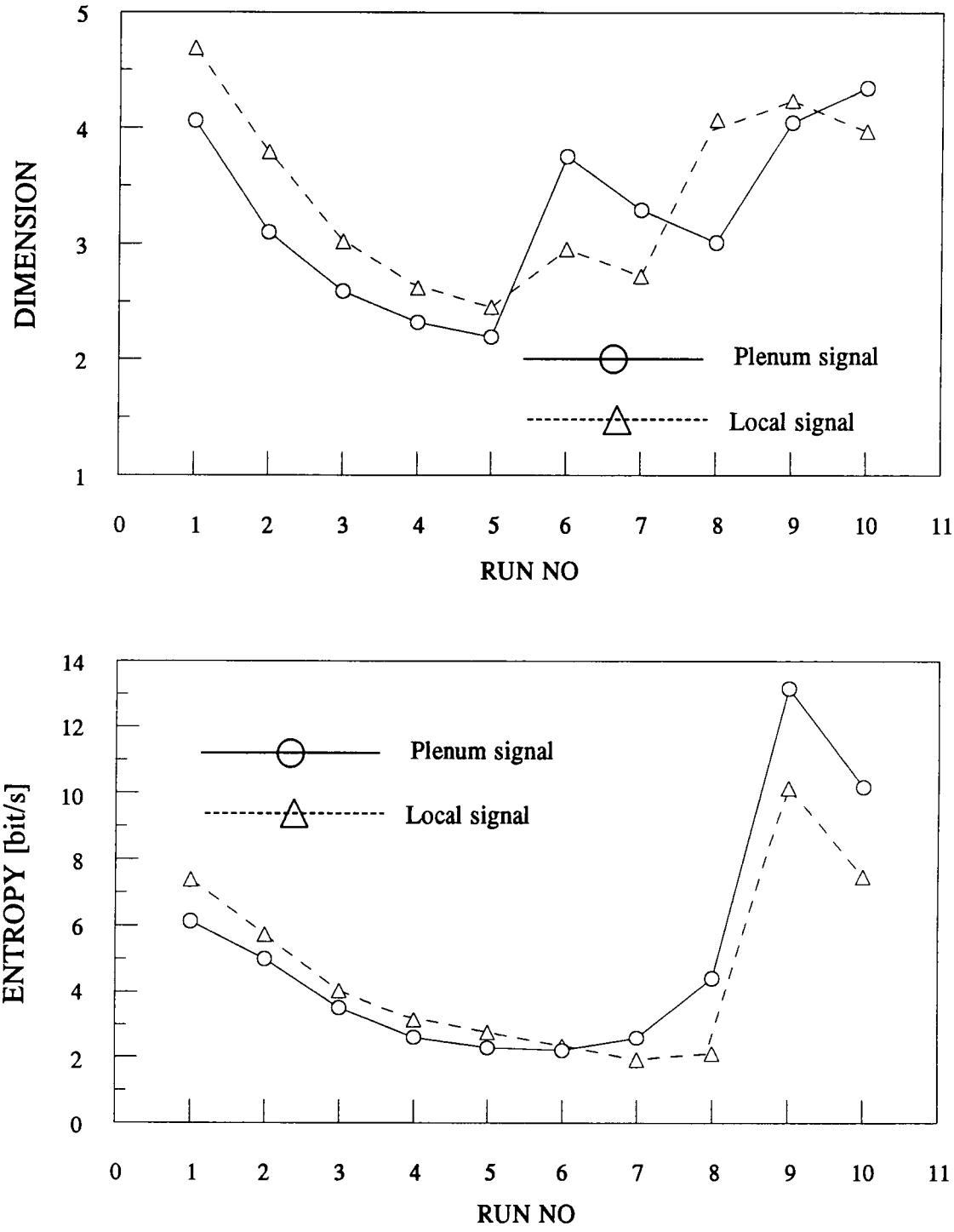


Figure 28. Effect of pulse timing on dimension and entropy estimations for steel at a constant pulse width of 50 ms and a velocity of U/Umf = 1.28.

Table 3. Control parameters for determining the optimum pulse width for steel at U_{MSS}.

Run No	Pulse Timing		Pulse Width [ms]	Control Mode
	Trigger Level [kPa]	Direction		
B1	+0.93	up	50	Stabilization
B2	+0.93	up	50	Stabilization
B3	+0.93	up	50	Stabilization
B4	+0.93	up	50	Stabilization
B5	+0.93	up	50	Stabilization
B6	-0.48	down	50	Destabilization
B7	-0.48	down	50	Destabilization
B8	-0.48	down	50	Destabilization
B9	-0.48	down	50	Destabilization
B10	-0.48	down	50	Destabilization

Results from some qualitative analysis tools for all runs are in Appendix C. Increasing the pulse width in stabilization mode generally results in a decrease in dimension and entropy and the trend is shown in Figure 29. There appears to be a minimum in dimension at 100 ms pulse width. But, considering the entropy trend and the marginal difference in dimension values between 100 ms and 150 ms, either one can be used as the optimum. The deciding factor may be economics; i.e., how much high pressure (or by-pass) air can be used?. Pulse width of 150 ms was used as the optimum for stabilization control.

Qualitative measures such as phase plots, cycle magnitude distribution also agree

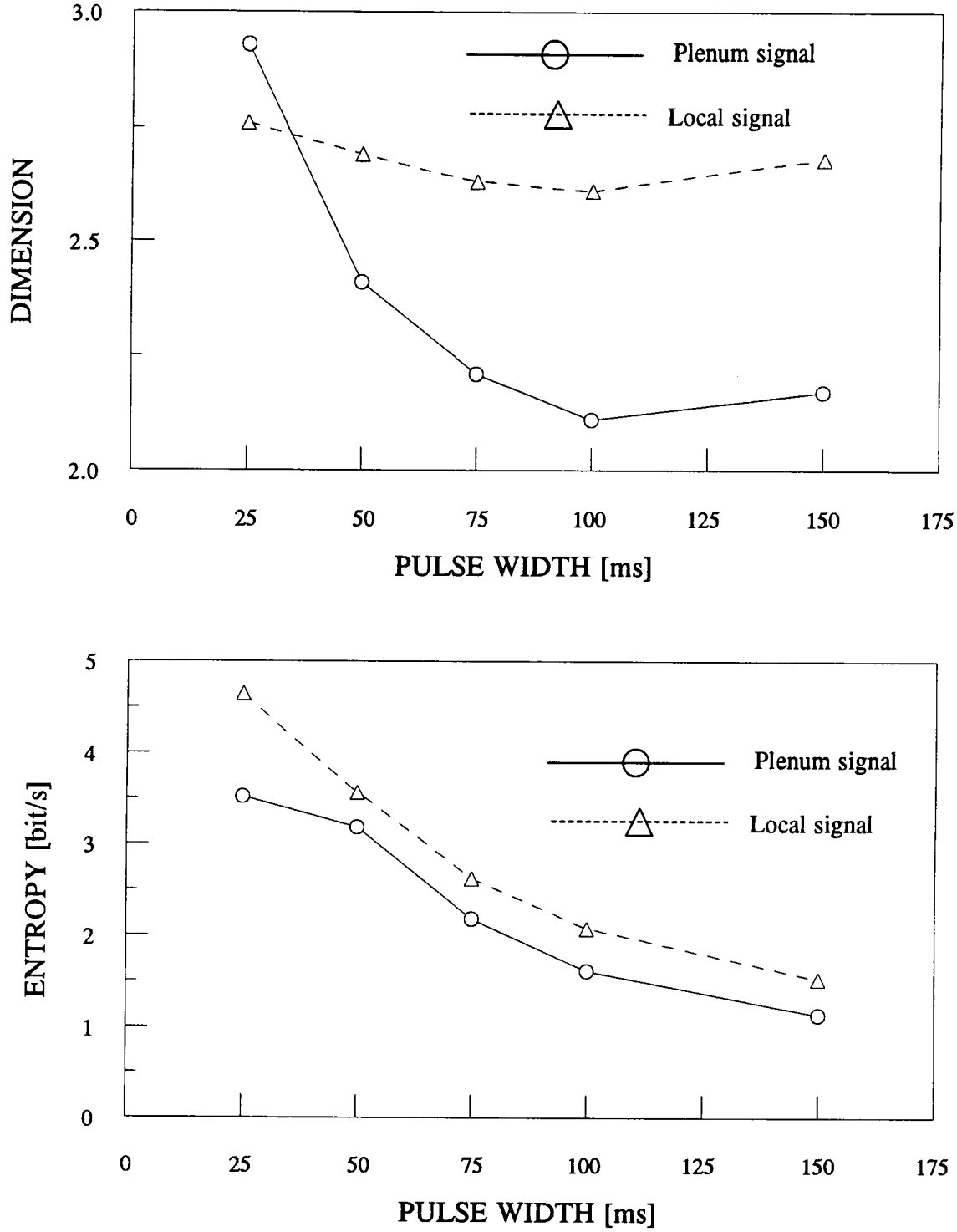


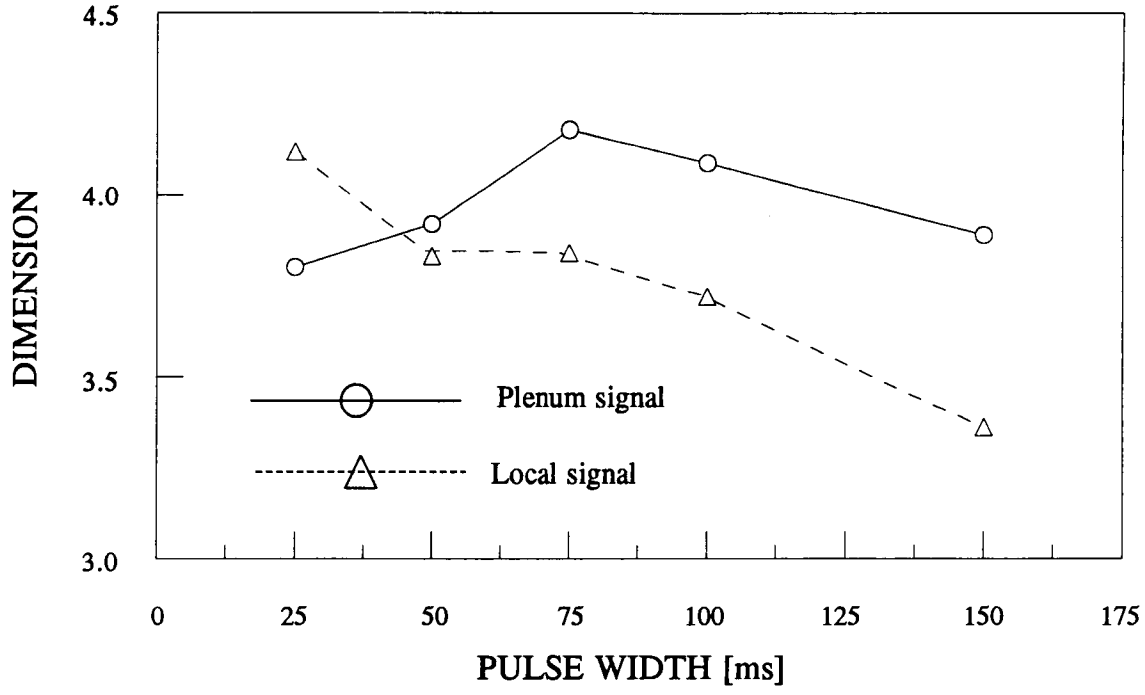
Figure 29. Effect of pulse width on dimension and entropy estimations for steel at optimum pulse timing of 0.93 kPa & up and stabilization control at a velocity of U/Umf = 1.28.

well with the entropy and dimension results. Dimension and entropy estimates for the destabilization runs are presented in Figure 30. Up to 75 ms pulse width, the system has higher entropy and dimension. Increasing the pulse width beyond 75 ms tends to stabilize the system, as indicated by the decrease in dimension and entropy.

5.2.2 DIFFERENCES BETWEEN PLENUM AND LOCAL SIGNAL

As discussed in section 3.1.1 two differential pressure measurements, plenum and local measurements were used in this study to monitor the dynamical behavior of the bed. However, there are some inherent differences between the local and plenum signal due to the measurement locations. The local signal measures the dynamical differential pressure fluctuations across a 10.2 cm high bed segment in the upper portion of the bed. Even though the signal reflects all the events occurring in the entire bed, it is dominated by local events, i.e., events occurring in the measurement window. Plenum signal measures the dynamical pressure fluctuations between the plenum below the distributor and atmosphere. It reflects all the events occurring in the entire bed and events occurring closer to the distributor such as detaching of a bubble/slug will be reflected in it. Additionally, the distributor pressure drop acts like a damping element and has an influence on the ability of the signal to correlate with the bed dynamics. Plenum signal can be viewed as a global pressure drop signal and is more complex compared to the local signal.

Normally global bed pressure drop is measured between a location just above the distributor and atmosphere. However, hazardous environment encountered in the case of



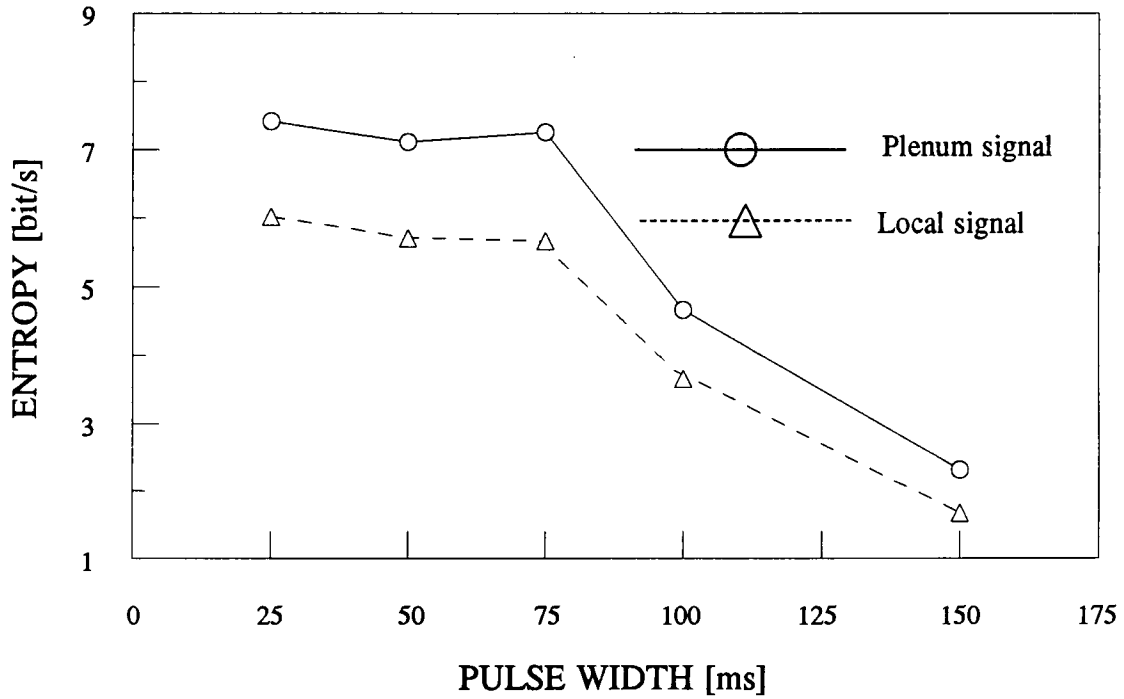


Figure 30. Effect of pulse width on dimension and entropy estimations for steel at optimum pulse timing of -0.48 kPa & down and destabilization control at a velocity of U/Umf = 1.28.

many industrial fluid bed devices such as combustors, chemical reactors, nuclear fuel processors, will be a problem for in-bed measurements. Hence, the effect of shifting the global measurement to the plenum below the distributor was investigated in an independent study and it was found that up to a distributor pressure drop of 34.5 kPa plenum signal correlates well with the bed dynamics. Distributor pressure drops for the velocity range used in this study are well within 34.5 kPa.

Typical time series measurements of both the signals at the maximum stable slugging state are shown in Figure 31. At this fluidization condition, the bubble / slug sizes as they detach from the distributor are not regular. As they move along the bed and reach the local window they reach a stable size by growth / coalescence. This behavior is clearly reflected in the irregular fluctuations in the plenum signal and regular fluctuations in the local signal.

Pulsing during control experiments introduces transient disturbances such as abrupt changes in the slope and increased magnitudes in the bed pressure signals. Depending on the fluidization condition, material used and control mode, the transient disturbance have a pronounced effect on any one or both signal. Figure 32 illustrates the effect of pulsing in the stabilization mode for steel and glass experiments. For steel in the maximum stable slugging state, local signal is affected more than the plenum signal as seen in Figure 32. For glass in the breaking slug regime, the transients can be seen in both plenum and local signal. Hence, the control experiment results for each case should be carefully interpreted. Generally, plenum signal is more robust than the local signal.

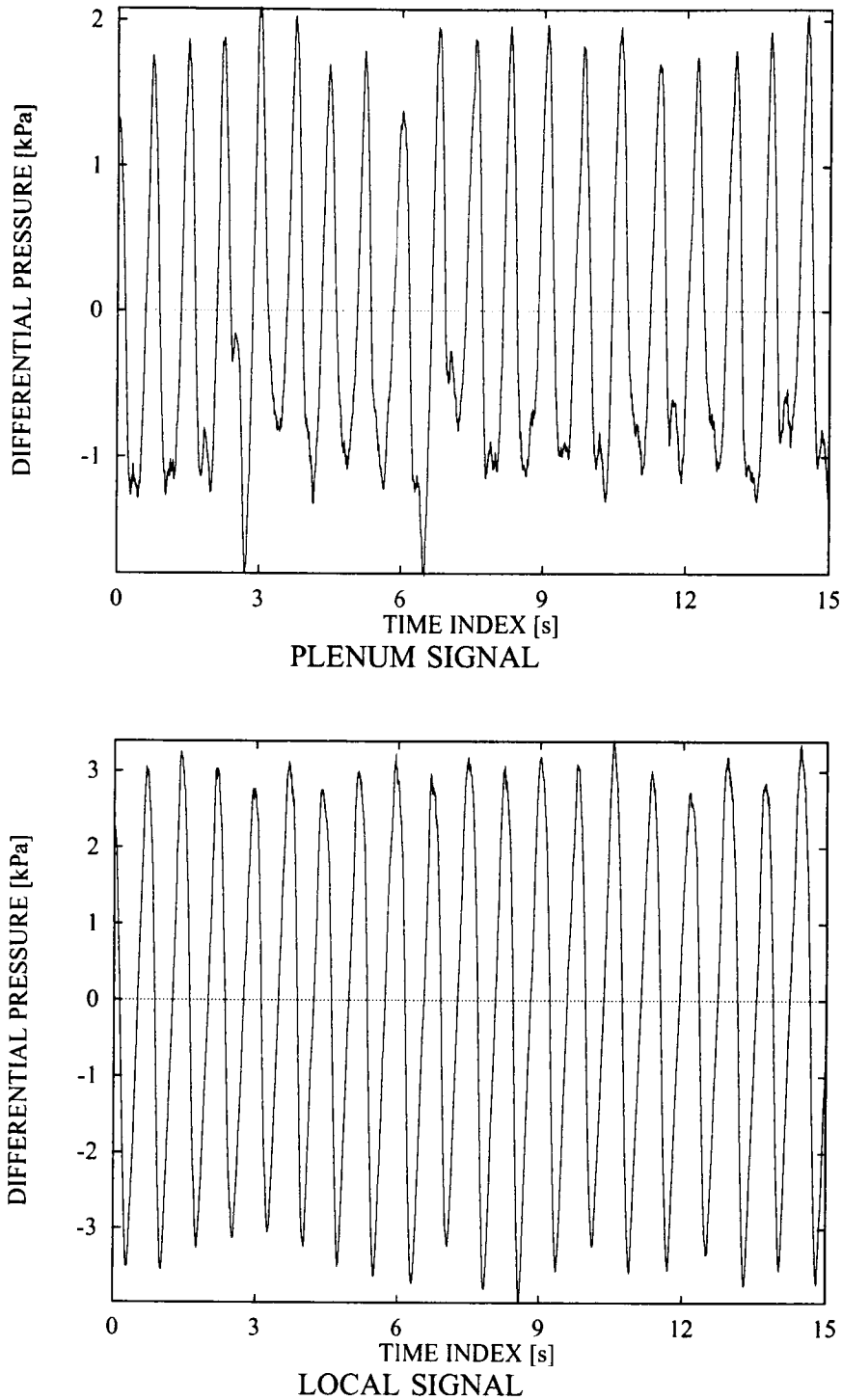
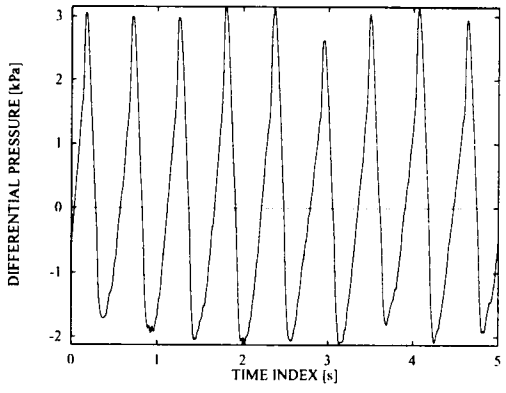
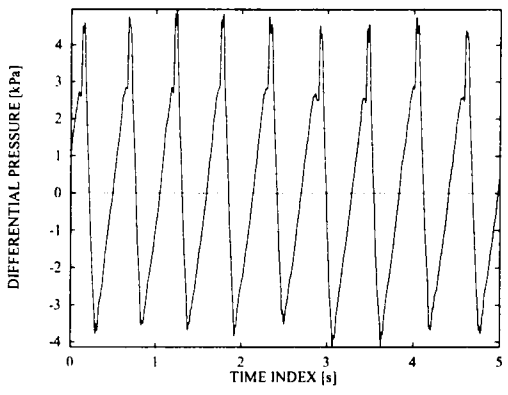


Figure 31. Complexity differences in plenum and local signals illustrated using typical time series segments for steel in the maximum stable slugging state (U/U_{MF} = 1.28).

STABILIZATION CONTROL FOR STEEL IN THE MAXIMUM STABLE SLUGGING STATE (U/U_{MF} = 1.28)

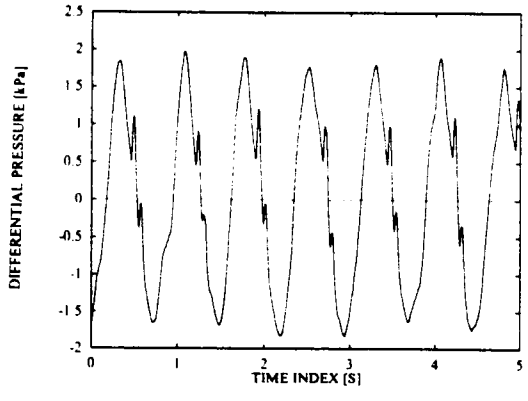


PLENUM SIGNAL

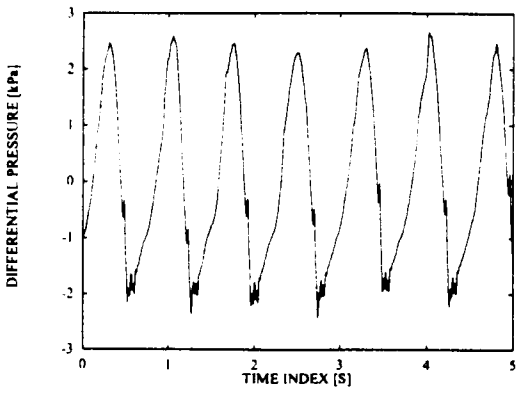


LOCAL SIGNAL

STABILIZATION CONTROL FOR GLASS IN THE BREAKING SLUG REGIME (U/U_{MF} = 1.59)



PLENUM SIGNAL



LOCAL SIGNAL

Figure 32. Typical time series segments illustrating the effect of transient disturbances introduced by pulsing.

5.3 EVALUATION OF CONTROL SCHEME

5.3.1 PHYSICAL EXPLANATION OF CONTROL PERTURBATION

Based on visual and video observations, the opening of the solenoid valve was seen to cause a sequence of two distinct events: a pressure pulse followed by a bubble or voidage pocket. The pressure pulse disrupts the solids circulation pattern and tends to increase the voidage in the bed above the nozzle, facilitating an increase in interstitial gas flow. The voidage pocket influences the slug-formation cycle and coalescence pattern in the bed.

In the stabilization mode, the solenoid valve is opened when the slug/bubble is just above the pulse nozzle. The pressure pulse tends to accelerate the slug upward, thus increasing the slugging frequency, and the voidage pocket introduced by the pulse coalesces with the slug/bubble. In the destabilization mode, the air pulse occurs when the slug/bubble is just beginning to form above the distributor. The pulse increases the voidage in the bed above the slug, causing the bubble to begin rising prematurely and reducing its size.

5.3.1 COMPARISON BETWEEN CONTROL BASED ON LOCAL SIGNAL AND PLENUM SIGNAL

The effectiveness of control based on local and plenum signal are compared in this section using results from experiments done with steel at the maximum stable slugging state. Optimum pulse timing and pulse width were empirically determined as discussed in section 5.2.1 and are listed in Table 4.

The characteristics of the local and plenum signals should always be considered

Table 4. Operating conditions for the set of experiments for comparing plenum and local control effectiveness.

Control Signal	Stabilization				Destabilization			
	Pulse Timing		Pulse Width [ms]	Pulse Gas* %	Pulse Timing		Pulse Width [ms]	Pulse Gas* %
	Trigger Level [kPa]	Direction			Trigger Level [kPa]	Direction		
Plenum	+0.93	up	150	3.8	-0.48	down	75	2.1
Local	-0.93	down	100	1.8	-0.48	up	100	3.7

* Time-averaged injector gas flow expressed as percentage of fluidization gas flow

while making comparisons. The local signal measures the differential pressure across a 10.2 cm high bed segment in the upper portion of the bed, and it is dominated by local events occurring in the window. Plenum signal measures the differential pressure between the plenum and atmosphere. It can be viewed as global pressure drop over the bed and is influenced by all the events happening in the bed.

Typical time series segments for no control, stabilization and destabilization mode are illustrated in Figures 33 and 34. In the stabilization mode, time series for plenum control seem to be more regular. Also a shift to higher frequency of oscillation and increased amplitude are observed in the plenum control case. In the destabilization mode, time series corresponding to plenum control have more small time-scale and low amplitude oscillations. In both cases, the regular behavior seen in the no control case is completely disrupted and occasional oscillations comparable in magnitude to the no control case can be seen.

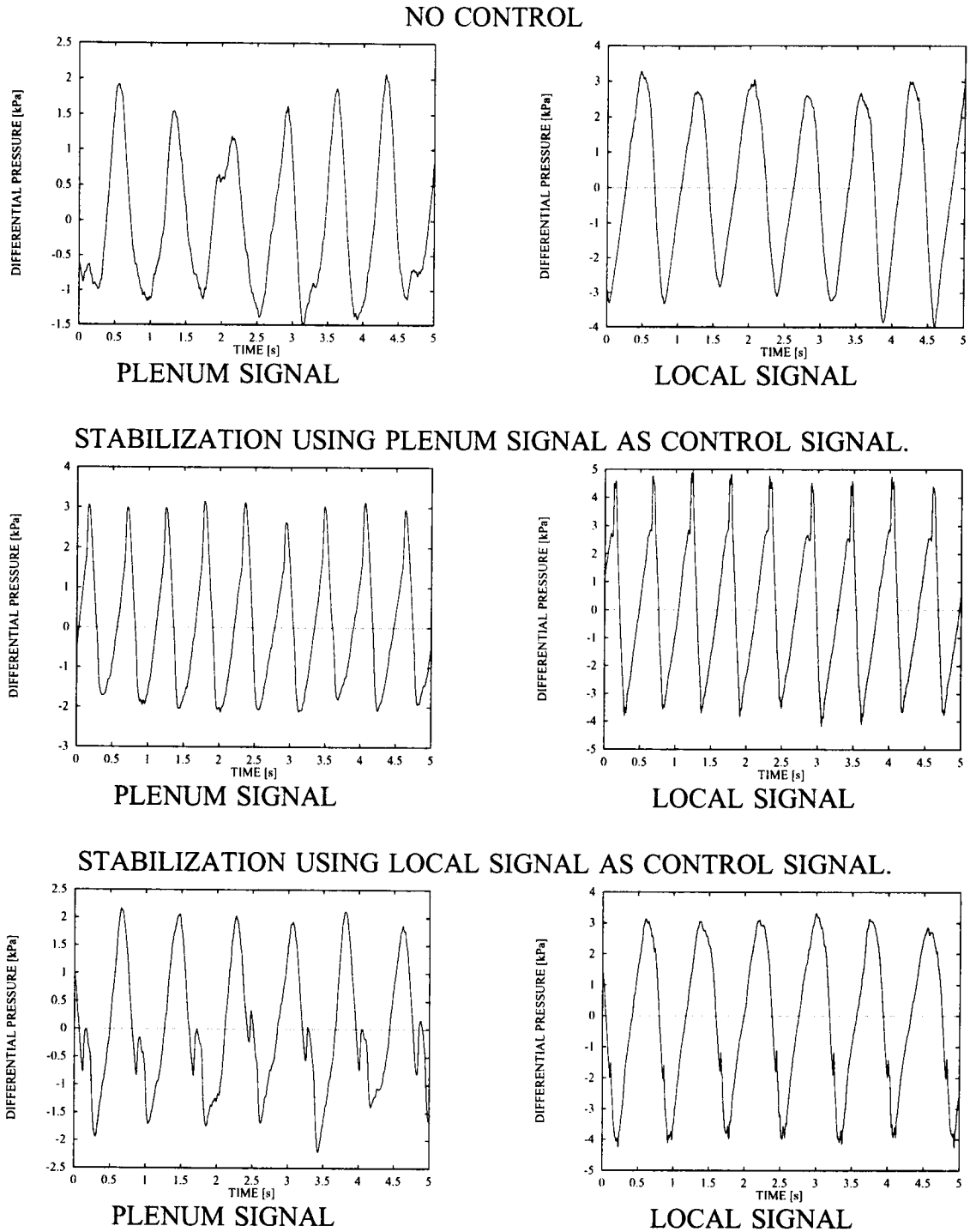


Figure 33. Typical segments of time series for steel with no control and stabilization control modes using plenum or local signal as the control signal. [U/Umf = 1.28]

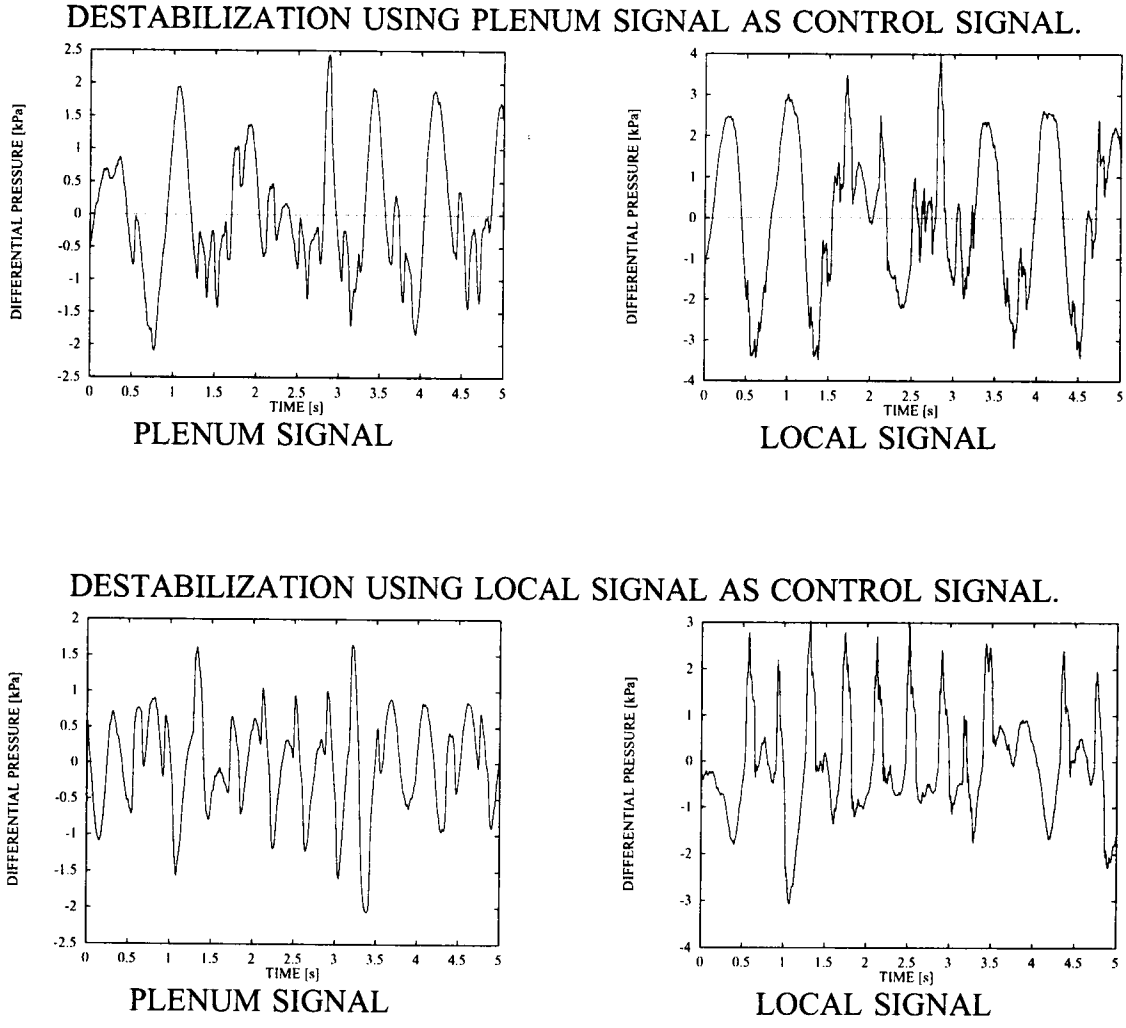


Figure 34. Typical segments of time series for steel with destabilization control using plenum or local signal as the control signal. [U/Umf = 1.28]

Fourier power spectra for the stabilization mode are shown in Figure 35 and for the destabilization mode in Figure 36. For stabilization mode, plenum control case shows a higher frequency shift and also higher peak power indicating that the slugging is more regular in this case. No such shift is seen in the case of local control. For destabilization mode, local control seems to be more effective with a more broad banded structure. But, in the 6-8 Hz region plenum control case signals have more power than the local control case.

Cycle magnitude plots for plenum and local control cases are presented in Figure 37. In the stabilization mode, the greater effectiveness of plenum control is confirmed by these plots. In the destabilization mode, for local signal control the magnitudes seem to be more widely distributed than for the plenum control. But, for plenum control the number of cycle are greater and the cycle magnitudes are lower indicating that the slugs are smaller and more frequent. This may be desirable in a slugging bed.

Dimension and entropy estimations presented in Figure 38 also confirms the general trends observed. Higher dimension and entropy estimates indicate that the system behavior is more complex. For the stabilization mode, the dimension estimate is lower and the entropy estimate is of the same order for plenum control compared to the local signal control. This trend indicates that plenum control may be better in this mode of operation. For destabilization mode, the increased entropy values seem to indicate that local control may be better for destabilization.

Considering the cycle magnitude distribution and the nature of the two signals (local bed segment vs global bed), for fluidized bed slug disruption it can be concluded

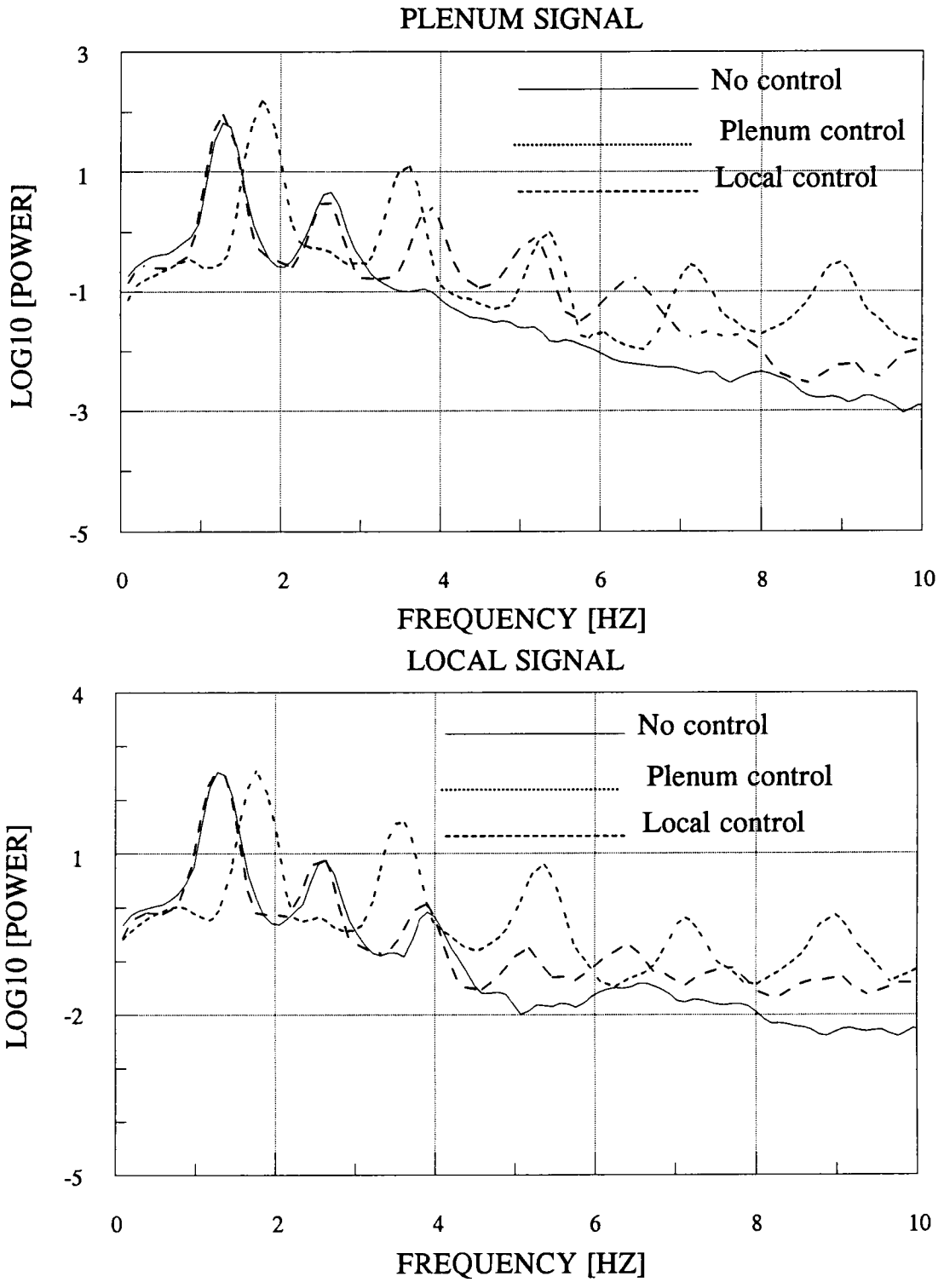


Figure 35. Fourier power spectra for steel illustrating the effect of using different signals for stabilization control compared with the no control case at the maximum stable slugging state [U/Umf = 1.28].

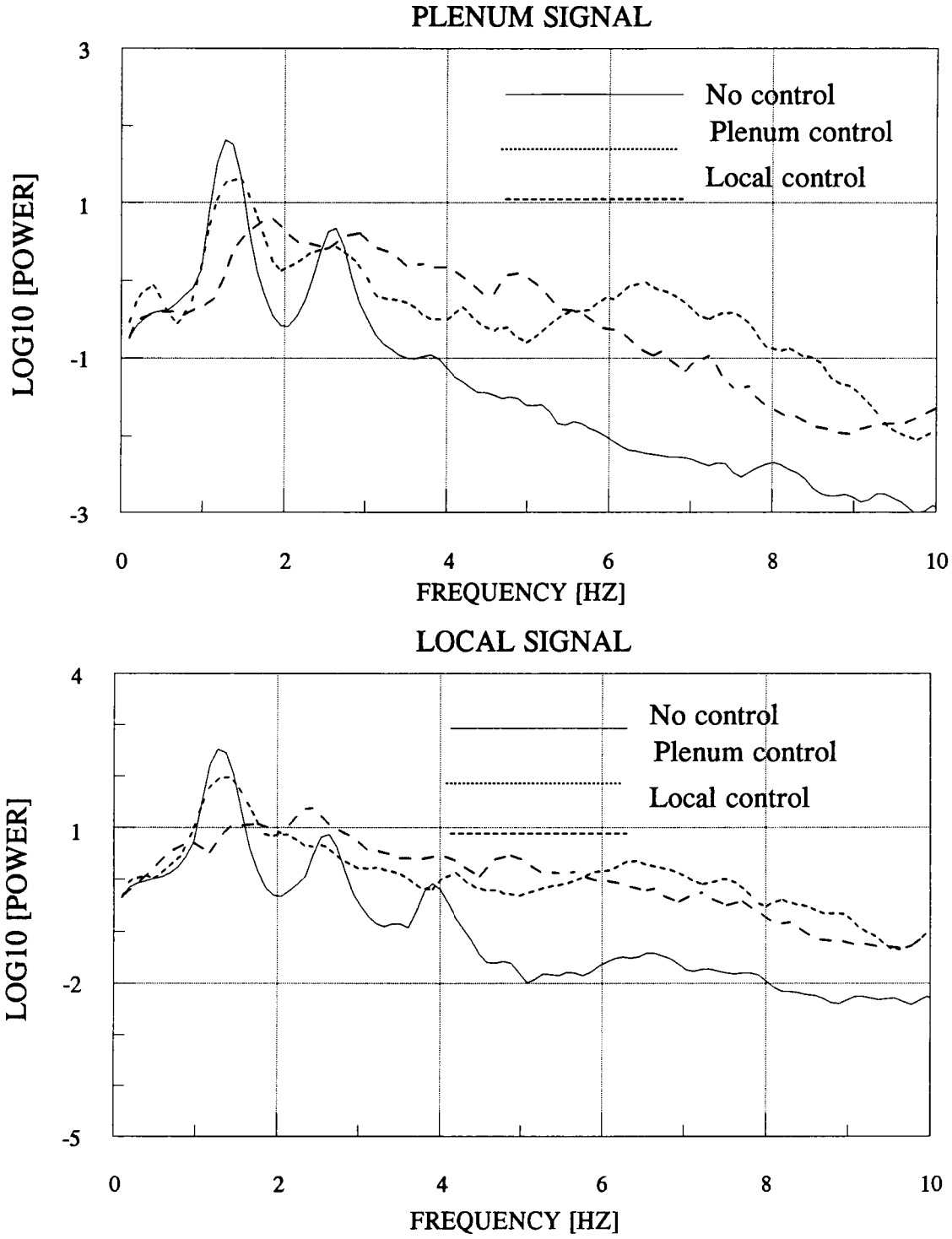


Figure 36. Fourier power spectra for steel illustrating the effect of using different signals for destablization control compared with no control case at the maximum stable slugging state [U/Umf = 1.28].

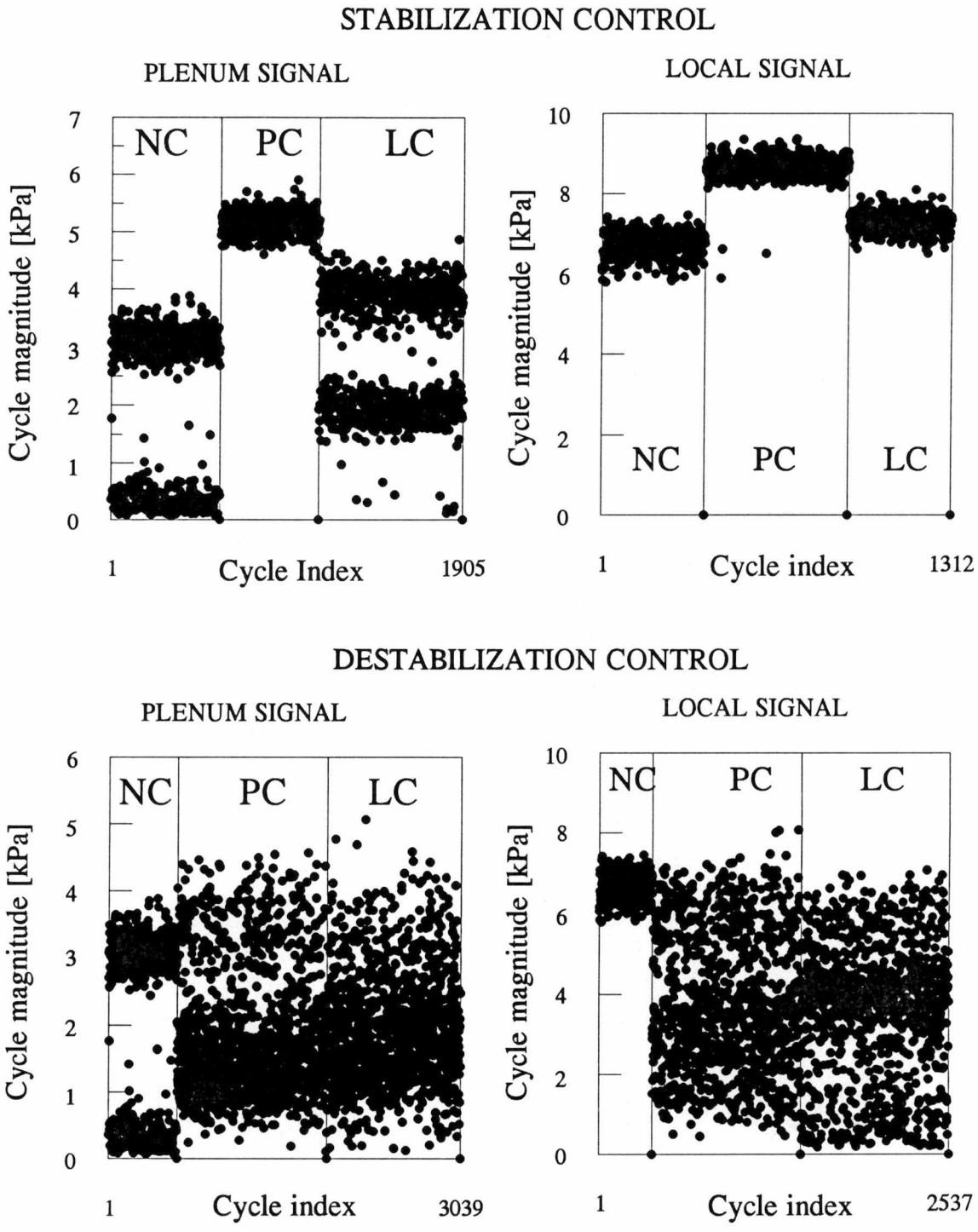


Figure 37. Variation in cycle magnitudes for steel with different control signals compared with no control case at the maximum stable slugging state [U/Umf = 1.28].
NC: No control; PC: Plenum control; LC: Local control

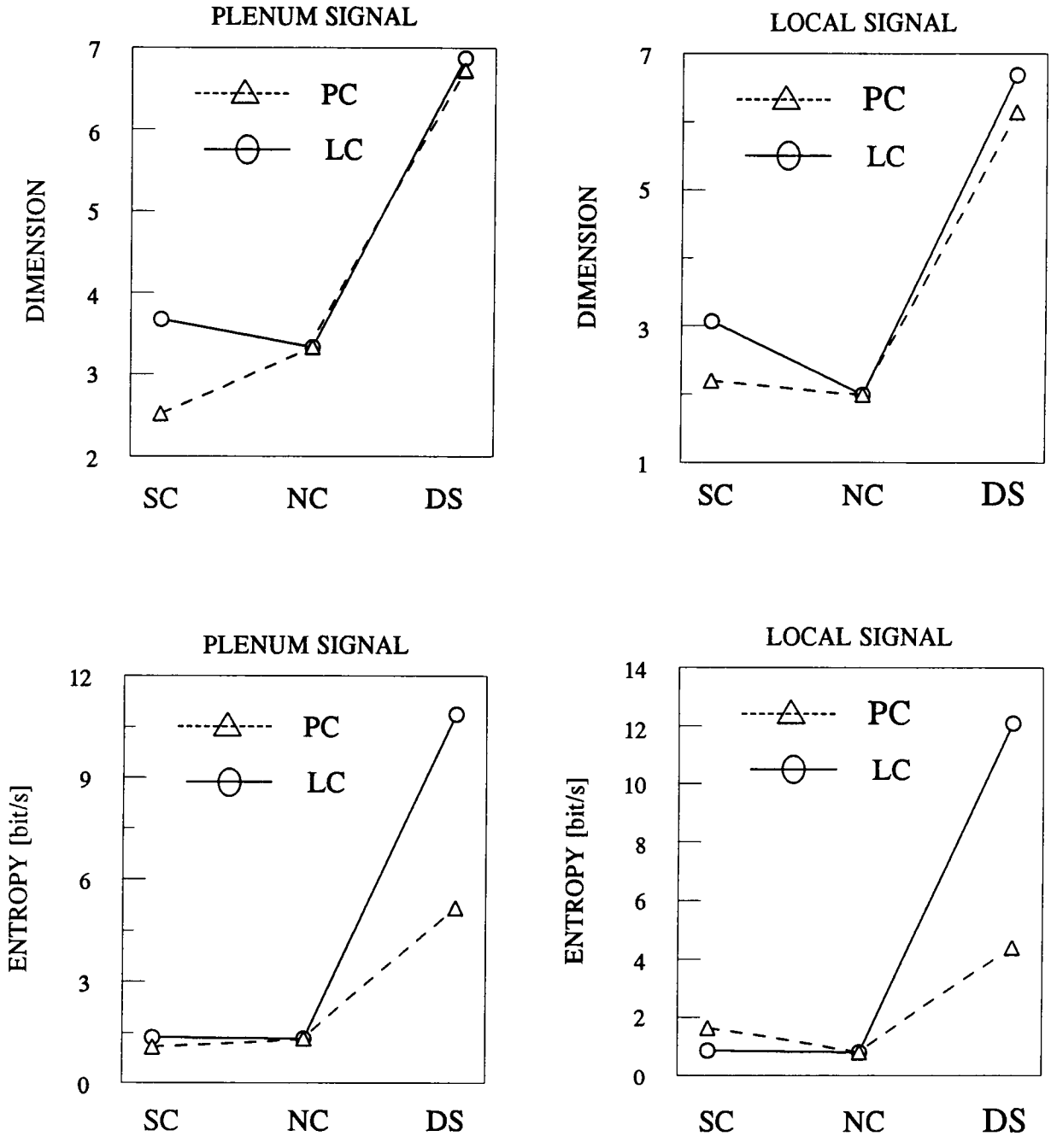


Figure 38. Variation of dimension and entropy for steel with different control signals for various contol modes at the maximum stable slugging state [U/Umf = 1.28].

NC : No control; SC: Stabilization control; DS : Destabilization control
PC : Plenum signal control; LC : Local signal control

that plenum based control may be as effective as the local control for destabilization. For stabilization mode, plenum control pulse gas consumption is higher and for the destabilization mode local control pulse gas flow is higher. In general, both signals are able to achieve stabilization and destabilization of slugging behavior. Particular choice of the control signal may be influenced by various factors such as the distributor pressure drop, the availability of in-bed pressure measurements, and the desired control effect.

5.3.3 EVALUATION OF CONTROL AT DIFFERENT FLUIDIZATION CONDITIONS WITH STEEL.

To evaluate the effectiveness of control at different fluidization states, experiments were conducted with steel at a static bed height of 23.5 cm. The bed was operated at three different fluidization regimes, developing slug regime, maximum stable slugging state and breaking slug regime, with control based on the plenum signal. The operating conditions and the control parameters for the experiments are listed in Table 5. System behavior with no control is compared with both stabilization and destabilization control runs.

Typical time series segments for all the control modes for the three runs at developing slug regime (run C1), at maximum stable slugging state (run C2) and at breaking slug regime (run C3) are shown in Figures 39, 40 and 41, respectively. The effect of control in runs C1 and C2 is similar but for run C3 the effect is different. For run C1 and C2, in the stabilization mode, the oscillations are more regular, and the oscillation time scales are reduced. In the destabilization mode, small time-scale and small amplitude oscillations dominate in both the signals. For run C3, there is no shift

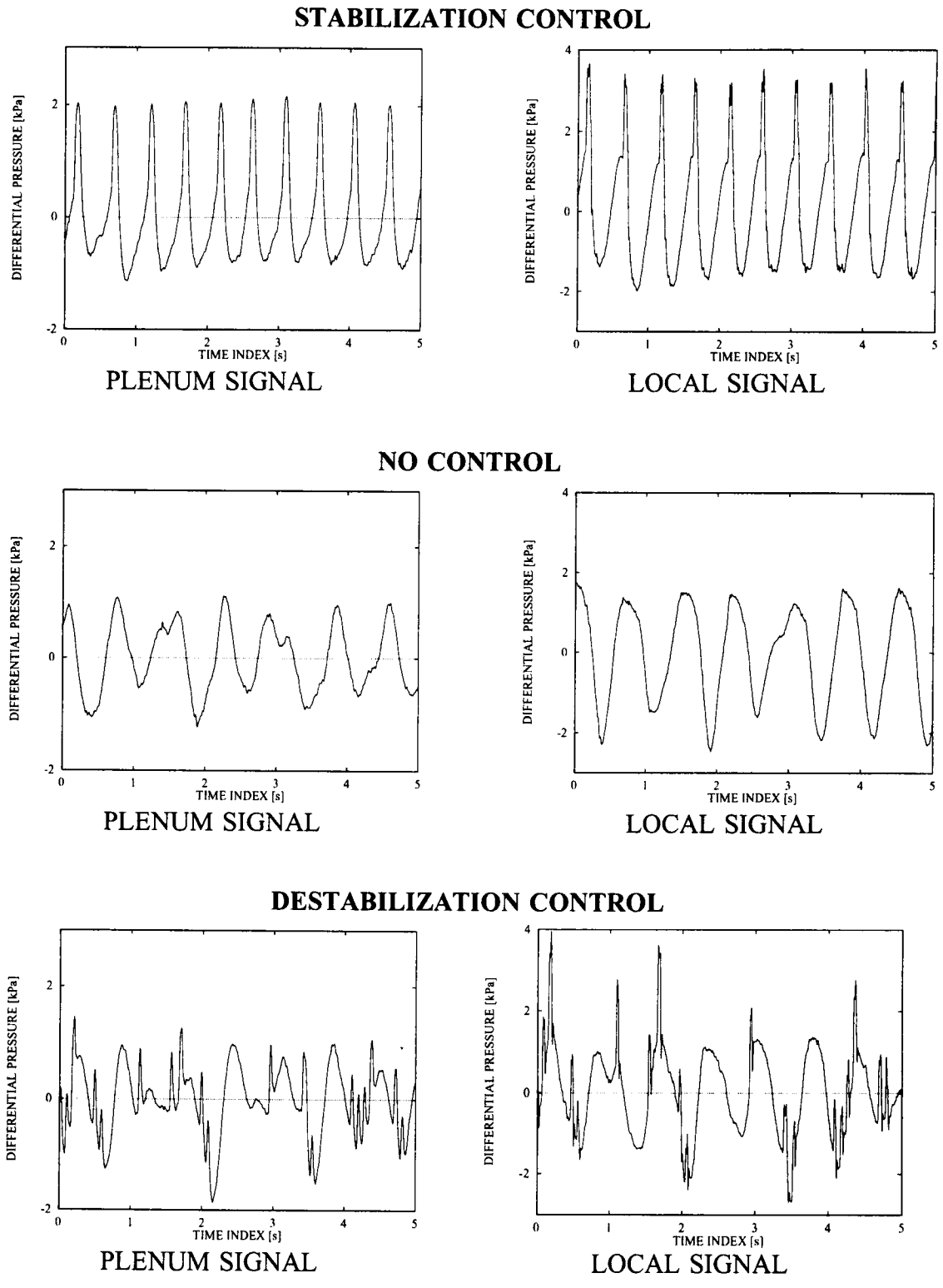


Figure 39. Typical time series segments for steel with different control modes at the developing slug regime (Run C1; U/U_{MF} = 1.16).

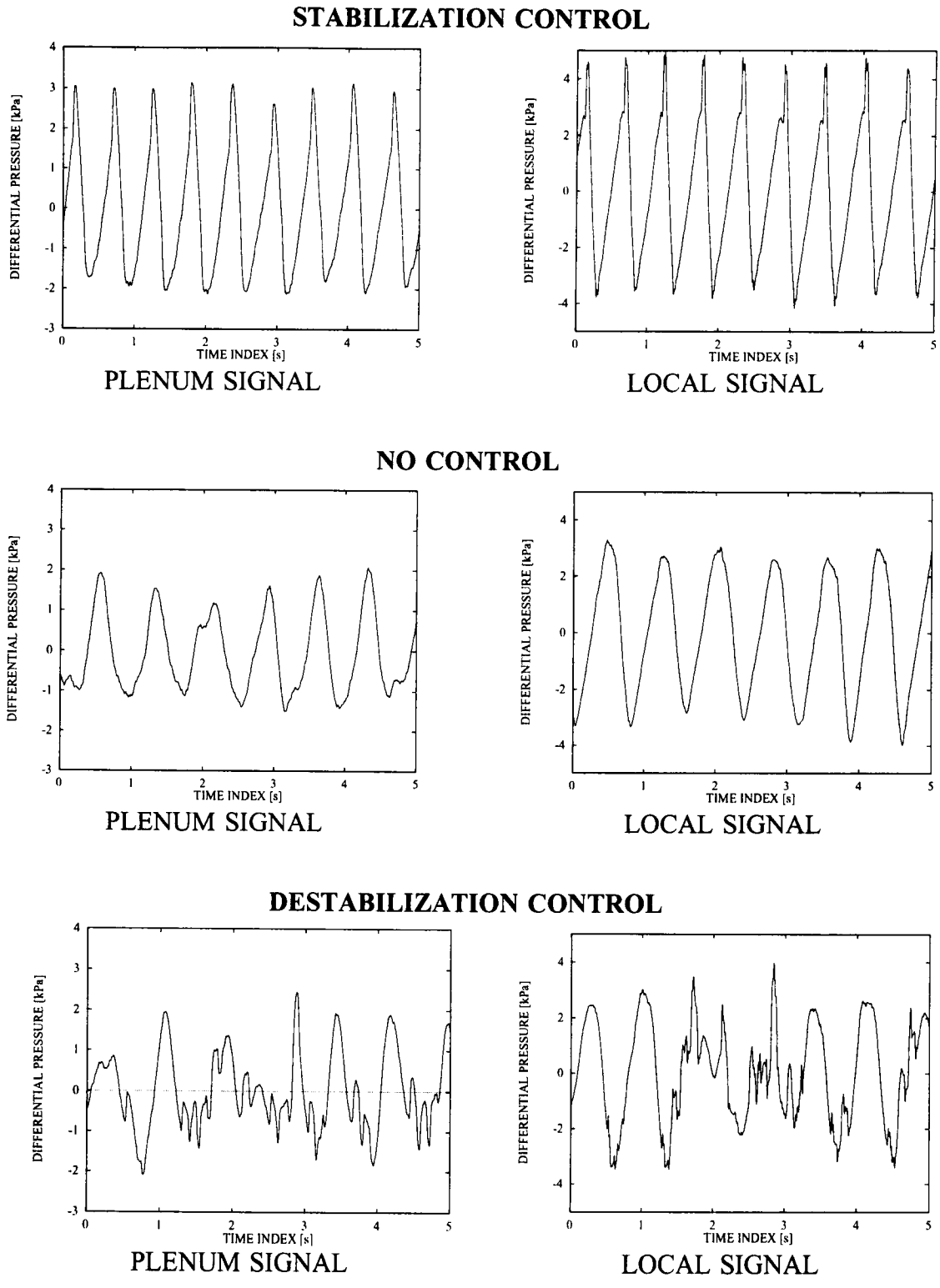


Figure 40. Typical time series segments for steel with different control modes at the maximum stable slugging state (Run C2; U/U_{MF} = 1.28).

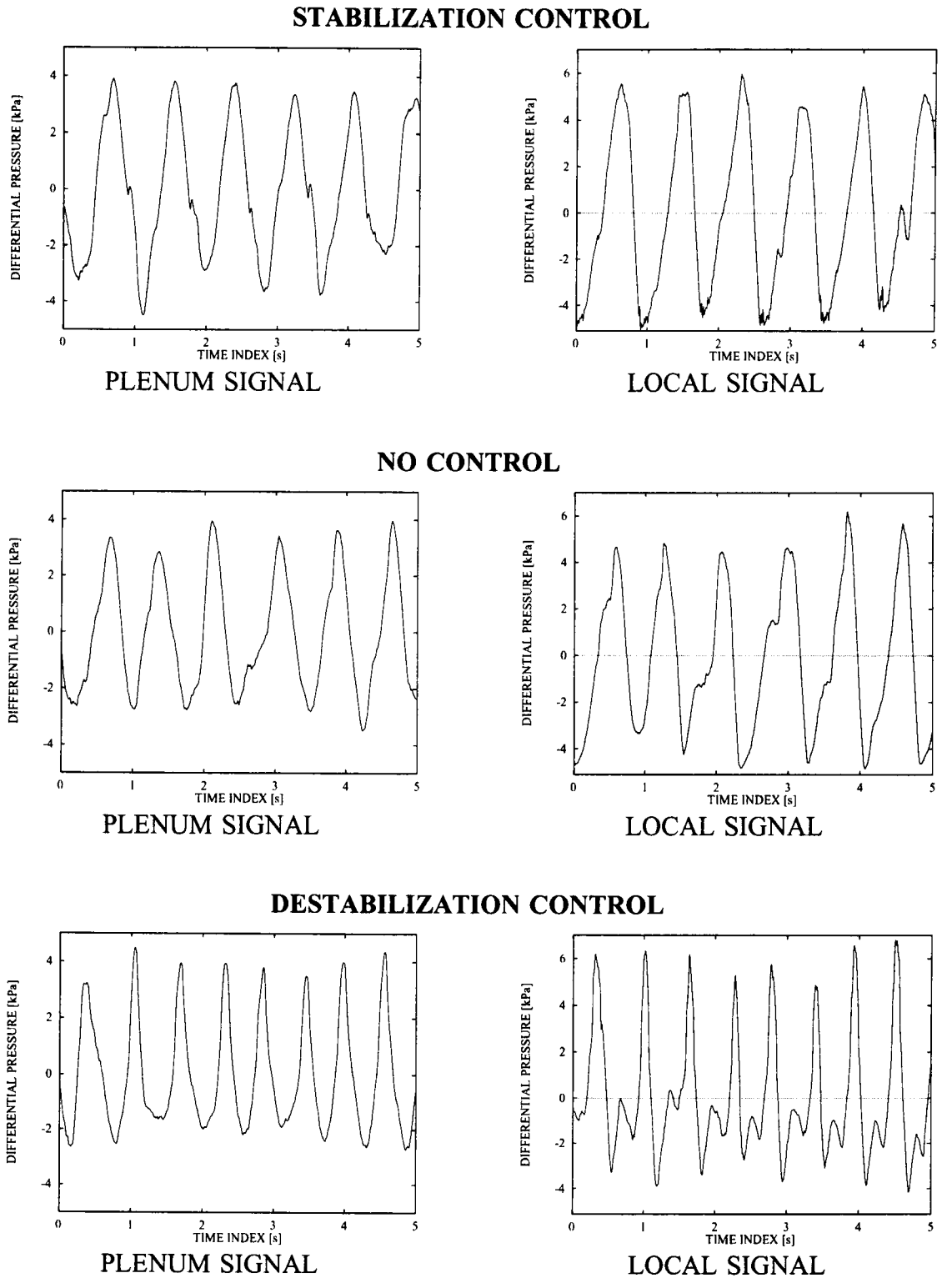


Figure 41. Typical time series segments for steel with different control modes at the breaking slug regime (Run C3; $U/U_{MF} = 1.55$).

Table 5. Operating conditions for control evaluation experiments for steel.

Run No.	U/U_{MF}	Stabilization				Destabilization			
		Pulse Timing		Pulse Width [ms]	Pulse Gas* %	Pulse Timing		Pulse Width [ms]	Pulse Gas* %
		Trigger Level [Kpa]	Dir.			Trigger Level [kPa]	Dir.		
C1	1.16	+0.09	up	60	1.9	-0.21	down	20	1.2
C2	1.28	+0.93	up	150	3.8	-0.48	down	75	2.1
C3	1.55	+0.60	down	100	1.4	-0.60	up	100	2.5

* Time-averaged injector gas flow expressed as percentage of fluidization gas flow

to higher frequency or reduced time-scale oscillations in the stabilization mode. In the destabilization mode the oscillation time scales are reduced, but not to the extent seen in other runs.

Figures 42, 43 and 44 show the Fourier power spectra for runs C1, C2 and C3, respectively. Compared with the no control case, stabilization results in a more distinct, narrow-band spectrum, whereas destabilization results in a more broad-band spectrum. In addition to the power distribution, the shift in peak frequencies is also interesting for understanding the system behavior. Section 5.1 discusses the shift of the unstable fixed point with change in gas velocity. Here, also such a shift to lower period or higher frequency is seen in the stabilization mode for runs C1 and C2. Time return maps show this shift more clearly. For Run C3 stabilization control, no such frequency shift occurs.

Three dimensional projections of typical segments of the reconstructed trajectories

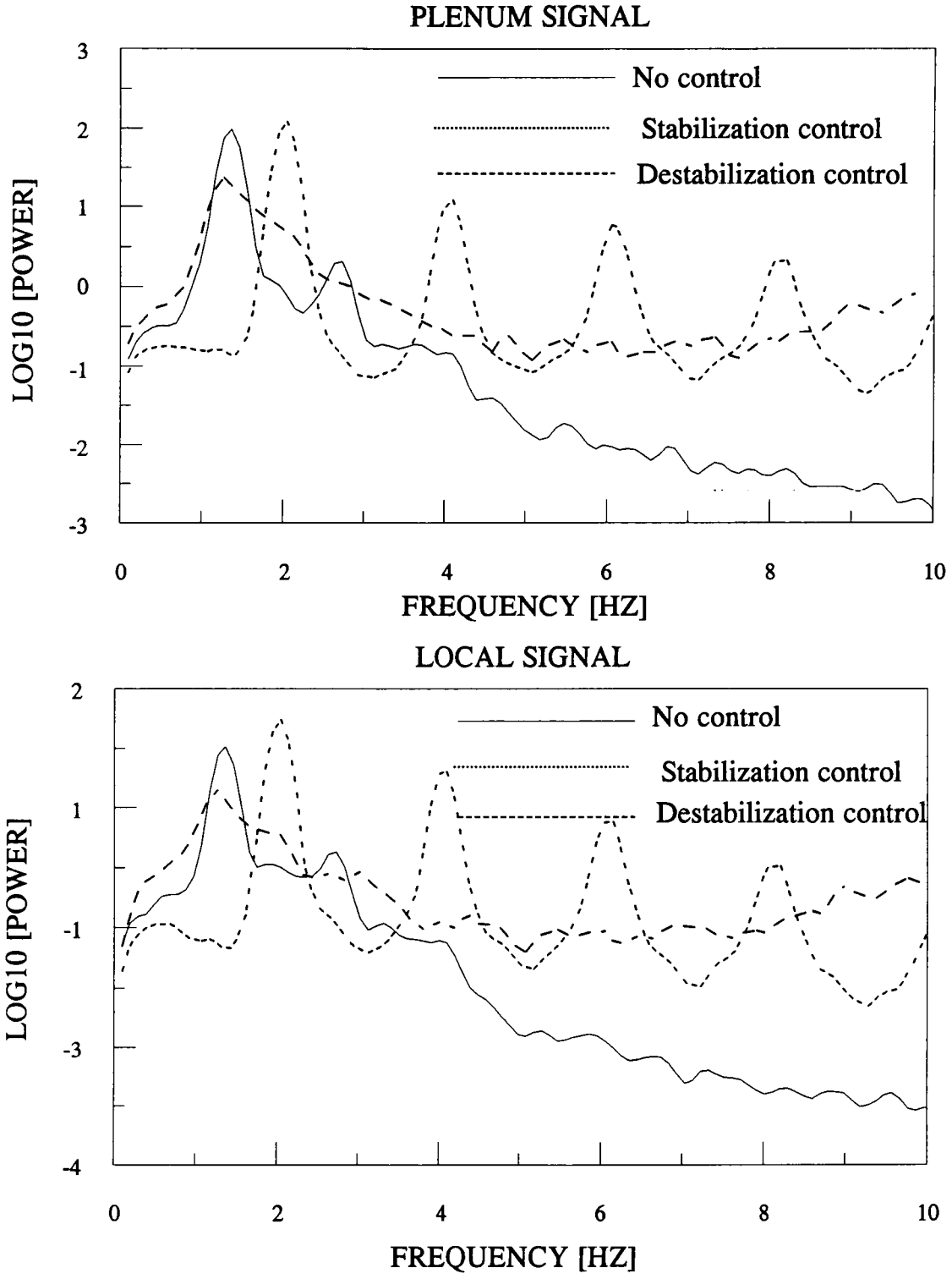


Figure 42. Fourier power spectra for steel with different control modes at the developing slug regime
[Run C1; U/Umf = 1.16]

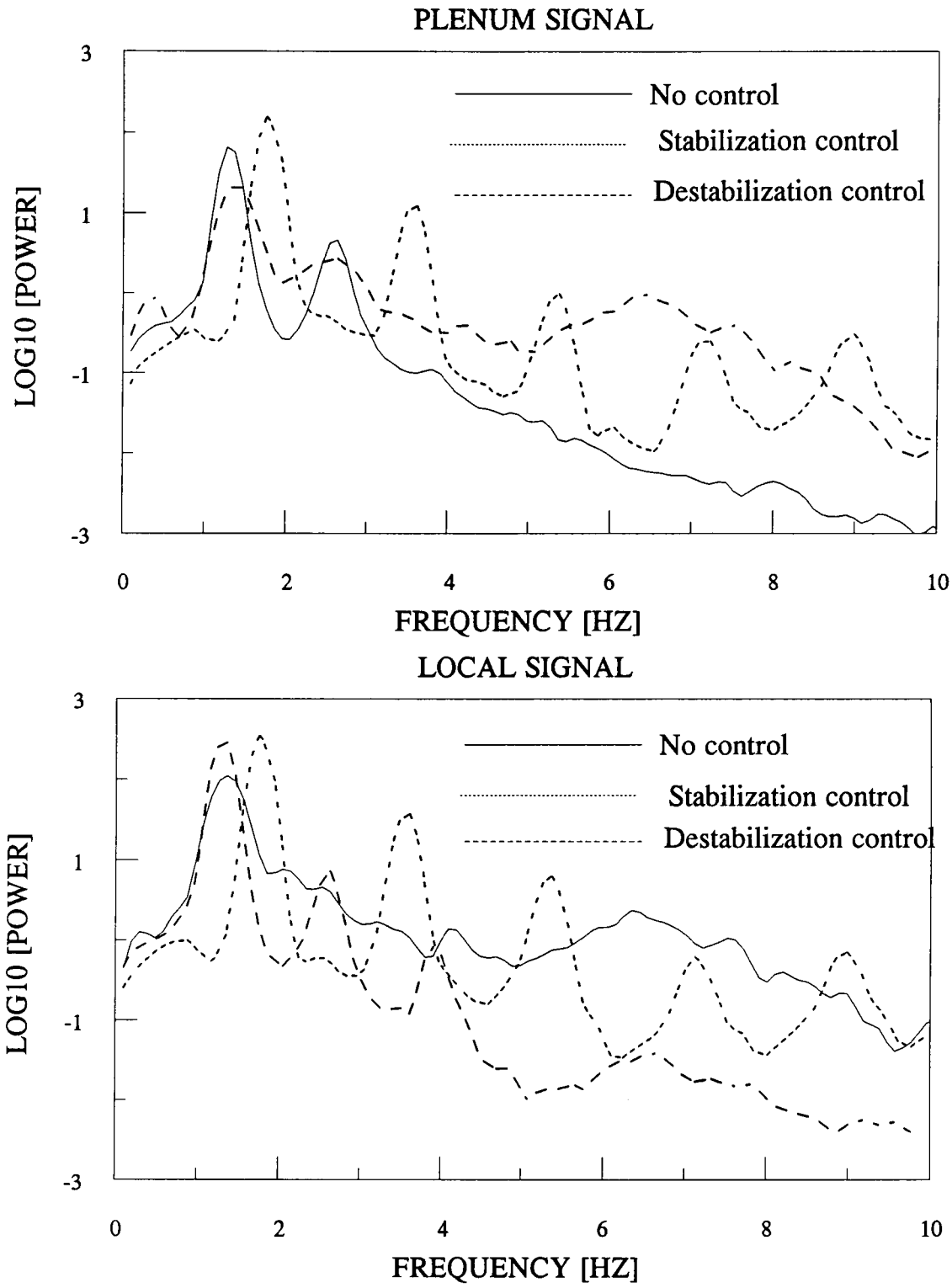


Figure 43. Fourier power spectra for steel with different control modes at the maximum stable slugging state [Run C2; U/Umf = 1.28].

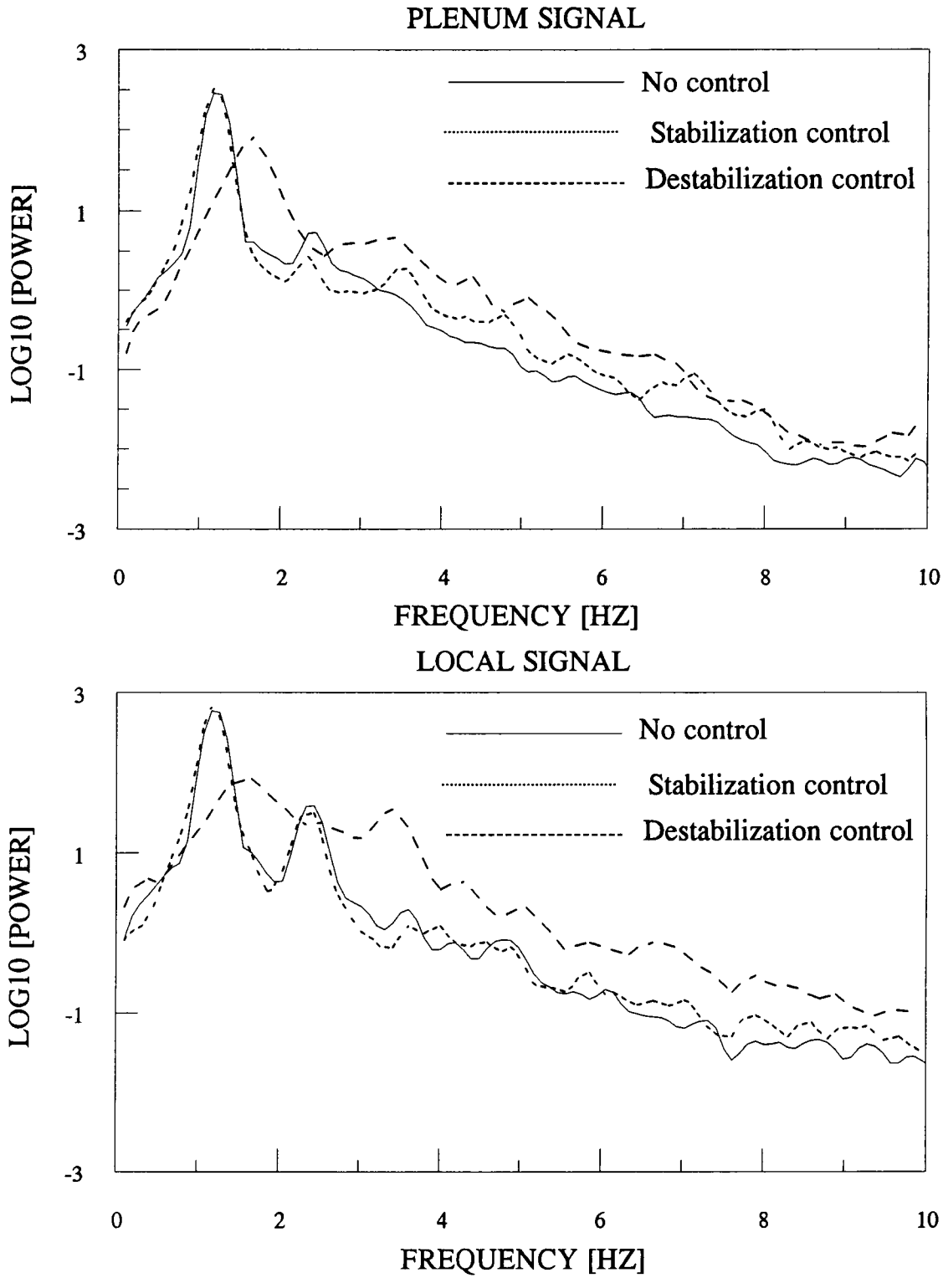


Figure 44. Fourier power spectra for steel with different control modes at the breaking slug regime [Run C3; U/Umf = 1.55].

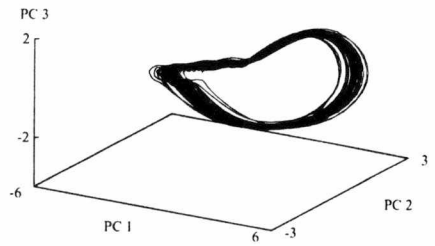
for different control modes for all the runs are shown in Figures 45 to 47. In the stabilization mode, phase plots are characterized by a tighter banding of trajectories and opening up in the middle indicating a more ordered behavior. In the destabilization mode, opening up of phase plots, a characteristic feature of slugging in fluidized beds, is completely lost. This clearly indicates that the ordered behavior imposed by slugging is completely disrupted. In run C3, the degree of stabilization and destabilization is less compared to other runs.

The effect of control mode on cycle magnitudes is shown in Figures 48, 49 and 50. Cycle magnitudes are closely linked to slug sizes. For runs C1 and C2, the control very effectively stabilizes the slugging, producing cycle magnitudes that are larger and more narrowly distributed. For Run C3, although there are fewer low-magnitude cycles than with the no control case, slugging is not effectively stabilized as in runs C1 and C2.

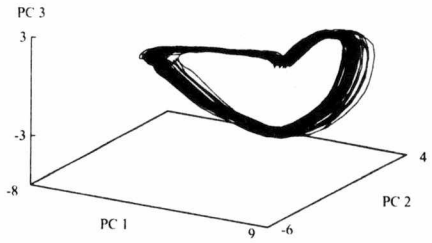
In destabilization control, the cycle magnitudes generally are lower because of the disruption of slugging by the control action. For runs C1 and C2, control is effective, resulting in the dense bands as seen in Figures 48 and 49. In Run C3, the slug-size distribution is very dispersed, and the reduction in cycle magnitudes is not as significant as in the other runs (Figure 50).

Time return maps for the runs are shown in Figures 51, 52 and 53. In stabilization control, the cycle periods can be seen to cluster tightly about a single value for the plenum signal. For the local signal such tight clusters are also seen for runs C1 and C3. The discrete clusters seen for run C2 in the local signal time return map is believed to be an artifact caused by the local disturbance introduced by pulsing. For

STABILIZATION CONTROL

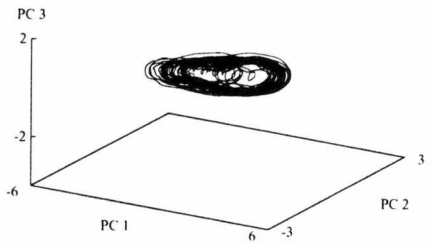


PLENUM SIGNAL

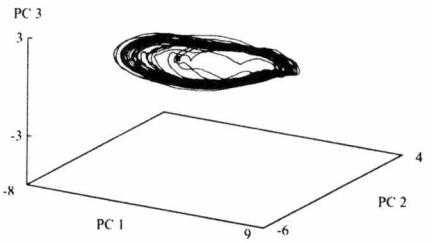


LOCAL SIGNAL

NO CONTROL

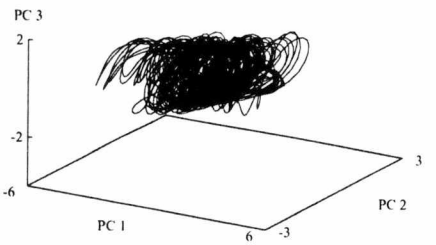


PLENUM SIGNAL

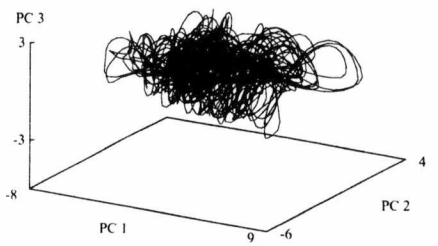


LOCAL SIGNAL

DESTABILIZATION CONTROL



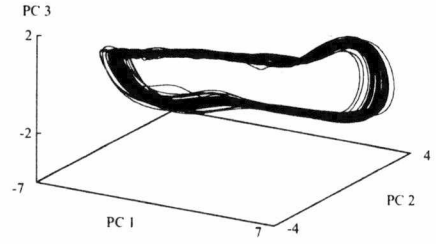
PLENUM SIGNAL



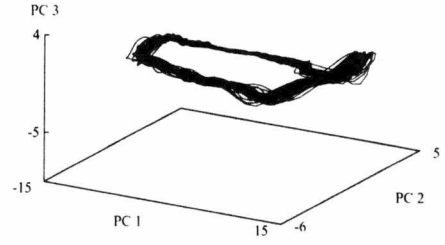
LOCAL SIGNAL

Figure 45. Three dimensional projection of the reconstructed trajectories for steel with different control modes at the developing slug regime (Run C1; U/U_{MF} = 1.16; Time span = 25 s).

STABILIZATION CONTROL

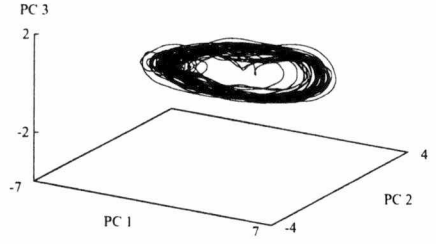


PLENUM SIGNAL

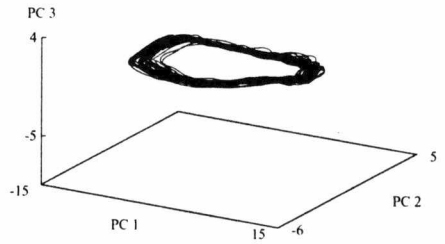


LOCAL SIGNAL

NO CONTROL

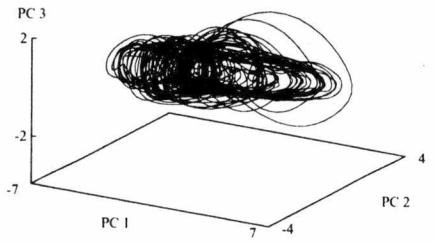


PLENUM SIGNAL

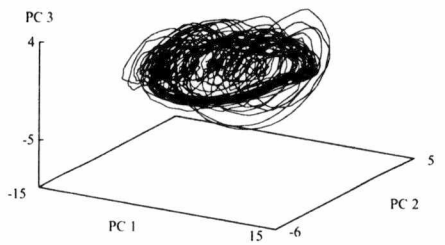


LOCAL SIGNAL

DESTABILIZATION CONTROL



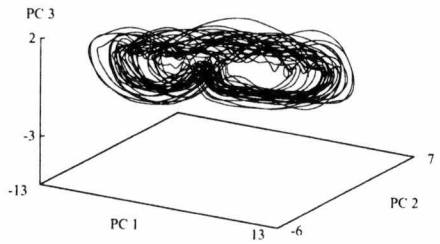
PLENUM SIGNAL



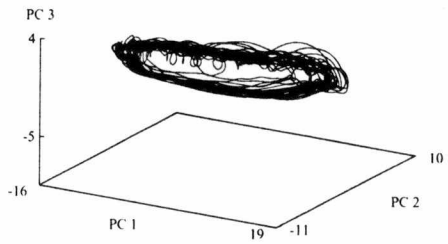
LOCAL SIGNAL

Figure 46. Three dimensional projection of the reconstructed trajectories for steel with different control modes at the maximum stable slugging state (Run C2; U/U_{MF} = 1.28; Time span = 25 s) .

STABILIZATION CONTROL

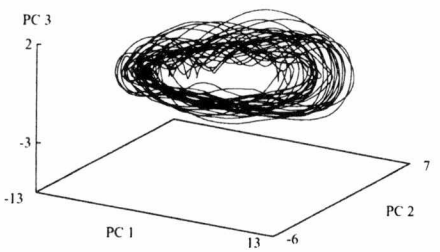


PLENUM SIGNAL

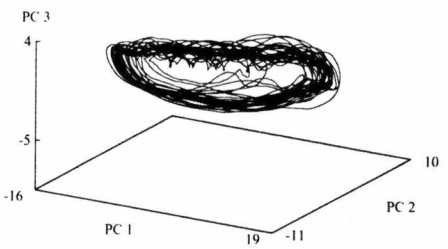


LOCAL SIGNAL

NO CONTROL

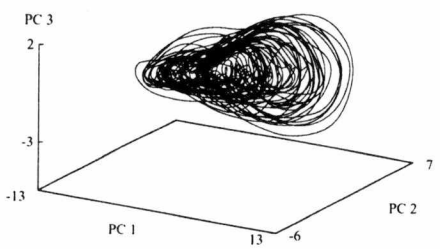


PLENUM SIGNAL

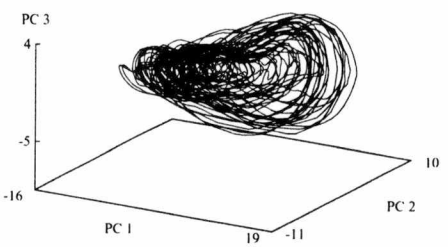


LOCAL SIGNAL

DESTABILIZATION CONTROL



PLENUM SIGNAL



LOCAL SIGNAL

Figure 47. Three dimensional projection of the reconstructed trajectories for steel with different control modes at the breaking slug regime (Run C3; U/U_{MF} = 1.55; Time span = 25 s) .

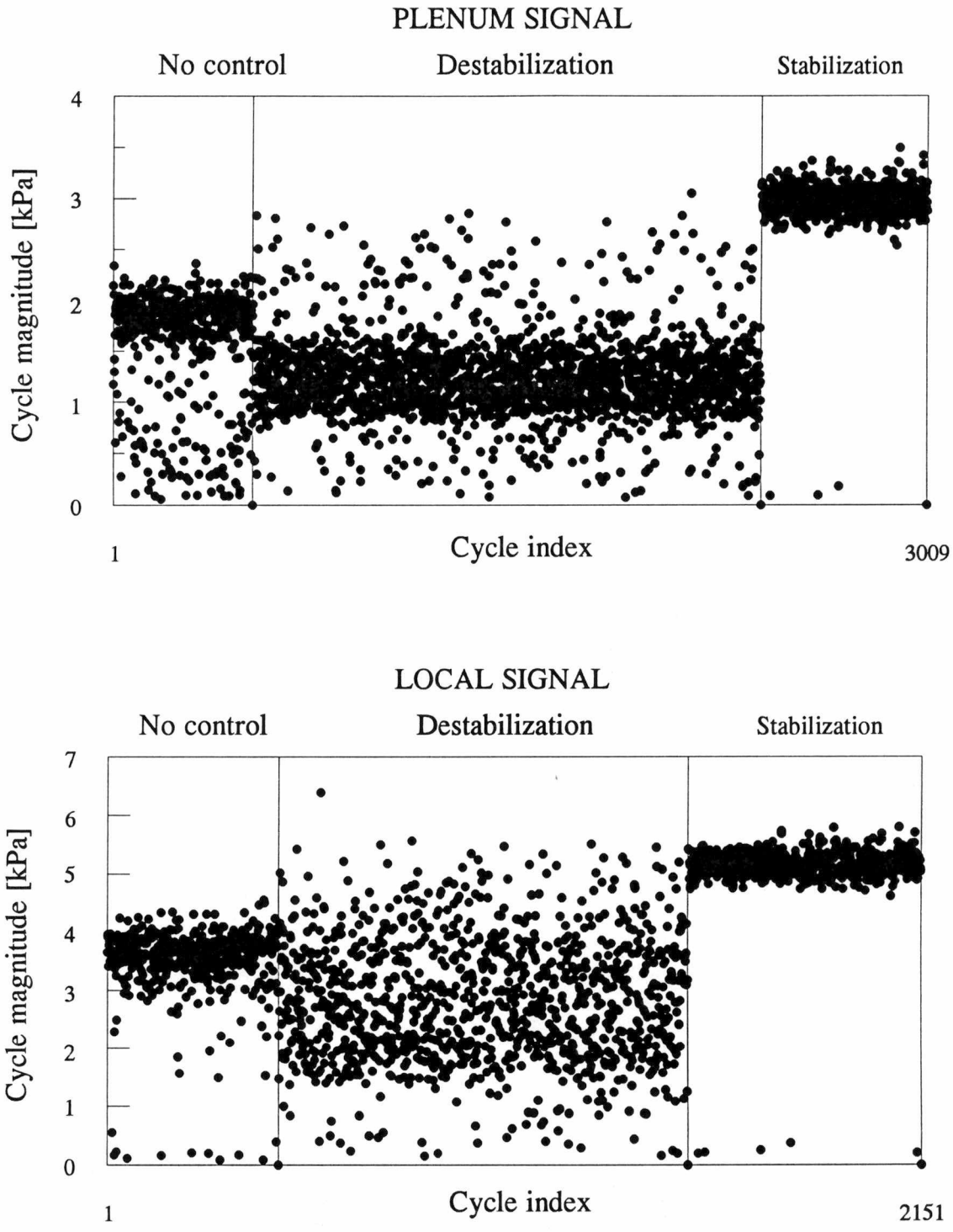


Figure 48. Variation in cycle magnitudes for steel with different control modes at the developing slug regime [Run C1; U/Umf = 1.16].

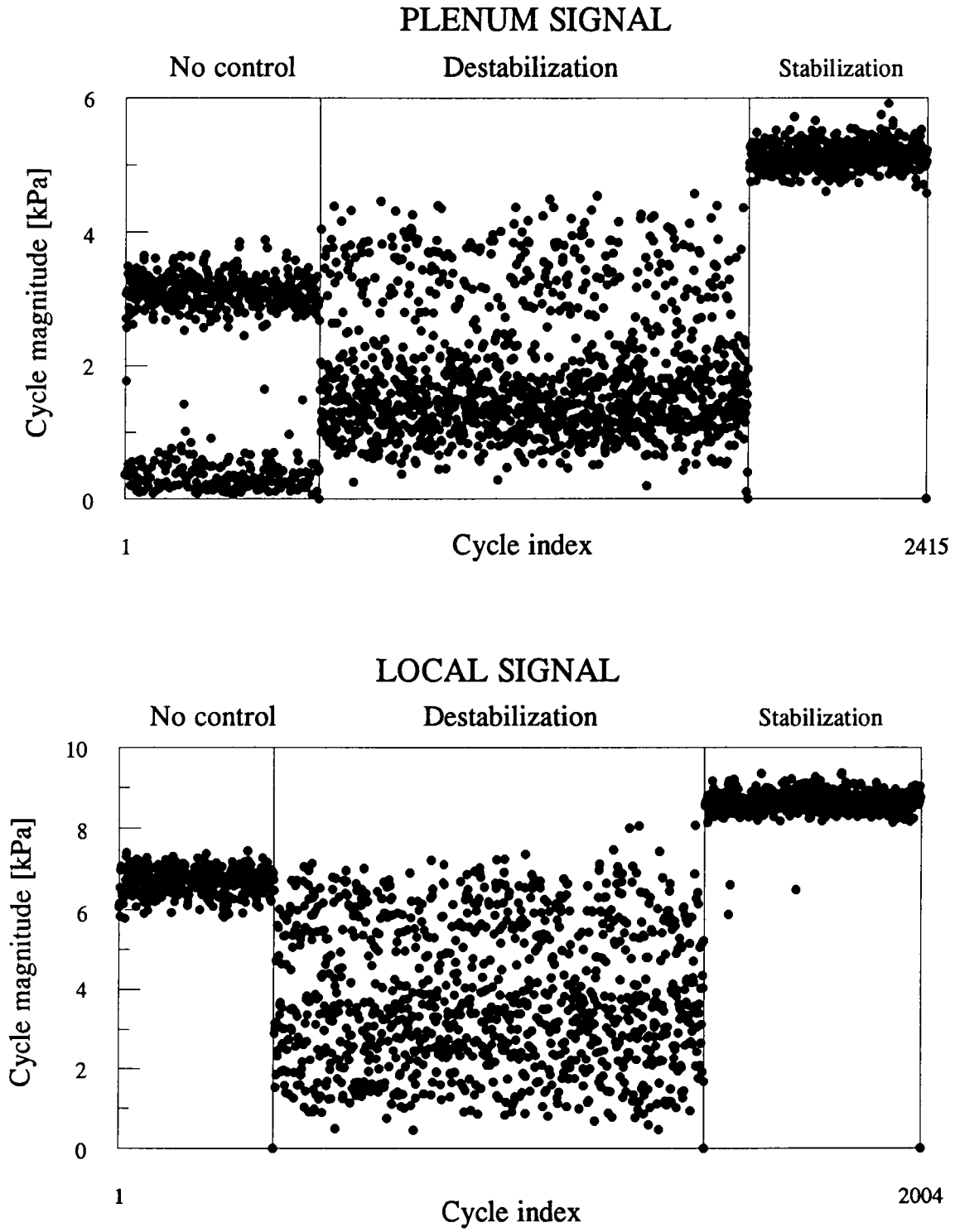


Figure 49. Variation in cycle magnitudes for steel with different control modes at the maximum stable slugging state [Run C2; U/Umf = 1.28].

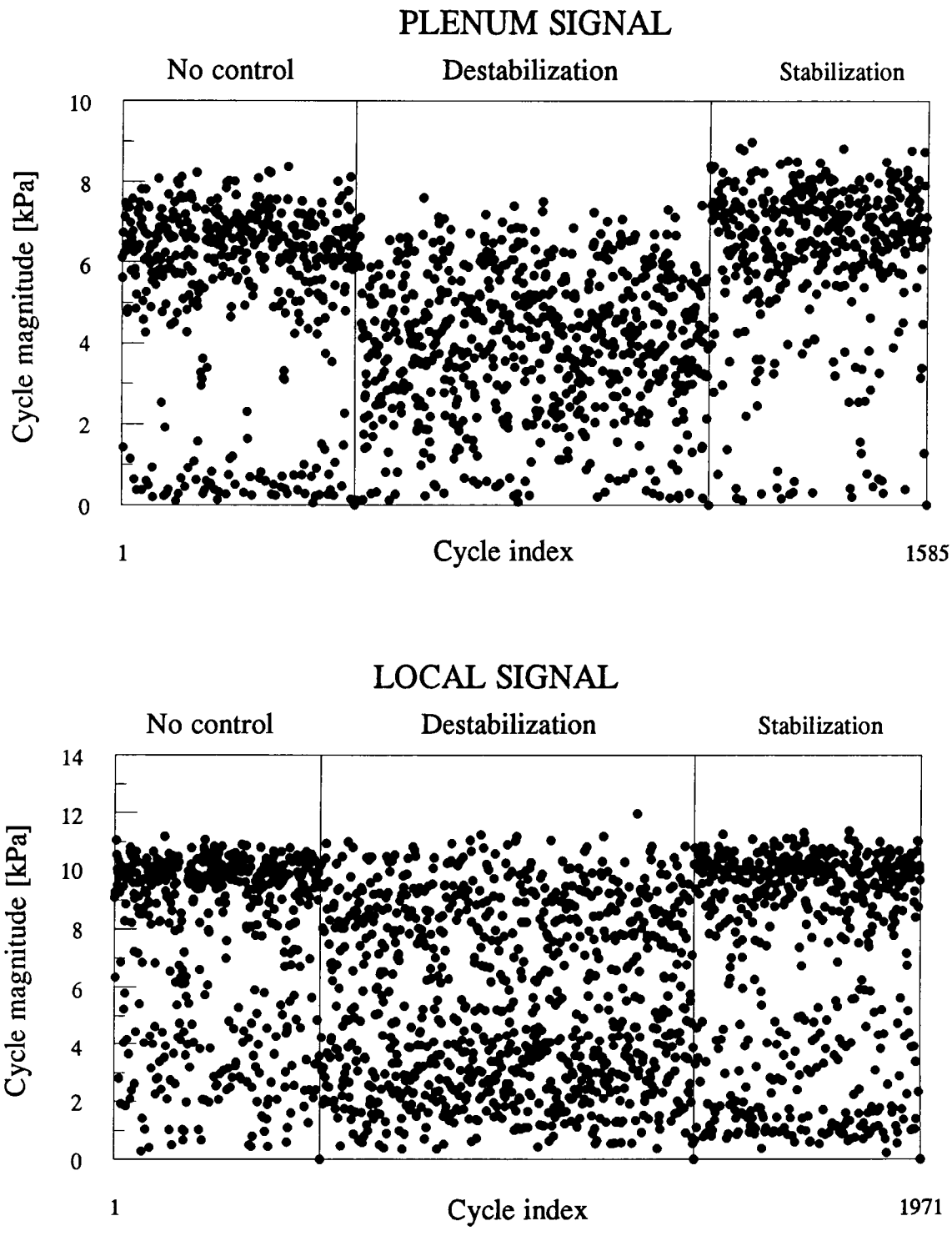
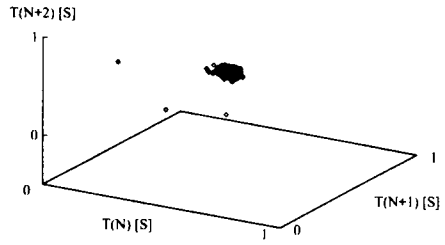
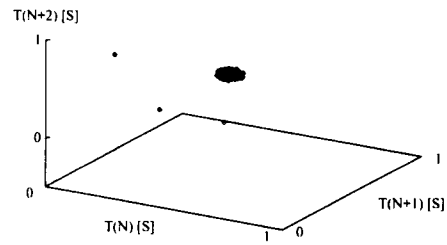


Figure 50. Variation in cycle magnitudes for steel with different control modes at the breaking slug regime [Run C3; U/Umf = 1.55].

STABILIZATION CONTROL

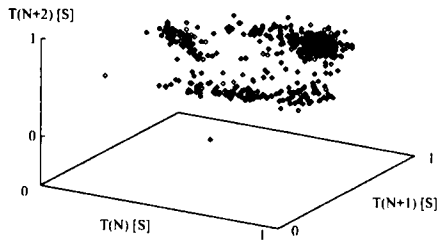


PLENUM SIGNAL

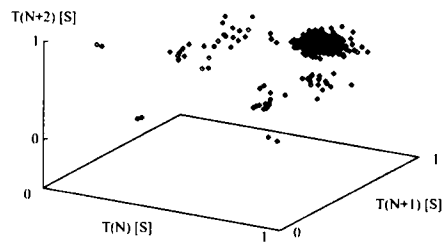


LOCAL SIGNAL

NO CONTROL

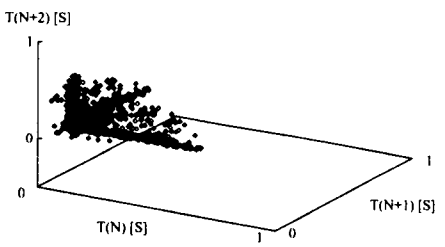


PLENUM SIGNAL

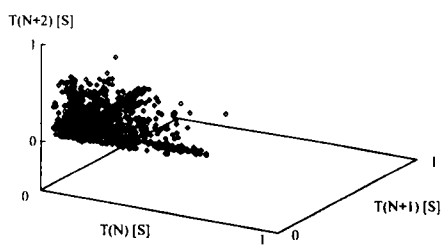


LOCAL SIGNAL

DESTABILIZATION CONTROL



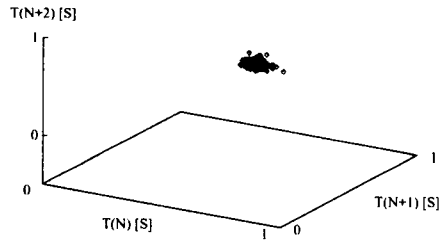
PLENUM SIGNAL



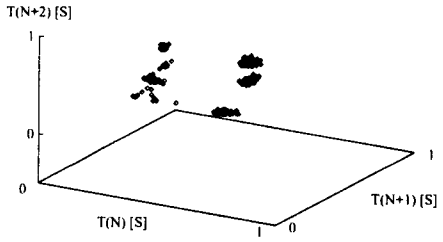
LOCAL SIGNAL

Figure 51. Time return maps for steel with different control modes at the developing slug regime (Run C1; U/U_{MF} = 1.16).

STABILIZATION CONTROL

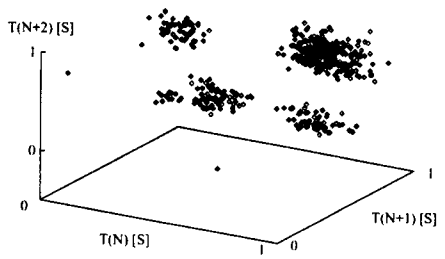


PLENUM SIGNAL

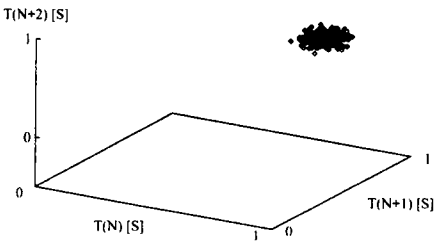


LOCAL SIGNAL

NO CONTROL

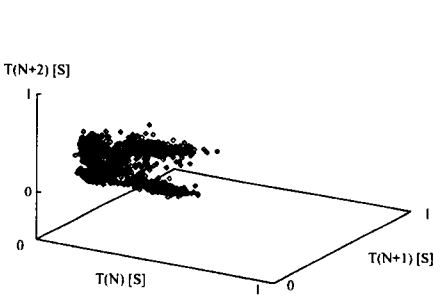


PLENUM SIGNAL

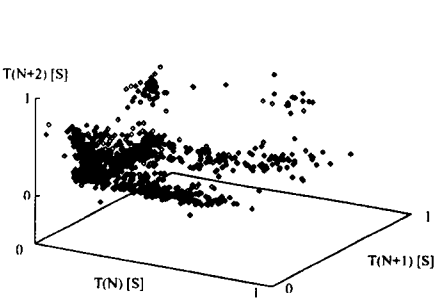


LOCAL SIGNAL

DESTABILIZATION CONTROL



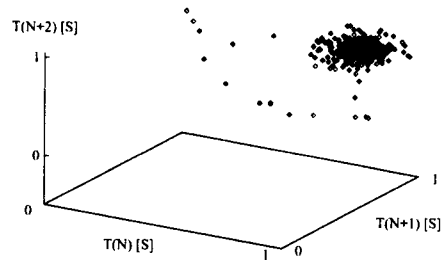
PLENUM SIGNAL



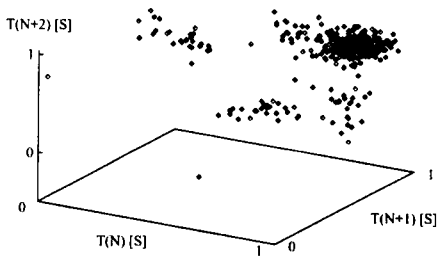
LOCAL SIGNAL

Figure 52. Time return maps for steel with different control modes at the maximum stable slugging state (Run C2; U/U_{MF} = 1.28).

STABILIZATION CONTROL

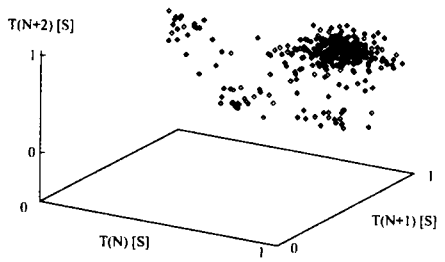


PLENUM SIGNAL

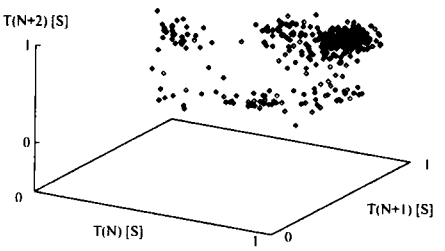


LOCAL SIGNAL

NO CONTROL

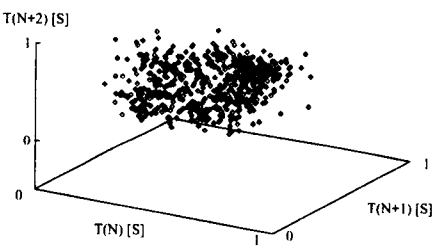


PLENUM SIGNAL

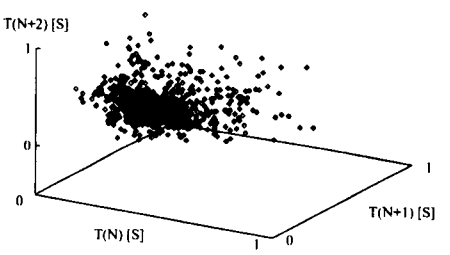


LOCAL SIGNAL

DESTABILIZATION CONTROL



PLENUM SIGNAL



LOCAL SIGNAL

Figure 53. Time return maps for steel with different control modes at the breaking slug regime (Run C3; U/U_{MF} = 1.55).

destabilization mode, the shift to highly variable, shorter periods is seen in all cases.

The shift in unstable fixed points for stabilization mode can be seen clearly in both plenum and local signals of run C1 and C2. For Run C3, the unstable fixed point does not shift, and there are fewer points away from the main cluster. Control seems to stabilize the existing fixed point in this case.

For evaluating control effectiveness, a change in convention for dimension and entropy estimates were made, using one average cycle time of the no control case as the common resolution scale for segment length. The results illustrated in Figures 54 and 55 clearly show the change in system behavior with different control modes. In destabilization control, entropy and dimension significantly increase, reflecting a more complex bed behavior. In stabilization control, entropy and dimension do not significantly change, but in a few cases, particularly in the local signal estimates, the added local signal complexity resulting from the air pulse yields slightly larger values. However, it is clear that the basic trends in these quantities are consistent with the observed dynamic complexity of the bed.

5.3.4 EVALUATION OF CONTROL AT DIFFERENT FLUIDIZATION CONDITIONS WITH GLASS.

Results from control experiments with glass at a static bed height of 23.5 cm are presented in this section. The bed was operated in the breaking slug regime, with control based on the plenum signal. The operating conditions and the control parameters for the experiments are listed in Table 6. Preliminary experiments indicated that the nozzle air supply pressure should be lower than 207 kPa used for steel, due to the lower overall bed

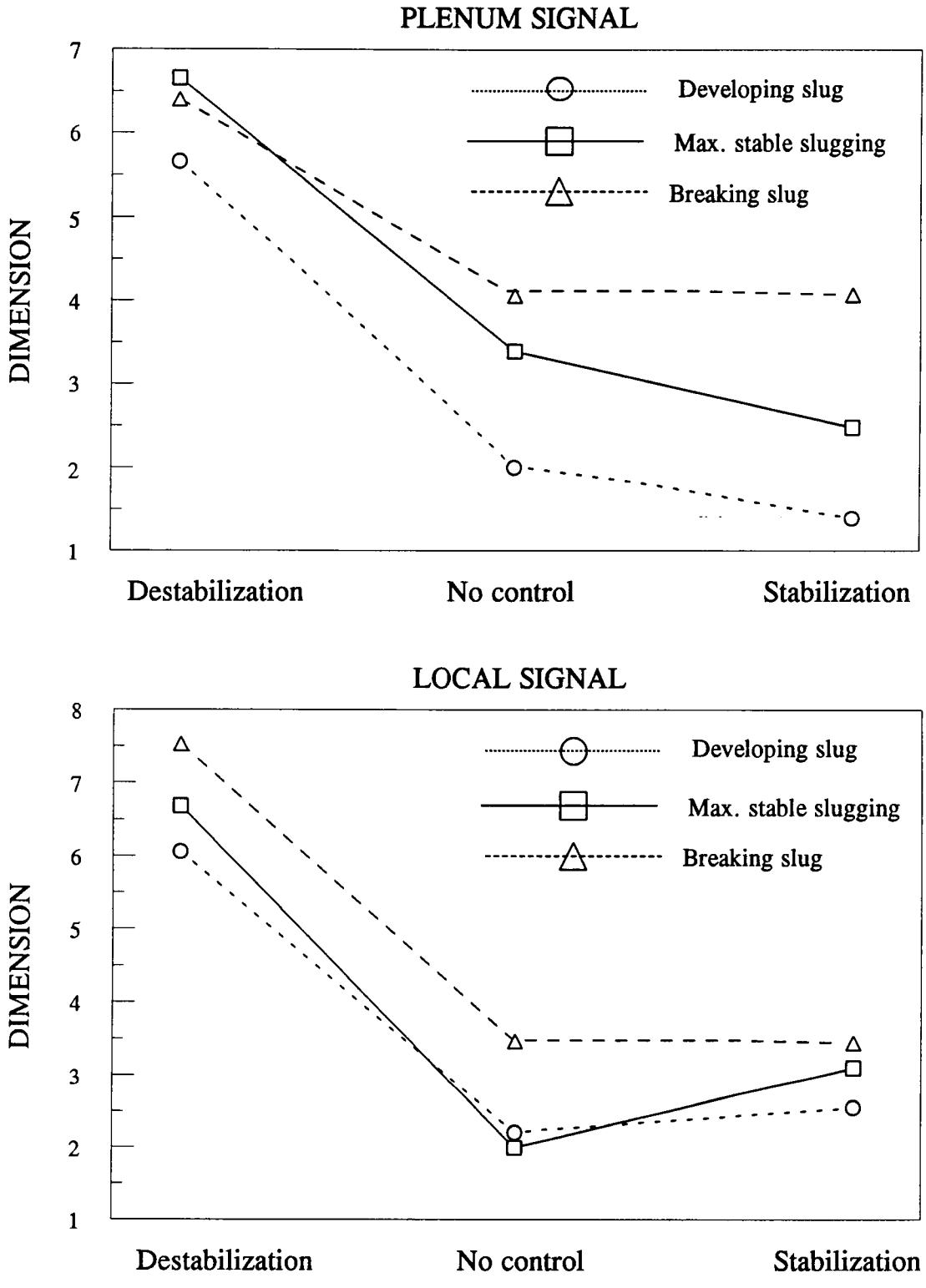


Figure 54. Variation in dimension with control mode for steel at three different fluidization regimes.

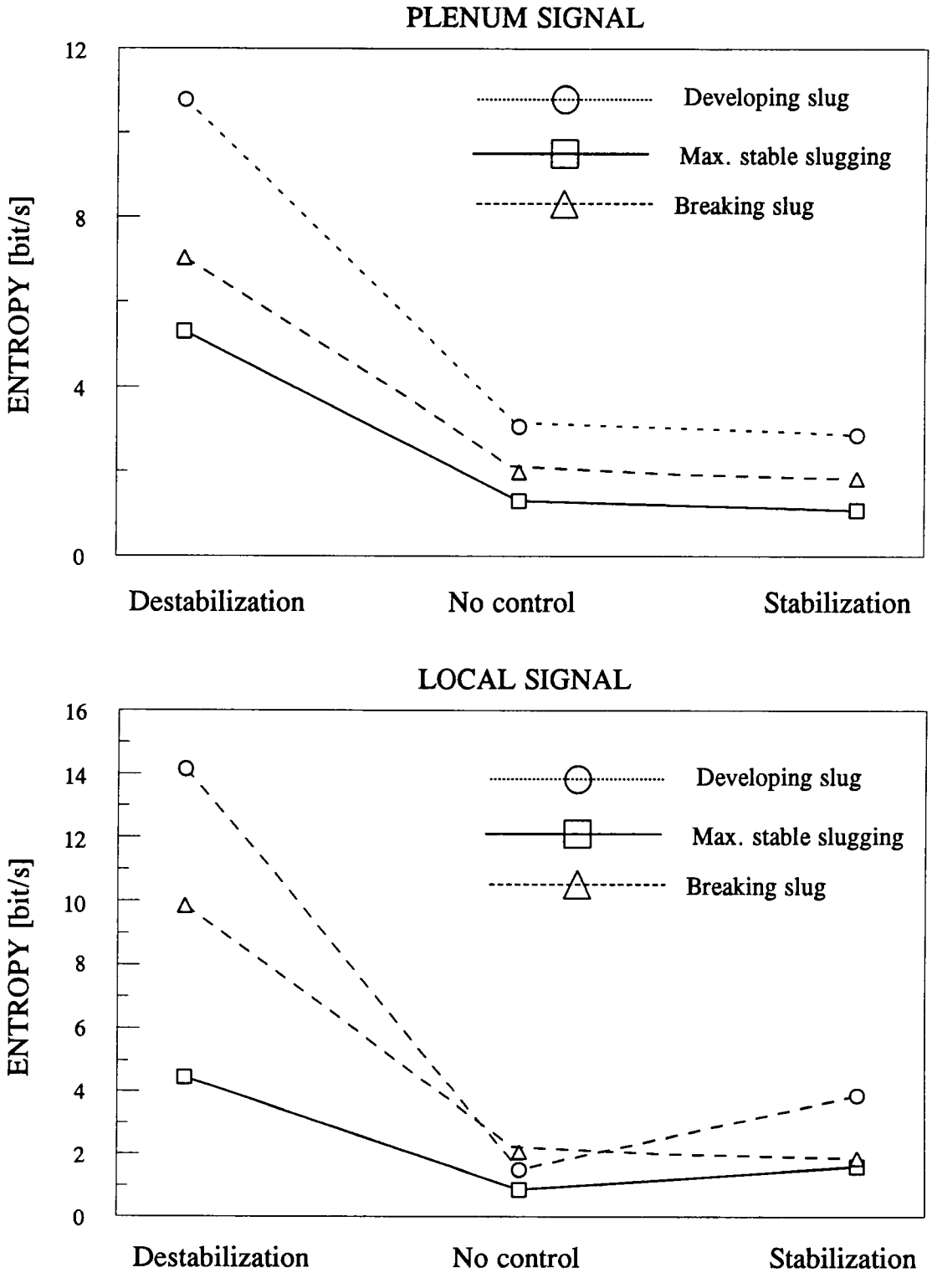


Figure 55. Variation in entropy with control mode for steel at three different fluidization regimes.

Table 6. Operating conditions for control evaluation experiments for glass.

Run No.	U/U_{MF}	Stabilization				Destabilization			
		Pulse Timing		Pulse Width [ms]	Pulse Gas* %	Pulse Timing		Pulse Width [ms]	Pulse Gas* %
		Trigger Level [kPa]	Dir.			Trigger Level [kPa]	Dir.		
D1	1.59	+0.72	down	30	1.5	-0.16	up	60	3.4

* Time-averaged injector gas flow expressed as percentage of fluidization gas flow

pressure drop. In this experiment, the nozzle air supply pressure is reduced to 138 kPa. System behavior with no control is compared with both stabilization and destabilization control runs.

Typical time series segments for all the control modes are shown in Figure 56. Because of the low overall pressure drop in the case of glass, the transient disturbances introduced by pulsing was clearly seen in both plenum and local signals. In the stabilization mode, the oscillations are more regular, and unlike the steel case the oscillation time scales are increased. In the destabilization mode, small time-scale and small amplitude oscillations dominate in both signals.

Figure 57 shows the Fourier power spectra for all the control modes. Compared with the no control case, stabilization results in a more distinct, sharply defined dominant peak, and the dominant peak is shifted to lower frequencies. The presence of harmonics indicating more regular behavior is muted in the case of glass and is attributed to the more pronounced transient disturbances introduced by pulsing. Destabilization results in

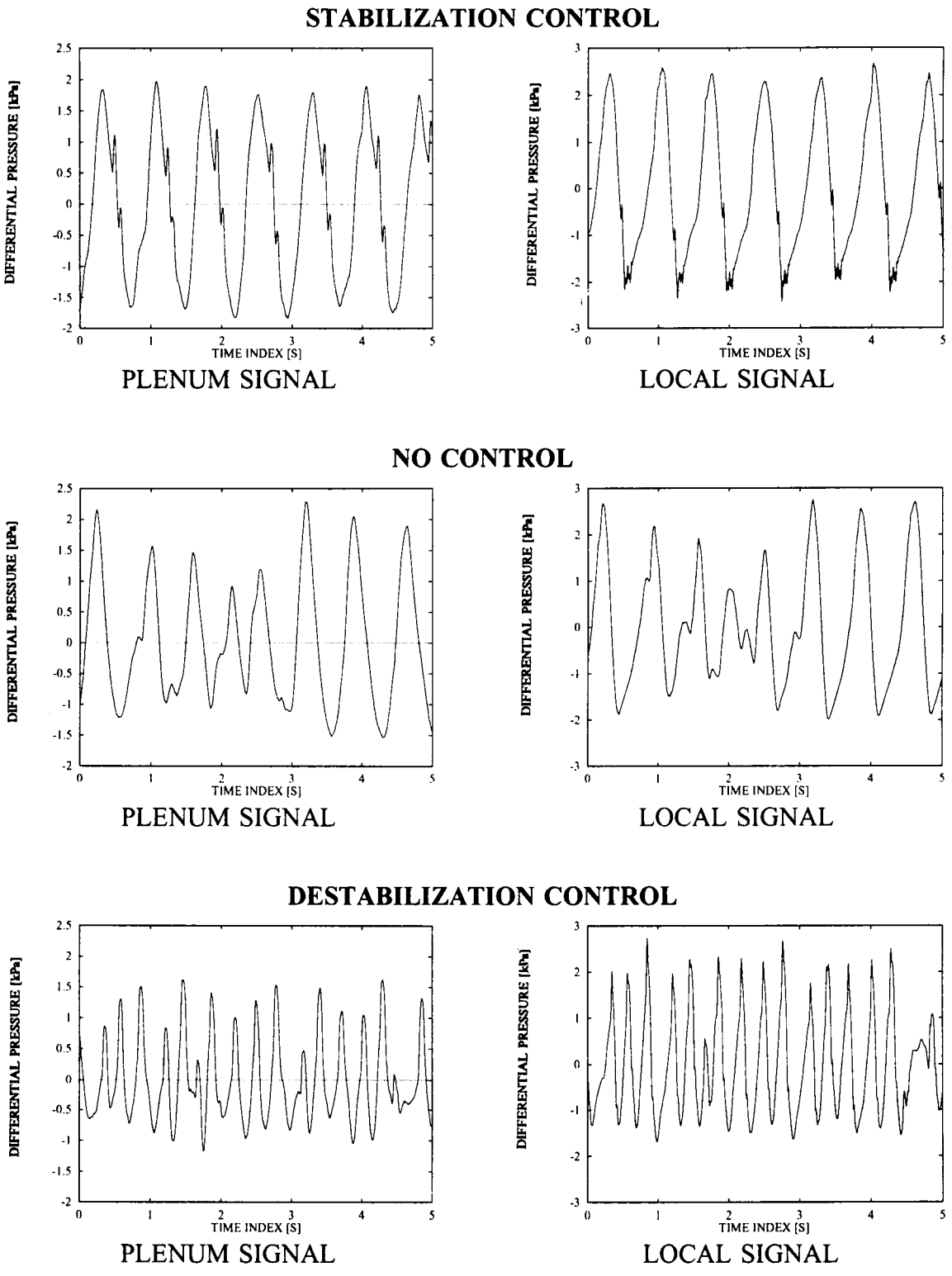


Figure 56. Typical time series segments for glass with different control modes at the breaking slug regime (U/U_{MF} = 1.59).

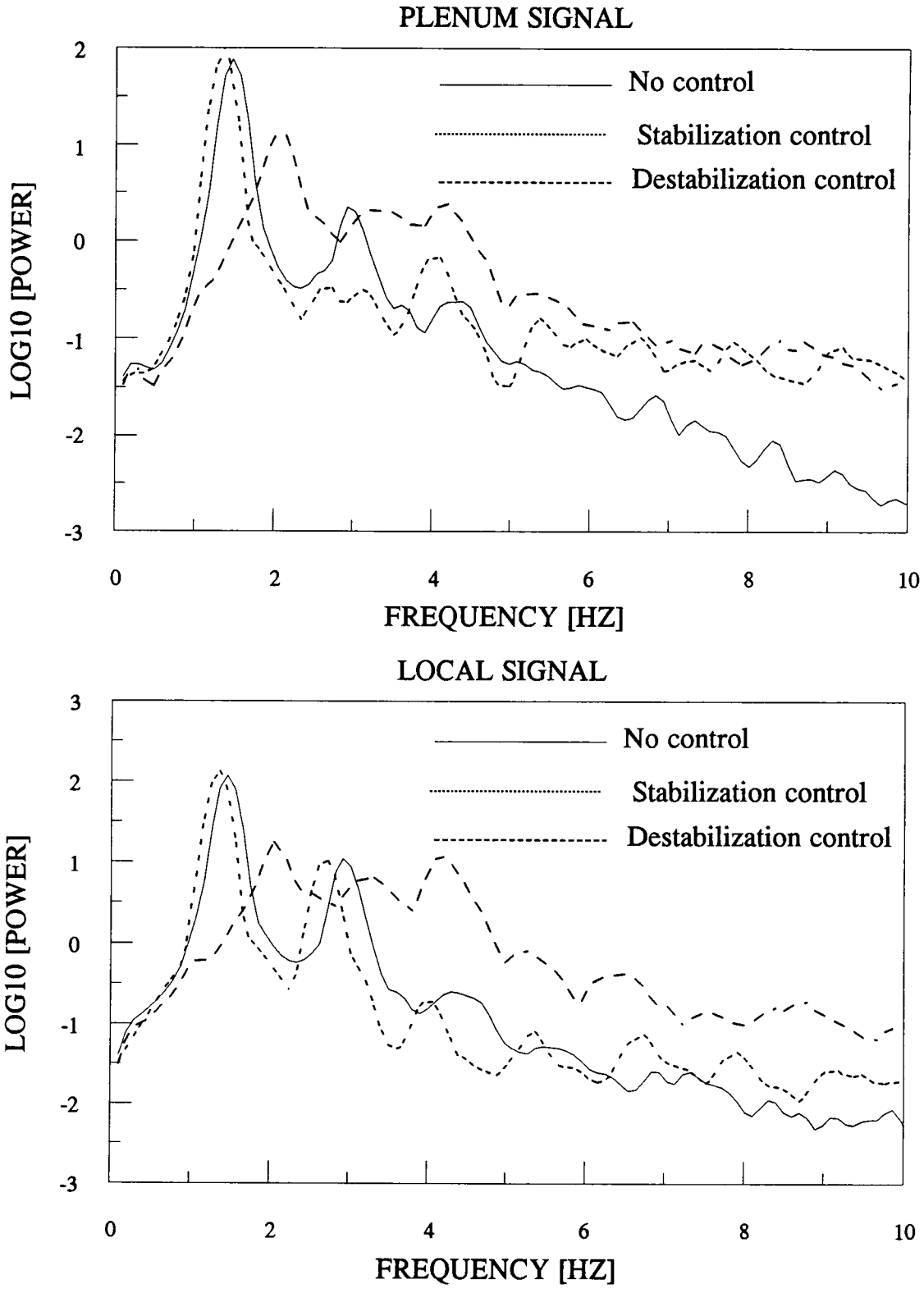


Figure 57. Fourier power spectra for glass with different control modes at the breaking slug regime [U/Umf = 1.59].

a more broad-band spectrum with a shift of the dominant peak to higher frequency.

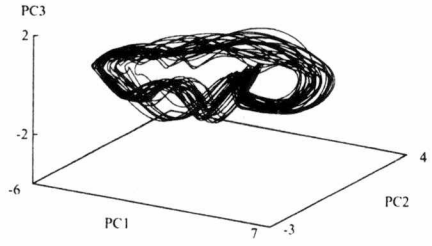
Three dimensional projections of typical segments of the reconstructed trajectories for different control modes are shown in Figure 58. In the stabilization mode, phase plots are characterized by a tighter banding of trajectories and opening up in the middle indicating a more ordered behavior. In the destabilization mode, opening up of phase plots , a characteristic feature of slugging in fluidized bed is completely lost. This clearly indicates that the ordered behavior imposed by slugging is completely disrupted.

The effect of control mode on cycle magnitudes is shown in Figure 59. In the breaking slug regime, the control scheme was able to effectively stabilize and destabilize the slugging behavior of glass in contrast to the steel experiments. In stabilization control, cycle magnitudes are larger and more narrowly distributed. In destabilization control, the cycle magnitudes are lower because of the disruption of slugging by the control action with very few cycles of magnitude comparable to the no control case.

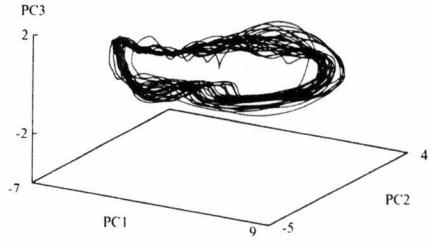
Time return maps for the three different control modes are shown in Figure 60. In stabilization control, the cycle periods can be seen to cluster more tightly about a single value for both the signals. In contrast to the steel experiments where at the breaking slug regime the existing unstable fixed point is stabilized, a shift to higher period is seen for glass. For destabilization mode, the shift to highly variable, shorter periods is seen indicating the system is dominated by small time-scale oscillations.

For dimension and entropy estimations, the control effectiveness comparison convention of using one average cycle time of the no control case as the common resolution scale for segment length is adopted. The results illustrated in Figure 61 clearly

STABILIZATION CONTROL

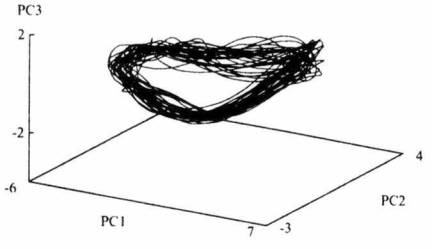


PLENUM SIGNAL

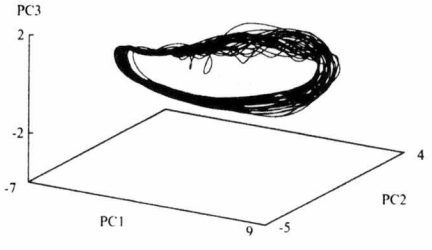


LOCAL SIGNAL

NO CONTROL

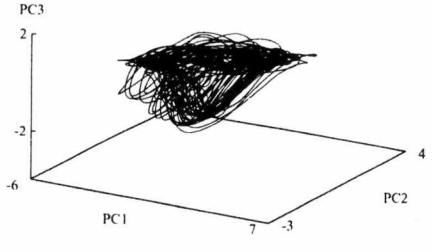


PLENUM SIGNAL

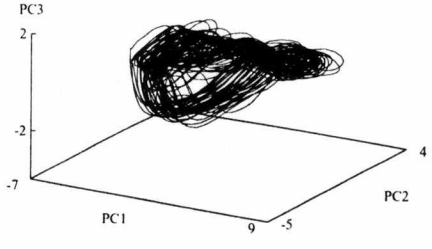


LOCAL SIGNAL

DESTABILIZATION CONTROL



PLENUM SIGNAL



LOCAL SIGNAL

Figure 58. Three dimensional projection of the reconstructed trajectories for glass with different control modes at the breaking slug regime (U/U_{MF} = 1.59; Time span = 20 s).

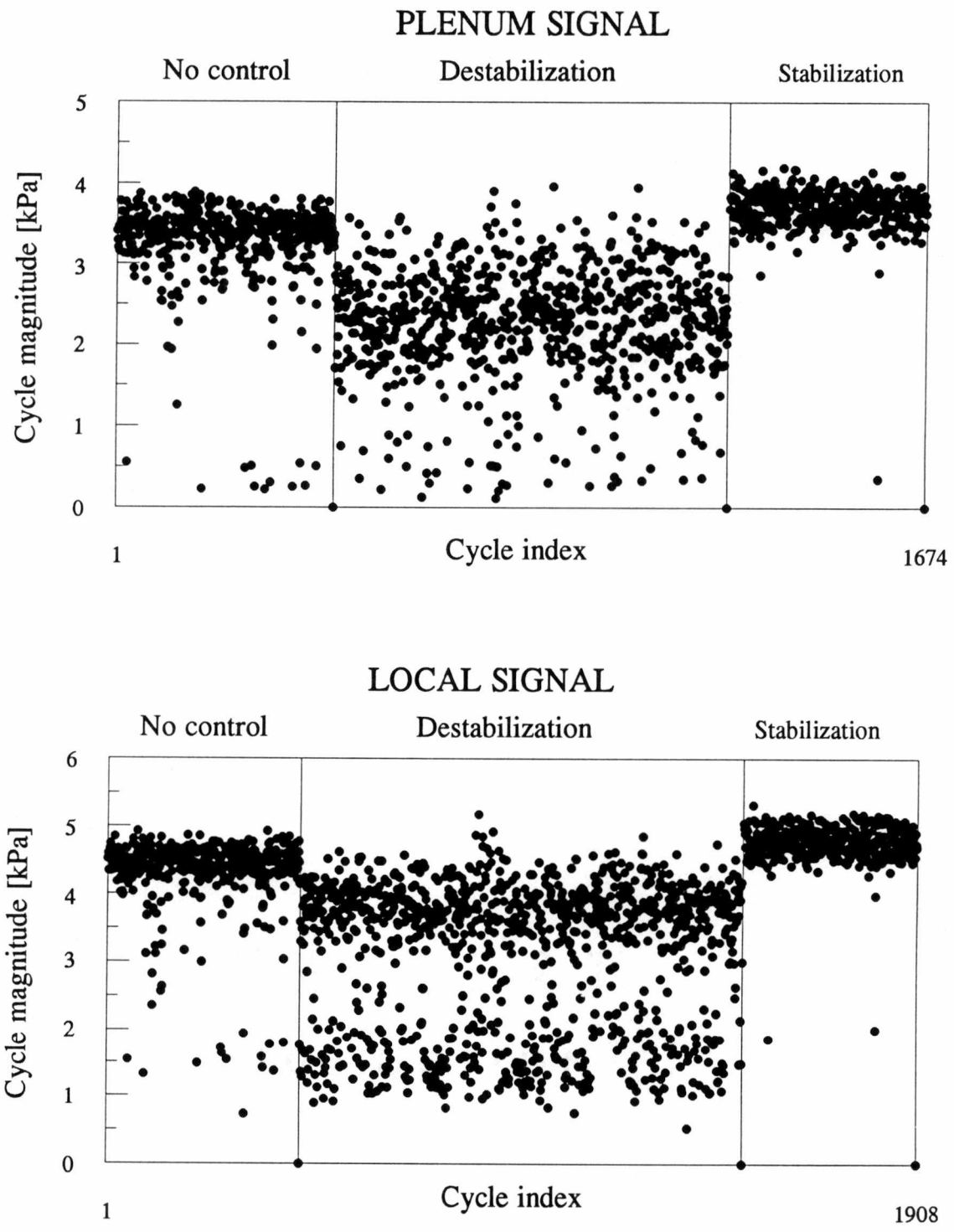
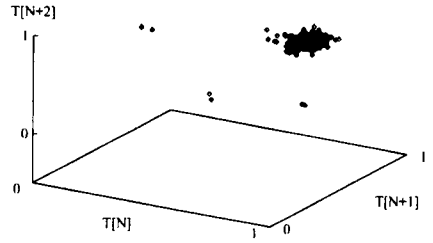
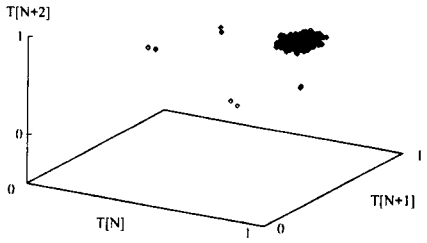


Figure 59. Variation in cycle magnitudes for glass with different control modes at the breaking slug regime [Run C3; U/Umf = 1.59].

STABILIZATION CONTROL

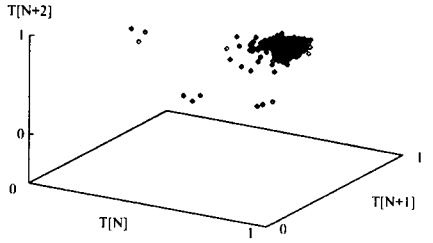


PLENUM SIGNAL

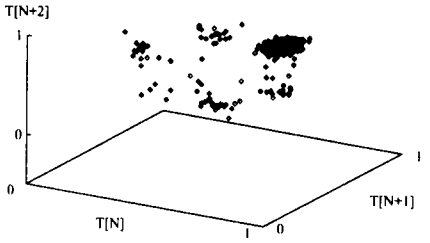


LOCAL SIGNAL

NO CONTROL

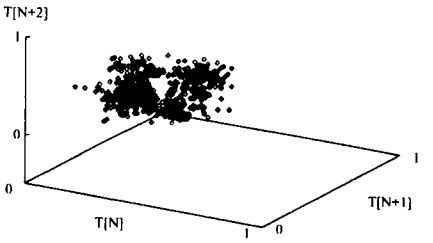


PLENUM SIGNAL

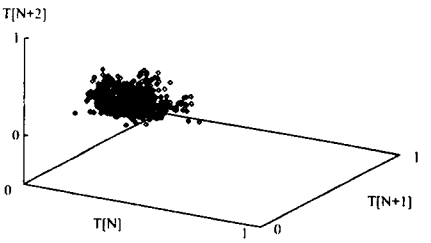


LOCAL SIGNAL

DESTABILIZATION CONTROL



PLENUM SIGNAL



LOCAL SIGNAL

Figure 60. Time return maps for glass with different control modes at the breaking slug regime (U/U_{MF} = 1.59).

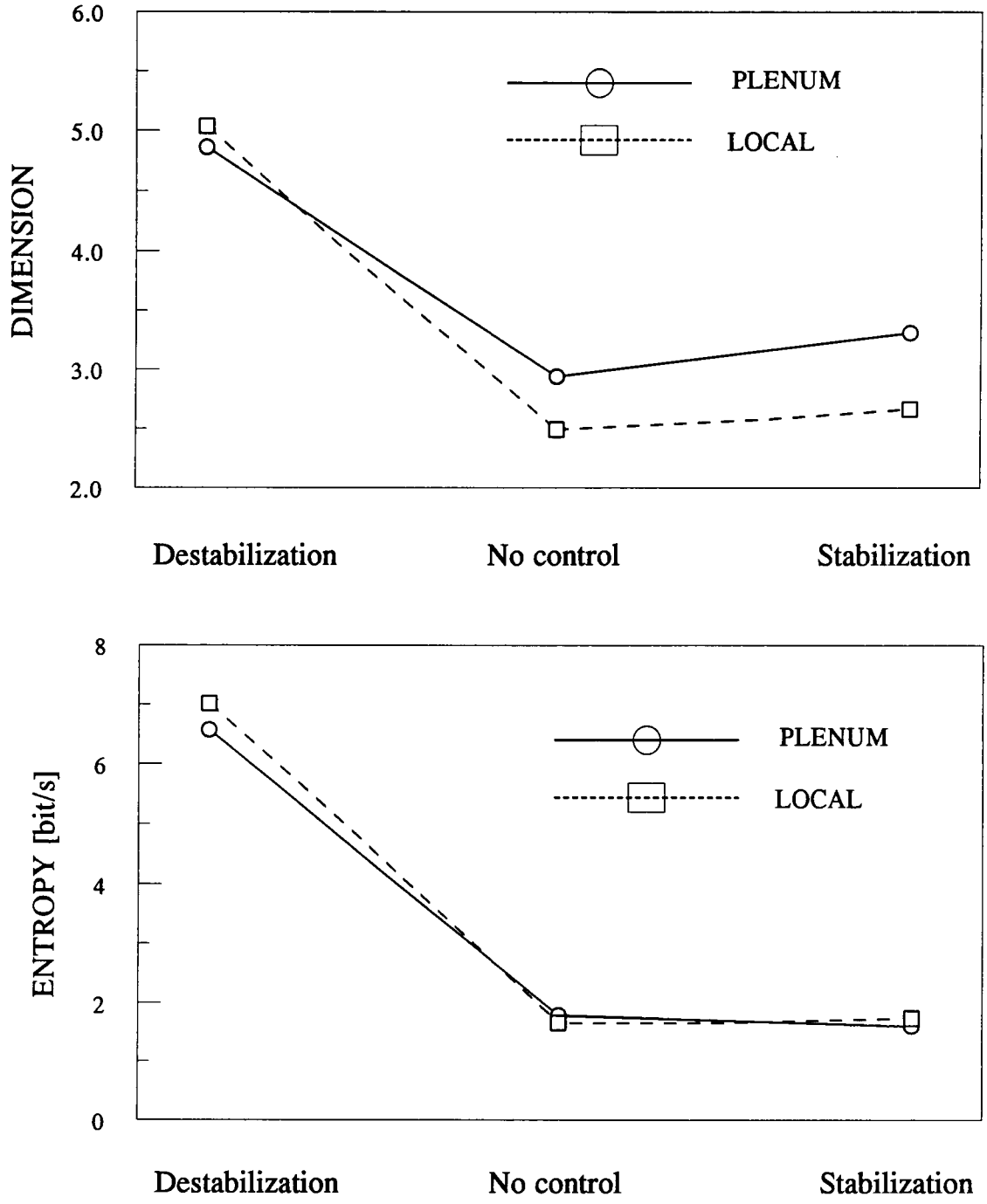


Figure 61. Variation in dimension and entropy with different control modes for glass at the breaking slug regime (U/Umf = 1.59).

show the change in system behavior with different control modes. In destabilization control, entropy and dimension significantly increase, reflecting a more complex bed behavior. In stabilization control, entropy and dimension do not significantly change, but in a few cases, the added signal complexity resulting from the air pulse yields slightly larger values. However, it is clear that the basic trends in these quantities are consistent with the observed dynamic complexity of the bed.

5.3.5 SUMMARY OF CONTROL EVALUATION EXPERIMENT RESULTS

Performance of the control scheme was evaluated using two Geldart's group D particles steel and glass. In stabilization control, the slugging intensity is increased and bed level fluctuations become more regular compared to the no control case. In destabilization control, even though occasional misfires were observed, generally the slugging intensity is decreased and a large number of smaller or partial slugs were seen. Conventional as well as chaotic time series analysis techniques such as power spectra, cycle magnitude comparisons, time return maps, dimension and entropy estimations confirm these observations. The dynamical feedback introduced by the control scheme is very effective in mode locking for glass, and for steel in the developing slug and regular slugging regime. However, for steel control effectiveness is affected at high gas flow rates as indicated by the results from the breaking slug regime (run C3). Future control strategies based on system dynamics extracted by further processing of the system variable (pressure) and utilizing the non-random structures associated with slugging may be able to achieve more effective control over a wider range of fluidization velocities.

Results of the control evaluation studies clearly demonstrate that the nonlinear sensitivity of chaotic systems to small perturbations can be used for control of slugging behavior of Geldart's group D particles. The control scheme based on small pressure pulse perturbation is able to achieve both stabilization and destabilization of slugging behavior.

CHAPTER 6

CONCLUSIONS AND RECOMMENDATIONS

Results of the slugging characterization study for Geldart's group D particles demonstrate that slugging behavior can be classified into different regimes based on the characteristic dynamical behaviors extracted by various chaotic time series analysis techniques. The dominant physical mechanisms and their characteristic signatures in the bed dynamics associated with each regime such as the small time-scale and low magnitude cycles near minimum fluidization, typical non-random patterns in time return maps in the developing slug regime, unstable limit cycle behavior in the regular slugging regime and the shift to lower time-scale motion and non-random patterns in the breaking slug regime, were identified. The transition to chaos at gas flow rates beyond regular slugging was identified as intermittency route to chaos.

Results of the control evaluation experiments demonstrate that introducing a high-pressure, short-duration gas pulse into a slugging fluidized bed can modify slugging behavior effectively. The pressure-drop feedback control strategy implemented in this study both stabilized and destabilized slugging based on simple choices of pulse timing and intensity. However, control effectiveness varies with the fluidization flow rate, and is not effective at higher flow rates in the breaking slug regime for steel.

The implemented method utilizes non-linear sensitivity of slugging dynamics to external perturbation for control. The implications of this strategy in relation to other chaos control schemes such as OGY method and PPF method, should be investigated. It is recommended that more sophisticated control strategies be adopted, based on recent

advances in adaptive or chaotic control, which might be able to utilize non-random patterns exhibited by the system dynamics and achieve better control effectiveness. It is also recommended to explore the possibility of applying the developed control strategy to a more general class of systems exhibiting intermittency behavior.

The perturbation system should be modified for larger and deeper beds used in industrial fluidized beds, to include pulse nozzles located in the distributor. This will allow perturbation of the interior portions of beds. A similar investigation of Geldart's group B particles such as sand, polymer beads used by a sizable proportion of commercial fluidized bed devices, is recommended.

REFERENCES

REFERENCES

1. Kunni, D., and Levenspiel, O., 1969, "Fluidization Engineering", *Robert E.Krieger Publishing company, Inc.*, pp. 1-3.

2. Geldart, D., 1973, "Types of Gas Fluidization", *Powder Technology*, Vol. 7, pp. 285-292.

3. Skrzycke, D. P., Ke Nguyen and Daw, C.S., 1993, "Characterization of the Fluidization Behavior of Different Solid Types Based on Chaotic Time Series Analysis of Pressure Signals", *12th International FBC Conference*, ASME, San Diego, Vol. 1, pp. 156-166.

4. Daw, C. S., Lawkins, W. F., Downing, D. J., and Clapp Jr., N. E., 1990, "Chaotic Characteristics of a Complex Gas-Solids Flow", *Physical Review A*, Vol. 4, pp. 1179-1181.

5. Daw, C.S. and Hallow, J.S., 1991, "Characterization of Voidage and Pressure Signals from Fluidized Beds Using Deterministic Chaos Theory", *International Conference on FBC*, Montreal, ASME, Vol. 2, pp. 777-786.

6. Daw, C.S. and Hallow, J.S., 1993, "Evaluation and Control of Fluidization Quality Through Chaotic Time Series Analysis of Pressure-drop Measurements", *AIChE Symposium Series*, Vol. 89, No. 296, pp. 103-122.

7. Schouten, J.C. and Van den Bleek, C.M., 1991, "Chaotic Behavior in a Hydrodynamic Model of a Fluidized Bed Reactor", *Proceedings of the 1991 Conference on FBC*, Montreal, pp. 459-466.

8. Ott, E., Gregobi, C., and Yorke, J.A., 1990, "Controlling Chaos", *Physical Review Letters*, Vol. 64, pp. 1196-1199.

9. Ditto, W.L., Rauseo, S.N., and Spano, M.L., 1990, "Experimental Control of Chaos", *Physical Review Letters*, Vol. 65, pp. 3211-3214.

10. Morse, R.D., 1955, "Sonic Energy in Granular Solid Fluidization", *Industrial and Engineering Chemistry*, Vol. 47, No. 6, pp. 1170-1175.

11. Moussa, N. A. and Fowle, A. A., 1985, "Exploratory Study of Pulsed Atmospheric Fluidized Bed combustion", *8th International FBC Conference*, Houston, Vol. 3, pp. 1300-1310.

12. Zabrodski, S.S. and Bokun, I.A., 1968, "Heat Transfer Between a Pulsating Bed of Moist Tetracycline and the Heating Surface", *Trans. USAEC Rept. ANL-Trans-593 (1968).*

13. Bokun, I.A. and Zabrodski, S.S., 1966, "Experimental Study of the Heat Transfer Between a Pulsating Bed and the Heating Surface", *Trans. USAEC Rept.ANl-Trans-592 (March 1968)* .

14. Massimilla, L., Volpicelli, G., and Raso, G., 1966, "A Study on Pulsing Gas Fluidization of Beds of Particles", *AIChE Symposium Series*, Vol. 62, No. 62, pp. 63-70.

15. Kobayashi, M., Ramaswami, D., and Brazelton, W. T., 1970, "Pulsed-bed Approach to Fluidization", *AIChE Symposium Series*, Vol. 66, No. 5, pp. 47-57.

16. Moussa, N. A., Fowle, A. A., and Hall, A. W., 1987, "An Experimental Study of Pulsed Fluidized Beds", *International FBC Conference*, Vol. 1, pp. 1141-1146.

17. Manneville, P., and Pomeau, Y., 1979, "Intermittency and the Lorenz Model", *Physics Letters*, Vol. 75A, No. 7.2, pp. 1-2.

18. Jeffries, C., and Perez, J., 1982, "Observation of a Pomeau-Manneville Intermittent Route to Chaos in a Nonlinear Oscillator", *Physical Review A*, Vol. 26, pp. 2117-2122.

19. Shinbrot, T., Gregobi, C., Ott, E., and Yorke, J.A., 1993, "Using Small Perturbations to Control Chaos", *Nature*, Vol. 363, pp. 411-417.

20. Garfinkel, A., Spano, M.L., Ditto, W.L., Weiss, J.N., 1992, "Controlling Cardiac Chaos", *Science*, Vol. 257, pp. 1230-1235.

21. Personal communication with Nick van Goor, May 1994.

22. Shannon, C.E., and Weaver, W., 1949, "The Mathematical Theory of Communications", University of Illinois Press, Urbana.

23. Takens, F., 1981, "Detecting Strange Attractors in Turbulence", *Lecture Notes in Mathematics*, Vol.898, Springer-Verlag, New York, pp. 366-381.

24. Broomhead, D.S., and King, G.P., 1986, "Extracting Qualitative Dynamics from Experimental Data", *Physica 20D*, pp. 217-236.

25. Schouten, J.C., Takens F. and Van den Bleek, C.M., 1994b, "Estimation of the Dimension of a Noisy Attractor", *Physical Review E*, Vol. 50, pp. 1851-1861.

26. Schouten, J.C., Takens F. and Van den Bleek, C.M., 1994a, "Maximum-Likelihood Estimation of the Entropy of an Attractor", *Physical Review E*, Vol. 49, pp. 126-129.

27. Martien, P., Pope, S.C., Scott, P.L., and Shaw, R.S., 1985 "The Chaotic Behavior of the Leaky Faucet", *Physics Letters*, Vol. 110A, No. 7-8, pp. 399-404.

APPENDICES

APPENDIX A

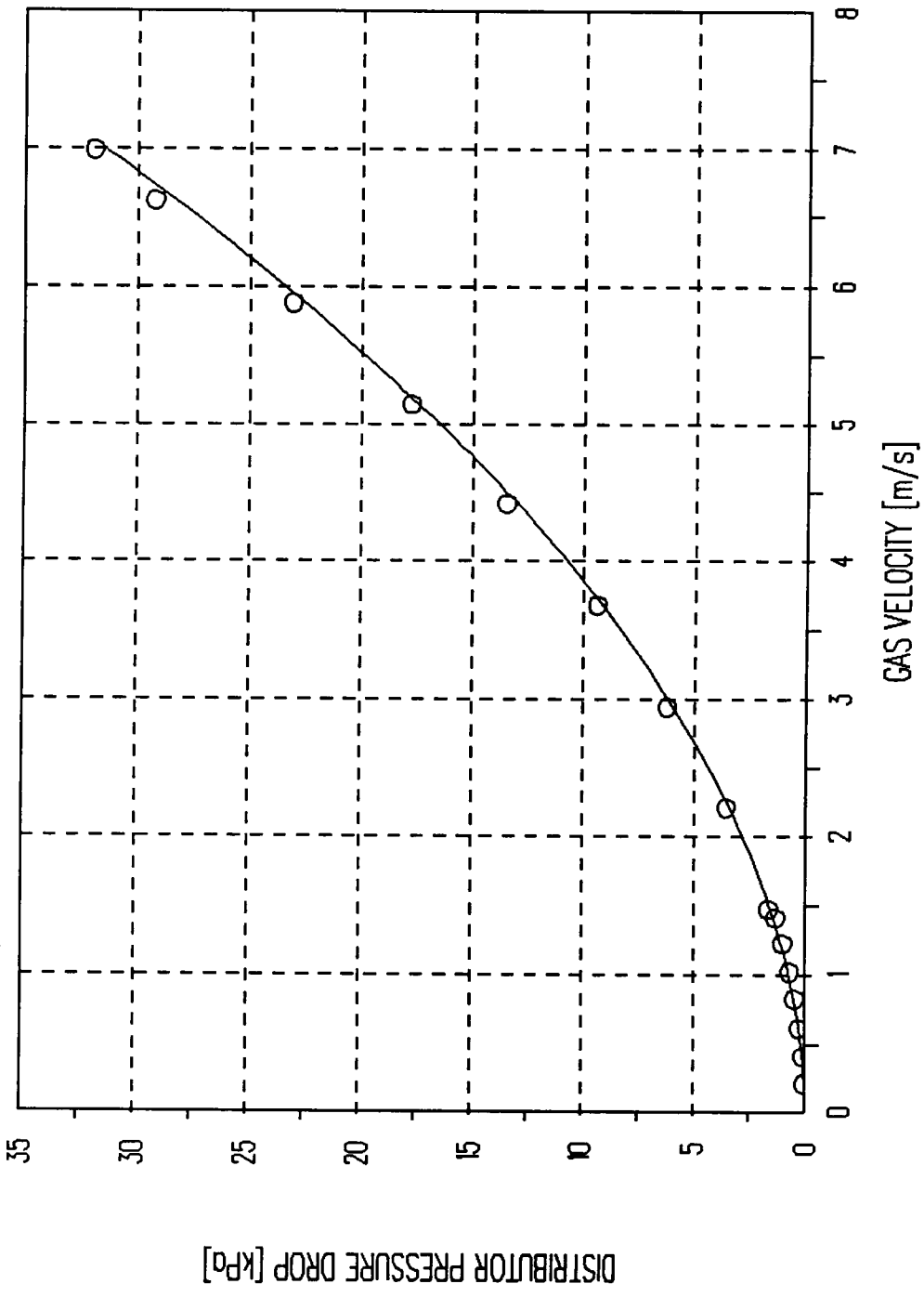


Figure A1. Pressure drop charecteristics of the tuyere-nozzle distributor used in the experiments.

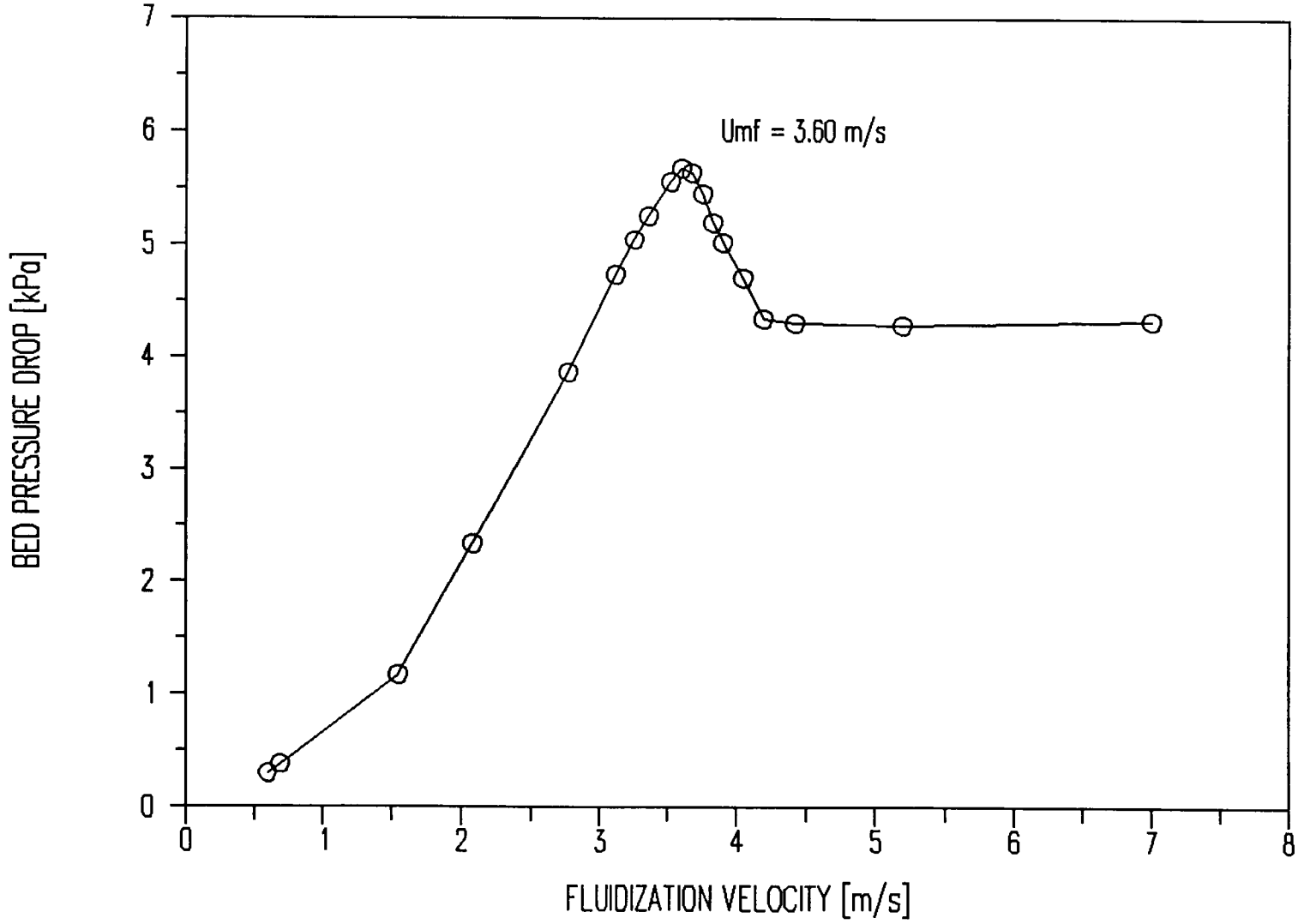


Figure A2. Minimum fluidization velocity for steel BB.

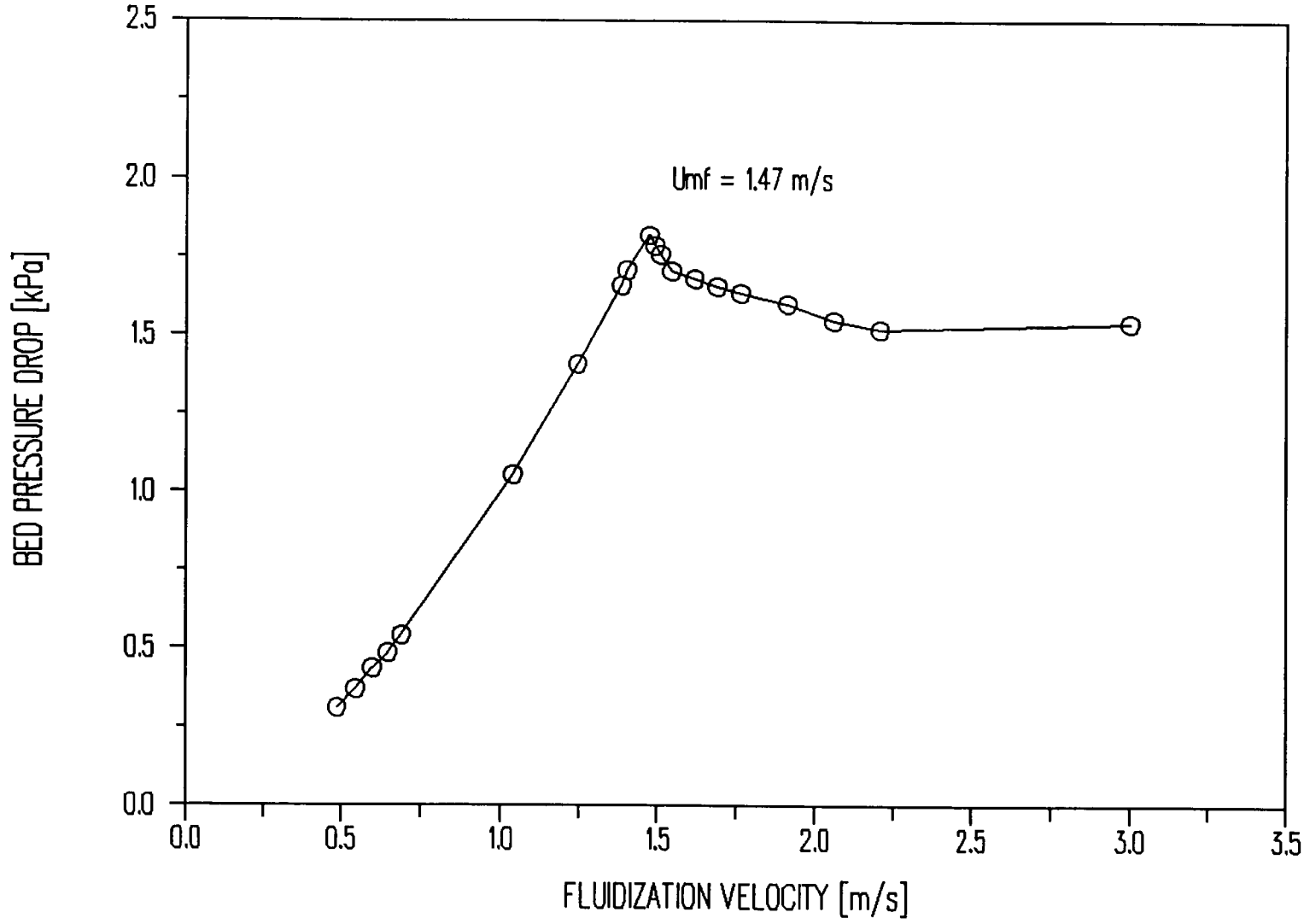


Figure A3. Minimum fluidization velocity for glass.

APPENDIX B

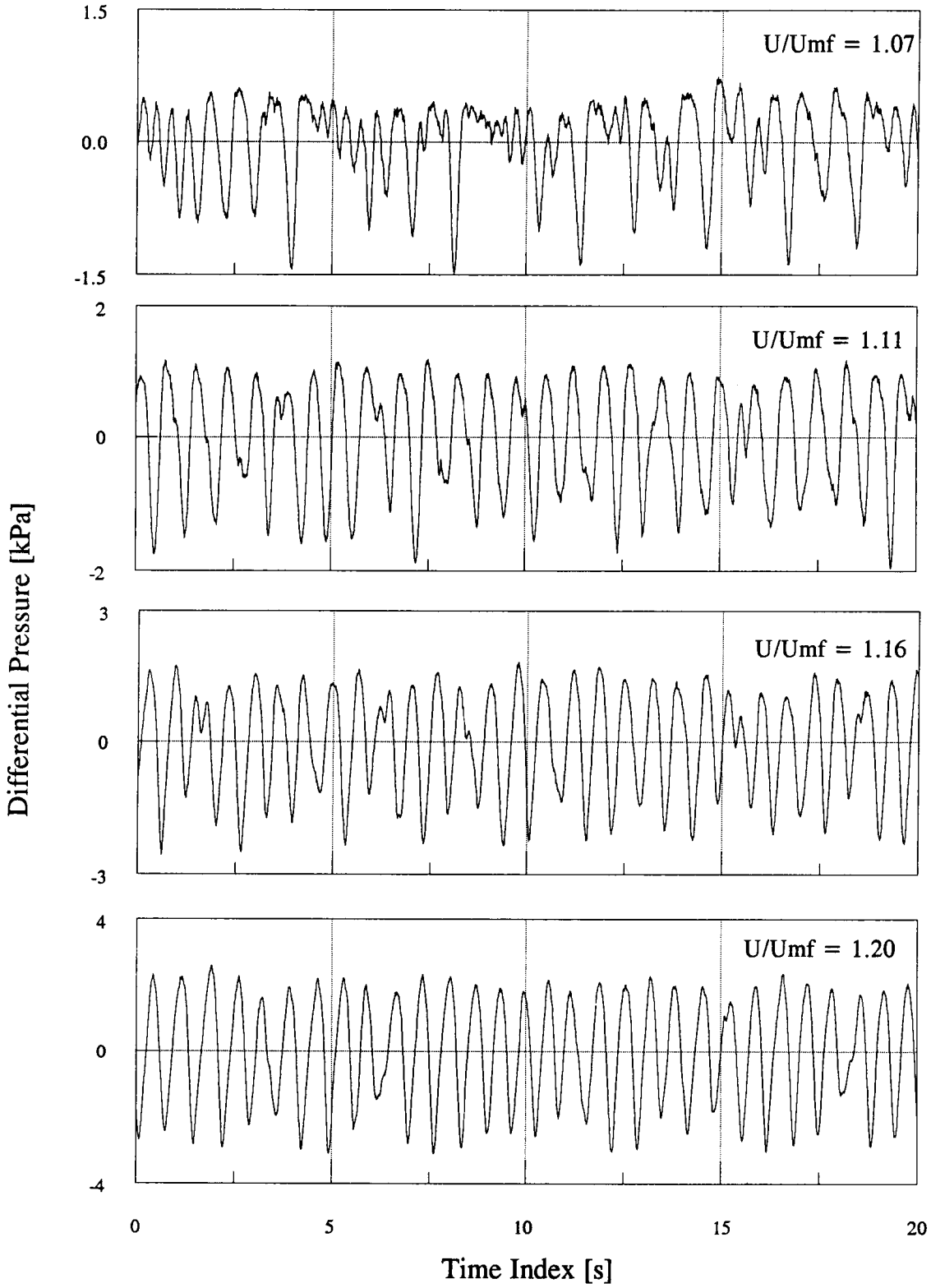


Figure B1. Typical time series segments of local pressure signal for steel over a velocity range of U/Umf = 1.07 to 1.20.

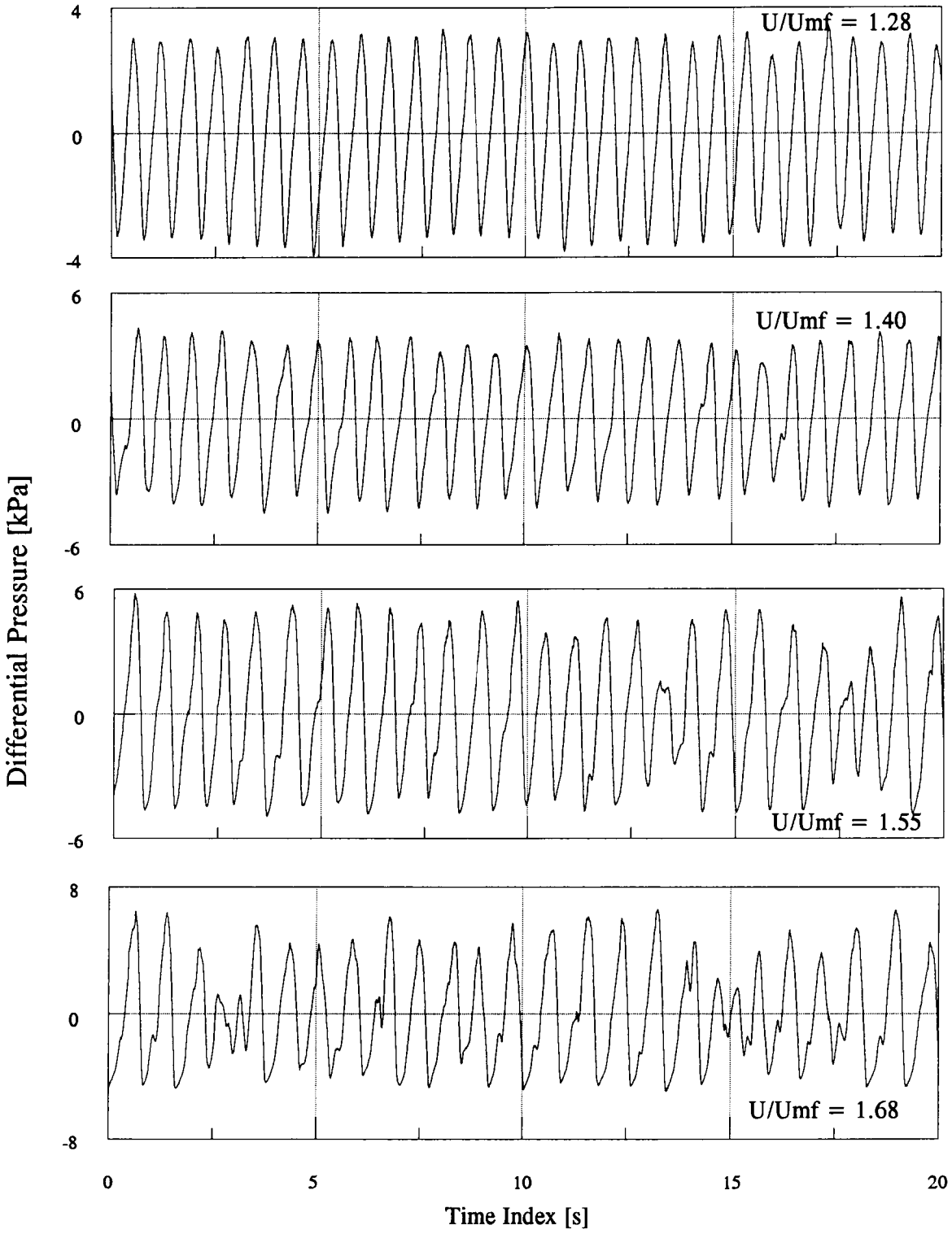


Figure B2. Typical time series segments of local pressure signal for steel over a velocity range of U/Umf 1.28 to 1.68.

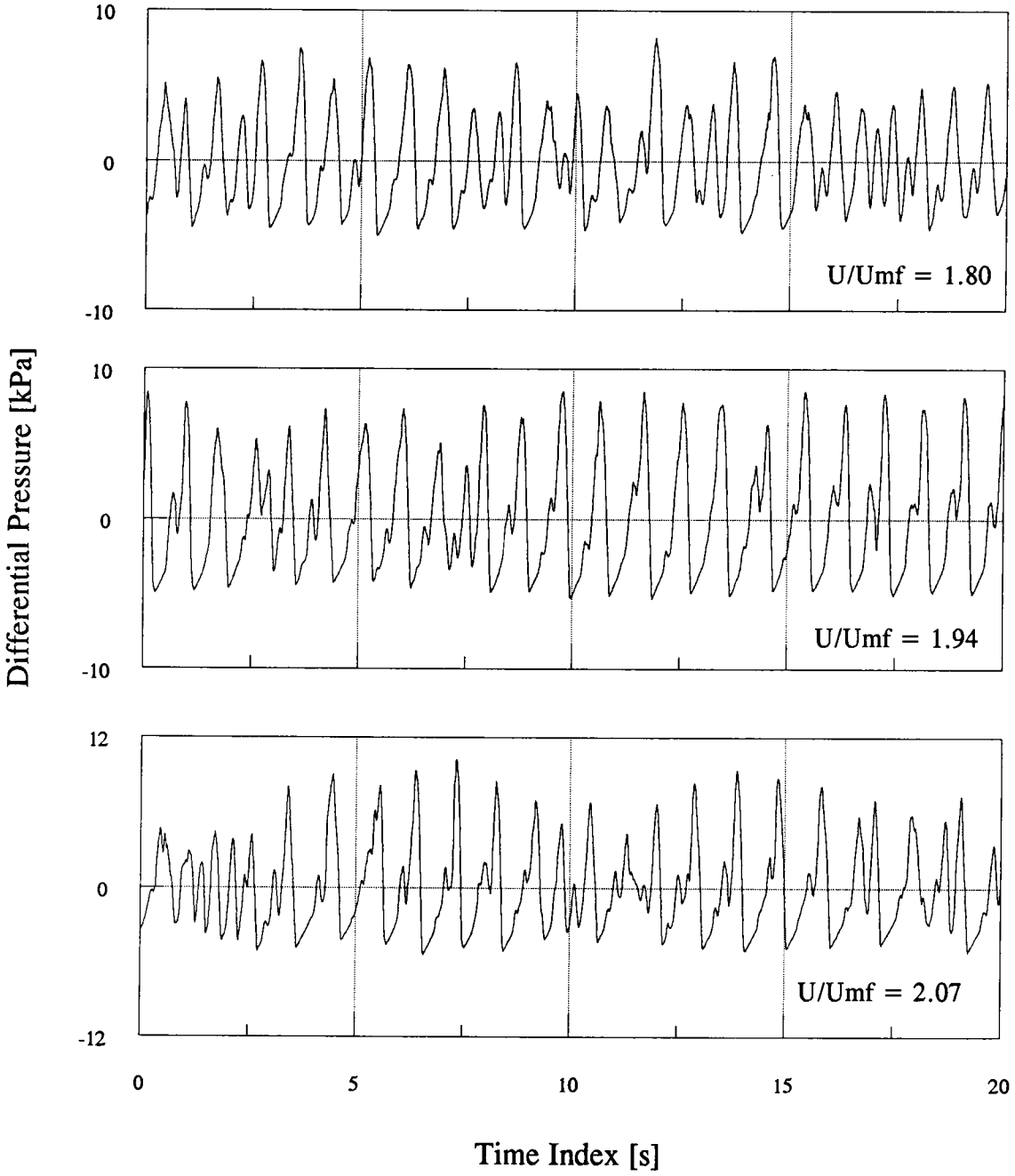


Figure B3. Typical timeseries segments of local pressure signal for steel over a velocity range of U/Umf = 1.80 to 2.07.

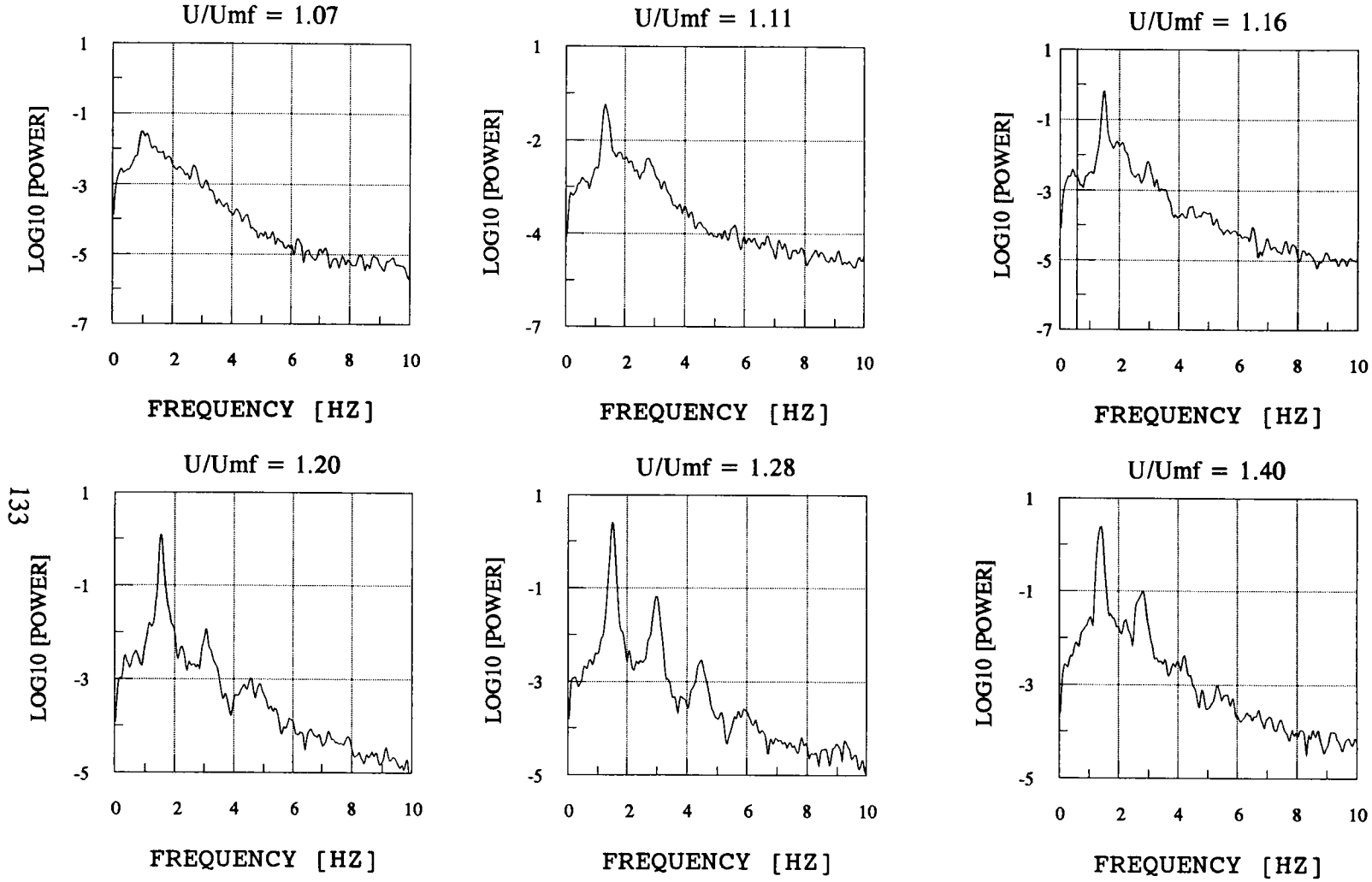


Figure B4. Fourier power spectra of local signal for steel over a velocity range of U/Umf = 1.07 to 1.40.

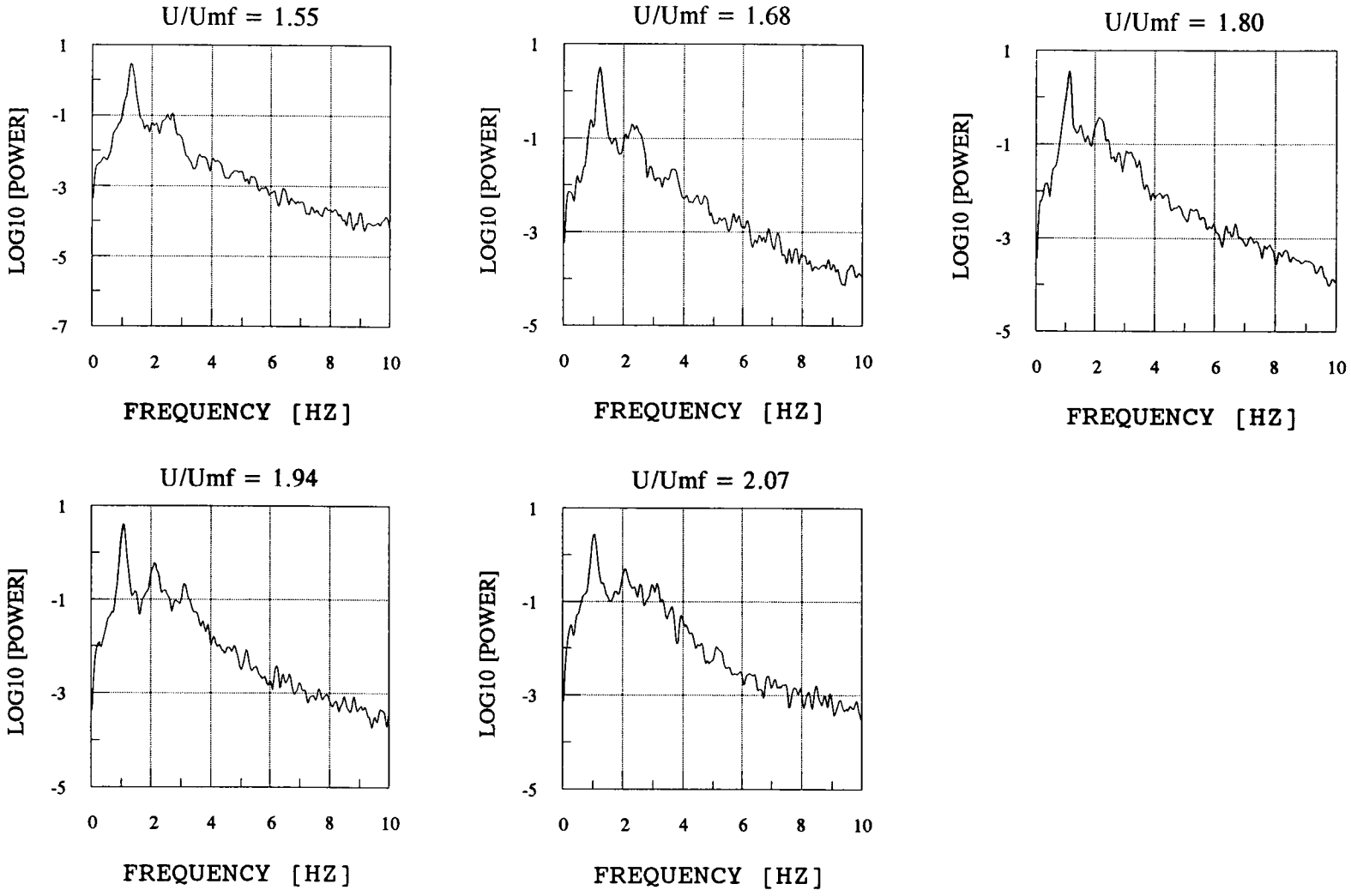


Figure B5. Fourier power spectra of local pressure signal for steel over a velocity range of U/Umf = 1.55 to 2.07.

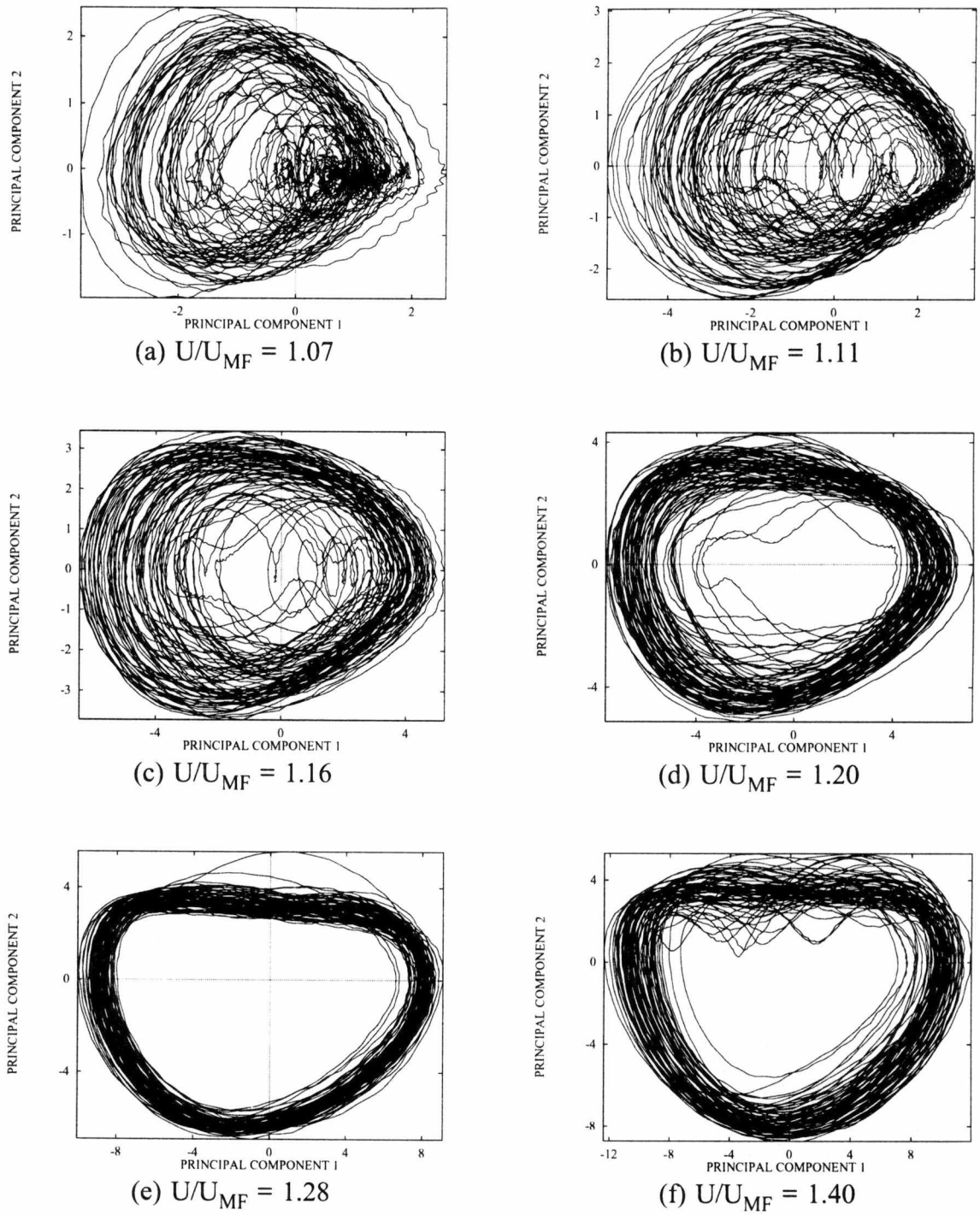
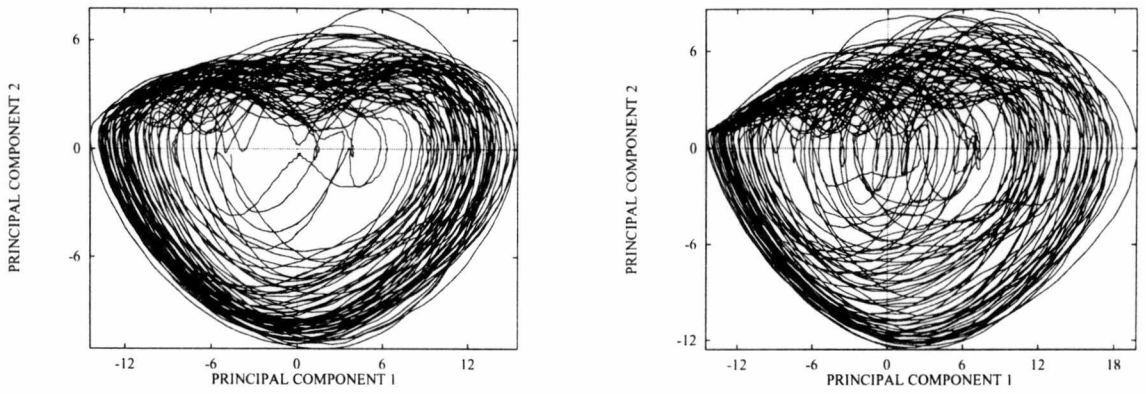
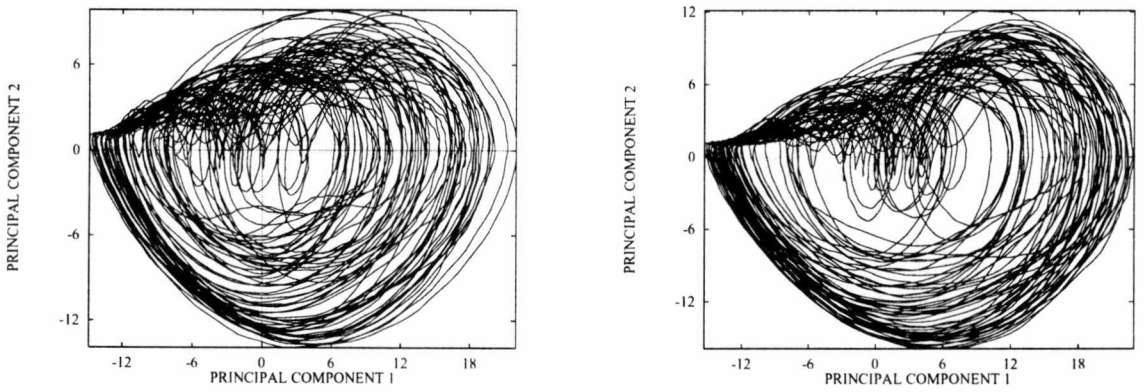


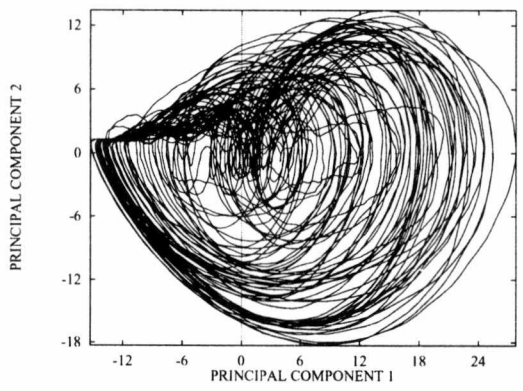
Figure B6. Two dimensional projection of reconstructed trajectories from local pressure signal for steel over a velocity range of U/U_{MF} = 1.07 to 1.40 [Time span = 50 s].



(g) U/U_{MF} = 1.55 (h) U/U_{MF} = 1.68

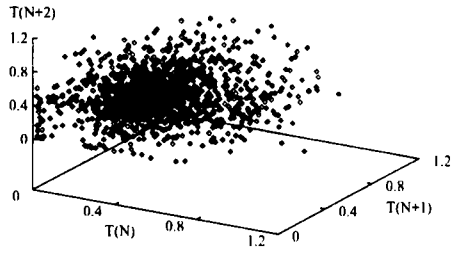


(i) U/U_{MF} = 1.90 (j) U/U_{MF} = 1.94

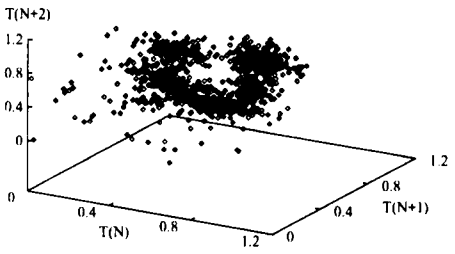


(k) U/U_{MF} = 2.07

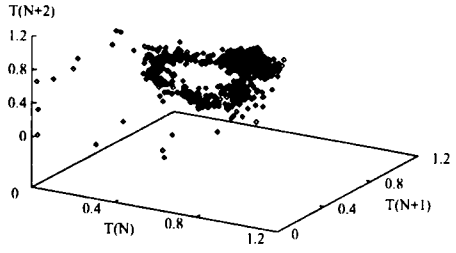
Figure B7. Two dimensional projection of reconstructed trajectories from local pressure signal for steel over a velocity range of U/U_{MF} = 1.55 to 2.07 [Time span = 50 s].



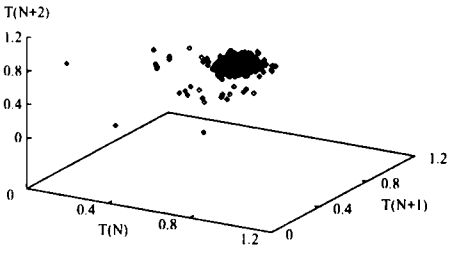
(a) U/U_{MF} = 1.07



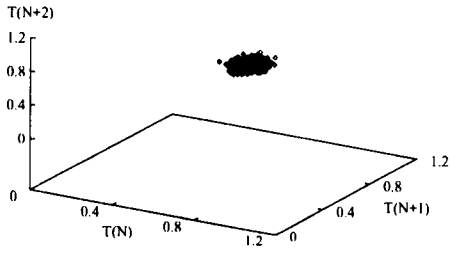
(b) U/U_{MF} = 1.11



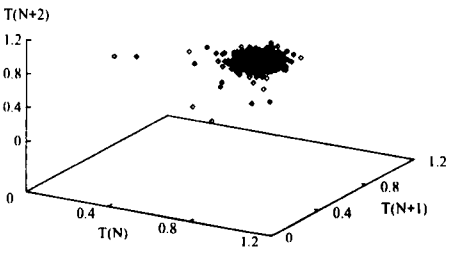
(c) U/U_{MF} = 1.16



(d) U/U_{MF} = 1.20

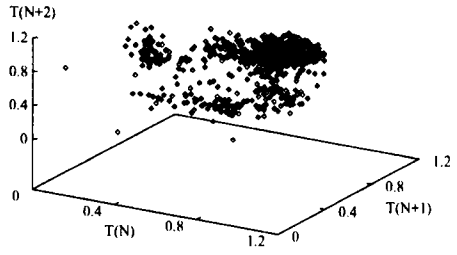


(e) U/U_{MF} = 1.28

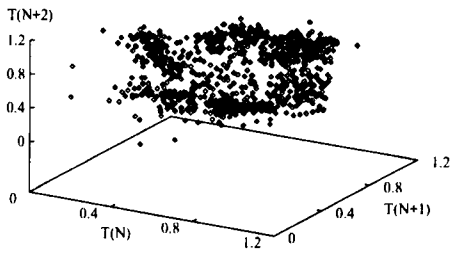


(f) U/U_{MF} = 1.40

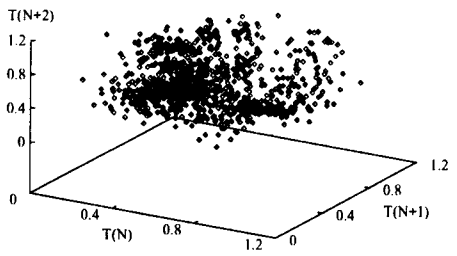
Figure B8. Time return maps using local pressure signal for steel over a velocity range of U/U_{MF} = 1.07 to 1.40.



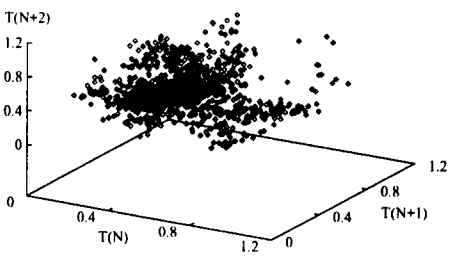
(g) U/U_{MF} = 1.55



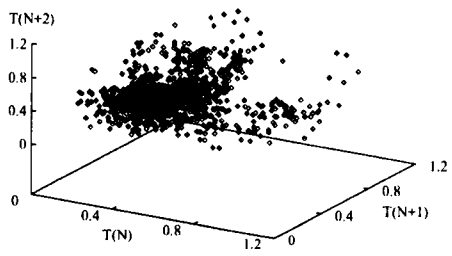
(h) U/U_{MF} = 1.68



(i) U/U_{MF} = 1.90



(j) U/U_{MF} = 1.94



(k) U/U_{MF} = 2.07

Figure B9. Time return maps using local pressure signal for steel over a velocity range of U/U_{MF} = 1.55 to 2.07.

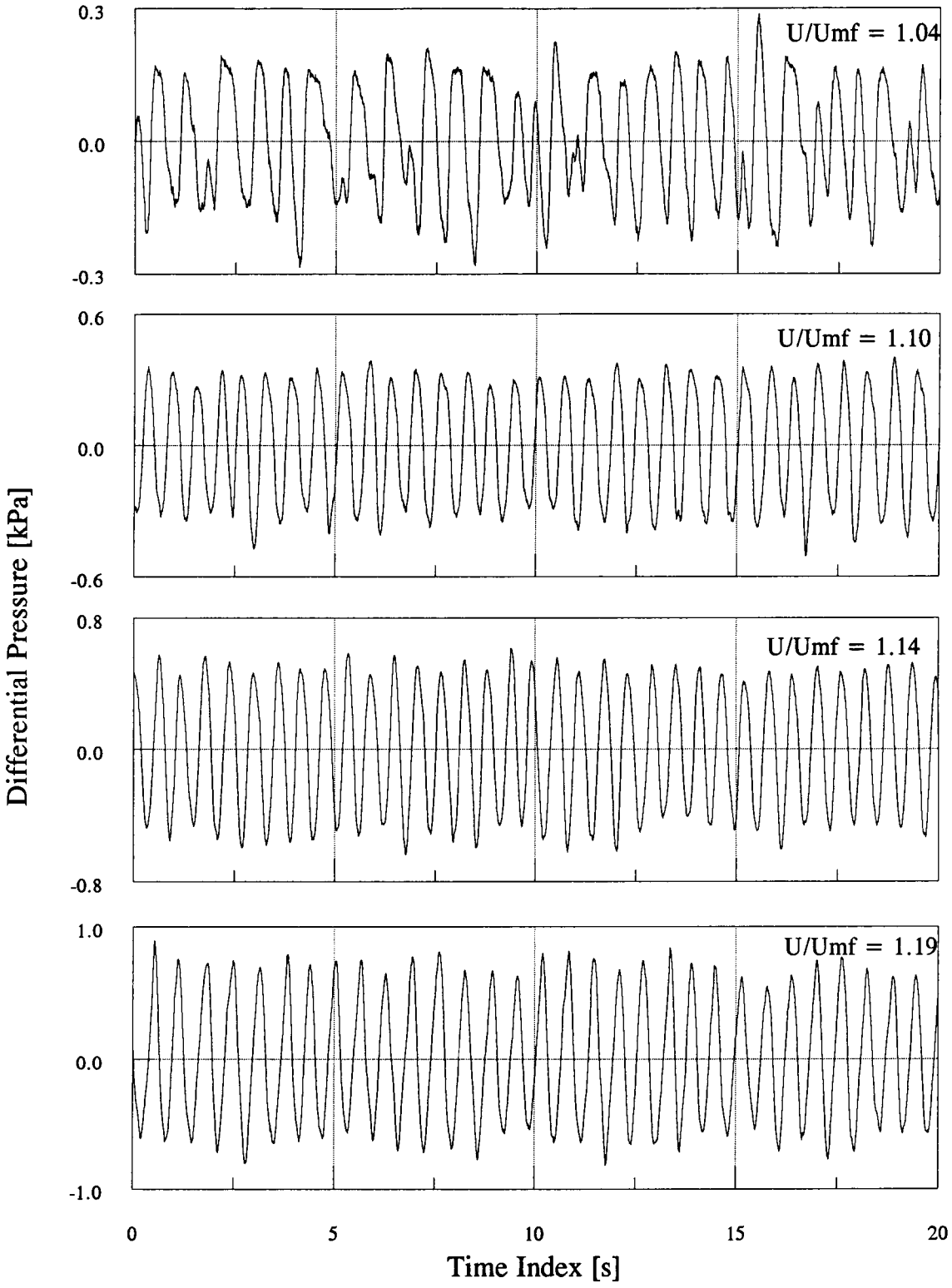


Figure B10. Typical time series segments of local pressure signal for glass over a velocity range of U/Umf = 1.04 to 1.19.

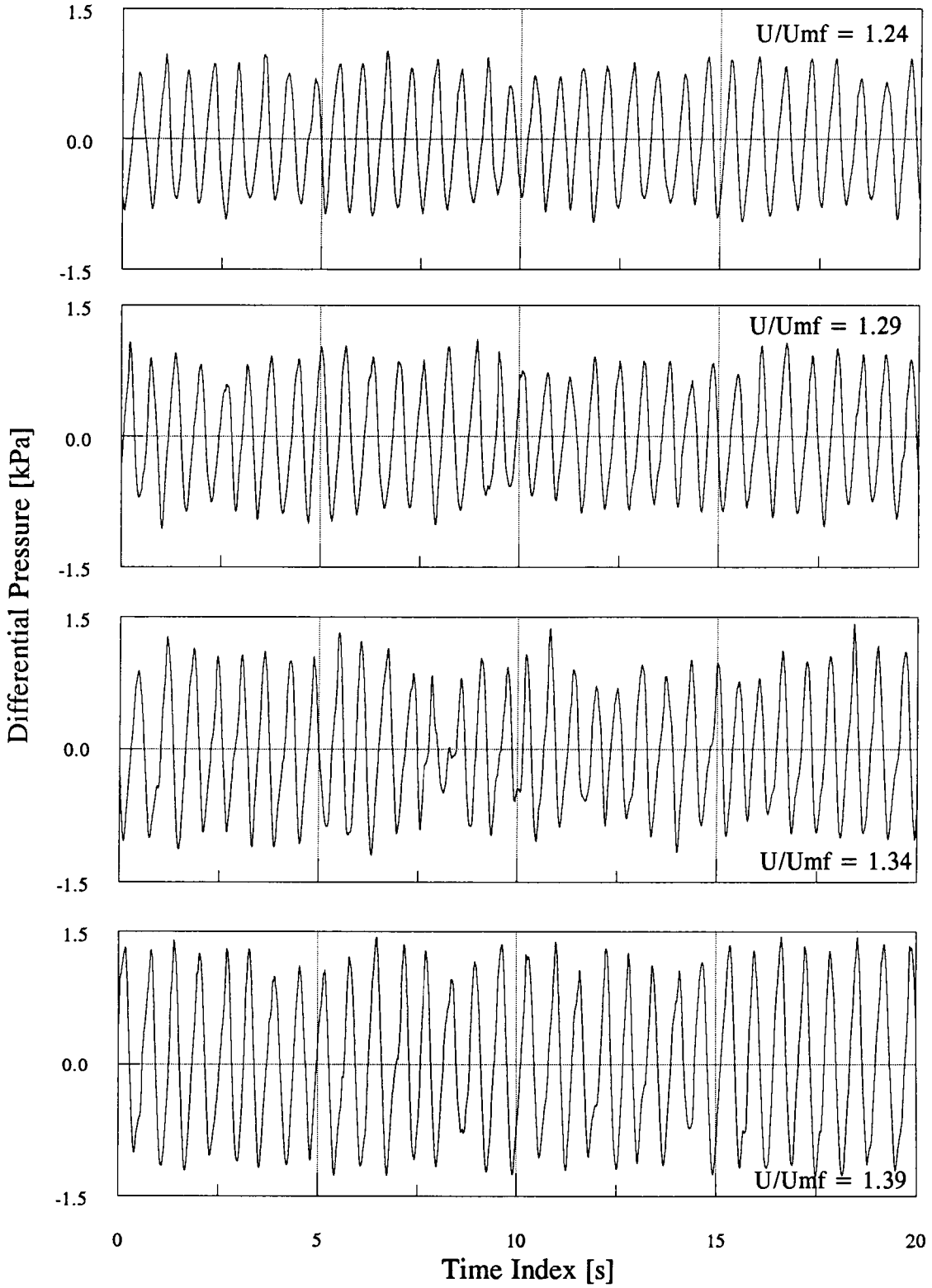


Figure B11. Typical time series segments of local pressure signal for glass over a velocity range of U/Umf = 1.24 to 1.39.

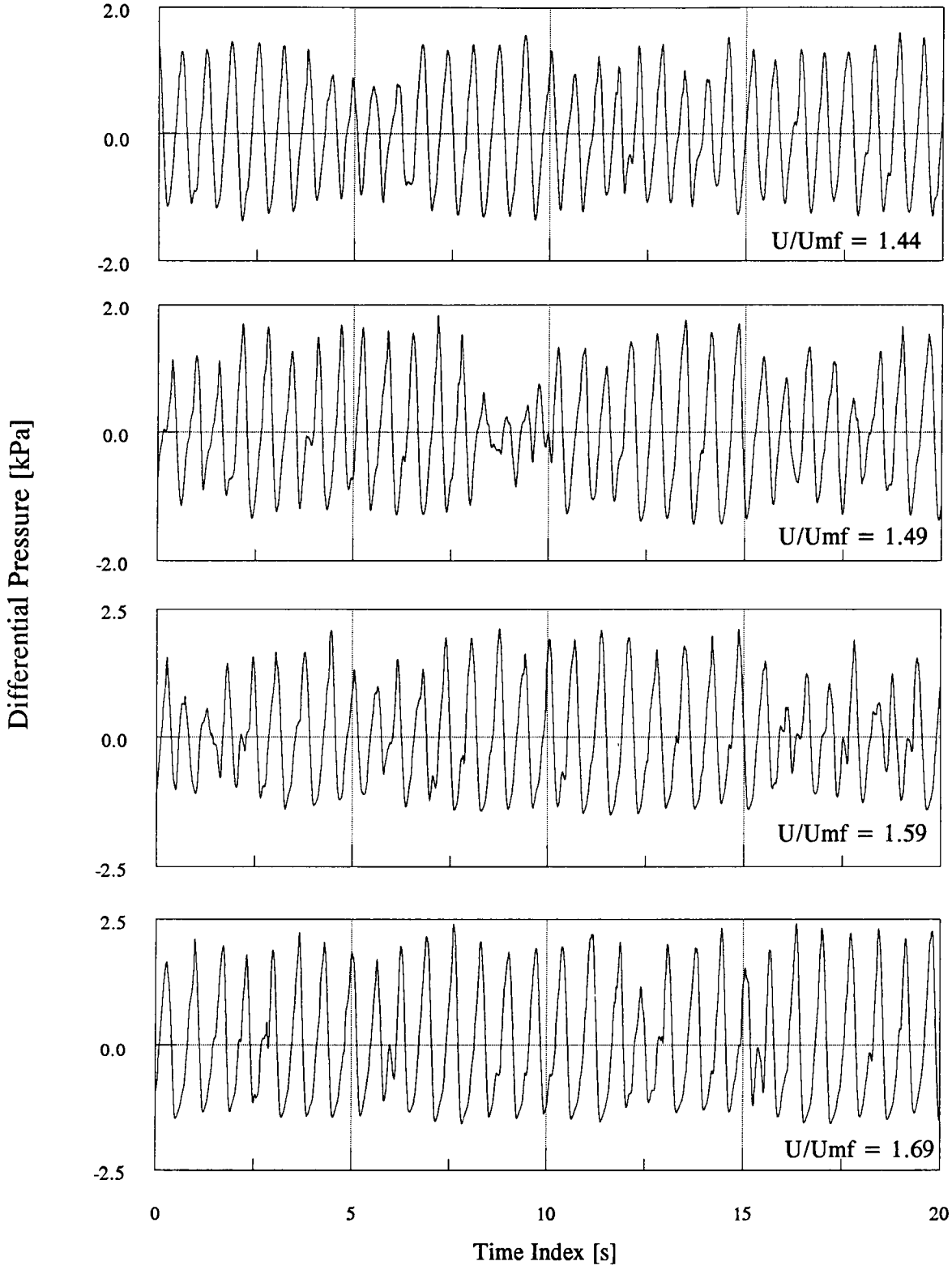


Figure B12. Typical time series segments of local pressure signal for glass over a velocity range of U/Umf = 1.44 to 1.69.

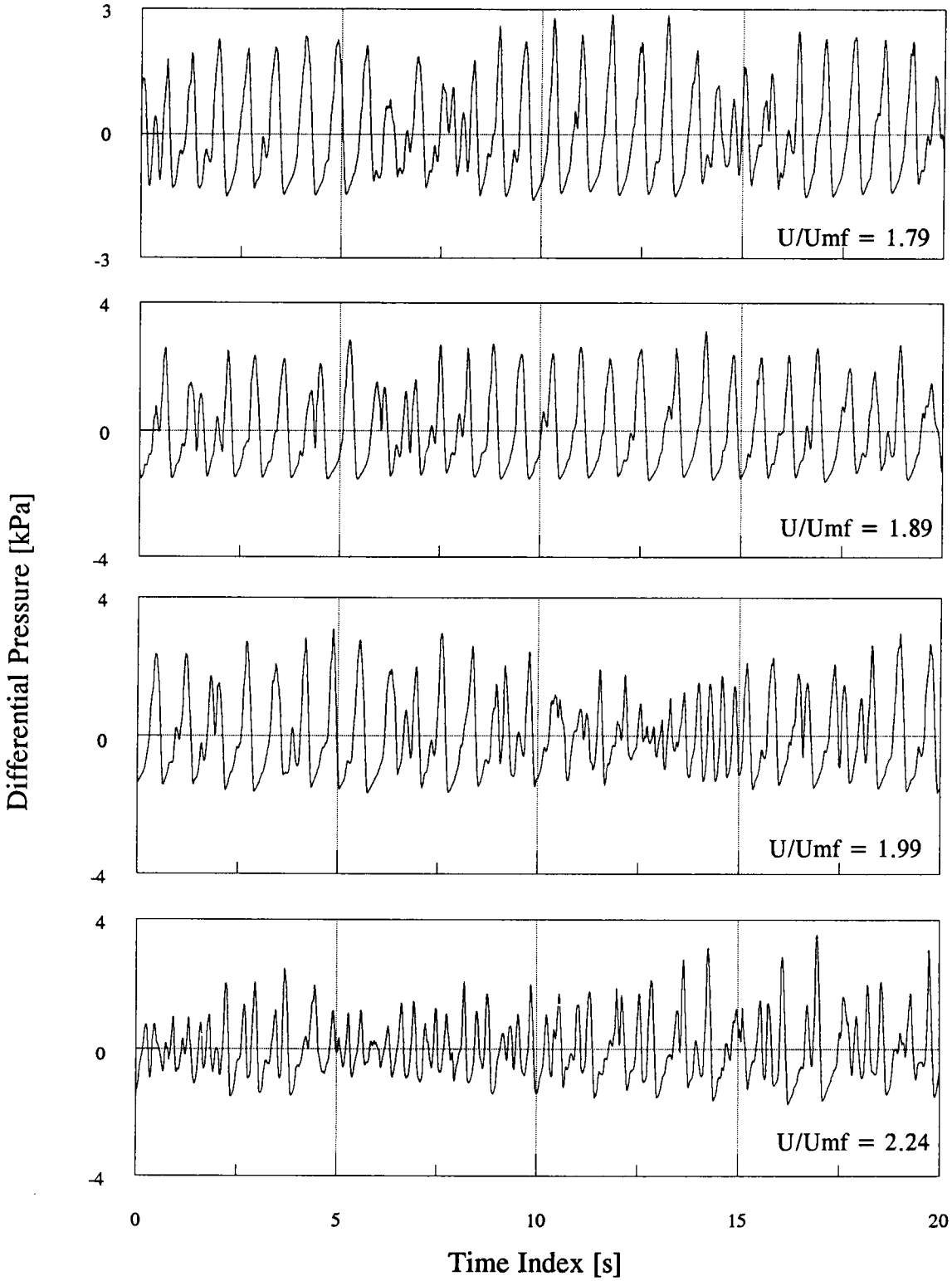


Figure B13. Typical time series segments of local pressure signal for glass over a velocity range of U/Umf = 1.79 to 2.24.

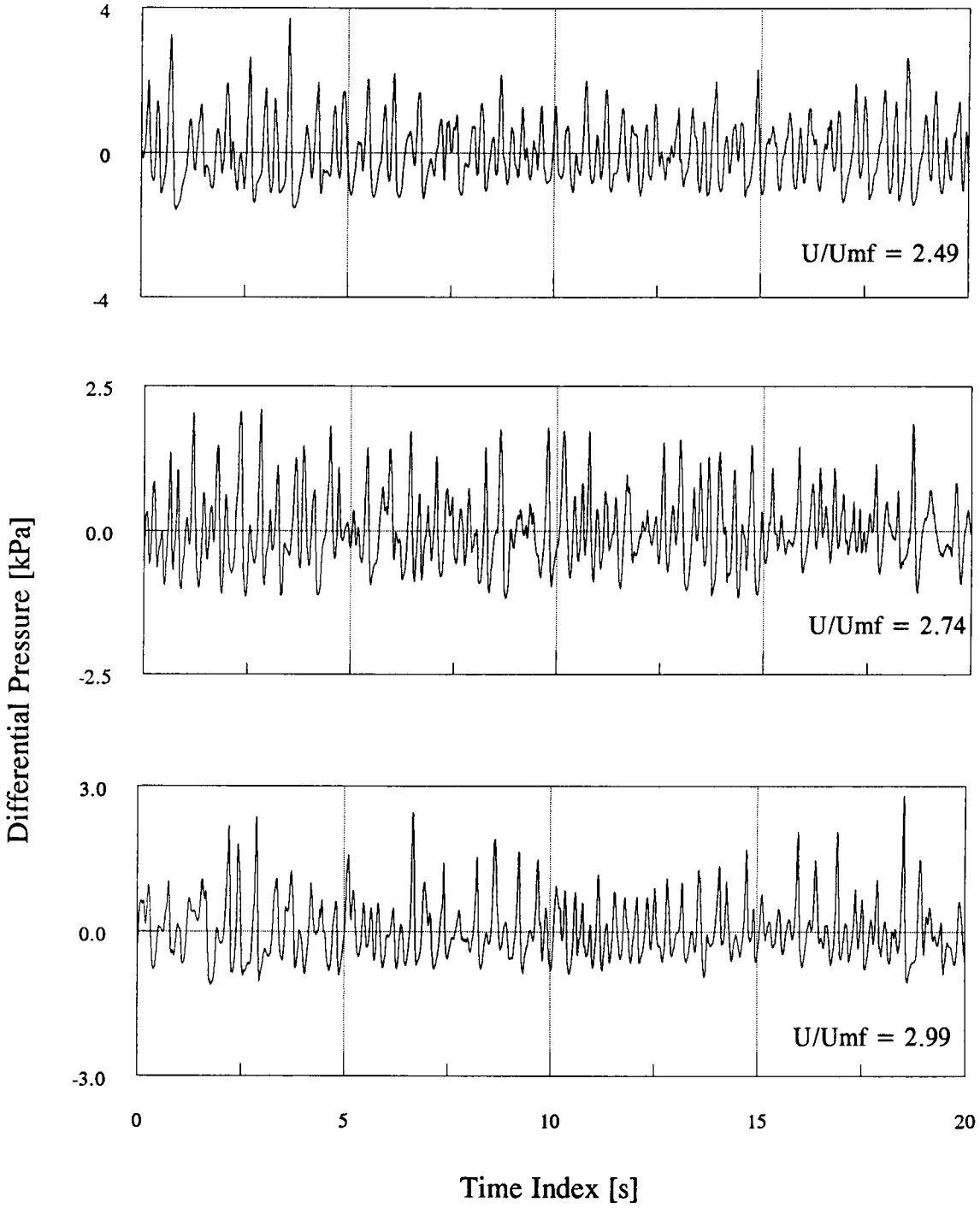


Figure B14. Typical time series segments of local pressure signal for glass over a velocity range of U/Umf = 2.49 to 2.99.

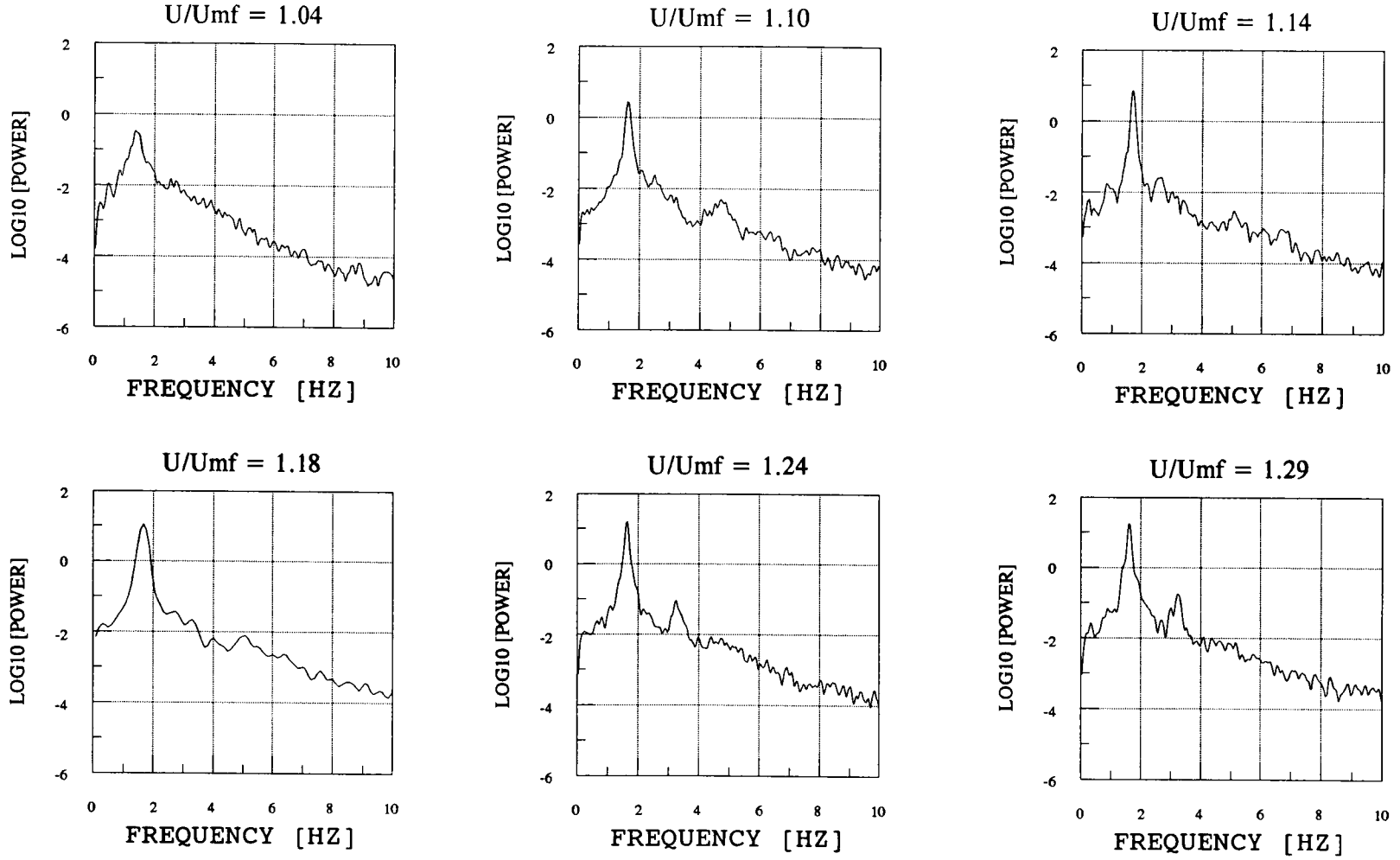


Figure B15. Fourier power spectra of local pressure signal for glass over a velocity range of U/Umf = 1.04 to 1.29.

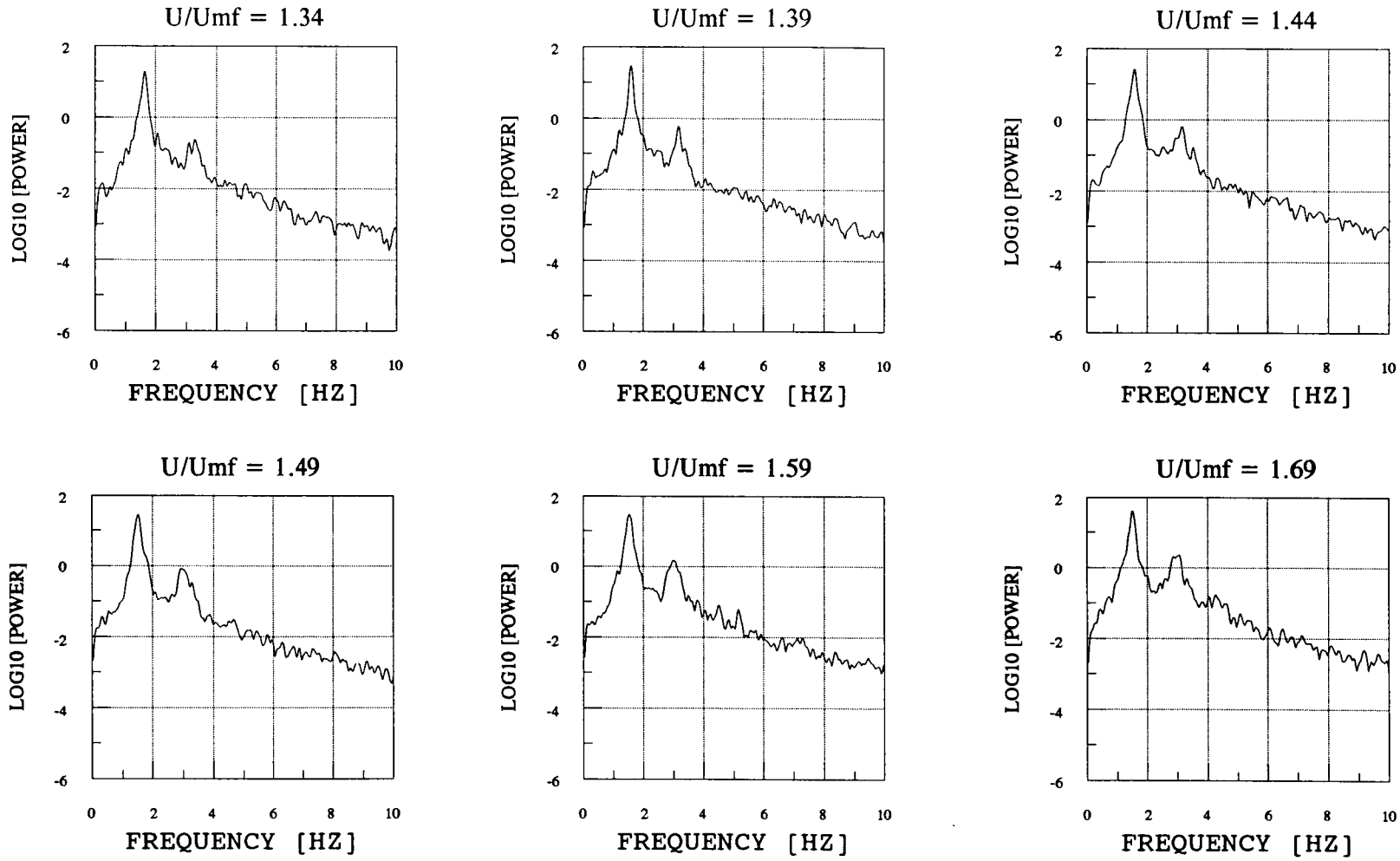


Figure B16. Fourier power spectra of local pressure signal for glass over a velocity range of U/Umf = 1.34 to 1.69.

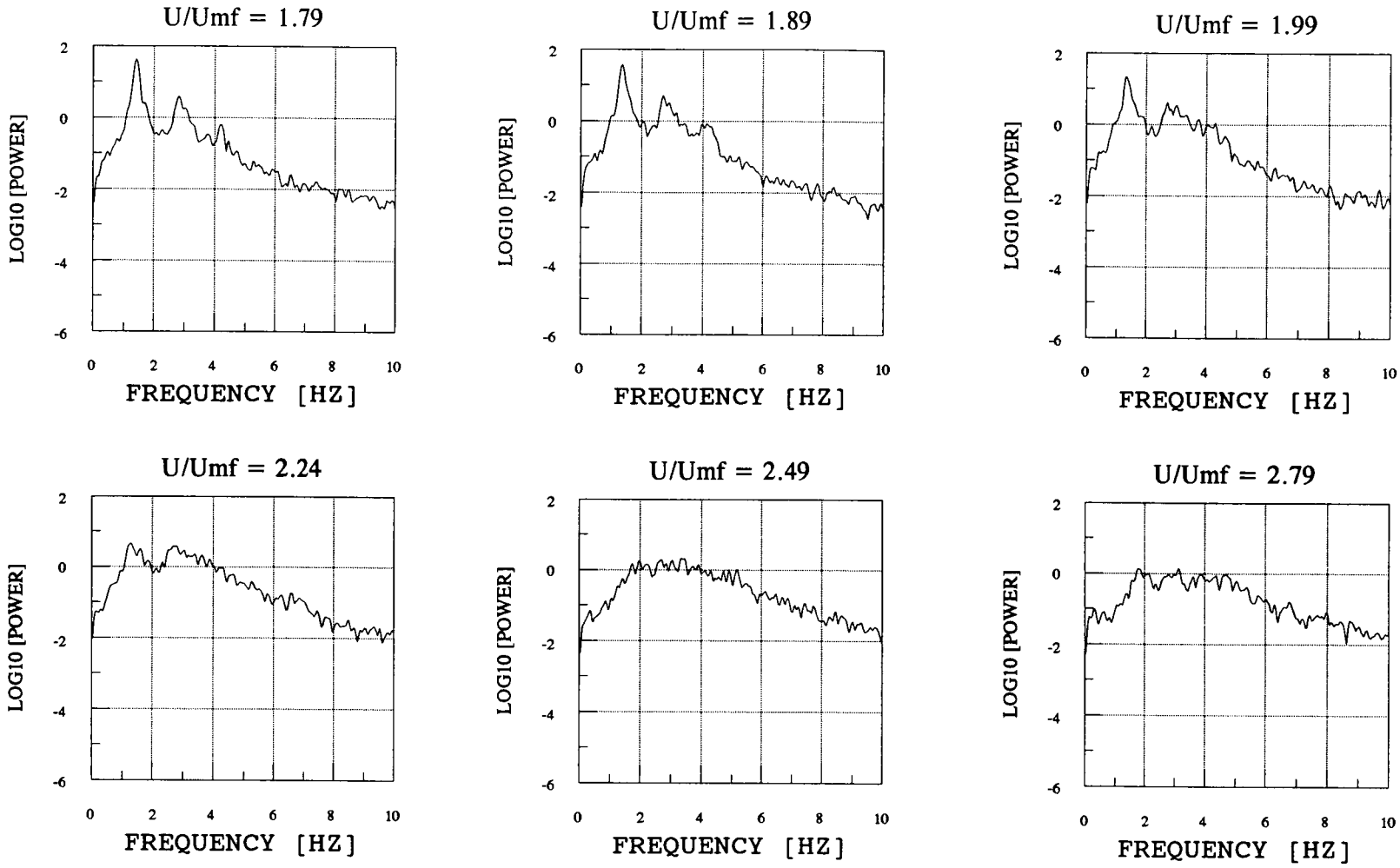


Figure B17. Fourier power spectra of local pressure signal for glass over a velocity range of U/Umf = 1.79 to 2.74.

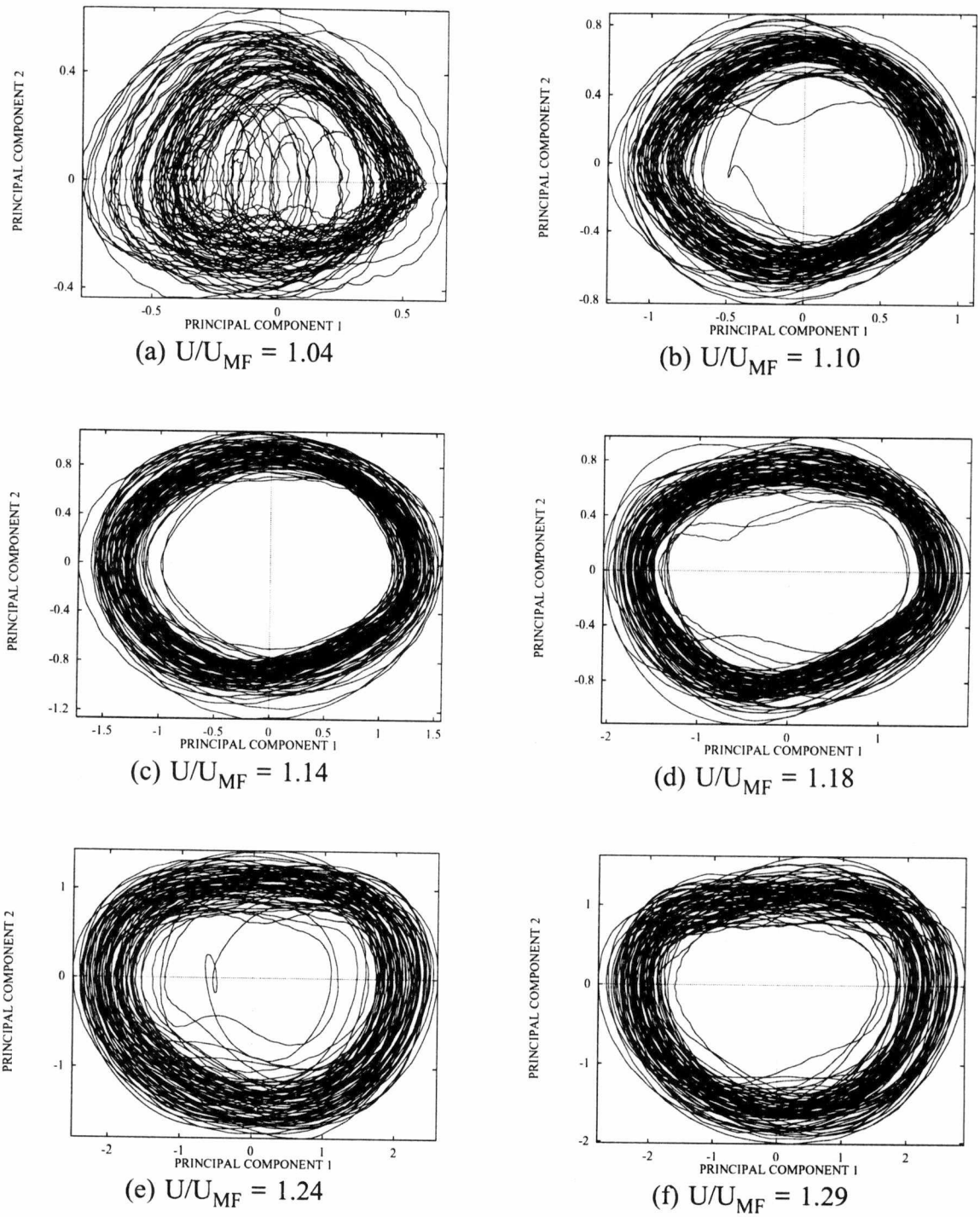
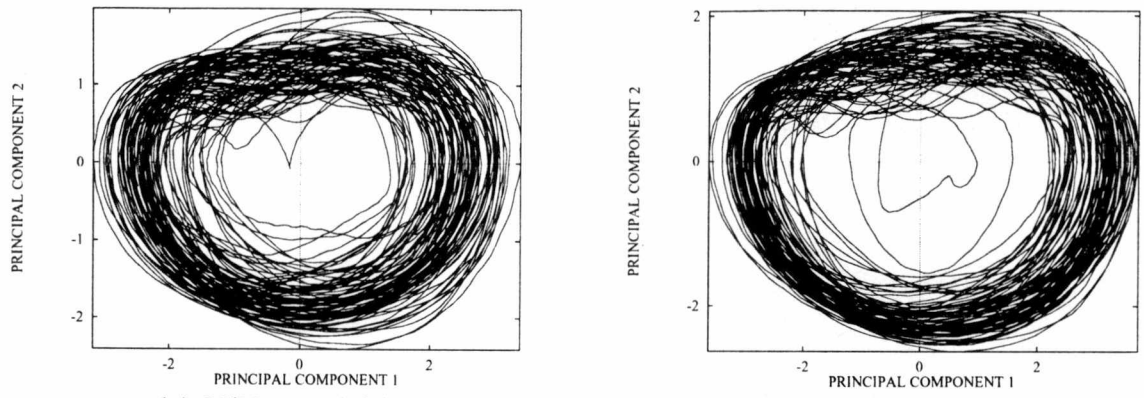
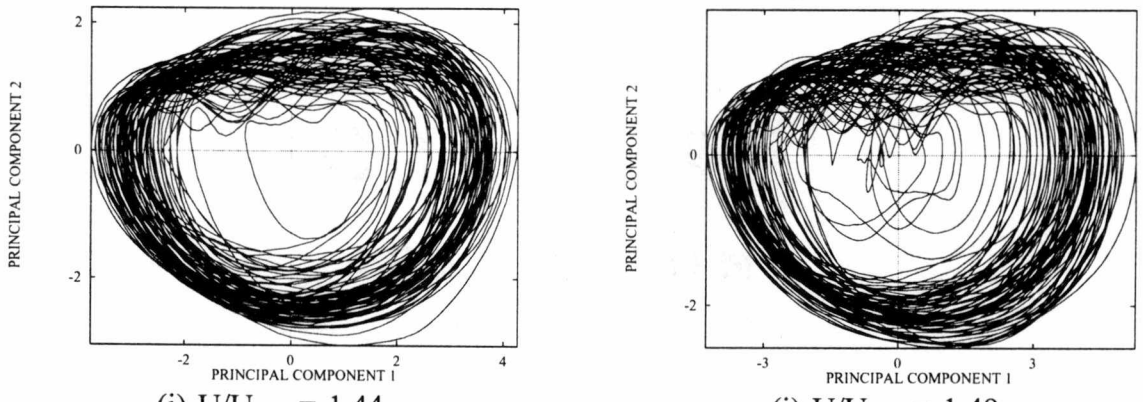


Figure B18. Two dimensional projection of reconstructed trajectories from local pressure signal for glass over a velocity range of U/U$_{MF}$ = 1.04 to 1.29 [Time span = 50 s].



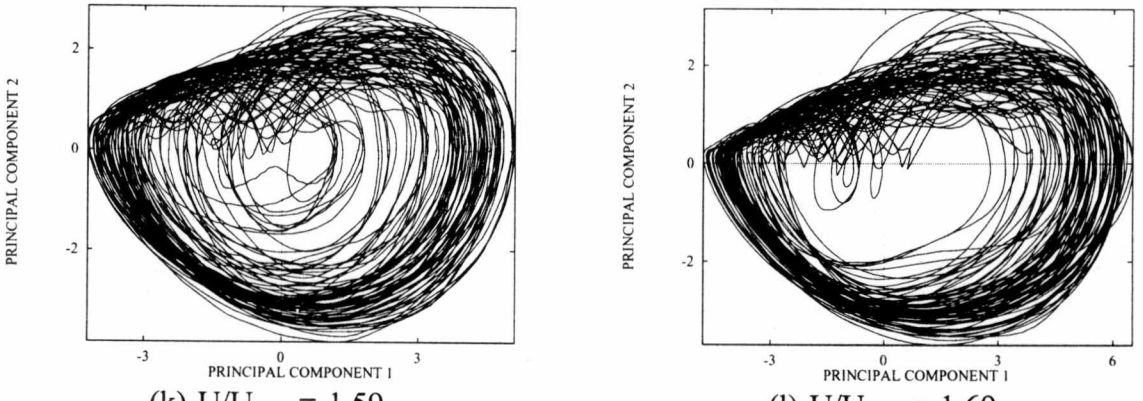
(g) U/U_{MF} = 1.34

(h) U/U_{MF} = 1.39



(i) U/U_{MF} = 1.44

(j) U/U_{MF} = 1.49



(k) U/U_{MF} = 1.59

(l) U/U_{MF} = 1.69

Figure B19. Two dimensional projection of reconstructed trajectories from local pressure signal for glass over a velocity range of U/U_{MF} = 1.34 to 1.69 [Time span = 50 s].

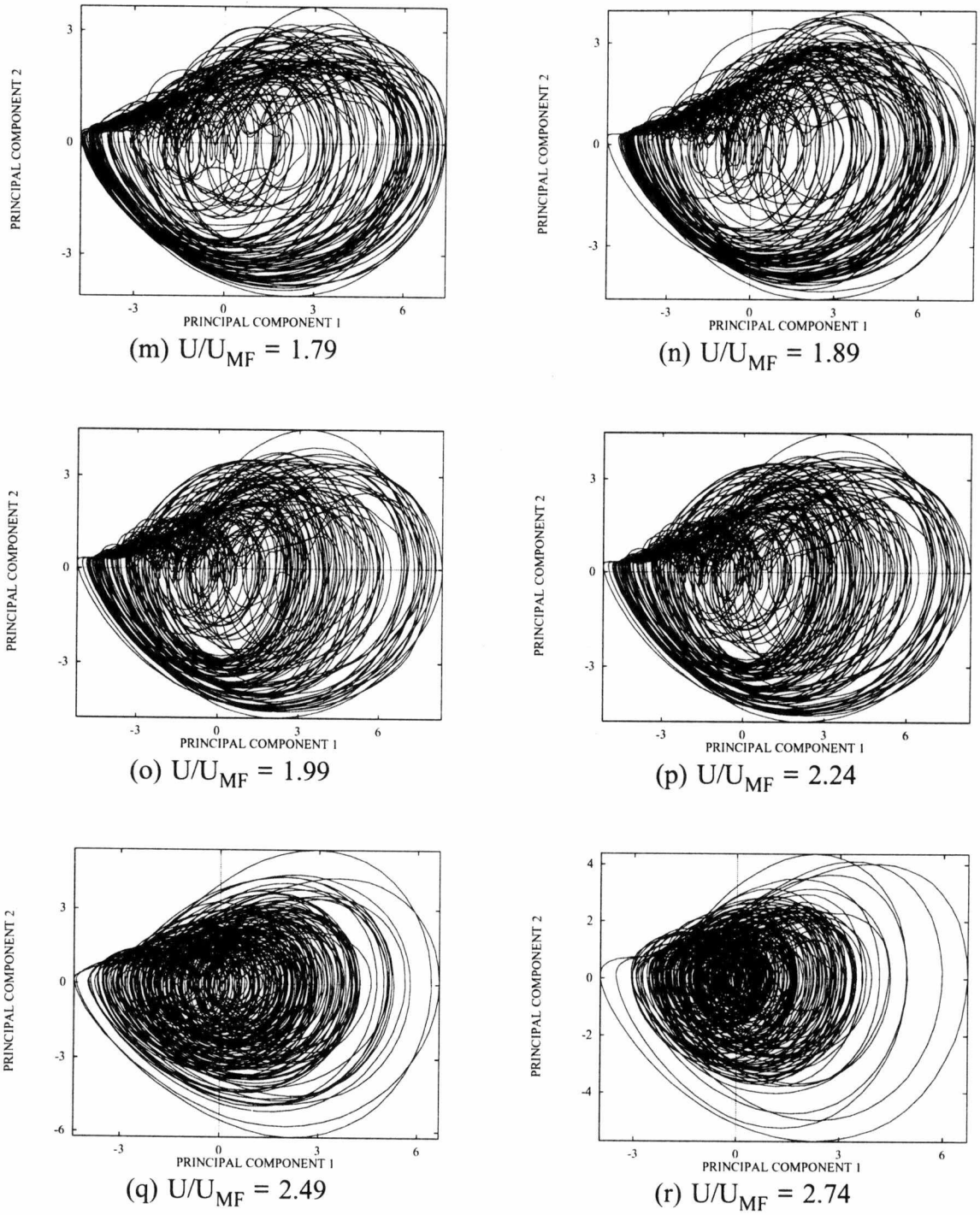
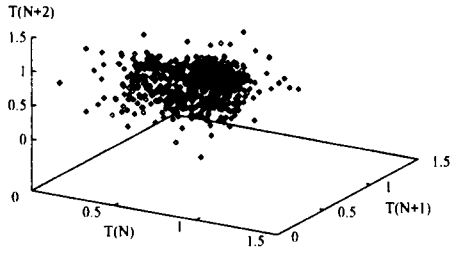
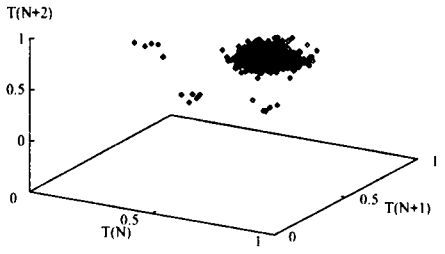


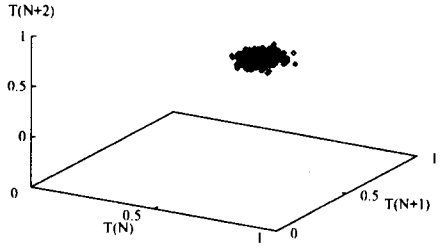
Figure B20. Two dimensional projection of reconstructed trajectories from local pressure signal for glass over a velocity range of U/U_{MF} = 1.79 to 2.74 [Time span = 50 s].



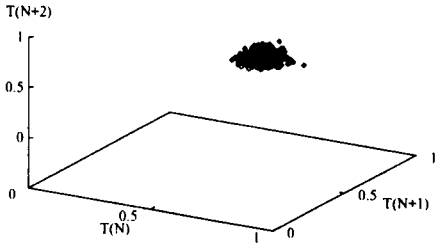
(a) U/U_{MF} = 1.04



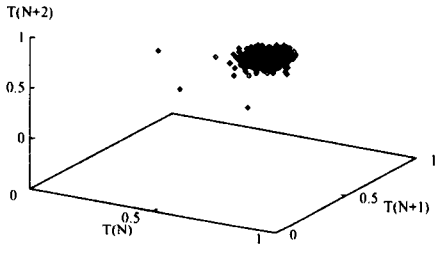
(b) U/U_{MF} = 1.10



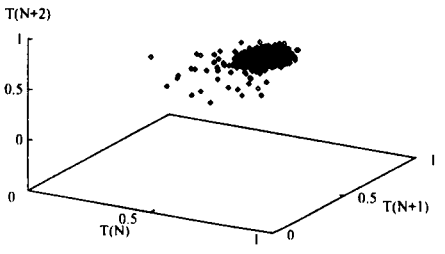
(c) U/U_{MF} = 1.14



(d) U/U_{MF} = 1.18

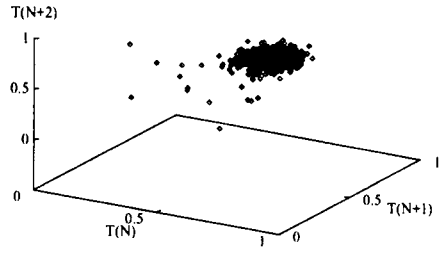


(e) U/U_{MF} = 1.24

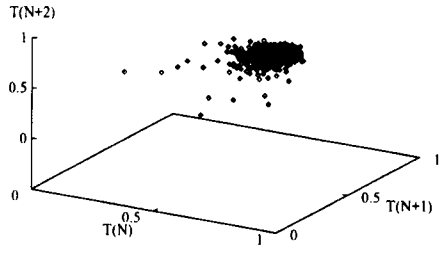


(f) U/U_{MF} = 1.29

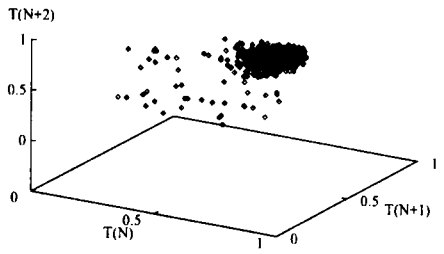
Figure B21. Time return maps using local pressure signal for glass over a velocity range of U/U_{MF} = 1.04 to 1.29.



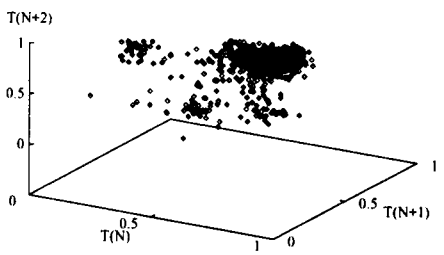
(g) U/U_{MF} = 1.34



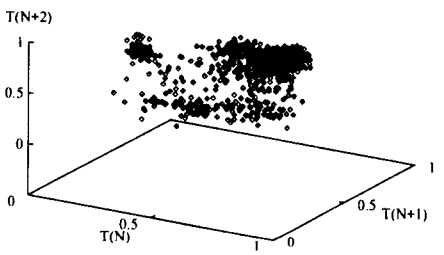
(h) U/U_{MF} = 1.39



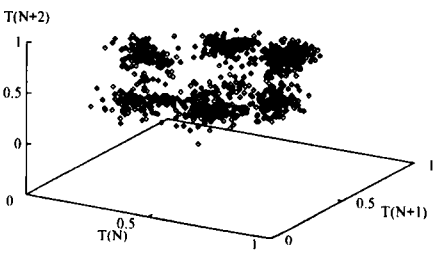
(i) U/U_{MF} = 1.44



(j) U/U_{MF} = 1.49

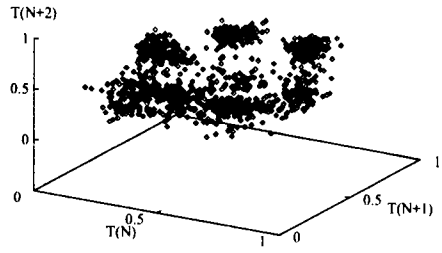


(k) U/U_{MF} = 1.59

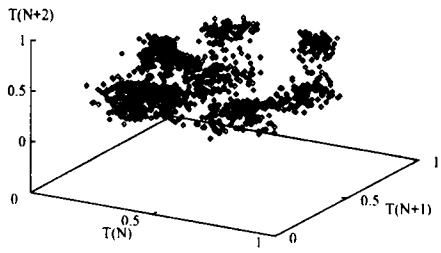


(l) U/U_{MF} = 1.69

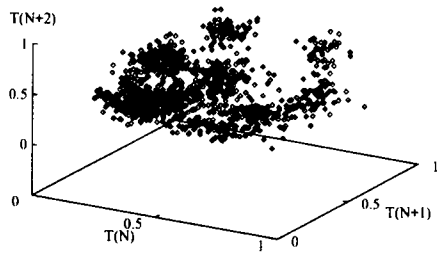
Figure B22. Time return maps using local pressure signal for glass over a velocity range of U/U_{MF} = 1.34 to 1.69.



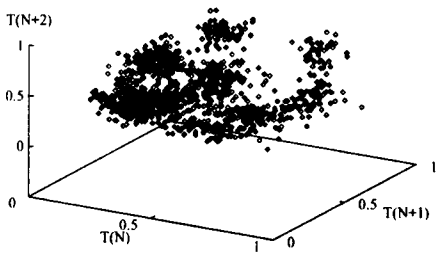
(m) U/U_{MF} = 1.79



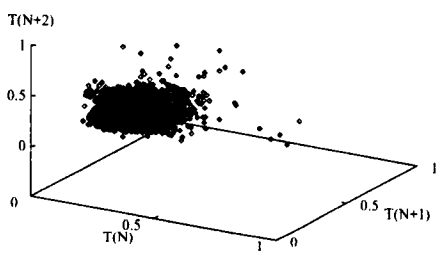
(n) U/U_{MF} = 1.89



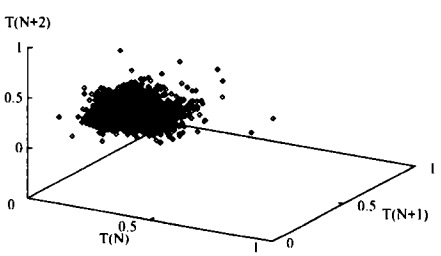
(o) U/U_{MF} = 1.99



(p) U/U_{MF} = 2.24



(q) U/U_{MF} = 2.49



(r) U/U_{MF} = 2.74

Figure B23. Time return maps using local pressure signal for glass over a velocity range of U/U_{MF} = 1.79 to 2.74.

Table B1. Dimension results based on the local signal for slugging characterization experiments using steel over a velocity range of U/U_{MF} = 1.07 to 2.07.

U/Umf	REPLI -CATE	CUT OFF [kPa]	SEGMENT LENGTH	DIMENSION [95 pct CI]
1.07	A	0.41629	127.0	4.60 ± 0.12
1.11	A	0.68663	130.4	4.11 ± 0.07
1.11	B	0.68577	129.9	4.05 ± 0.07
1.16	A	0.99570	130.2	3.47 ± 0.06
1.16	B	1.02255	128.1	3.44 ± 0.05
1.20	A	1.41181	129.4	2.75 ± 0.07
1.20	B	1.43500	129.8	2.68 ± 0.05
1.28	A	1.92022	135.3	1.88 ± 0.03
1.28	B	1.91955	135.8	1.88 ± 0.04
1.40	A	2.20251	141.6	2.69 ± 0.06
1.40	B	2.19058	143.7	2.76 ± 0.04
1.55	A	2.55693	143.8	3.60 ± 0.08
1.55	B	2.56358	148.7	3.59 ± 0.06
1.68	A	2.72854	137.4	4.06 ± 0.07
1.68	B	2.77197	137.2	4.01 ± 0.07
1.80	A	2.88124	128.5	4.08 ± 0.06
1.80	B	2.90488	129.3	4.08 ± 0.08
1.94	A	3.08231	117.0	3.88 ± 0.06
1.94	B	3.03133	113.3	3.75 ± 0.08
2.07	A	3.08433	109.3	3.58 ± 0.08
2.07	B	3.06232	109.1	3.73 ± 0.08

Table B2. Dimension results based on the local signal for slugging characterization experiments using glass over a velocity range of U/U_{MF} = 1.04 to 1.99.

U/Umf	REPLI -CATE	CUT OFF [kPa]	SEGMENT LENGTH	DML [95 pct CI]
1.04	A	0.11843	125.9	3.89 ± 0.06
1.04	B	0.12079	130.9	3.87 ± 0.05
1.10	A	0.22407	123.5	2.80 ± 0.06
1.10	B	0.22087	123.9	2.87 ± 0.07
1.14	A	0.32565	118.2	2.38 ± 0.05
1.14	B	0.32244	117.9	2.43 ± 0.06
1.18	A	0.36143	119.9	2.26 ± 0.04
1.18	B	0.35618	120.2	2.26 ± 0.04
1.24	A	0.47767	122.8	2.77 ± 0.07
1.24	B	0.47772	122.7	2.69 ± 0.06
1.29	A	0.52508	121.9	2.84 ± 0.05
1.29	B	0.52938	122.7	2.98 ± 0.06
1.34	A	0.59328	122.2	3.24 ± 0.05
1.34	B	0.60755	122.8	3.15 ± 0.07
1.39	A	0.66053	123.9	3.27 ± 0.07
1.39	B	0.67907	124.5	2.93 ± 0.08
1.44	A	0.71404	124.2	3.22 ± 0.08
1.44	B	0.72808	126.1	3.23 ± 0.08
1.49	A	0.75743	123.4	3.37 ± 0.06
1.49	B	0.74563	123.9	3.43 ± 0.07
1.59	A	0.81617	116.2	3.63 ± 0.08
1.59	B	0.83369	119.1	3.51 ± 0.07
1.69	A	0.92472	116.9	3.45 ± 0.07
1.69	B	0.91590	113.6	3.46 ± 0.08
1.79	A	0.98878	111.2	3.55 ± 0.06
1.79	B	0.96993	108.1	3.48 ± 0.08
1.89	A	0.98197	99.2	3.61 ± 0.08
1.89	B	1.00680	101.6	3.58 ± 0.07
1.99	A	0.97029	89.5	3.63 ± 0.07
1.99	B	0.97296	91.1	3.56 ± 0.08

Table B3. Entropy results based on the local signal for slugging characterization experiments using steel over a velocity range of U/U_{MF} = 1.07 to 2.07.

U/Umf	REPLI -CATE	CUT OFF [kPa]	SEGMENT LENGTH	ENTROPY [BIT/S] [95 Pct CI]
1.07	A	0.4163	127.0	8.28 ± 1.68
1.07	B	0.3826	119.8	6.66 ± 1.18
1.11	A	0.6866	130.4	8.13 ± 0.75
1.11	B	0.6858	129.9	9.30 ± 1.03
1.16	A	0.9957	130.2	7.38 ± 0.95
1.16	B	1.0225	128.1	8.49 ± 0.96
1.20	A	1.4118	129.4	6.27 ± 0.94
1.20	B	1.4350	129.8	6.08 ± 1.00
1.28	A	1.9202	135.3	4.26 ± 0.89
1.28	B	1.9196	135.8	4.01 ± 0.87
1.40	A	2.2025	141.6	4.06 ± 0.77
1.40	B	2.1906	143.7	4.85 ± 0.68
1.55	A	2.5569	143.8	5.64 ± 0.57
1.55	B	2.5636	148.7	6.25 ± 0.59
1.68	A	2.7285	137.4	7.02 ± 0.93
1.68	B	2.7720	137.2	7.25 ± 0.76
1.80	A	2.8812	128.5	7.36 ± 1.19
1.80	B	2.9049	129.3	8.61 ± 1.22
1.94	A	3.0823	117.0	7.57 ± 1.27
1.94	B	3.0313	113.3	8.27 ± 1.27
2.07	A	3.0843	109.3	9.18 ± 1.70
2.07	B	3.0623	109.1	9.64 ± 1.26

Table B4. Entropy results based on the local signal for slugging characterization experiments using glass over a velocity range of U/U_{MF} = 1.04 to 1.99.

U/Umf	REPLI -CATE	CUT OFF [kPa]	SEGMENT LENGTH	ENTROPY [BIT/S] [95 Pct CI]
1.04	A	0.1184	125.9	4.08 ± 0.15
1.04	B	0.1208	130.9	3.75 ± 0.11
1.10	A	0.2241	123.5	1.87 ± 0.12
1.10	B	0.2209	123.9	1.98 ± 0.10
1.14	A	0.3256	118.2	1.04 ± 0.06
1.14	B	0.3224	117.9	1.15 ± 0.07
1.18	A	0.3614	119.9	1.04 ± 0.08
1.18	B	0.3562	120.2	0.96 ± 0.09
1.24	A	0.4777	122.8	1.39 ± 0.11
1.24	B	0.4777	122.7	1.43 ± 0.11
1.29	A	0.5251	121.9	1.58 ± 0.11
1.29	B	0.5294	122.7	1.67 ± 0.10
1.34	A	0.5933	122.2	1.93 ± 0.13
1.34	B	0.6075	122.8	1.83 ± 0.09
1.39	A	0.6605	123.9	1.99 ± 0.08
1.39	B	0.6791	124.5	1.59 ± 0.07
1.44	A	0.7140	124.2	2.01 ± 0.10
1.44	B	0.7281	126.1	1.88 ± 0.10
1.49	A	0.7574	123.4	2.32 ± 0.14
1.49	B	0.7456	123.9	2.00 ± 0.13
1.59	A	0.8162	116.2	2.71 ± 0.12
1.59	B	0.8337	119.1	2.66 ± 0.15
1.69	A	0.9247	116.9	2.69 ± 0.13
1.69	B	0.9159	113.6	2.89 ± 0.12
1.79	A	0.9888	111.2	2.95 ± 0.14
1.79	B	0.9699	108.1	3.25 ± 0.17
1.89	A	0.9820	99.2	4.06 ± 0.24
1.89	B	1.0068	101.6	3.59 ± 0.23
1.99	A	0.9703	89.5	5.38 ± 0.20
1.99	B	0.9730	91.1	5.30 ± 0.21

APPENDIX C

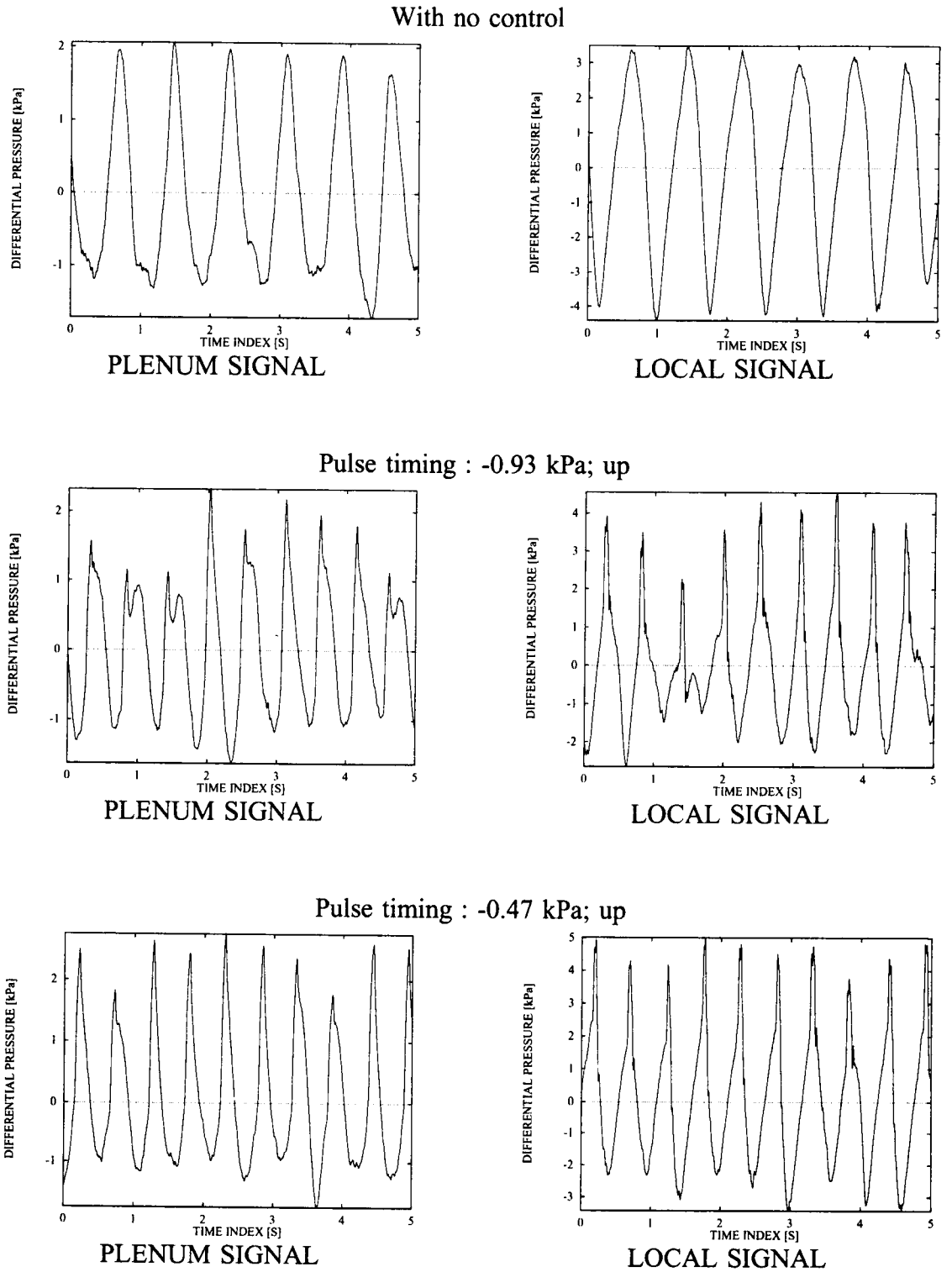


Figure C1. Typical time series segments for steel illustrating the effect of pulse timing at a velocity of U/Umf = 1.28, a fixed pulse width of 50 ms and over a range of pulse timing (No control to -0.47 kPa & up).

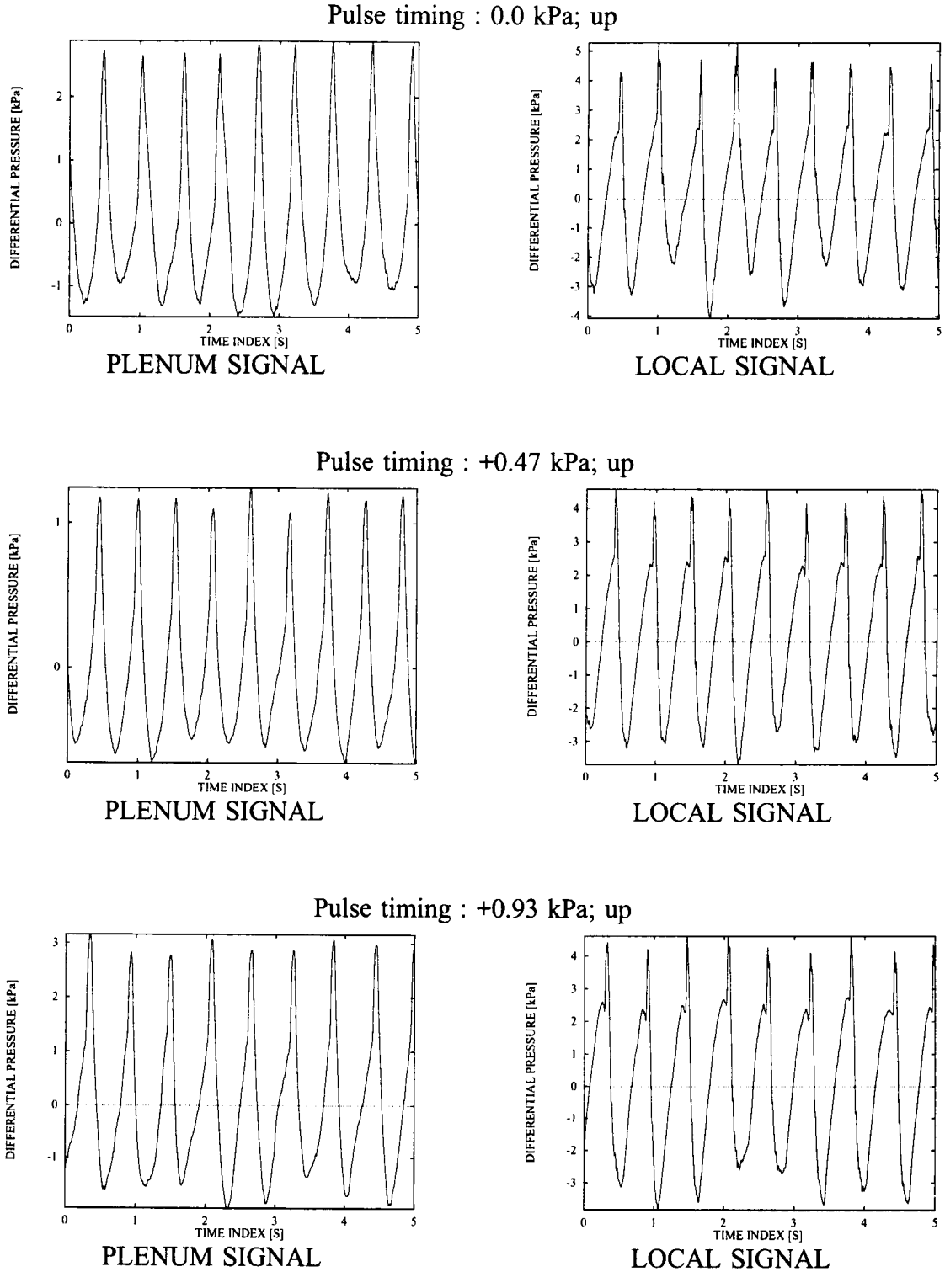


Figure C2. Typical time series segments for steel illustrating the effect of pulse timing at a velocity of U/Umf = 1.28, a fixed pulse width of 50 ms and over a range of pulse timing (0.0 kPa & up to +0.93 kPa & up).

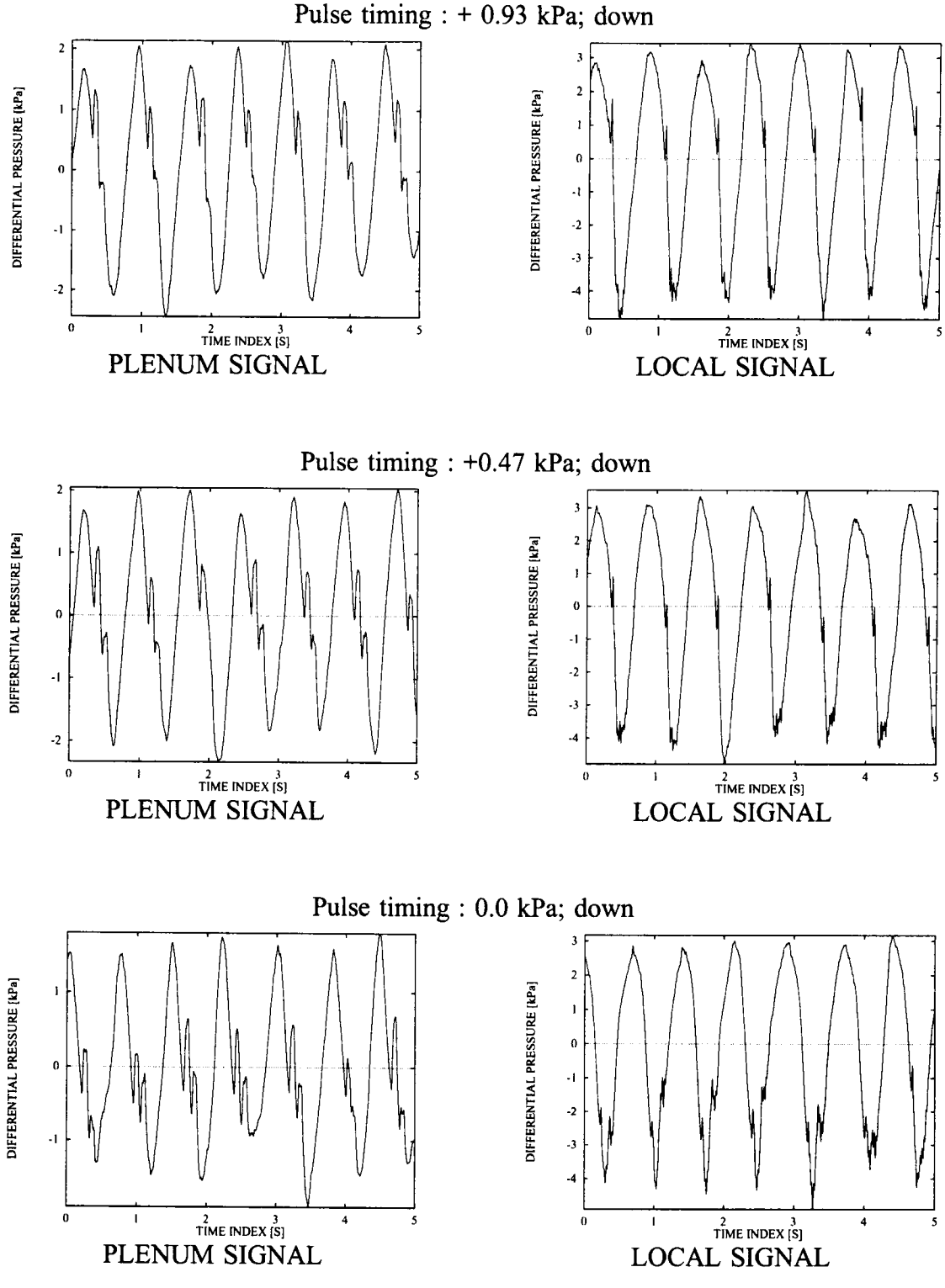


Figure C3. Typical time series segments for steel illustrating the effect of pulse timing at a velocity of U/Umf = 1.28, a fixed pulse width of 50 ms and over a range of pulse timing (+0.93 kPa & down to 0.0 kPa & down).

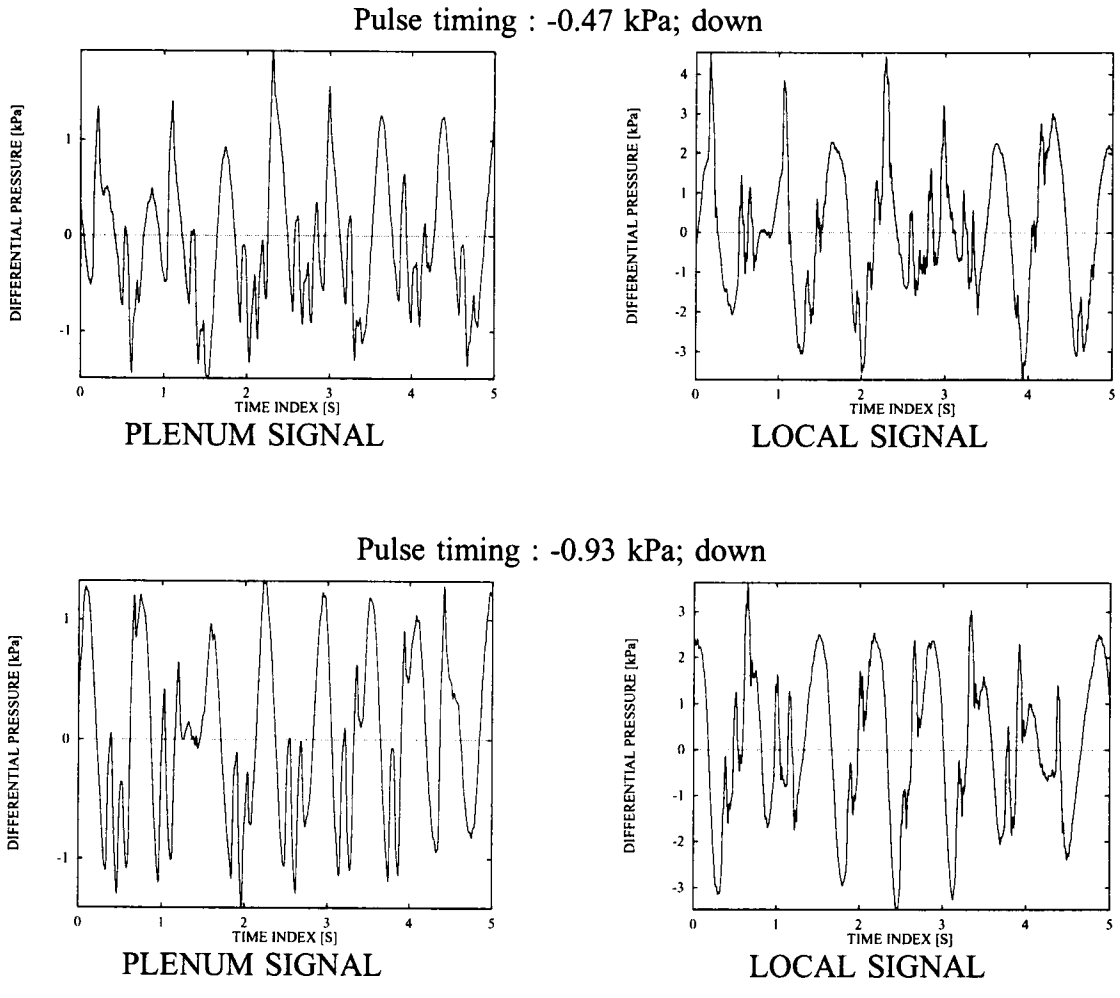
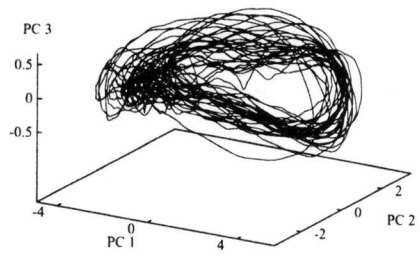
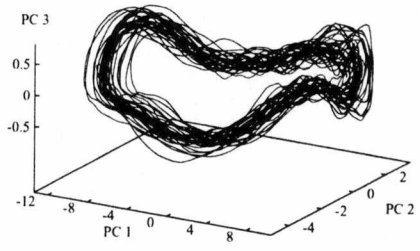


Figure C4. Typical time series segments for steel illustrating the effect of pulse timing at a velocity of U/Umf = 1.28, a fixed pulse width of 50 ms and over a range of pulse timing (-0.47 kPa & down to -0.93 kPa & down).

With no control

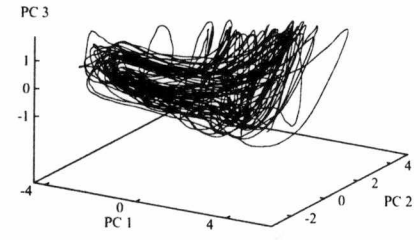


PLENUM SIGNAL

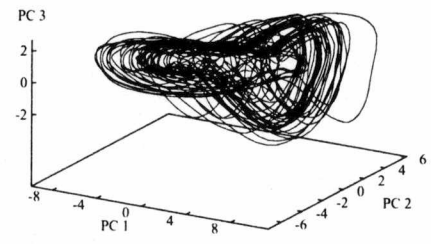


LOCAL SIGNAL

Pulse timing : -0.93 kPa; up

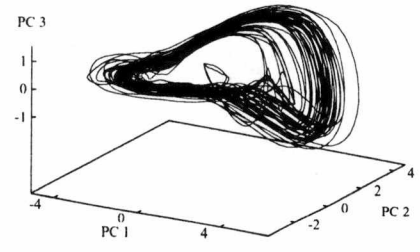


PLENUM SIGNAL

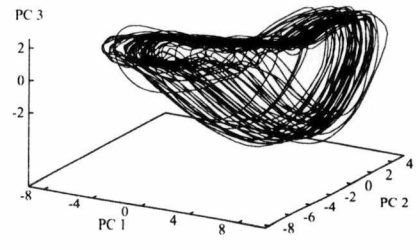


LOCAL SIGNAL

Pulse timing : -0.47 kPa; up



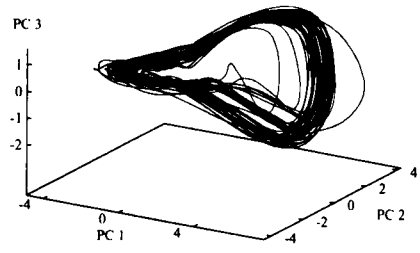
PLENUM SIGNAL



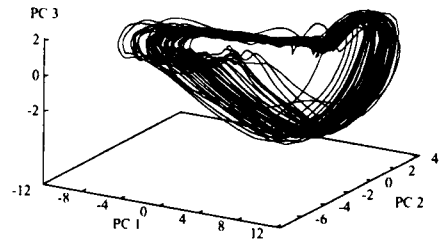
LOCAL SIGNAL

Figure C5. Three dimensional projection of the reconstructed trajectory for steel illustrating the effect of pulse timing at a velocity of U/Umf = 1.28, a fixed pulse width of 50 ms and over a range of pulse timing (No control to -0.47 kPa & up) [Time span = 25 s].

Pulse timing : 0.0 kPa; up

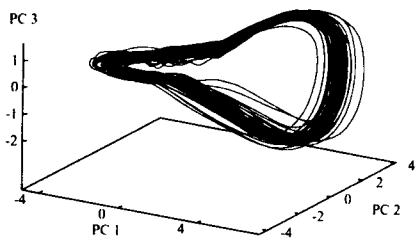


PLENUM SIGNAL

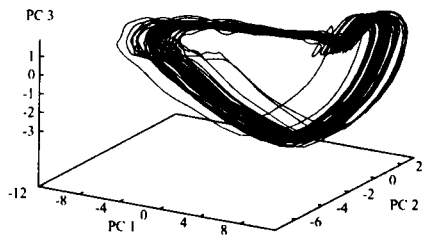


LOCAL SIGNAL

Pulse timing : +0.47 kPa; up

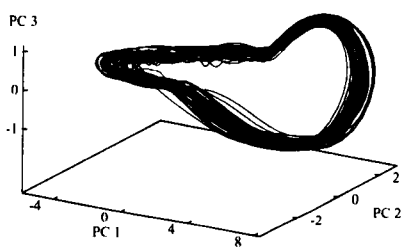


PLENUM SIGNAL

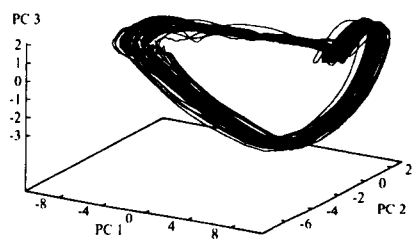


LOCAL SIGNAL

Pulse timing : +0.93 kPa; up



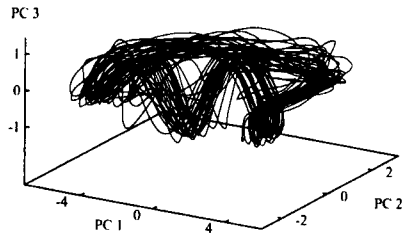
PLENUM SIGNAL



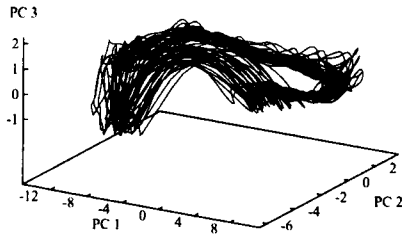
LOCAL SIGNAL

Figure C6. Three dimensional projection of the reconstructed trajectory for steel illustrating the effect of pulse timing at a velocity of U/Umf = 1.28, a fixed pulse width of 50 ms and over a range of pulse timing (0.0 kPa & up to +0.93 kPa & up) [Time span = 25 s].

Pulse timing : + 0.93 kPa; down

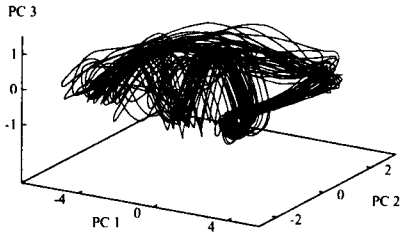


PLENUM SIGNAL

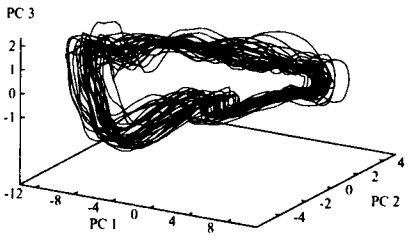


LOCAL SIGNAL

Pulse timing : +0.47 kPa; down

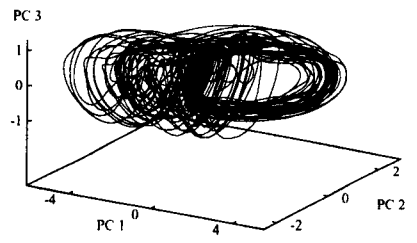


PLENUM SIGNAL

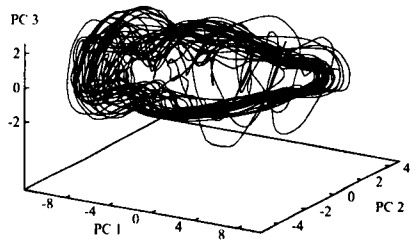


LOCAL SIGNAL

Pulse timing : 0.0 kPa; down



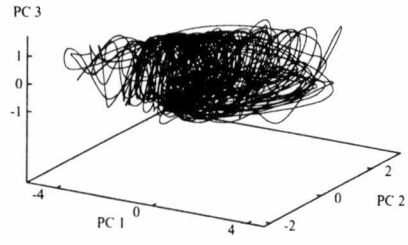
PLENUM SIGNAL



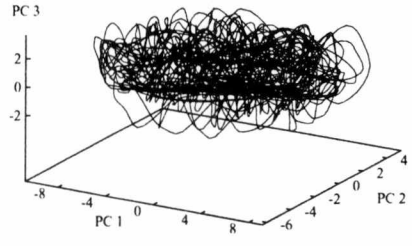
LOCAL SIGNAL

Figure C7. Three dimensional projection of the reconstructed trajectory for steel illustrating the effect of pulse timing at a velocity of U/Umf = 1.28, a fixed pulse width of 50 ms and over a range of pulse timing (+0.93 kPa & down to 0.0 kPa & down). [Time span = 25 s].

Pulse timing : -0.47 kPa; down

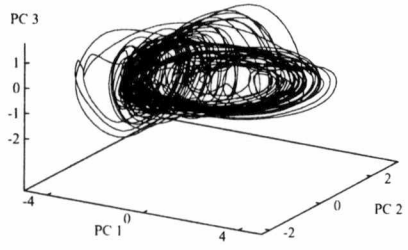


PLENUM SIGNAL

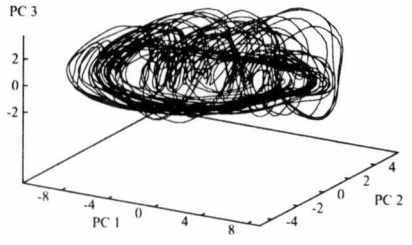


LOCAL SIGNAL

Pulse timing : -0.93 kPa; down



PLENUM SIGNAL



LOCAL SIGNAL

Figure C8. Three dimensional projection of the reconstructed trajectory for steel illustrating the effect of pulse timing at a velocity of U/Umf = 1.28, a fixed pulse width of 50 ms and over a range of pulse timing (-0.47 kPa & down to -0.93 kPa & down) [Time span = 25 s].

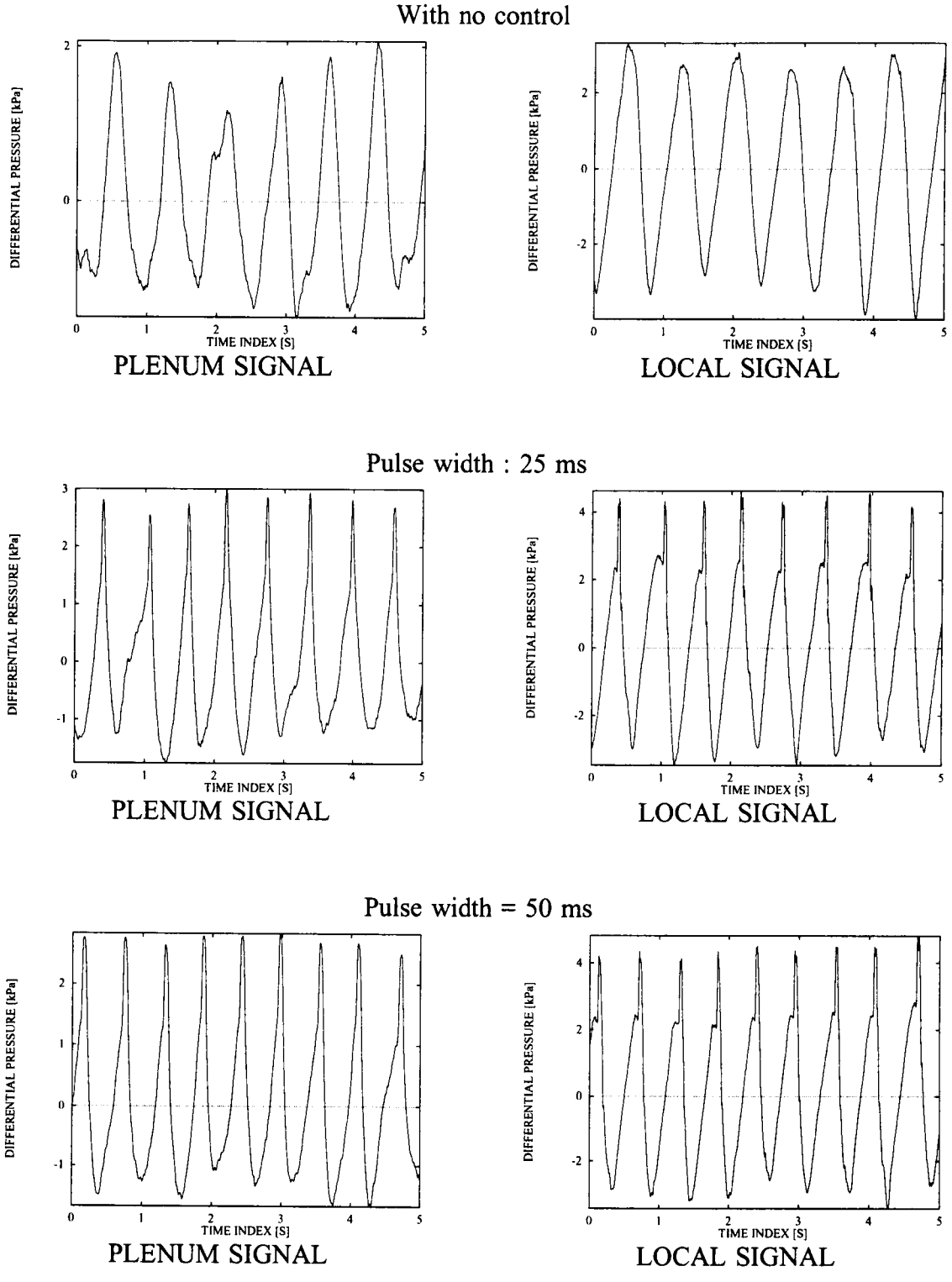


Figure C9. Typical time series segments for steel illustrating the effect of pulse width at a velocity of $U/U_{MF} = 1.28$, a fixed pulse timing of +0.93 kPa & up and over a range of pulse width (No control to 50 ms).

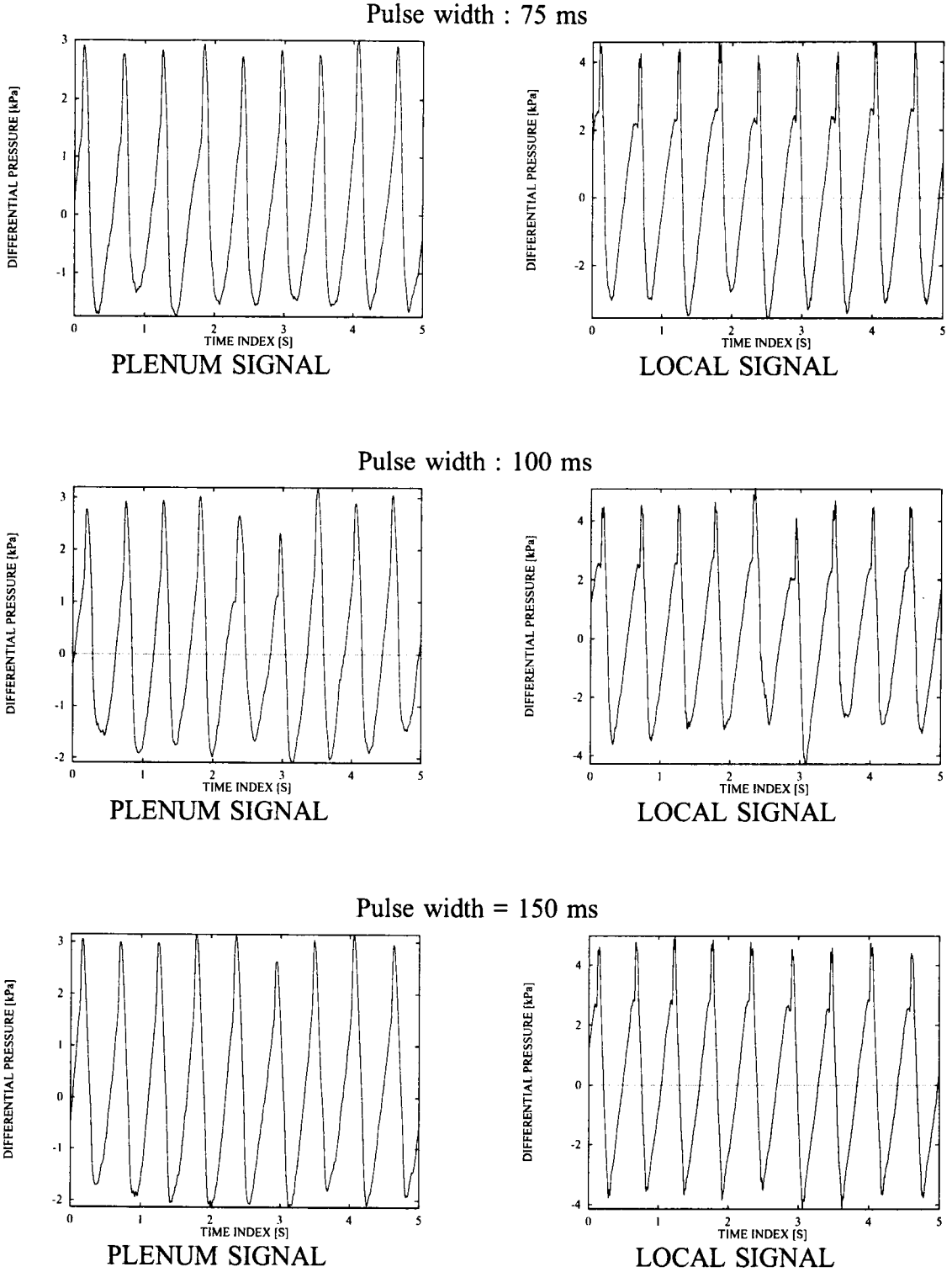


Figure C10. Typical time series segments for steel illustrating the effect of pulse width at a velocity of $U/U_{MF} = 1.28$, a fixed pulse timing of +0.93 kPa & up and over a range of pulse width (75 ms to 150 ms).

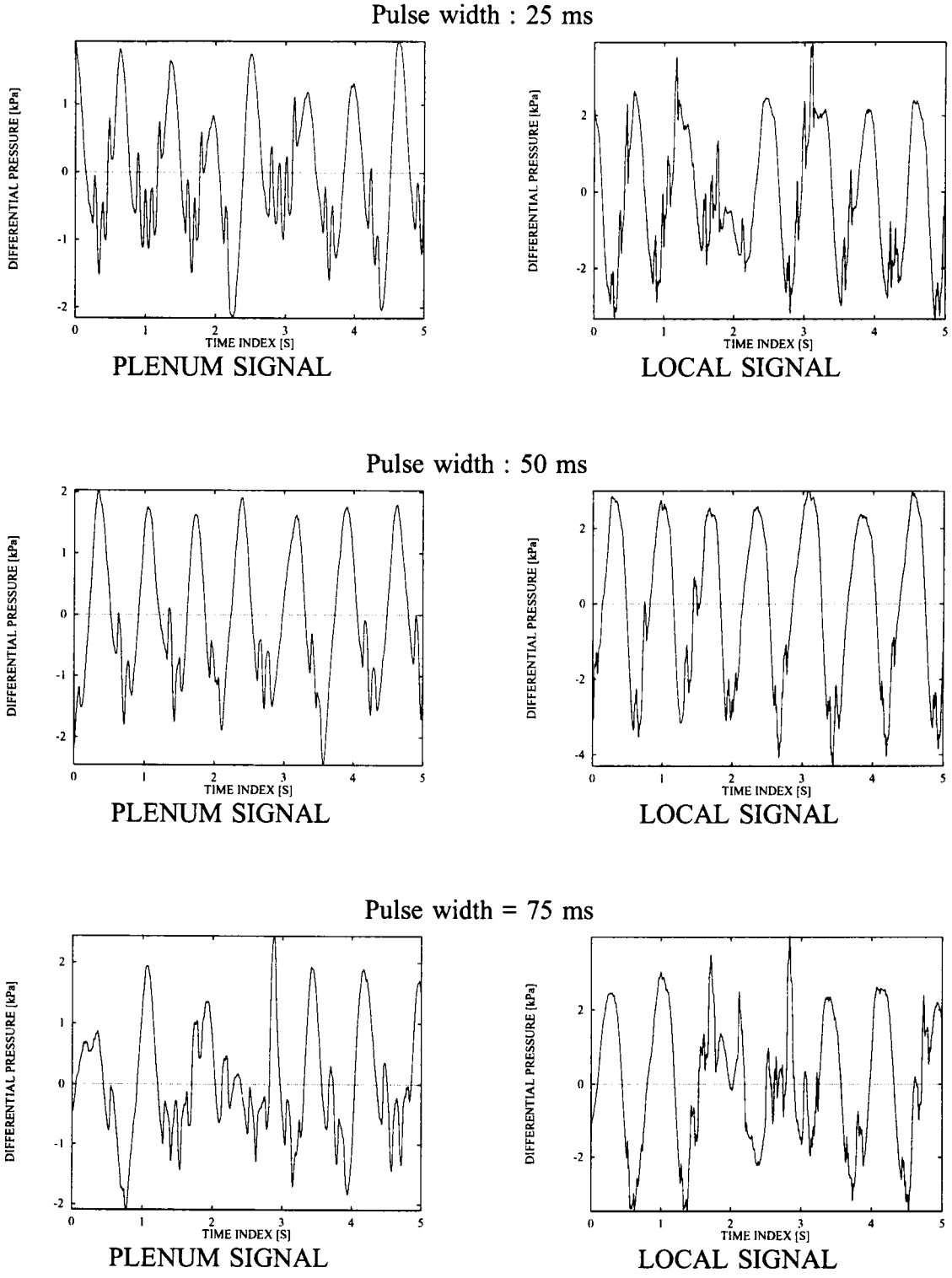
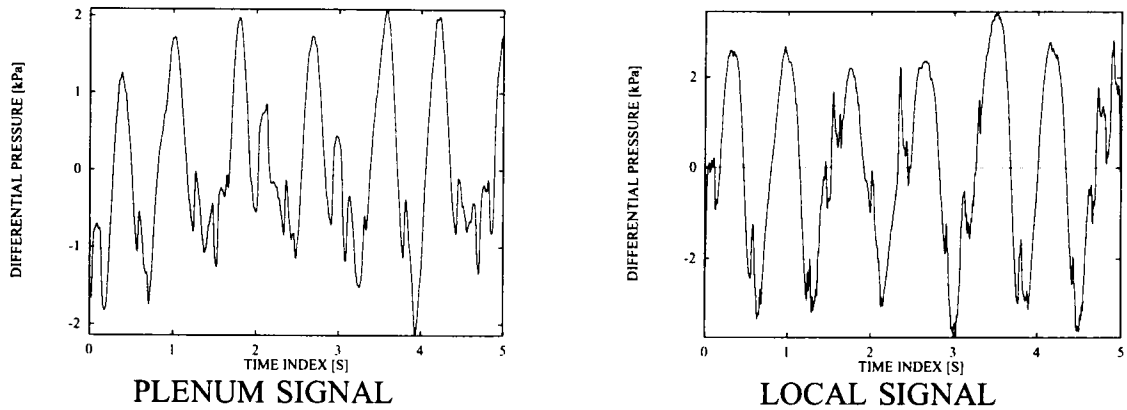


Figure C11. Typical time series segments for steel illustrating the effect of pulse width at a velocity of U/U_{MF} = 1.28, a fixed pulse timing of -0.47 kPa & down and over a range of pulse width (25 ms to 75 ms).

Pulse width : 100 ms



Pulse width = 150 ms

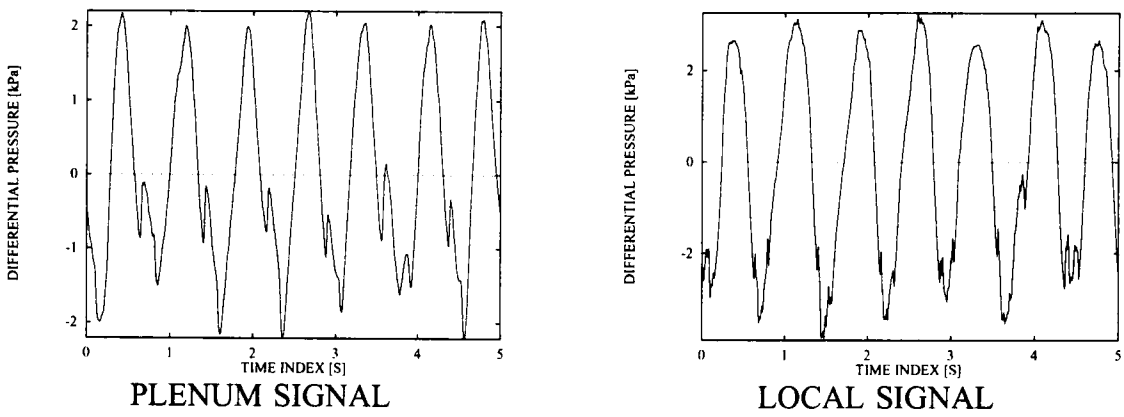
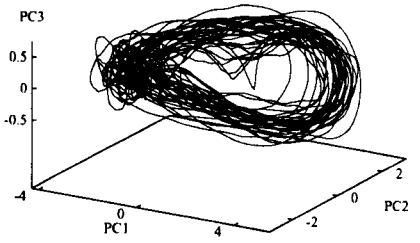
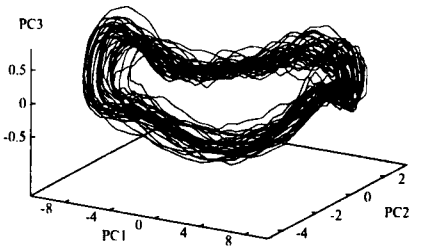


Figure C12. Typical time series segments for steel illustrating the effect of pulse width at a velocity of U/U_{MF} = 1.28, a fixed pulse timing of -0.47 kPa & down and over a range of pulse width (100 ms to 150 ms).

With no control

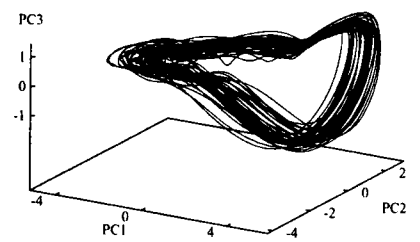


PLENUM SIGNAL

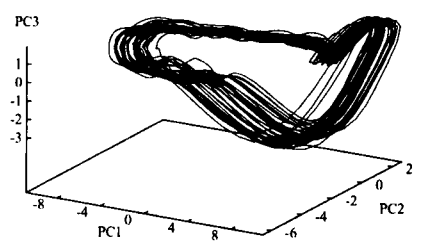


LOCAL SIGNAL

Pulse width : 25 ms

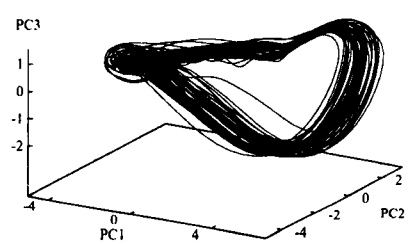


PLENUM SIGNAL

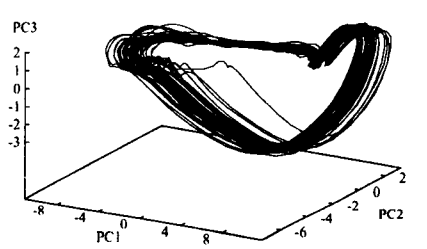


LOCAL SIGNAL

Pulse width = 50 ms



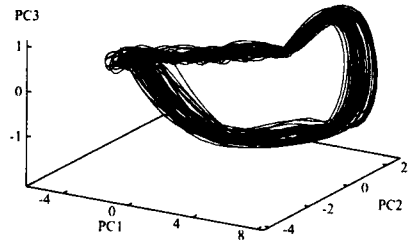
PLENUM SIGNAL



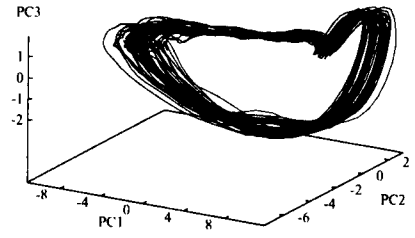
LOCAL SIGNAL

Figure C13. Three dimensional projection of the reconstructed trajectories for steel illustrating the effect of pulse width at a velocity of U/U_{MF} = 1.28, a fixed pulse timing of +0.93 kPa & up and over a range of pulse width (No control to 50 ms) [Time span = 25 s]

Pulse width : 75 ms

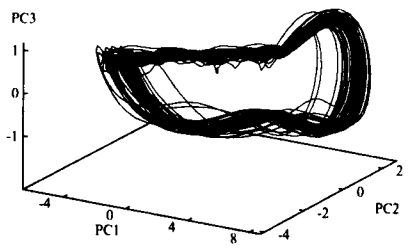


PLENUM SIGNAL

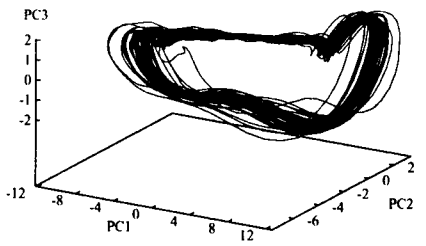


LOCAL SIGNAL

Pulse width : 100 ms

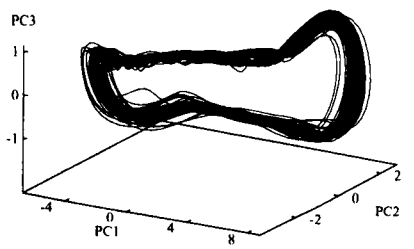


PLENUM SIGNAL

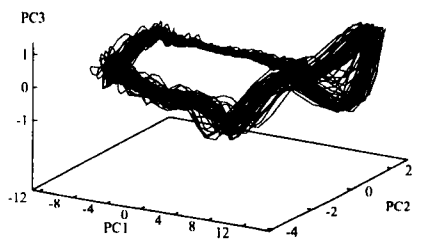


LOCAL SIGNAL

Pulse width = 150 ms



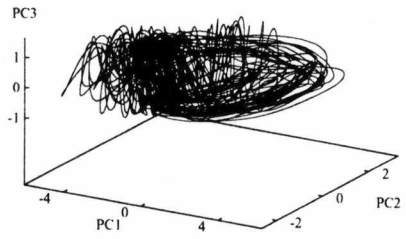
PLENUM SIGNAL



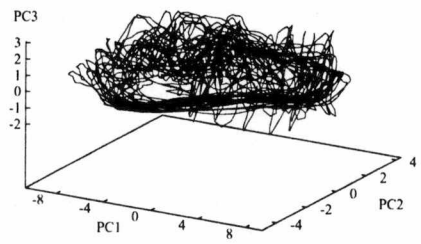
LOCAL SIGNAL

Figure C14. Three dimensional projection of the reconstructed trajectories for steel illustrating the effect of pulse width at a velocity of U/U_{MF} = 1.28, a fixed pulse timing of +0.93 kPa & up and over a range of pulse width (75 ms to 150 ms) [Time span = 25 s].

Pulse width : 25 ms

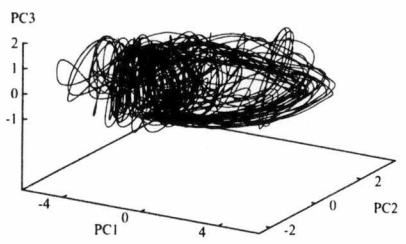


PLENUM SIGNAL

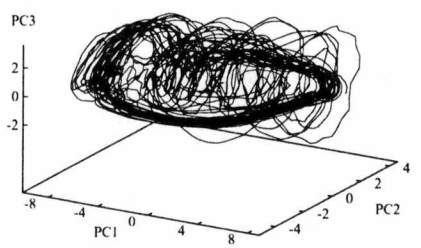


LOCAL SIGNAL

Pulse width : 50 ms

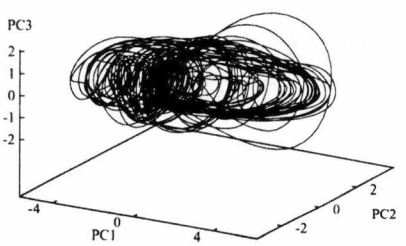


PLENUM SIGNAL

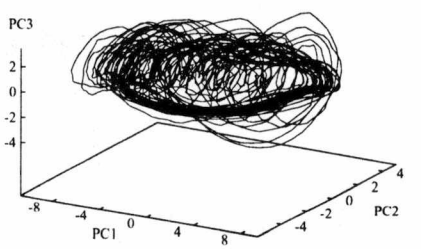


LOCAL SIGNAL

Pulse width = 75 ms



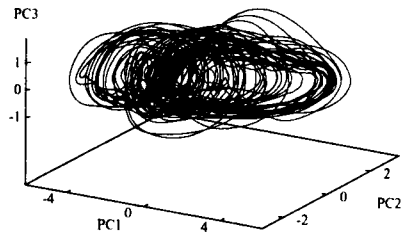
PLENUM SIGNAL



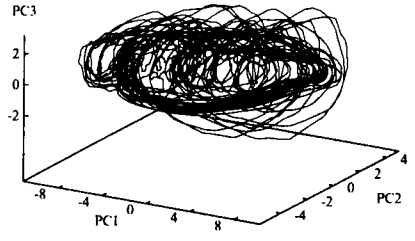
LOCAL SIGNAL

Figure C15. Three dimensional projection of the reconstructed trajectories for steel illustrating the effect of pulse width at a velocity of U/U_{MF} = 1.28, a fixed pulse timing of -0.47 kPa & down and over a range of pulse width (25 ms to 75 ms) [Time span = 25 s].

Pulse width : 100 ms

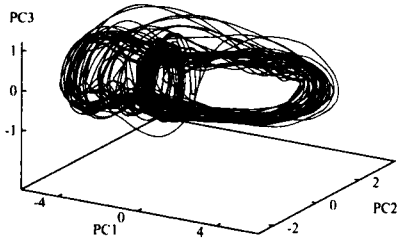


PLENUM SIGNAL

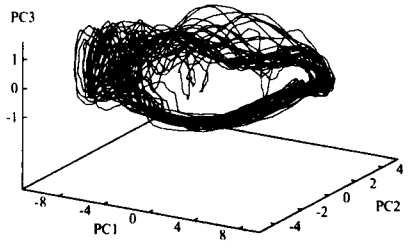


LOCAL SIGNAL

Pulse width = 150 ms



PLENUM SIGNAL



LOCAL SIGNAL

Figure C16. Three dimensional projection of the reconstructed trajectories for steel illustrating the effect of pulse width at a velocity of U/U_{MF} = 1.28, a fixed pulse timing of -0.47 kPa & down and over a range of pulse width (100 ms to 150 ms) [Time span = 25 s].

Table C1. Dimension results for evaluation of control experiments at different control modes for steel

CONTROL MODE	SIGNAL	CUT OFF [kPa]	SEGMENT LENGTH	DIMENSION [95 pct CI]
DEVELOPING SLUG REGIME [U/Umf = 1.16]				
NO CONTROL	LOCAL	1.08861	147.0	2.84 ± 0.07
NO CONTROL	PLENUM	0.49176	136.0	4.03 ± 0.06
DESTABILIZATION	LOCAL	0.78814	147.0	5.99 ± 0.31
DESTABILIZATION	PLENUM	0.40938	136.0	5.09 ± 0.20
STABILIZATION	LOCAL	1.23472	147.0	2.56 ± 0.04
STABILIZATION	PLENUM	0.70398	136.0	2.32 ± 0.04
MAXIMUM STABLE SLUGGING STATE [U/Umf = 1.28]				
NO CONTROL	LOCAL	1.95758	154.0	2.00 ± 0.04
NO CONTROL	PLENUM	0.89926	153.0	3.35 ± 0.07
DESTABILIZATION	LOCAL	1.60695	154.0	6.73 ± 0.10
DESTABILIZATION	PLENUM	0.78870	153.0	6.69 ± 0.07
STABILIZATION	LOCAL	2.06596	154.0	3.13 ± 0.06
STABILIZATION	PLENUM	1.35839	153.0	2.48 ± 0.05
BREAKING SLUGGING REGIME [U/Umf = 1.55]				
NO CONTROL	LOCAL	2.72976	152.0	3.51 ± 0.09
NO CONTROL	PLENUM	1.85719	159.0	4.08 ± 0.06
DESTABILIZATION	LOCAL	1.83583	152.0	7.63 ± 0.16
DESTABILIZATION	PLENUM	1.26794	159.0	6.43 ± 0.08
STABILIZATION	LOCAL	2.83192	152.0	3.38 ± 0.07
STABILIZATION	PLENUM	1.87748	159.0	4.09 ± 0.06

Table C2. Entropy results for evaluation of control experiments at different control modes for steel.

CONTROL MODE	SIGNAL	CUT OFF [kPa]	SEGMENT LENGTH	KML [BIT/S] [95 pct CI]
DEVELOPING SLUG REGIME [U/Umf = 1.16]				
NO CONTROL	LOCAL	1.0886	147.0	1.51 ± 0.07
NO CONTROL	PLENUM	0.4918	136.0	2.41 ± 0.10
DESTABILIZATION	LOCAL	0.7881	147.0	9.65 ± 1.83
DESTABILIZATION	PLENUM	0.4094	136.0	11.28 ± 0.54
STABILIZATION	LOCAL	1.2347	147.0	3.93 ± 0.07
STABILIZATION	PLENUM	0.7040	136.0	2.75 ± 0.08
MAXIMUM STABLE SLUGGING STATE [U/Umf = 1.28]				
NO CONTROL	LOCAL	1.9576	154.0	0.82 ± 0.06
NO CONTROL	PLENUM	0.8993	153.0	1.28 ± 0.10
DESTABILIZATION	LOCAL	1.6069	154.0	4.65 ± 0.09
DESTABILIZATION	PLENUM	0.7887	153.0	5.39 ± 0.11
STABILIZATION	LOCAL	2.0660	154.0	1.72 ± 0.07
STABILIZATION	PLENUM	1.3584	153.0	1.12 ± 0.08
BREAKING SLUGGING REGIME [U/Umf = 1.55]				
NO CONTROL	LOCAL	2.7298	153.0	2.06 ± 0.08
NO CONTROL	PLENUM	1.8572	159.0	1.96 ± 0.09
DESTABILIZATION	LOCAL	1.8358	153.0	10.16 ± 0.23
DESTABILIZATION	PLENUM	1.2679	159.0	6.75 ± 0.14
STABILIZATION	LOCAL	2.8319	153.0	1.93 ± 0.09
STABILIZATION	PLENUM	1.8775	159.0	1.76 ± 0.08

Table C3. Dimension results for evaluation of control experiment for glass at the breaking slug regime (U/U_{MF} = 1.59).

CONTROL MODE	SIGNAL	CUT OFF [kPa]	SEGMENT LENGTH	DIMENSION [95 pct CI]
NO CONTROL	LOCAL	1.23292	132.0	2.49 ± 0.05
NO CONTROL	PLENUM	0.96350	136.0	2.94 ± 0.06
DESTABILIZATION	LOCAL	0.86344	132.0	5.04 ± 0.08
DESTABILIZATION	PLENUM	0.58983	136.0	4.86 ± 0.07
STABILIZATION	LOCAL	1.27794	132.0	2.66 ± 0.07
STABILIZATION	PLENUM	1.09474	136.0	3.31 ± 0.06

Table C4. Entropy results for evaluation of control experiment for glass at the breaking slug regime (U/U_{MF} = 1.59).

CONTROL MODE	SIGNAL	CUT OFF [kPa]	SEGMENT LENGTH	KML [BIT/S] [95 pct CI]
NO CONTROL	LOCAL	1.2329	132.0	1.67 ± 0.11
NO CONTROL	PLENUM	0.9635	136.0	1.79 ± 0.13
DESTABILIZATION	LOCAL	0.8634	132.0	7.02 ± 0.15
DESTABILIZATION	PLENUM	0.5898	136.0	6.57 ± 0.13
STABILIZATION	LOCAL	1.2779	132.0	1.74 ± 0.12
STABILIZATION	PLENUM	1.0947	136.0	1.61 ± 0.08

VITA

M. Vasudevan was born in Palayam kottai, Tamil Nadu, India on May 19, 1963. He graduated from Coimbatore Institute of Technology, University of Madras in January 1985 earning the degree of Bachelor of Science in Mechanical Engineering. He then worked for Bharat Heavy Electricals Limited, a power plant equipment manufacturer in their Industrial Power Products Division. In January 1993, he began graduate study at the University of Tennessee, Knoxville and received the degree of Master of Science in Mechanical Engineering in August 1995.